

NASA - TM-X-72605

2024-1



76-06

National Space Science Data Center
World Data Center A For Rockets and Satellites

AP-8 Trapped Proton Environment for Solar Maximum and Solar Minimum

(NASA-TM-X-72605) AP-8 TRAPPED PROTON
ENVIRONMENT FOR SOLAR MAXIMUM AND SOLAR
MINIMUM (NASA) 176 p HC A09/MF A01 CSCL 03B

N 77-18983

Unclassified
G3/92 13122

DECEMBER 1976

NSSDC/WDC-A-R&S 76-06

AP-8 Trapped Proton Environment for
Solar Maximum and Solar Minimum

by

Donald M. Sawyer
James I. Vette

December 1976

National Space Science Data Center
National Aeronautics and Space Administration
Goddard Space Flight Center
Greenbelt, Maryland 20771

CONTENTS

	<u>Page</u>
I. INTRODUCTION	1
II. DATA ANALYSIS AND TIME VARIATIONS	2
III. MODEL GENERATION	6
IV. MODEL PRESENTATION FORMATS	7
V. MODEL COMPARISONS	8
VI. FUTURE IMPROVEMENTS	9
APPENDIX: AP8MAX and AP8MIN Data Card Deck Formats	11
REFERENCES	13

TABLE

Table

1. Data Used in Making AP8MAX and AP8MIN Models	19
---	----

ILLUSTRATIONS

Figure

1 Ten-Day Average Counting Rates for Proton Energies 25 to 100 MeV as Seen by Satellite 1963-038C	23
2 Ten-Day Average Counting Rates for Proton Energies 8.2 to 25 MeV as Seen by Satellite 1963-038C	24
3 Ten-Day Average Counting Rates for Proton Energies 2.2 to 8.2 MeV as Seen by Satellite 1963-038C	25
4 Counting Rates for Protons in the Range of 0.25 to 13.5 MeV at L = 2.0 R _E as Seen by Satellite Azur	26
5 Counting Rates for Protons in the Range of 0.25 to 13.5 MeV at L = 3.04 R _E as Seen by Satellite Azur	27
6 Counting Rates for Protons in the Range of 0.25 to 1.65 MeV at L = 4.85 R _E as Seen by Satellite Azur	28
7 Integral Spectra Obtained by a Generalized Least Squares Curve-Fitting Procedure	29
8-27 AP8MIN Omnidirectional Flux Distributions with L Values between 1.2 to 3.2 R _E and Energies between 0.1 and 400 MeV	30-49

ILLUSTRATIONS (concluded)

<u>Figure</u>		<u>Page</u>
28-38	AP8MIN Omnidirectional Flux Distributions with L Values between 3.0 to 6.6 RE and Energies between 0.1 and 400 MeV	50-60
39-58	AP8MAX Omnidirectional Flux Distributions with L Values between 1.2 to 3.2 RE and Energies between 0.1 and 400 MeV	61-80
59-64	AP8MIN and AP8MAX B-L Plots of Constant Intensity Flux Contours with Energies between 0.1 and 400 MeV	81-86
65-70	AP8MIN R- λ Plots of Constant Intensity Flux Contours with Energies between 0.1 and 400 MeV	87-92
71	AP8MIN Equatorial Radial Profiles with Energies between 0.1 and 400 MeV	93
72-79	AP8MIN Orbit-Integrated Omnidirectional Fluxes with Energies \leq 10 MeV and Altitudes between 150 and 18,000 Nautical Miles	94-101
80-87	AP8MIN Orbit-Integrated Omnidirectional Fluxes with Energies \geq 10 MeV and Altitudes between 150 and 9000 Nautical Miles	102-109
88-95	AP8MAX Orbit-Integrated Omnidirectional Fluxes with Energies between 0.1 and 400 MeV for Altitudes between 150 and 1000 Nautical Miles	110-117
96-105	AP8MIN and Data Flux vs B/B_0 Comparison Plots for Selected L Values between 1.15 and 6.60 RE	118-127
106-115	AP8MIN and Data Flux vs Energy Comparison Plots for Selected L Values between 1.15 and 6.60 RE	128-137
116-120	AP8MAX and Data Flux vs B/B_0 Comparison Plots for Selected L Values between 1.17 and 2.50 RE	138-142
121-125	AP8MAX and Data Flux vs Energy Comparison Plots for Selected L Values between 1.17 and 2.50 RE	143-147
126-130	AP8MIN and AP8MAX Flux vs B/B_0 Comparison Plots for Selected L Values between 1.17 and 2.50 RE	148-152
131-135	AP8MIN and AP8MAX Flux vs Energy Comparison Plots for Selected L Values between 1.17 and 2.50 RE	153-157
136-143	AP8MIN and AP-1, -5, -6, and -7 Flux vs B/B_0 Comparison Plots for Selected L Values between 1.2 and 6.60 RE ...	158-165
144-151	AP8MIN and AP-1, -5, -6, and -7 Flux vs Energy Comparison Plots for Selected L Values between 1.2 and 6.60 RE	166-173

I. INTRODUCTION

The purpose of this report is to provide a new computer-accessible model of the stably trapped proton flux with energies between 0.1 and 400 MeV. This model will be called AP-8.

The need for a new model arises from two main factors. First, to cover this approximate energy range, it was previously necessary to use the four separate models designated AP-1,¹ AP-5,² AP-6,³ and AP-7.⁴ Each of these models was derived independently, and this resulted in significant discontinuities in the energy spectra (see Section V. Model Comparisons). Second, new data have become available that indicate a need for improvement in the previous models in certain regions of space. Particularly useful for this effort have been the OV3-3⁵ and Azur^{6,7} data sets.

The basic approach in this effort has been empirical, with a reliance on theory in those regions of space where the data are uncertain or nonexistent. Comparison of the Azur data (beginning in November 1969) with data acquired prior to 1967 indicates that a reduction in the flux has occurred at low altitudes. This reduction is associated with the much discussed solar-cycle dependence.⁸⁻¹² Sufficient Azur data are available to generate a solar maximum version of AP-8, which is designated AP8MAX, epoch 1970. This version should also serve for the coming solar maximum period around 1980. The reduction in solar maximum fluxes may be smaller than that for the epoch 1970, depending upon the general solar activity and the X-ray/EUV output.

Because most of the data used in generating AP-8 were acquired around the solar minimum period of 1964, this version is designated AP8MIN, epoch 1964. AP8MAX differs from AP8MIN only for altitudes less than about 1000 km and for L values less than 3.0 Earth radii (see Section V. Model Comparisons).

Sections II and III, respectively, present the analysis of the data and the generation of the model elements.

Section IV discusses the presentation of the models in the form of nomographs, B-L plots, R-λ plots, and equatorial radial profiles. It also discusses nomographs of the orbit-integrated fluxes.

Section V discusses the comparison of the AP8MAX and AP8MIN models with each other, with the data, and with the previous AP models.

Section VI discusses the future needs to improve the models, such as more complete data coverage and periodic comparisons with newly available data sets.

The Appendix describes the machine-sensible format in which the models are available.

II. DATA ANALYSIS AND TIME VARIATIONS

Table 1 shows the data sets that have been considered in the construction of the models. Many of the old data sets and most of the new ones are unidirectional measurements. Therefore, we have converted all the omnidirectional measurements to unidirectional values. Where B field coverage was lacking, extrapolated points were generated by referring to similar data sets and the previous models. All further work was carried out using unidirectional values.

The next problem was to assess the effect of time variations on the intercomparability of the various data sets. Many authors have observed temporal variations of the trapped proton flux.¹⁰⁻⁴² In addition, time variations have been discussed in some detail in the documents for AP-5,² AP-6,³ and AP-7.⁴ Particularly useful for observing long-term variations was the continual coverage of satellite 1963-038C for over 5 years. Results have been published¹² for L values less than 3 Earth radii covering the period between October 1963 and December 1968. The following statements and observations describe the temporal variations for trapped protons.

As indicated in Figure 1,¹³ the inner zone is quite stable for protons^{22,23} with energies greater than 25 MeV. Above L = 2 Earth radii, some depletion occurs in response to major magnetic storms such as those of September 1963 and May 1967. The May 1967 storm had a maximum |Dst| value of about 370 gammas, and the 25- to 100-MeV proton flux at L = 2.2 Earth radii decreased by about a factor of four. The flux had nearly recovered to its prestorm value after 1 year 6 months, during which time there were no other large storms.¹³

In the energy range between 8.2 and 25 MeV, there are no large, rapid changes in the flux except in response to major storms such as those of September 1963 and May 1967 at L values above 2.2 Earth radii. However, satellite 1963-038C data indicated a steady decrease with a decay time of approximately 7 years for L values in the range between 1.35 and 2.2 Earth radii. These data are shown in Figure 2.¹³

In the energy range between 2.2 and 8.2 MeV, the flux at L = 3 Earth radii may either increase or decrease following a magnetic storm. The May 1967 storm resulted in an enhancement of more than a factor of 10, which was peaked at approximately L = 2.2 Earth radii. Depletion was observed at both higher and lower L values. In addition, there is evidence of a decrease in flux with a decay time of approximately 3 years 6 months for L values between 1.5 and 3 Earth radii. These data are shown in Figure 3.¹³

Protons with energies between 0.1 and 1.0 MeV have been difficult to measure at L < 2.0 Earth radii because of background problems from high-energy protons and electrons. Results from the Azur satellite have indicated substantially less flux in this region than previously believed.⁷ The National Space Science Data Center (NSSDC) has received temporal plots of these data covering the time period between November 1969 and July 1970

and including L values between 1.26 and 5.2 Earth radii. The energy response is composed of four contiguous channels covering the range between 0.25 and 13.5 MeV. The largest storm during this period occurred in March 1970 and had a maximum |Dst| value of 270 gammas. The first observable storm variation, which is an increase of less than a factor of two, occurs at L = 2 Earth radii in the 0.25- to 0.5- and 0.5- to 1.0-MeV channels. At lower L values, no obvious storm effects are evident in any channel; the maximum long-term variation is less than a factor of two. A sample of these data is shown as Figure 4.

At altitudes less than about 1000 km, atmospheric variations have produced observable changes in the inner zone trapped proton flux, which are in reasonable agreement with theory.⁹⁻¹² Heckman et al.¹² have observed the 50- to 90-MeV proton flux at $h_{\min} = 350$ km decrease by 60 percent between 1966 and 1969. They have also presented evidence of a semi-annual variation in the fluxes, which they relate to an observed semiannual atmospheric density variation. Dragt⁸ has made extensive calculations predicting the solar-cycle dependence of the proton flux, based on the solar-cycle atmospheric density variation and a neutron decay source in a time-independent magnetic field. It is now known that the secular decrease of the Earth's magnetic field must be included in a complete theoretical description of the inner belt protons.^{43,44} In addition, the neutron spectrum between 10 and 100 MeV has been measured^{45,46} and found to be harder than that used by Dragt.⁸ Nevertheless, these calculations may still qualitatively represent the expected solar-cycle variations. Quantitatively, they are the best currently available. For example, at L = 1.6 Earth radii and $h_{\min} = 510$ km the differential energy flux at 24 MeV is predicted to vary by a factor of 10 during the solar cycle while this flux at 760 MeV varies by a factor of three and lags the atmospheric density variation by about 1 year.⁸

A temporal perturbation occurred within the inner zone as a result of the Starfish nuclear detonation on July 9, 1962. Filz and Holeman¹⁹ reported an abrupt increase of about a factor of seven in the 55-MeV trapped proton flux at an altitude of 350 ± 50 km. The flux decayed to a constant level within 1 year, as the solar-cycle increase offset the Starfish decay. However, Starfish protons contributed significantly to the measured flux for a period of about 4 years after the detonation.

McIlwain²⁴ has observed the inward radial diffusion of a secondary peak of unknown origin in the 40- to 110-MeV equatorial proton flux. The peak was seen to move from L = 2.25 to L = 2.1 Earth radii between January 1963 and January 1965. At this rate, it should have merged with the primary peak by 1969 although we have no additional equatorial data at these energies to confirm this conclusion.

A new low-energy proton population in the inner zone has been found deep in the atmosphere at L = 1.0 to L = 1.1 Earth radii.^{47,48} This population appears to originate from the breakup of neutral particles that charge exchange produced in the outer zone ring current during storms.

The outer zone is considerably less stable than the inner zone, particularly on short time scales, because of the larger variations in the magnetic field during storms. The first short-term variation seen in the outer zone protons was reported by Davis and Williamson.²⁷ A sudden commencement on September 30, 1961, followed by a storm with a maximum $|D_{st}|$ value of 159 gammas, was associated with a factor-of-three decrease in the greater than 0.1-MeV proton fluxes at high latitudes in the L region between 3 and 4.5 Earth radii. Such decreases during storms have been reported by others.^{33,40} These decreases have recently been found to be adiabatic responses to the decreased magnetic field during storms.⁴²

Between December 1962 and February 1965, Davis and Williamson²⁸ observed a factor-of-two or more increase in the proton flux having energies greater than 0.5 MeV in the region between $L = 2.5$ and $L = 5$ Earth radii. At the same time, the 0.1- to 0.3-MeV flux decreased about a factor of three. White³⁰ has reported similar observations at high B values.

The Azur data of Moritz⁴⁹ show a large response to the March 1970 storm at high B values. At $L = 3.04$ Earth radii and $B = 0.15$ gauss, the 0.25- to 0.5-MeV flux increased by a factor of 20. After 4 months, which included three small storms, the flux was still a factor of four above the prestorm level. At the same time, the 1.65- to 13.5-MeV flux decreased by a factor of eight and then recovered in about 15 days. However, the net effect of the magnetic activity during the first 6 months of 1970 resulted in a factor-of-two decrease in the flux at $L = 3.04$ Earth radii as shown in Figure 5. At $L = 4.85$ Earth radii and $B = 0.17$ gauss, the 0.25- to 0.5- and 1.0- to 1.65-MeV fluxes showed order-of-magnitude fluctuations during the first 6 months of 1970. These data are shown in Figure 6.

Above $L = 5$ Earth radii, order-of-magnitude fluctuations were observed by Davis and Williamson²⁸ on time scales as short as 10 minutes. The Azur data of Moritz⁴⁹ also showed fluctuations up to factors of 50 at $L = 5.2$ Earth radii and $B = 0.17$ gauss.

At the synchronous orbit ($L = 6.6$ Earth radii), the particle population exhibits extremely dynamic behavior.¹⁴ At times, the solar wind momentum is sufficient to compress the boundary of the Earth's magnetic field on the sunward side to a position inside the synchronous orbit. As a result, the higher energy trapped particles disappear. In addition, solar protons have easy access to the synchronous region, especially during disturbed times.⁵⁰ (For a quantitative estimate of the relative importance of solar and trapped fluxes for various spacecraft orbits, see the report by King and Stassinopoulos.⁵¹) Stevens et al.³⁸ have measured protons in the range between 0.06 and 3.3 MeV at $L = 6.6$ Earth radii. Quiet time fluxes showed a factor-of-four variation between noon and midnight because of the distortion of the magnetosphere. Magnetic storms resulted in an increase of the 2.6-MeV flux by more than a factor of 10 while the fluxes at intermediate energies dropped by a factor of 10. As the activity subsided, the fluxes rose to slightly above prestorm levels.

In summary, the inner zone is quite stable except at altitudes less than 1000 km where the solar-cycle variation becomes increasingly important. The long-term decrease seen in the lower energies is not understood, and therefore, its projection into the future is uncertain. Beyond $L = 2$ Earth radii, the effect of major storms becomes noticeable as nonadiabatic changes in the fluxes that recover with time constants varying from months to years. Beyond about $L = 5$ Earth radii, order-of-magnitude fluctuations occur on time scales as short as 10 minutes.

The results from the Azur spacecraft have provided sufficient data to observe the effects of the solar-cycle variation and to permit the generation of a solar maximum model. However, the absolute accuracy of the models at low altitudes is uncertain. The atmosphere below approximately 600 km causes a rapid drop in the fluxes with decreasing altitude. The resulting large spatial gradients are difficult to model accurately because small errors in the B and L coordinates can result in large flux changes. Nevertheless, the two models should provide a useful representation of the solar-cycle variation and also allow for updating as new data become available.

No attempt has been made to model the long-term decrease seen in the inner zone by satellite 1963-038C.¹³ A confirmation of this decrease by another satellite would be useful. Because the decay time varies from 3 to 7 years, a satellite with a comparable operating lifetime would be ideal.

No attempt has been made to model the temporal variations between $L = 2$ and 4.5 Earth radii with altitudes greater than 1000 km. These variations are produced by large storms in ways that depend on the details of each storm. It is expected that these storm effects will generally be less than a factor of two when averaged over a year.

As more data are obtained in the region $L \geq 4.5$ Earth radii, a time statistical treatment may be feasible. The present modeling effort in that region has relied primarily on quiet time data, which may underestimate the average flux at some energies. In addition, the local time variation, which can amount to a factor of four at $L = 6.6$ Earth radii, has not been included explicitly. Instead, the model flux has been based on the higher flux observed at local noon.³⁸

III. MODEL GENERATION

The previous models used an analytic function in the form of either a power law or an exponential to fit the energy spectrum. However, the entire energy range between 0.1 and 400 MeV cannot be fit by such a simple function in the inner zone.^{4,52} Because the models are now being issued in tabular form, it was decided to use an analytic function only as an aid in the comparison of various data sets. The functional form chosen was the sum of two exponential-like terms having a total of six coefficients. This function was written as

$$j = A_1 e^{A_2 E^{A_3}} + B_1 e^{B_2 E^{B_3}}$$

where A_1 , A_2 , A_3 , B_1 , B_2 , and B_3 are the coefficients, E is the energy, and j is the differential flux. This function was then employed in a least squares program that simultaneously minimized the deviations for both energy interval and energy threshold points. The result was a single integral energy spectrum at a given B-L point. This technique was useful in the inner zone where there were more than six measurements available at each point. Typical spectra for various B values at $L = 1.6$ Earth radii are shown in Figure 7. A heavy line gives the resulting best-fit spectrum for each B (B/B_0) value. The energy interval data points were plotted at the minimum interval energy, and a line was drawn to the fitted spectrum at the maximum interval energy. Where sufficient data were unavailable for the least squares approach, spectra were drawn by hand. All spectra were then digitized and compared again with the data.

From the spectra, flux versus B value curves were generated and smoothed by slight adjustment of the B values. The flux versus B curves were then used to generate radial profiles that were also smoothed and digitized. These profiles were then used to generate new spectra. This completed one iteration. Two iterations were found to give smooth spectra and flux versus B curves, as well as reasonable radial profiles. The smoothed flux versus B curves were then converted to omnidirectional values for incorporation into the final model format. This format is discussed in the Appendix.

IV. MODEL PRESENTATION FORMATS

The models are displayed in several formats within this report. The most extensive presentation is in the form of nomographs that provide rapid interpolation of omnidirectional integral flux values as a function of B and L . A description of the use of these nomographs (also called carpet plots) is given in Appendix A of The Inner Zone Electron Model AE-5.⁵³

Figures 8 through 27 present the solar minimum model AP8MIN nomographs for L values between 1.2 and 3.2 Earth radii with energies between 0.1 and 400 MeV. Figures 28 through 38 contain the L values between 3 and 6.6 Earth radii. Because the solar maximum model AP8MAX does not differ from AP8MIN for L values above 2.9 Earth radii, nomographs for the solar maximum model are not shown for all L values. Figures 39 through 58 present the AP8MAX nomographs for L values between 1.2 and 3.2 Earth radii.

Plots of constant intensity contours are presented in both $B-L$ and $R-\lambda$ plots. Figures 59 through 64 show the $B-L$ contours at six energies for the AP8MIN and AP8MAX models. Figures 65 through 70 show the corresponding $R-\lambda$ plots for AP8MIN.

Equatorial radial profiles at several energies are shown in Figure 71 for the model AP8MIN. The AP8MAX equatorial radial profiles differ from AP8MIN only for L below 1.3 Earth radii and, therefore, are not shown.

The final set of model presentation figures shows orbit-integrated fluxes in the nomograph format. Figures 72 through 79 and Figures 80 through 87 give the AP8MIN orbit-integrated fluxes for energies less than or equal to 10 MeV and greater than or equal to 10 MeV, respectively. The AP8MAX model differs from the AP8MIN model only at low altitudes. Therefore, Figures 88 through 95 include only the AP8MAX orbit-integrated fluxes below 1000 nautical miles.

It should be noted that high-altitude orbits can pass through regions of space with significant fluxes where the L values are greater than 6.6 Earth radii. Although the models are only valid up to $L = 6.6$ Earth radii, the models will give flux values at higher L values based on an extrapolation to zero flux at $L = 11$ Earth radii. The maximum orbit altitude presented here is 18,000 nautical miles, which corresponds to an L value of about 6.3 Earth radii. The maximum contribution to an orbit-integrated flux value from regions $L > 6.6$ Earth radii is less than 15 percent.

V. MODEL COMPARISONS

Figures 96 through 151 show comparisons of the AP8MIN and AP8MAX models with the data, with themselves, and with the earlier models designated AP-1,¹ AP-5,² AP-6,³ and AP-7.⁴ The models are displayed as flux versus B field curves and as flux versus energy curves at a given L value for each type of comparison. The data set codes are listed in each figure when data are presented. Table 1 describes the data set associated with each code. The plotting symbol corresponding to a given code is also shown. For a few of the figures, the large number of data sets required the association of a plotting symbol with more than one code. The ambiguity can be removed by noting the data set energy range and then referring to Table 1.

The flux versus B (B/B_0) field curves are plotted against log-log or log linear scales for selected integral energies. B_0 is the equatorial B value as given in the upper right-hand corner of each figure. This B_0 value is computed from

$$B_0 = 0.311653/L^3 \text{ (gauss)}$$

where L is the L value in Earth radii. Each model curve is labeled with the corresponding integral energy value.

The flux versus energy curves are plotted against log-log scales. The model curves are labeled with the corresponding B/B_0 values. Data points associated with a given curve have their symbols followed by a numerical subscript. Number one refers to the spectral curve with the smallest B/B_0 value, and the higher numbers are matched with the larger B/B_0 values in a monotonically ascending order. Some data points represent fluxes measured within an energy interval. An interval flux is added to the model flux obtained at the upper interval energy, and the resulting flux is plotted with the appropriate symbol at the lower interval energy. A dashed line is drawn from the model curve at the upper interval energy to the plotted symbol.

Figures 96 through 115 present flux versus B/B_0 and flux versus energy curves from the AP8MIN model and compare them with selected data sets for 10 different L values.

Figures 116 through 125 present the corresponding curves from the AP8MAX model and compare them with the Azur data sets for five different L values.

The AP8MIN and AP8MAX models are compared directly in Figures 126 through 135.

The final set of figures from 136 through 151 shows the comparison between the AP8MIN model and the earlier models designated AP-1,¹ AP-5,²

AP-6,³ and AP-7.⁴ A major difference is apparent in the inner zone low-energy flux at $L = 1.5$ Earth radii as shown in Figure 145. The new model (AP8MIN) has less flux at the equator for energies below about 1.0 MeV in accordance with the Azur results.⁷ At the higher L values, such as $L = 6.6$ Earth radii shown in Figure 143, the AP8MIN flux versus B/B_0 curves are cut off at lower B/B_0 values. This is also in accordance with the Azur results.⁷

VI. FUTURE IMPROVEMENTS

Despite the large number of data sets available for this modeling effort, there are some regions of space, time, and energy that are not well covered.

The spectrum in the inner zone for energies above 150 MeV is not well supported by data in these models. Results from the OV1-19 satellite should improve this situation.

There are few equatorial measurements for energies above 10 MeV at L values between 2.0 and 3.5 Earth radii. This is the region in which McIlwain observed a secondary radial peak in the 40- to 110-MeV flux that was seen to diffuse inward.²⁴

A long-term monitor should be initiated for proton fluxes out to $L = 3$ Earth radii with energies less than 25 MeV. Satellite 1963-038C instruments have measured decay times of 3 to 7 years in this region.¹³ Such a monitor could be expected to yield considerable information on the sources and losses of these particles.

Additional observations of the low-energy fluxes above $L = 5$ Earth radii should eventually allow a statistical treatment of these rapidly varying fluxes.

The solar-cycle dependence of the low-altitude fluxes is very difficult to model accurately. It is hoped that sufficient data will be obtained through the coming solar maximum period to improve the model considerably in this area.

As significant new data sets become available, it is expected that brief reports will be issued comparing the data with the AP8MAX and AP8MIN models.

APPENDIX

AP8MAX and AP8MIN Data Card Deck Formats

The models AP8MAX and AP8MIN are available as separate data card decks. This is in contrast to the recent electron models, such as AE-5,⁵³ which are available as BLOCK DATA decks.⁵⁴ The only difference between these two forms is in the method of input to the programs. The BLOCK DATA deck is a FORTRAN subprogram that inputs the data before execution. The current AP-8 decks may be input with FORTRAN read statements. The BLOCK DATA deck format was impractical for the AP-8 models because AP8MIN requires 16,591 storage locations and AP8MAX requires 16,304 storage locations. Because this amount of storage will be prohibitive to some users, compressed versions of approximately 7000 words each are available in BLOCK DATA statement form. These versions are designated AP8MIC and AP8MAC and are compatible with programs MODEL and ORP⁵⁴ issued previously.

The data deck cards have the following two formats:

<u>Card Number</u>	<u>Variable Name</u>	<u>Columns</u>	<u>Format</u>	<u>Function</u>
1	DESCR(1)	1- 4	1A4	Model name
	DESCR(2)	5- 8	1A4	Model name (concluded)
	DESCR(3)	11-20	F10.3	Epoch year
	DESCR(4)	21-30	F10.3	Energy scaling factor
	DESCR(5)	31-40	F10.3	L value scaling factor
	DESCR(6)	41-50	F10.3	B/B ₀ value scaling factor
	DESCR(7)	51-60	F10.3	Flux scaling factor
	DESCR(8)	61-70	I10	Length of data array minus one
	LB	71-74	A4	Card sequence identifier
	IC	75-78	I4	Card sequence number
2 through N	LIST(I), I=1,7	1-70	7I10	Model integer values ⁵⁴⁻⁵⁶
	LB	71-74	A4	Card sequence identifier
	IC	75-78	I4	Card sequence number

where N is 2370 and 2329 for AP8MIN and AP8MAX, respectively.

It is recommended that the model data be read into common block arrays of the form

COMMON/AP8MIN/D8MIN(8),L8MIN(16583)
COMMON/AP8MAX/D8MAX(8),L8MAX(16296)

for the AP8MIN and AP8MAX models, respectively. A subroutine that will

read in and print the model data is as follows:

```
SUBROUTINE MODINT(JUNIT,DESCR,LIST)
DIMENSION DESCRIPTOR(8),LIST(1)
EQUIVALENCE(LENGTH,DUMD)
READ(JUNIT,1000,END=30)(DESCRIPTOR(I),I=1,7),LENGTH,LB,IC
DESCRIPTOR(8)=DUMD
WRITE(6,1002)(DESCRIPTOR(I),I=1,7),LENGTH,LB,IC
LNT=LENGTH+1
LP=LNT/7
LPP=LP*7
IF(LPP.NE.LNT) LP=LP+1
LP=LP+1
K1=1
DO 20 IC=2,LP
K2=K1+5
READ(JUNIT,1001,END=30)(LIST(K),K=K1,K2),LB,IC
WRITE(6,1003)(LIST(K),K=K1,K2),LB,IC
20 K1=K2+1
RETURN
30 WRITE(6,1004)
RETURN
1000 FORMAT(2A4,2X,5F10.3,I10,A4,I4)
1001 FORMAT(7I10,A4,I4)
1002 FORMAT(2X,2A4,2X,5F10.3,I10,2X,A4,I4)
1003 FORMAT(2X,7I10,2X,A4,I4)
1004 FORMAT(5X,'***READ EOF ON JUNIT***')
END
```

The AP8MIN model would be read in from data cards with the following call:

```
CALL MODINT(JUNIT,D8MIN,L8MIN)
```

where JUNIT is the card reader unit number.

NOTE: The dimension of LIST is determined in the calling routine.

REFERENCES

1. Vette, J. I., Models of the Trapped Radiation Environment, Volume I: Inner Zone Protons and Electrons, NASA SP-3024, 1966.
2. King, J. H., Models of the Trapped Radiation Environment, Volume IV: Low Energy Protons, NASA SP-3024, 1967.
3. Lavine, J. P., and J. I. Vette, Models of the Trapped Radiation Environment, Volume V: Inner Belt Protons, NASA SP-3024, 1969.
4. Lavine, J. P., and J. I. Vette, Models of the Trapped Radiation Environment, Volume VI: High Energy Protons, NASA SP-3024, 1970.
5. Paulikas, G., J. Blake, and S. Freden, private communication, 1972.
6. Hovestadt, D., private communication, 1971.
7. Moritz, J., "Measurements of Radiation Belt Protons in the Energy Range 0.25 to 1.65 MeV on Board the Satellite 'AZUR,'" Z. Geophys., 37, 179-194, July 1971.
8. Dragt, A. J., "Solar Cycle Modulation of the Radiation Belt Proton Flux," J. Geophys. Res., 76, 2313-2344, April 1971.
9. Blanchard, R. C., and W. N. Hess, "Solar Cycle Changes in Inner-Zone Protons," J. Geophys. Res., 69, 3927-3938, October 1964.
10. Nakano, G. H., and H. H. Heckman, "Evidence for Solar-Cycle Changes in the Inner-Belt Protons," Phys. Rev. Lett., 20, 806-809, April 1968.
11. Imhof, W. L., "The Low-Altitude Radiation Environment," Models of the Trapped Radiation Environment, Volume VII: Long Term Time Variations, NASA SP-3024, 1971.
12. Heckman, H. H., P. J. Lindstrom, and G. H. Nakano, "Long-Term Behavior of Energetic Inner-Belt Protons," Models of the Trapped Radiation Environment, Volume VII: Long Term Time Variations, NASA SP-3024, 1971.
13. Bostrom, C. O., D. S. Beall, and J. C. Armstrong, "Time History of the Inner Radiation Zone," Models of the Trapped Radiation Environment, Volume VII: Long Term Time Variations, NASA SP-3024, 1971.
14. Paulikas, G. A., and J. B. Blake, "The Particle Environment at the Synchronous Altitude," Models of the Trapped Radiation Environment, Volume VII: Long Term Time Variations, NASA SP-3024, 1971.

15. Imuda, A. J., G. F. Pieper, and C. O. Bostrom, "Trapped Protons in the South Atlantic Magnetic Anomaly, July through December 1961 3. Magnetic Storms and Solar Proton Events," J. Geophys. Res., 70, 2045-2056, May 1965.
16. Pizzella, G., "On the Inner Van Allen Zone of the Earth," Nuovo Cimento, 29, 867-882, August 1963.
17. Heckman, H. H., and G. H. Nakano, "Low-Altitude Trapped Protons During Solar Minimum Period, 1962-1966," J. Geophys. Res., 74, 3575-3590, July 1969.
18. Bostrom, C. O., and J. C. Armstrong, "The Effects of the September 20-23, 1963, Magnetic Disturbances on the Inner Zone Protons," (abstract) Trans. Am. Geophys. Union, 47, 479, September 1966.
19. Filz, R. C., and E. Holeman, "Time and Altitude Dependence of 55-MeV Trapped Protons, August 1961 to June 1964," J. Geophys. Res., 70, 5807-5822, December 1965.
20. Fillius, R. W., "Trapped Protons of the Inner Radiation Belt," J. Geophys. Res., 71, 97-123, January 1966.
21. Krimigis, S. M., and A. L. Burns, "The Time Dependence of Low Energy Protons and Alpha Particles in the Radiation Belts," paper presented at International Symposium on the Physics of the Magnetosphere, Washington, D. C., September 3-13, 1968 (not published).
22. McIlwain, C. E., "Redistribution of Trapped Protons During a Magnetic Storm," Space Research V, North-Holland Publishing Company, Amsterdam, The Netherlands, 1965.
23. Pieper, G. F., "Temporal Stability of Inner Zone Protons," in Radiation Trapped in the Earth's Magnetic Field, edited by B. M. McCormac, D. Reidel Publishing Company, Dordrecht, The Netherlands, 1966.
24. McIlwain, C. E., "Long-Term Changes in the Distribution of the 40- to 110-MeV Trapped Protons," (abstract) Trans. Am. Geophys. Union, 46, 141, March 1965.
25. Bostrom, C. O., D. S. Beall, and J. C. Armstrong, "Trapped Particles in the Inner Zone, 1963 through 1967," paper presented at International Symposium on the Physics of the Magnetosphere, Washington, D. C., September 3-13, 1968 (not published).
26. "Collected Papers on the Artificial Radiation Belt from the July 9, 1962, Nuclear Detonation," edited by W. N. Hess, J. Geophys. Res., 68, 605-946, February 1963.

27. Davis, L. R., and J. M. Williamson, "Low-Energy Trapped Protons," in Space Research III, North-Holland Publishing Company, Amsterdam, The Netherlands, 1963.
28. Davis, L. R., and J. M. Williamson, "Outer Zone Protons," in Radiation Trapped in the Earth's Magnetic Field, edited by B. M. McCormac, D. Reidel Publishing Company, Dordrecht, The Netherlands, 1966.
29. Fillius, R. W., and C. E. McIlwain, A Survey of Inner Zone Protons, University of California, San Diego, NAS 5-1683, April 1965.
30. White, R. S., "Time Dependence of the Low-Energy Proton Belts," J. Geophys. Res., 72, 943-950, February 1967.
31. Fillius, R. W., "Storm Time Changes in Low-Energy Trapped Protons," (abstract) Trans. Am. Geophys. Union, 47, 129, March 1966.
32. Brown, W. L., L. J. Cahill, L. R. Davis, C. E. McIlwain, and C. S. Roberts, "Acceleration of Trapped Particles During a Magnetic Storm on April 18, 1965," J. Geophys. Res., 73, 153-161, January 1968.
33. Smith, P. H., and R. A. Hoffman, "Ring Current Particle Distributions During the Magnetic Storms of December 16-18, 1971," J. Geophys. Res., 78, 4731-4737, August 1973.
34. Gabbe, J. D., and W. L. Brown, "Some Observations of the Distribution of Energetic Protons in the Earth's Radiation Belts Between 1962 and 1964," in Radiation Trapped in the Earth's Magnetic Field, edited by B. M. McCormac, D. Reidel Publishing Company, Dordrecht, The Netherlands, 1966.
35. Burns, A. L., and S. M. Krimigis, "Changes in the Distribution of Low-Energy Trapped Protons Associated with the April 17, 1965, Magnetic Storm," J. Geophys. Res., 77, 112-130, January 1972.
36. Soraas, F., and L. R. Davis, "Temporal Variations of the 100 Kev to 1700 Kev Trapped Protons Observed on Satellite Explorer 26 During First Half of 1965," NASA TMX-63320, Goddard Space Flight Center, Greenbelt, Md., August 1968.
37. Randall, B. A., "Time Variations of Magnetospheric Intensities of Outer Zone Protons, Alpha Particles and Ions ($Z>2$)," University of Iowa Report 73-3, Iowa City, Iowa, NASA CR-130860, January 1973.
38. Stevens, J. R., E. F. Martina, and R. S. White, "Proton Energy Distributions from 0.060 to 3.3 MeV at 6.6 Earth Radii," J. Geophys. Res., 75, 5373-5385, October 1970.

39. Imhof, W. L., and J. b. Reagan, "Studies of Outer Belt and Slot Region Protons at Low Altitudes," J. Geophys. Res., 77, 4128-4144, August 1972.
40. Williams, D. J., "Trapped Protons \geq 100 KeV and Possible Sources," in Particles and Fields in the Magnetosphere, edited by B. M. McCormac, D. Reidel Publishing Company, Dordrecht, The Netherlands, 1970.
41. Smith, P. H., and R. A. Hoffman, "Direct Observations in the Dusk Hours of the Characteristics of the Storm Time Ring Current Particles During the Beginning of Magnetic Storms," J. Geophys. Res., 79, 966-971, March 1974.
42. Lyons, L. R., and D. J. Williams, "Storm-Associated Variations of Equatorially Mirroring Ring Current Protons, 1-800 Kev, at Constant First Adiabatic Invariant," J. Geophys. Res., 81, 216-220, January 1976.
43. Heckman, H. H., and P. J. Lindstrom, "Response of Trapped Particles to a Collapsing Dipole Moment," J. Geophys. Res., 77, 740-743, February 1972.
44. Schulz, M., and G. A. Paulikas, "Secular Magnetic Variation and the Inner Proton Belt," J. Geophys. Res., 77, 744-747, February 1972.
45. Preszler, A. M., G. M. Simnett, and R. S. White, "Earth Albedo Neutrons from 10 to 100 MeV," Phys. Rev. Lett., 28, 982-985, April 1972.
46. Heidbreder, E., K. Pinkau, C. Reppin, and V. Schonfelder, "Measurements of the Distribution in Energy and Angle of High-Energy Neutrons in the Lower Atmosphere," J. Geophys. Res., 76, 2905-2916, May 1971.
47. Hovestadt, D., B. Häusler, and M. Scholer, "Observation of Energetic Particles at Very Low Altitudes Near the Geomagnetic Equator," Phys. Rev. Lett., 28, 1340-1344, May 1972.
48. Moritz, J., "Energetic Protons at Low L-Values of the Equatorial Magnetosphere," in Space Research XIII, North-Holland Publishing Company, Amsterdam, The Netherlands, 1973.
49. Moritz, J., private communication, 1972.
50. Lanzerotti, L. J., "Access of Solar Particles to Synchronous Altitude," in Intercorrelated Satellite Observations Related to Solar Events, edited by V. Manno and D. E. Page, D. Reidel Publishing Company, Dordrecht, The Netherlands, 1970.

51. King, J. H., and E. G. Stassinopoulos, "Energetic Solar Proton vs. Terrestrially Trapped Proton Fluxes," J. Spacecraft and Rockets, 12, 122-124, February 1975.
52. Valot, P., "Differential Energy Spectrum of Geomagnetically Trapped Protons with the ESRO 2 Satellite," J. Geophys. Res., 77, 2309-2318, May 1972.
53. Teague, M. J., and J. I. Vette, "The Inner Zone Electron Model AE-5," NSSDC 72-10, NASA TMX-69987, Goddard Space Flight Center, Greenbelt, Md., November 1972.
54. Teague, M. J., K. W. Chan, and J. I. Vette, "AE 6: A Model Environment of Trapped Electrons for Solar Maximum," NSSDC/WDC-A-R&S 76-04, NASA TMX-72597, Goddard Space Flight Center, Greenbelt, Md., May 1976.
55. Teague, M. J., and J. I. Vette, "A Model of the Trapped Electron Population for Solar Minimum," NSSDC 74-03, NASA TMX-69909, Goddard Space Flight Center, Greenbelt, Md., April 1974.
56. Kluge, G., and K. G. Lenhart, "A Unified Computing Procedure for Trapped Radiation Models," ESOC Internal Note 78, March 1971.
57. McIlwain, C. E., "Coordinates for Mapping the Distribution of Magnetically Trapped Particles," J. Geophys. Res., 66, 3681-3691, November 1961.
58. Bostrom, C. O., A. J. Zmuda, and G. F. Pieper, "Trapped Protons in the South Atlantic Magnetic Anomaly, July through December 1961 1. The General Characteristics," J. Geophys. Res., 70, 2021-2033, May 1965.
59. Ackerson, K. L., and L. A. Frank, "Explorer 12 Observations of Charged Particles in the Inner Radiation Zone," J. Geophys. Res., 72, 951-957, February 1967.
60. Gabbe, J. D., M. B. Wilk, and W. L. Brown, "Statistical Analysis and Modeling of the High-Energy Proton Data from the Telstar 1 Satellite," Bell Sys. Tech. J., 46, 1301-1450, September 1967.
61. Freden, S. C., and G. A. Paulikas, "Trapped Protons at Low Altitudes in the South Atlantic Magnetic Anomaly," J. Geophys. Res., 69, 1259-1269, April 1964.
62. Brown, W. L., and J. D. Gabbe, "Final Report on Bell Telephone Laboratories Experiments on Explorer XV, Project SERB, Study on the Enhanced Radiation Belts," June 30, 1964 (not published).
63. Brown, W. L., and J. D. Gabbe, private communication, approximately 1966.

64. McIlwain, C. E., "The Radiation Belts, Natural and Artificial," Science, 142, 355-361, October 1963.
65. Valerio, J., "Protons from 40 to 110 Mev Observed in Injun 3," J. Geophys. Res., 69, 4949-4958, 1964.
66. Brown, W. L., L. W. Davidson, and L. V. Medford, "The Energetic Particle Environment of Relay 1," in Relay 1 Program Final Report, NASA SP-76, 403-427, 1965.
67. McIlwain, C. E., R. W. Fillius, J. Valerio, and A. Dave, "Relay 1 Trapped Radiation Measurements," NASA TN D-2516, December 1964.
68. Brown, W. L., and J. D. Gabbe, "Telstar II Radiation Experiments - Preliminary Results," Supplement to Telstar I, 4, 2327-2373, NASA SP-32, December 1965.
69. Beall, D. S., "Graphs of Selected Data from Satellite 1963 038C for 1967," Johns Hopkins University, Applied Physics Laboratory Technical Memorandum TG-1050-5, April 1969.
70. Imhof, W. L., and J. B. Reagan, "Source of High-Energy Protons Trapped on Low L Shells," J. Geophys. Res., 74, 5054-5064, October 1969.
71. Vette, J. I., private communication, 1971.
72. Mihalov, J. P., and R. S. White, "Low-Energy Proton Radiation Belts," J. Geophys. Res., 71, 2207-2216, May 1966.
73. Freden, S. C., J. B. Blake, and G. A. Paulikas, "Spatial Variation of the Inner Zone Trapped Proton Spectrum," J. Geophys. Res., 70, 3113-3116, July 1965.
74. Paulikas, G. A., private communication, 1972.
75. Vette, J. I., private communication, 1971.
76. Thede, A. L., "OV3-4 Dose Rate and Proton Spectral Measurements," Air Force Weapons Laboratory Technical Report AFWL-TR-68-128, January 1969 (not published).
77. Pizzella, G., and B. A. Randall, "Differential Energy Spectrum of Geomagnetically Trapped Protons with the Injun 5 Satellite," J. Geophys. Res., 76, 2306-2312, April 1971.

Table 1. Data Used in Making AP8MAX and AP8MIN Models

Laboratory	Satellite	Data Time Period	Type of Measurement	Source of Data	Nominal Energy Range (MeV)	Text Code for Data
University of Iowa	Explorer 4	July - Oct. 1958	J, Geiger Tube	McIlwain Reference 57	> 31 > 43	01AA 01BA
Applied Physics Laboratory	Injun 1	July - Dec. 1961	j ₁ , Solid State J, Geiger Tube	Bostrom et al. Reference 58	1 - 15 > 40	02AA 02BA
Goddard Space Flight Center	Explorer 12 and Explorer 14	Aug. - Dec. 1961 Oct. - Dec. 1962	j ₁ , Scintillator	Davis and Williamson Reference 27	> 0.1 > 0.27 > 0.51	04AA 04BA 04CA 04DA 04EA
University of Iowa	Explorer 12	Aug. - Sept. 1961	j ₁ , Geiger Tube	Ackerson and Frank Reference 59	> 1.7 > 21 > 70	04FA 04GA
Bell Telephone Laboratories	Telstar 1	Oct. 1962 - Feb. 1963	J, Solid State	Gabbe and Brown Reference 34 Gabbe et al. Reference 60	26 - 33 50 - 75	07AA 07BA
Aerospace Corporation	1962 alpha 1 1962 beta 1	Sept. - Oct. 1962	J, Solid State	Freden and Paulikas Reference 61	5 - 20 60 - 120	08AA 08BA
Bell Telephone Laboratories	Explorer 15	Oct. 1962 - Jan. 1963	J, Solid State	Brown and Gabbe References 62, 63	4 - 13	11AA
University of California, San Diego	Explorer 15	Oct. 1962 - Jan. 1963	j ₁ , Scintillator	McIlwain Reference 64	40 - 110	11BA
University of California, San Diego	Injun 3	Dec. 1962 - Sept. 1963	j ₁ , Scintillator	Valerio Reference 65	40 - 110	12AA
Bell Telephone Laboratories	Relay 1	Dec. 1962 - Jan. 1963	j ₁ , Solid State	Brown et al. Reference 66	2.5 - 3.8 5.0 - 8.6	13AA 13BA

Table 1. Data Used in Making AP8MAX and AP8MIN Models (continued)

Laboratory	Satellite	Data Time per jd	Type of Measurement	Source of Data	Nominal Energy Range (MeV)	Text Code for Data
University of Iowa and University of California, San Diego	Relay 1	Dec. 1962 - Jan. 1963	j ₁ , Solid State	Filius and McIlwain Reference 29 Filius Reference 20	1.1 - 14 1.1 - 14 1.6 - 7.1 2.25 - 4.7	13CA 13DA 13EA 13FA
University of California, San Diego	Relay 1	May - Sept. 1963	j ₁ , Solid State	McIlwain et al. Reference 67 Filius Reference 20 McIlwain et al. Reference 67	> 5.2 18.2 - 35	13GA 13IA
		May - Sept. 1963	j ₁ , Scintillator		> 34	13IA
		Sept. 1963 - Feb. 1964	j ₁ , Scintillator	Filius Reference 20	> 34	13JA
		Jan. 1963	j ₁ , Solid State	Brown and Gabbe Reference 68	18.2 - 25	13KA
		Jan. 1963	j ₁ , Solid State	Bell	35 - 63	13MA
Bell Telephone Laboratories	Telstar 2	May - July 1963	j ₁ , Solid State	Reference 69	4 - 13	14AA
Applied Physics Laboratory	1963-038C	Oct. 12 - 27, 1967	j ₁ , Solid State		8.5 - 25 25 - 100 1.2 - 2.2 2.2 - 8.5	15CA 15DA 15EA 15FA
Lockheed Missile and Space Company	1963-042A	Oct. - Nov. 1963	j, Scintillator	Imhof and Reagan Reference 70	> 70	16AA
	ERS 13	July - Dec. 1964	J, Solid State	Vette Private Communication Reference 71	12 - ~3	17AA

Table 1. Data Used in Making AP8MAX and AP8MIN Models (continued)

Laboratory	Satellite	Data Time Period	Type of Measurement	Source of Data	Nominal Energy Range (MeV)	Text Code for Data
Aerospace Corporation	P11-AS	Aug. 1964	j ₁ , Scintillator	Mihalov and White Reference 72	0.17 - 0.21 0.21 - 0.29 0.29 - 0.42 0.42 - 0.55 0.55 - 1.2 1.2 - 1.5 1.5 - 1.9 1.9 - 2.4 2.4 - 3.4	18AA 18BA 18CA 18DA 18EA 18FA 18GA 18HA 18IA
Goddard Space Flight Center	Explorer 26	Aug. 1964 - Feb. 1965	J, Solid State	Freden et al. Reference 73 Data from Paulikas Reference 74	6 - 20 12 - 35 21 - 40 40 - 80 80 - 110 > 80	18JA 18KA 18LA 18MA 18NA 18OA
Lockheed Missile and Space Company	Gemini 4	May 1965	j ₁ , Scintillator	Davis and Williamson Reference 28	> 0.098 > 0.134 > 0.180 > 0.513 > 0.775 > 1.70 > 0.345 > 1.14	20AA 20BA 20CA 20DA 20EA 20GA 20HA 20IA
Lockheed Missile and Space Company	ERS 17	June 1964	J, Scintillator	Imhof and Reagan Reference 70	> 64	21AA
Lockheed Missile and Space Company	Gemini 7	July - Oct. 1965	J, Solid State	Vette Private Communication Reference 75	8 - 21	22AA
		Dec. 1965	J, Scintillator	Imhof and Reagan Reference 70	> 70	24AA

Table 1. Data Used in Making AP8MAX and AP8MIN Models (concluded)

Laboratory	Satellite	Data Time Period	Type of Measurement	Source of Data	Nominal Energy Range (MeV)	Text Code for Data
Air Force Weapons Laboratory	OV3-4	June - July 1966	j, Solid State	Tlode Reference 76	> 15 > 30 > 55.50 > 105.5 > 170	26AA 26BA 26CA 26DA 26EA
Aerospace Corporation	OV3-3	Sept. - Oct. 1966	j, Solid State	Data from Paulikas et al. Reference 5	12 - 22 21 - 40 40 - 80 80 - 140 80 - 400	27AA 27BA 27CA 27DA 27EA
University of Kiel	Azur	Nov. 1969 - June 1970	j ₁ , Solid State	Moritz Reference 7	0.25 - 1.65	28AA
Max Planck Institute for Physics and Astrophysics	Azur	Nov. 1969	j ₁ , Solid State	Data from Hovestadt Reference 6	1.5 - 2.7 2.7 - 5.2 5.2 - 10.4 10.4 - 22 22 - 49 49 - 104	28BA 28CA 28DA 28EA 28FA 28GA
Aerospace Corporation	OV2-5	Oct. 1968	j ₁ , Solid State	Stevens et al. Reference 38	.06 - .3.3 .1 - .3 .3 - .6 .6 - 1 1 - 1.5	29AA 29BA 29CA 29DA
University of Iowa	Injun 5	Aug. - Nov. 1968	j ₁ , Solid State	Pizzella and Randall Reference 77	.3 - .74 .3 - .6 .6 - 1 1 - 1.5 1.5 - 2 2 - 5 5 - 10 10 - 15 .8 - 1.43 1.43 - 4.2 4.2 - 9.2	30AA 30EA 36CA 30DA 30EA 30FA 30GA 30HA 30IA 30JA

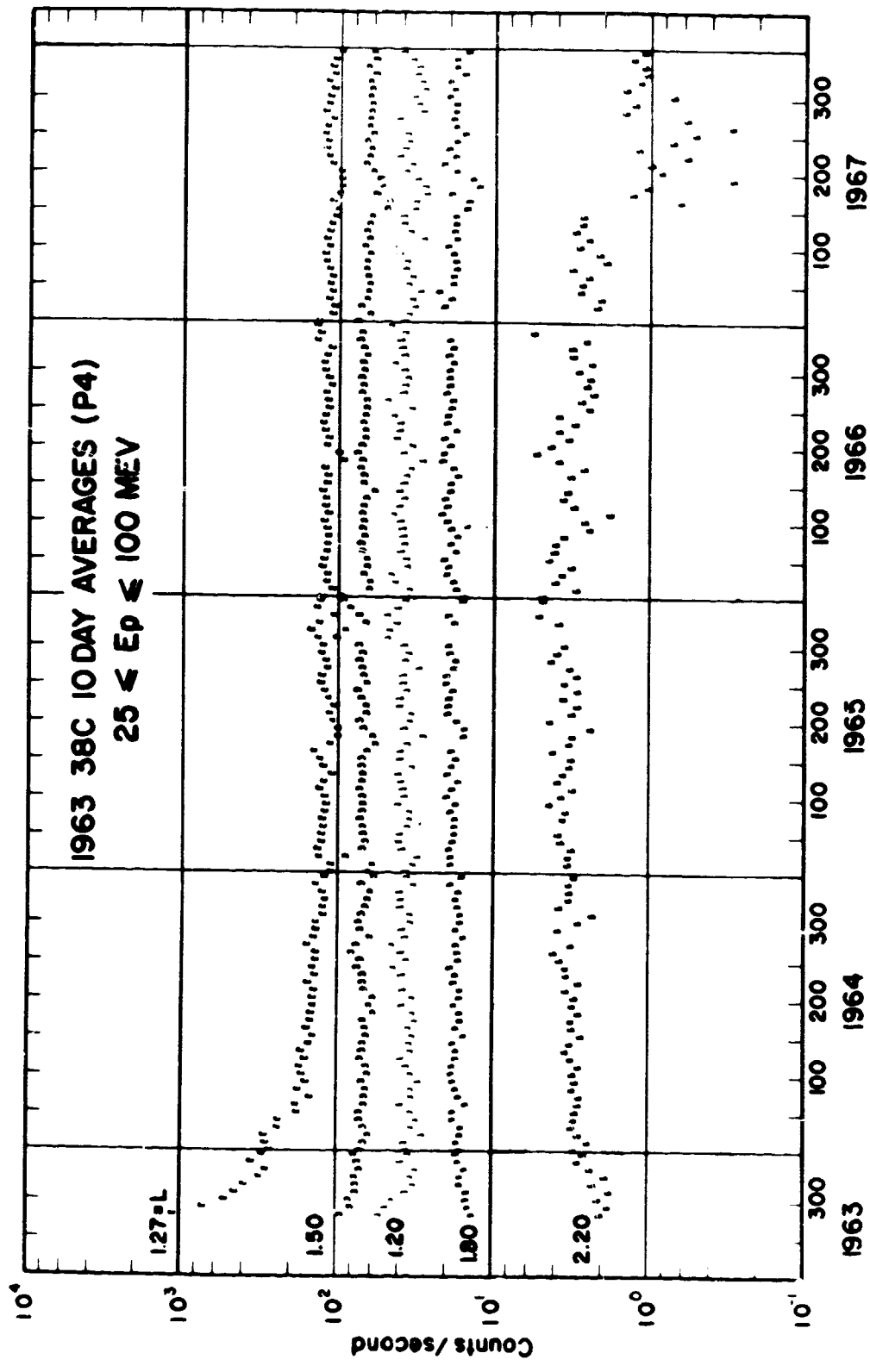


Figure 1. Ten-day Average Counting Rates for Proton Energies 25 to 100 MeV as Seen by Satellite 1963-038C₁₃. (The decrease in the $L = 1.27$ R_p curve during 1965 is a decay of Starfish electrons which contaminated the measurement.)

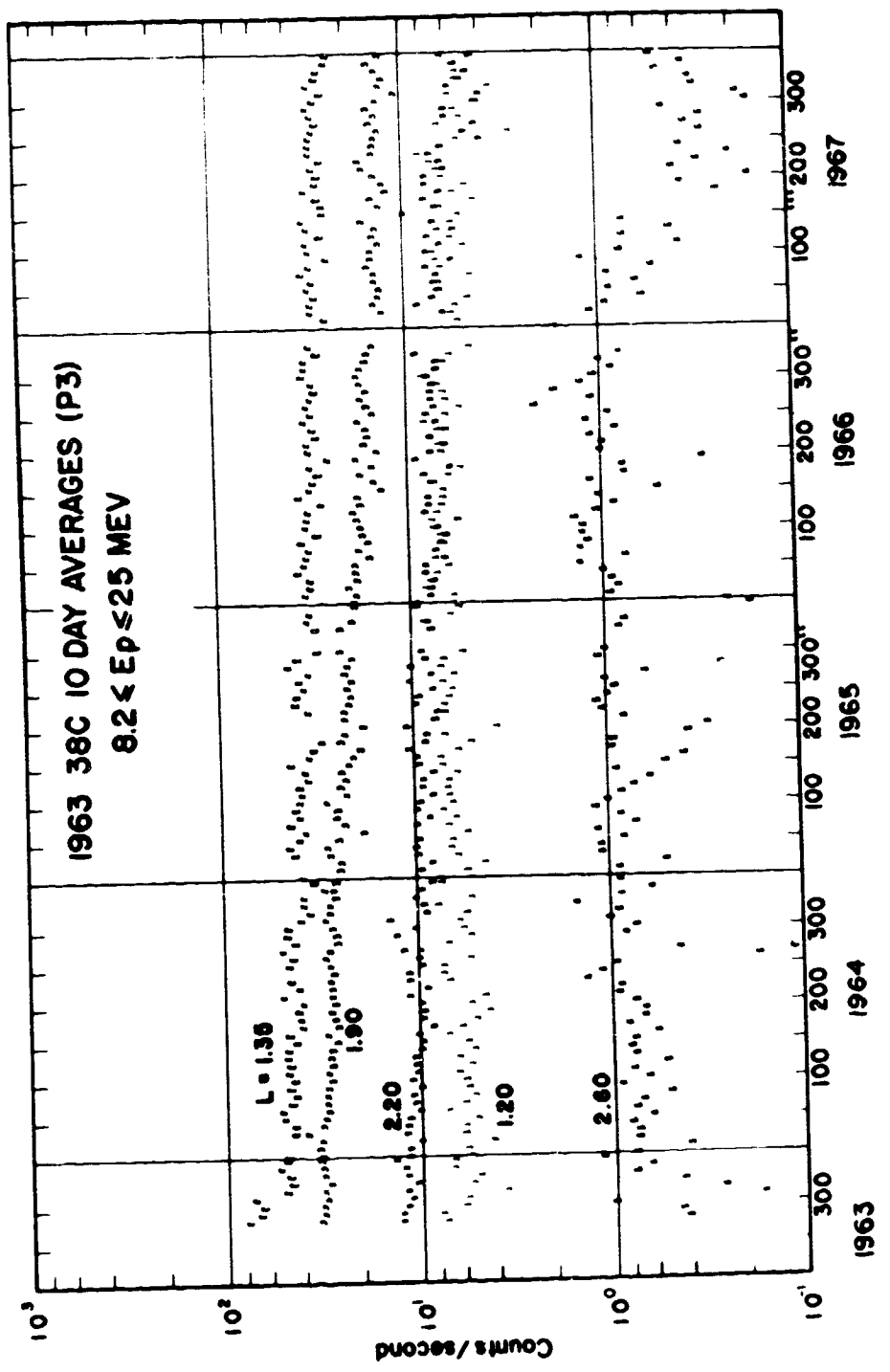


Figure 2. Ten-day Average Counting Rates for Proton Energies 8.2 to 25 MeV as Seen by Satellite 1963-038C¹³

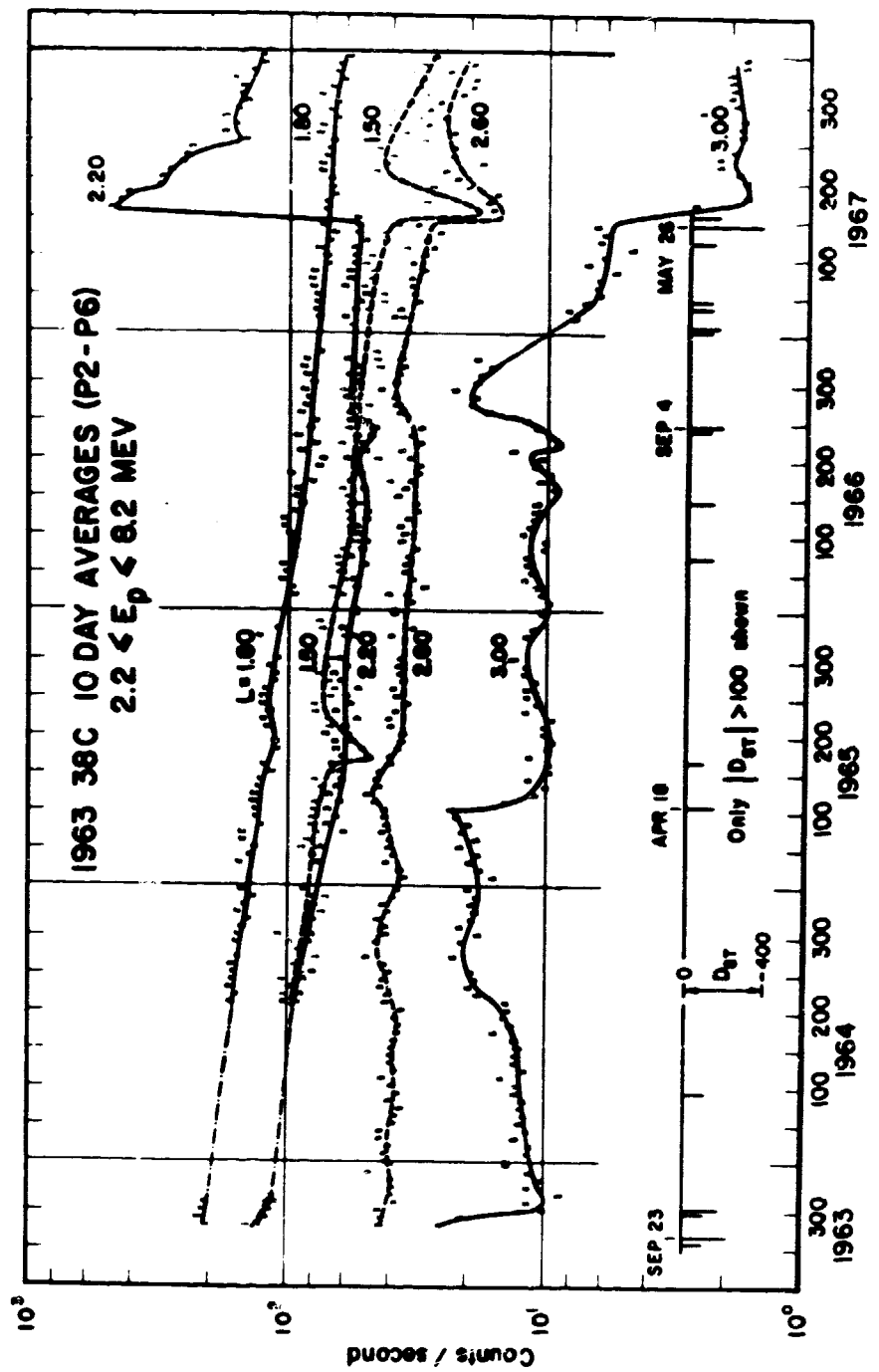


Figure 3. Ten-Day Average Counting Rates for Proton Energies 2.2 to 8.2 MeV as Seen by Satellite
 1963-038C13

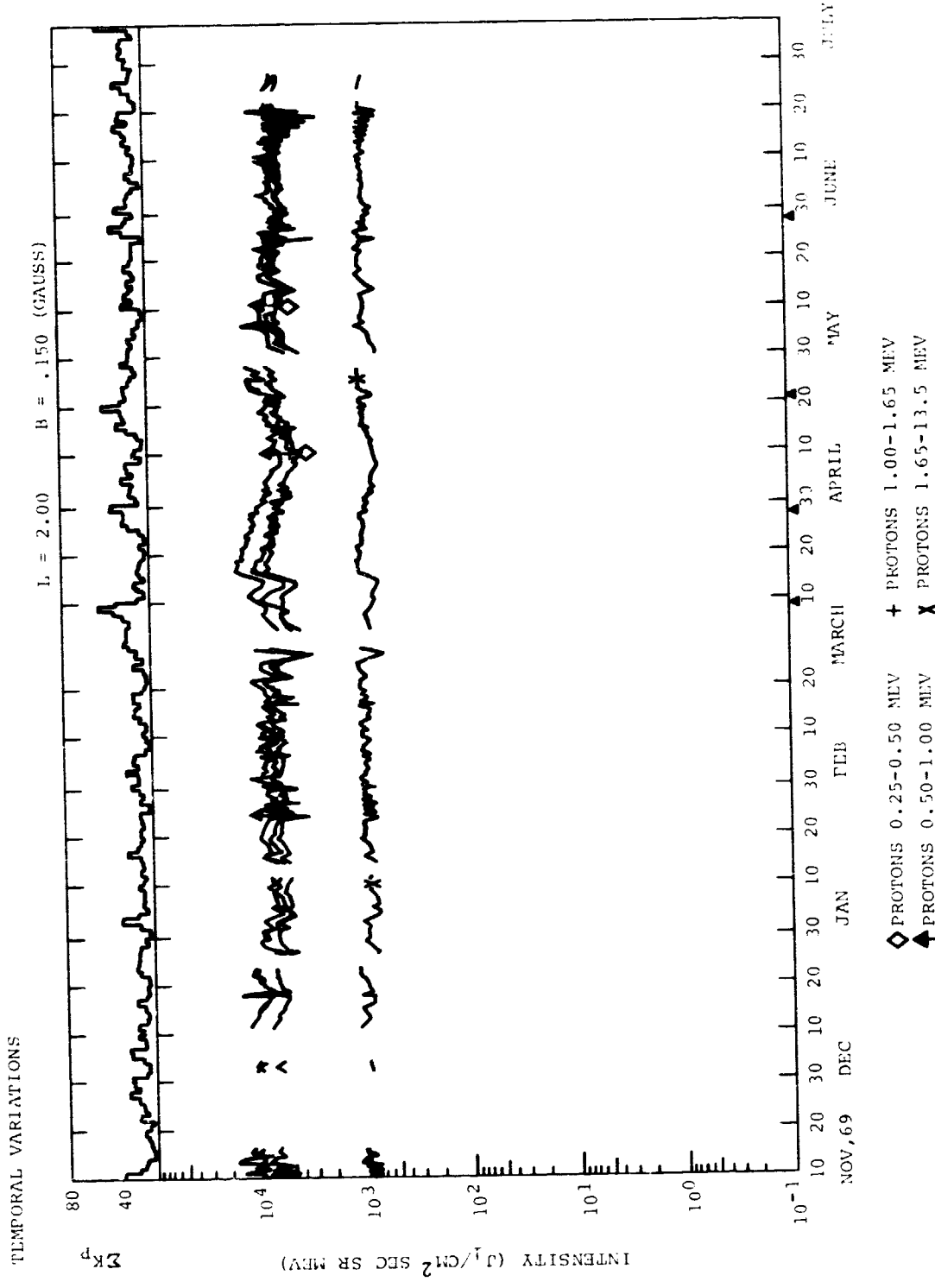


Figure 4. Counting Rates for Protons in the Range of 0.25 to 13.5 MeV at $L = 2.0 R_E$ as Seen by Satellite Azur⁴⁹

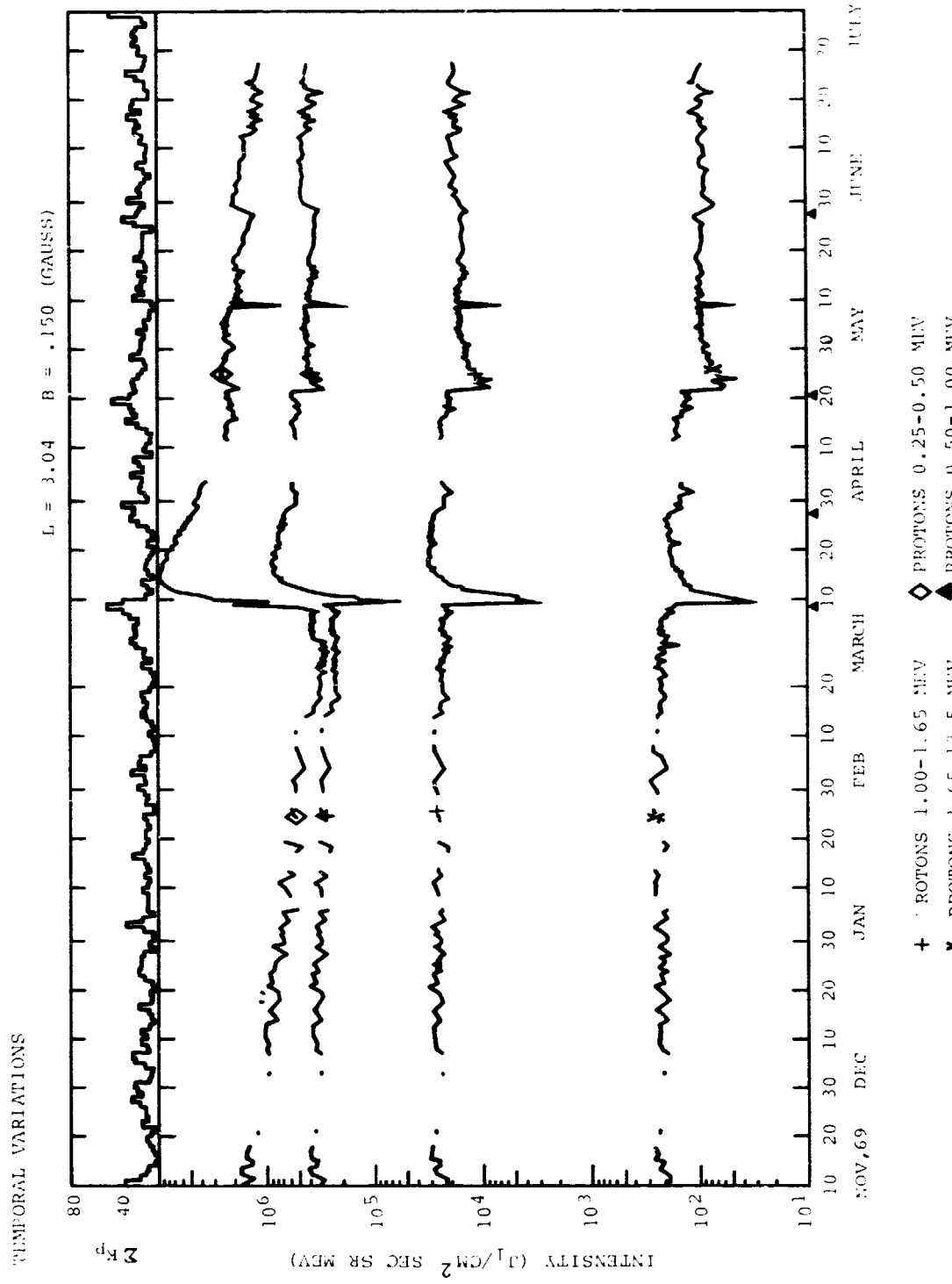


Figure 5. Counting Rates for Protons in the Range of 0.25 to 13.5 MeV at $L = 3.04 R_E$ as Seen by Satellite Azur₄

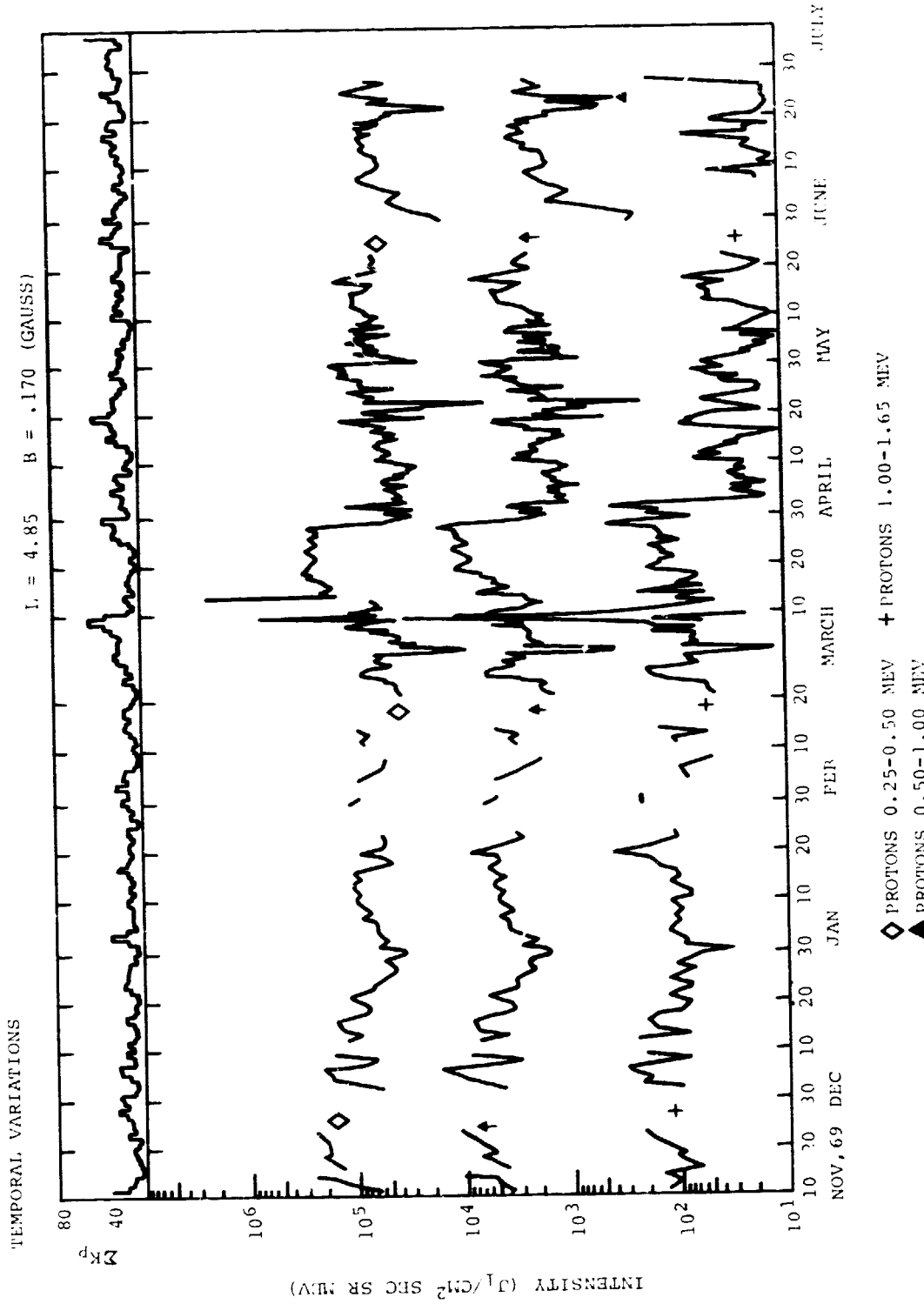


Figure 6. Counting Rates for Protons in the Range of 0.25 to 1.65 MeV at $L = 4.85$ Re as Seen by Satellite Azur₄₉

INTEGRAL ENERGY SPECTRA GENERALIZED CURVE FITTING

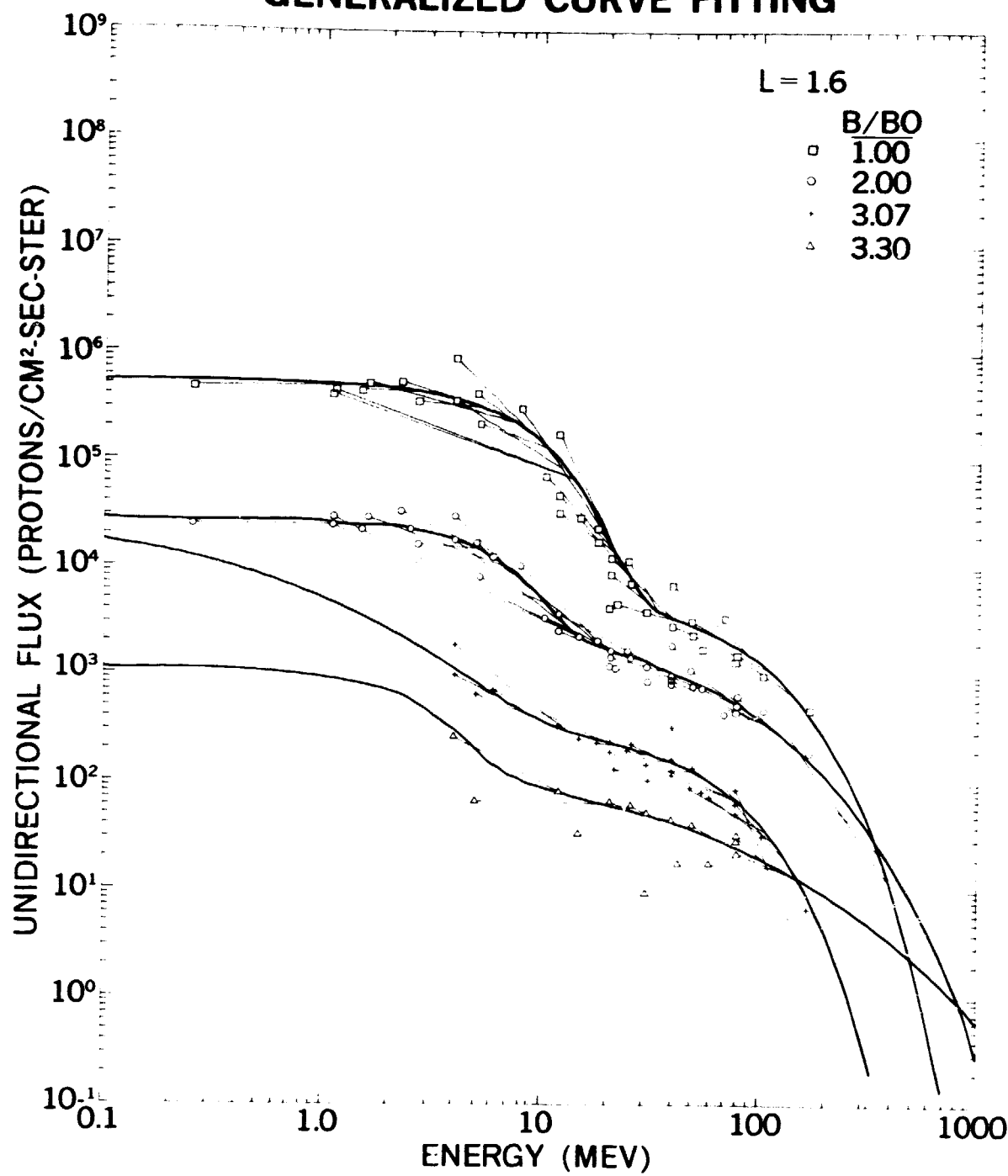
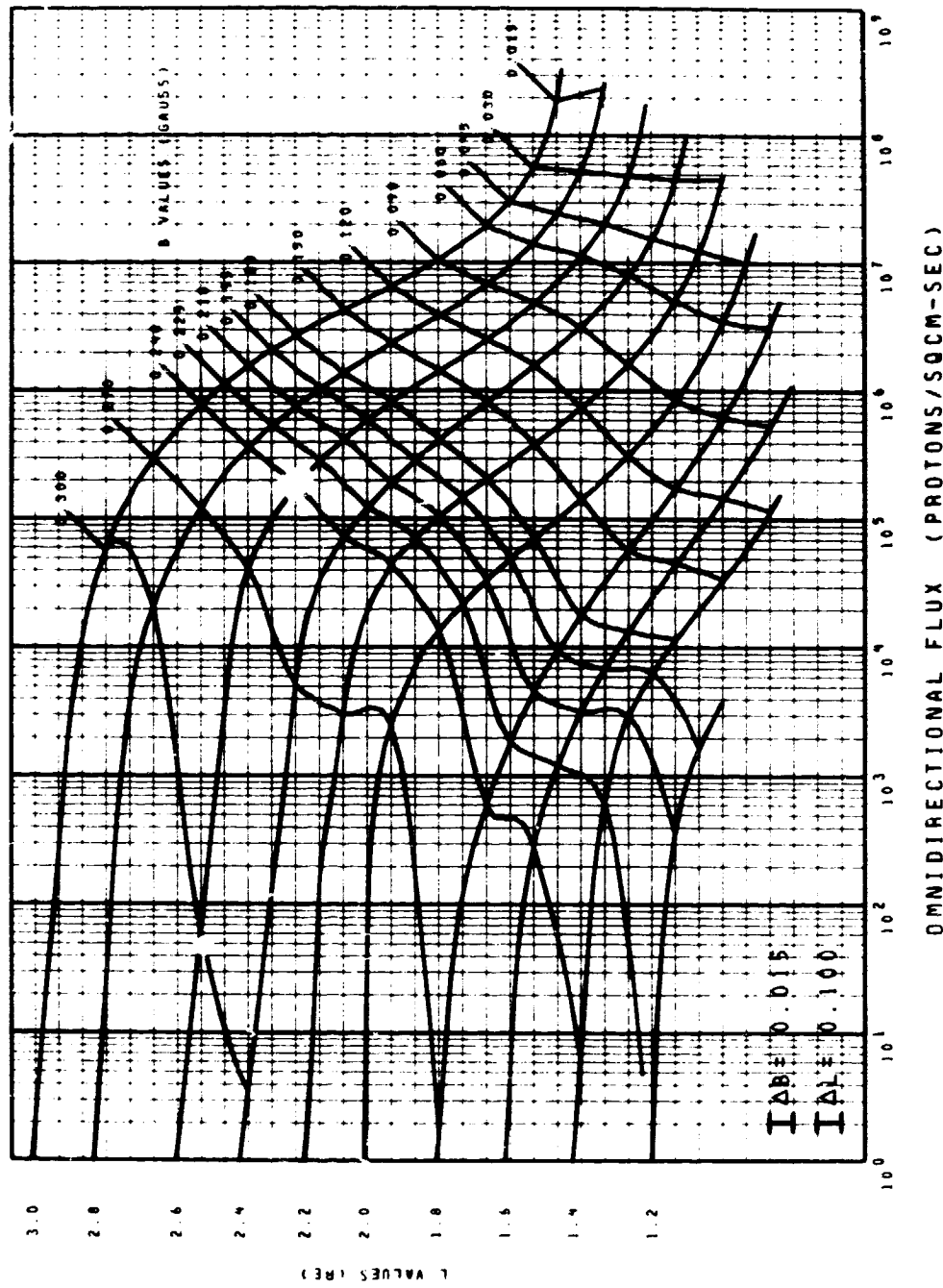


Figure 7. Integral Spectra Obtained by a Generalized Least Squares Curve-Fitting Procedure (Data points are also shown.)

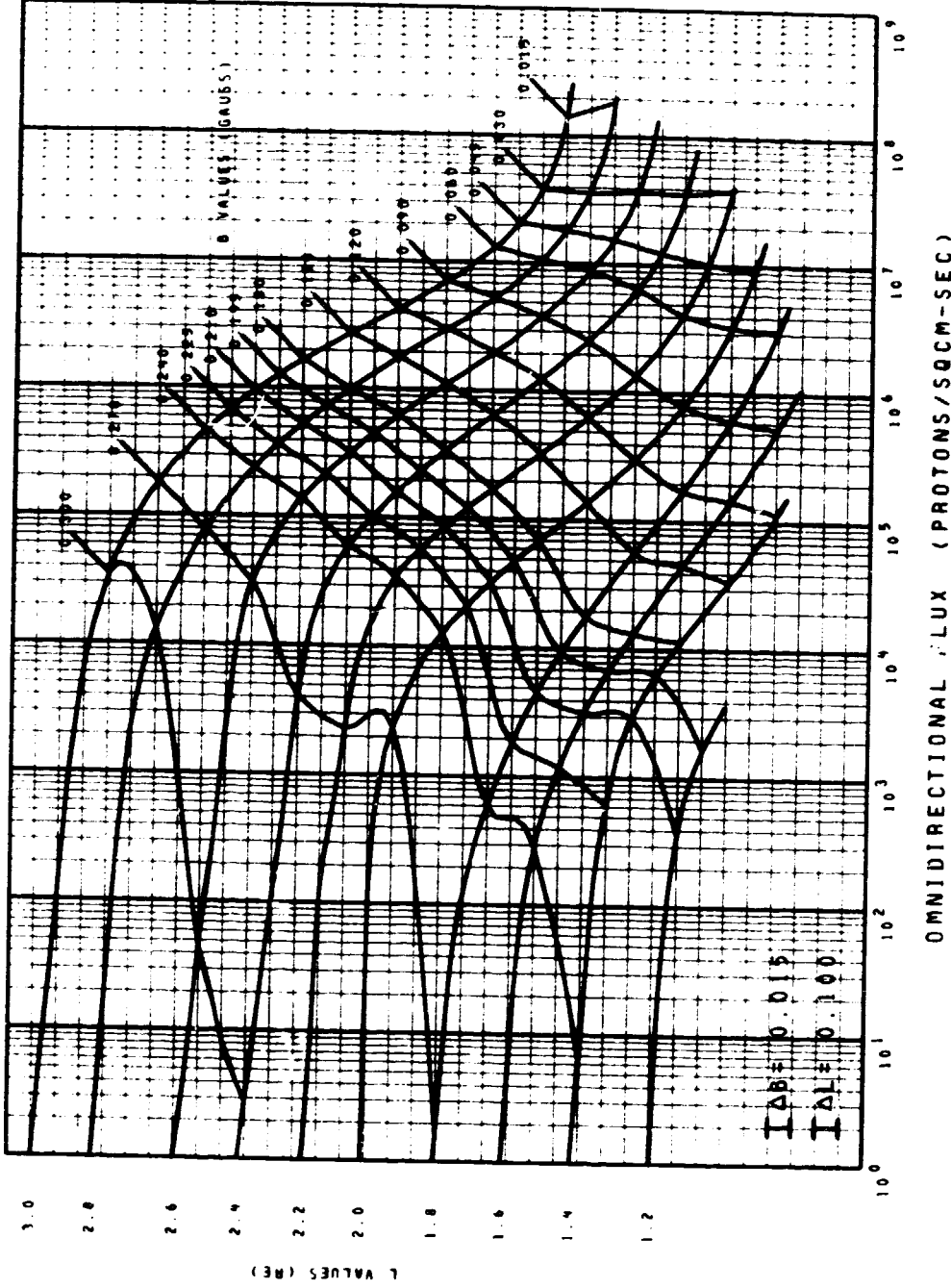
MODEL AP8 MIN FLUX DISTRIBUTIONS

ENERGY = 0.1 MEV

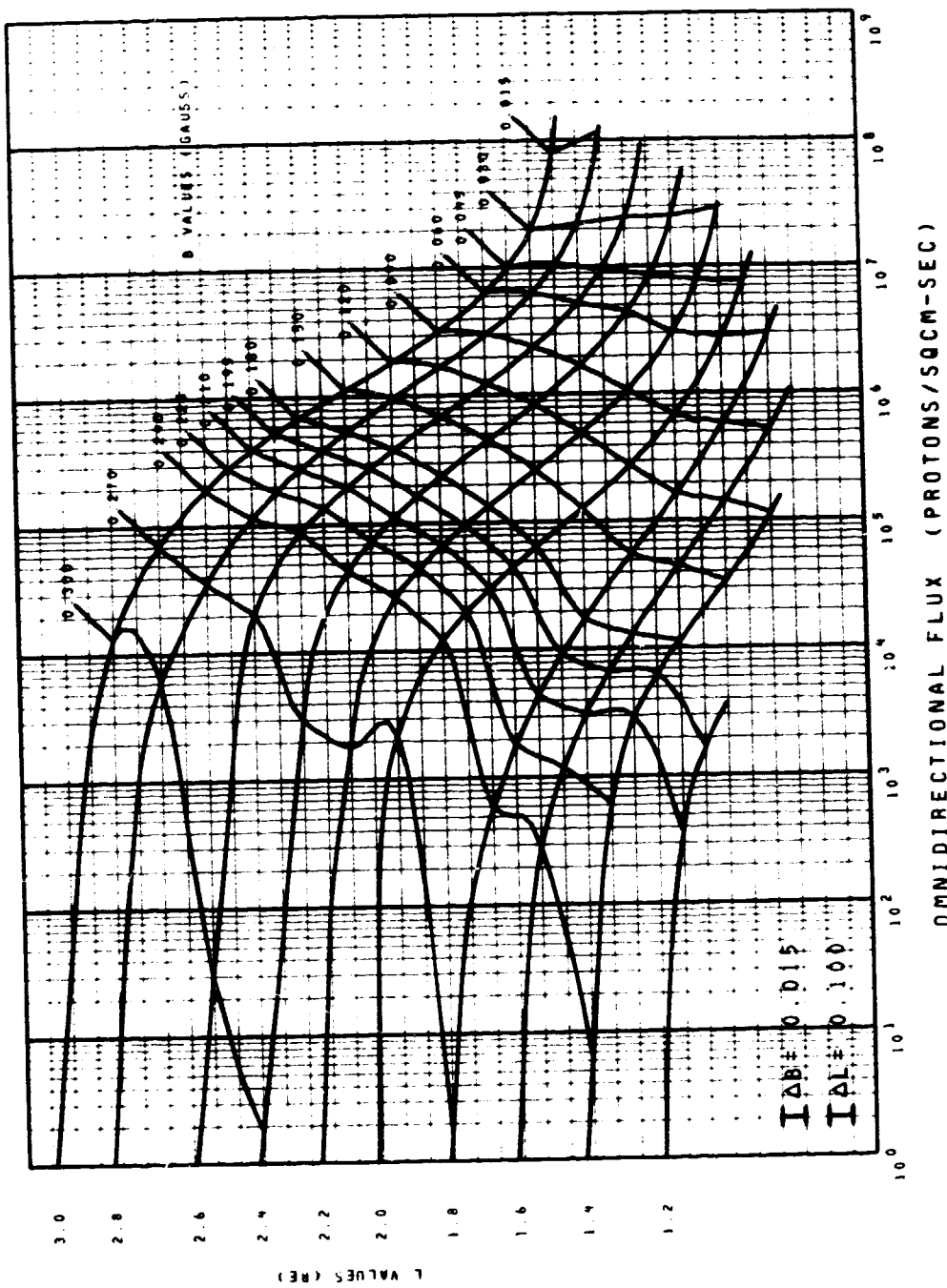
SOLAR MINIMUM FIG. 8



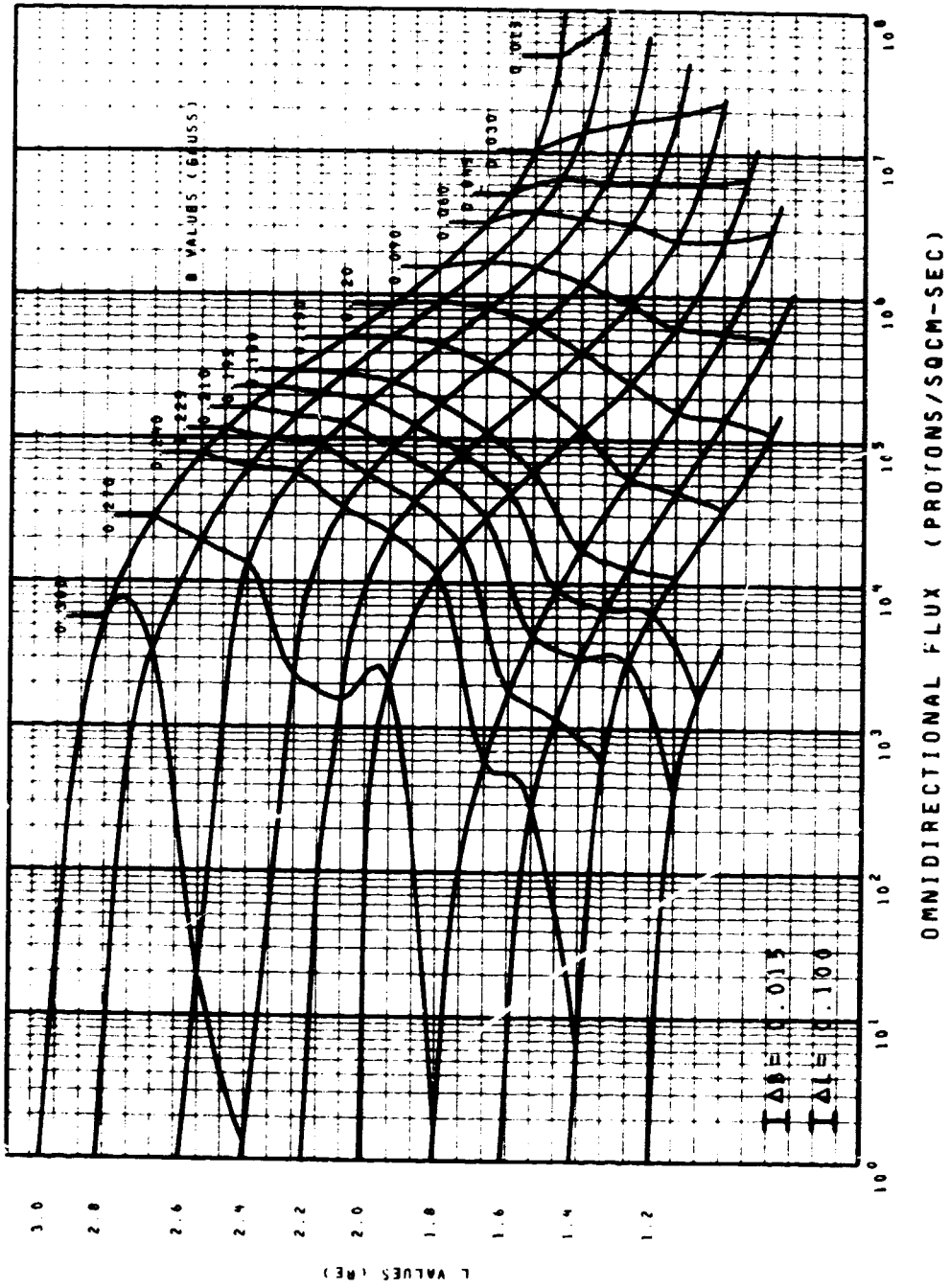
MODEL AP8 MIN FLUX DISTRIBUTIONS
 ENERGY = 0.2 MEV
 SOLAR MINIMUM FIG. 9



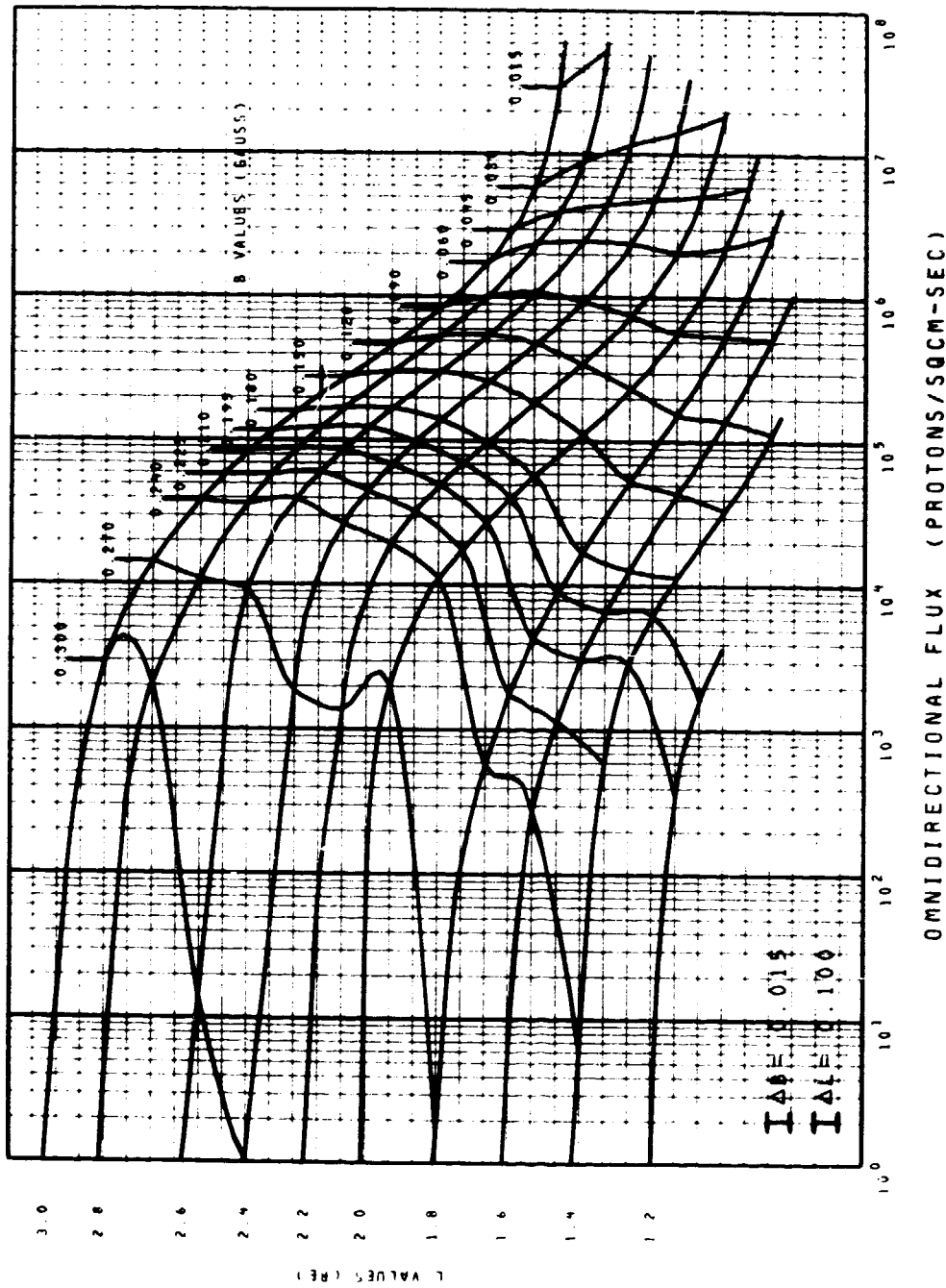
MODEL AP8 MIN FLUX DISTRIBUTIONS
ENERGY = 0.4 MEV
SOLAR MINIMUM FIG. 10



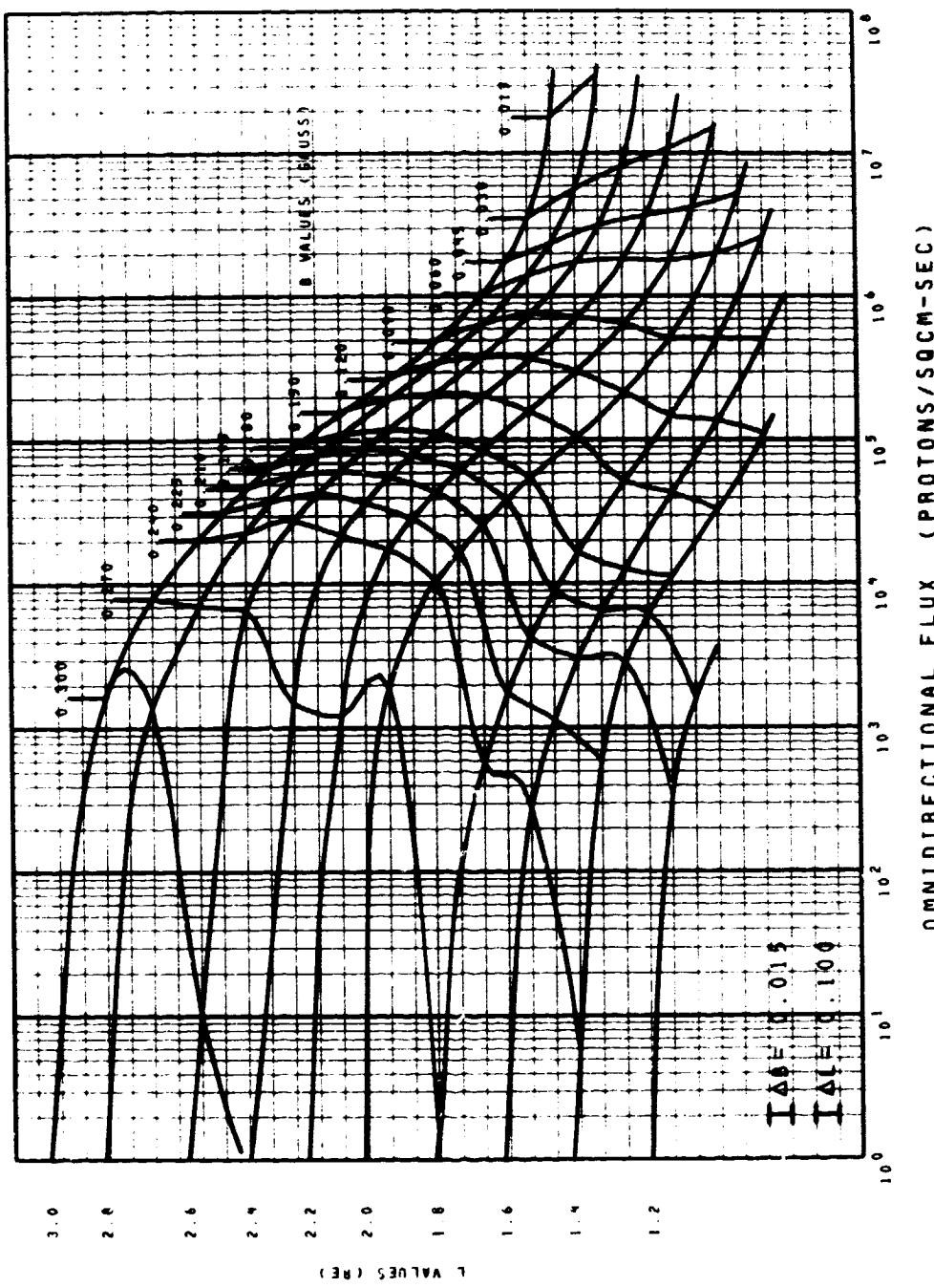
MODEL APO MIN FLUX DISTRIBUTIONS
 ENERGY = 0.6 MEV
 SOLAR MINIMUM FIG. 11



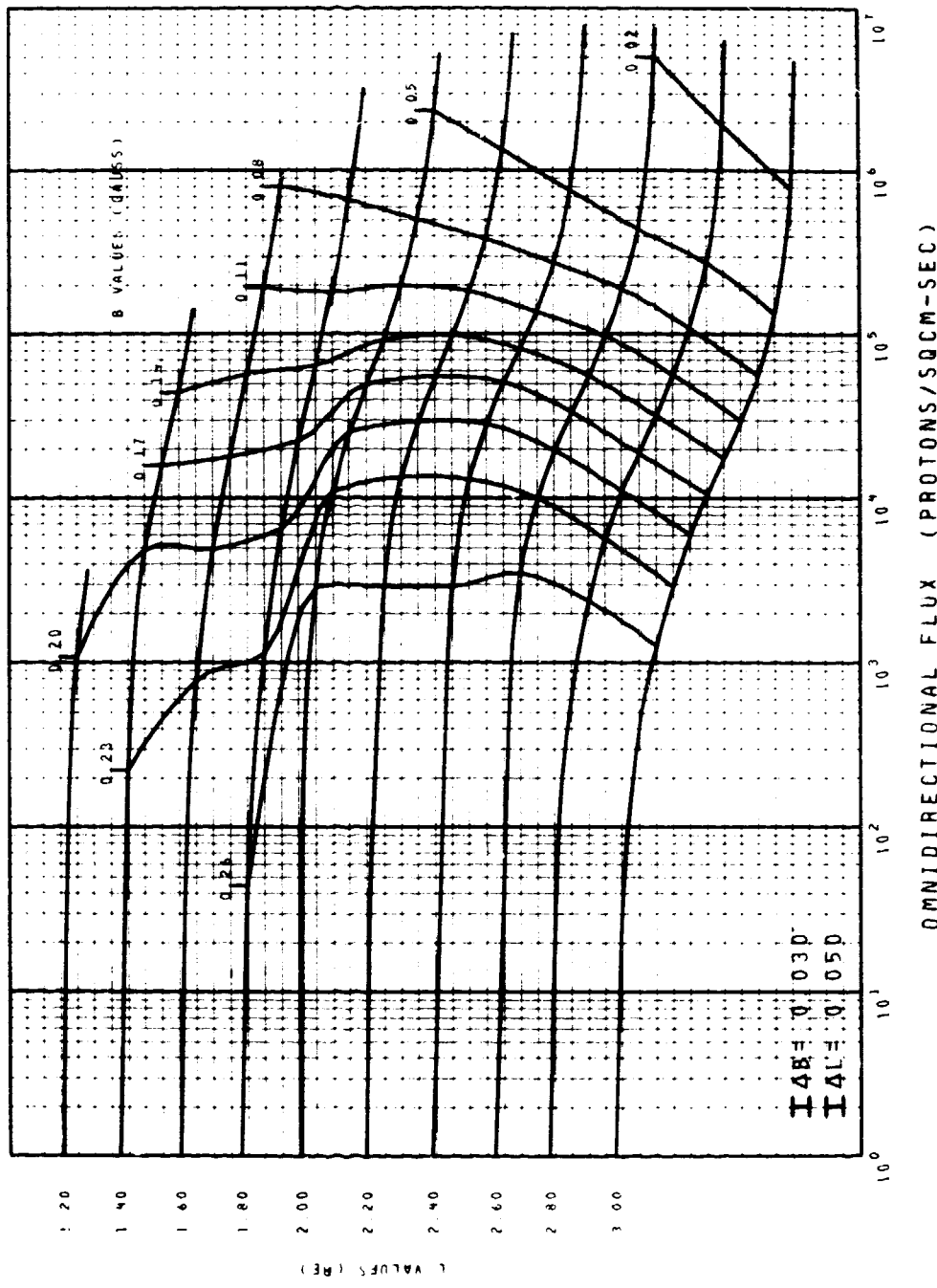
MODEL AP8 MIN FLUX DISTRIBUTIONS
 ENERGY = 0.8 MEV
 SOLAR MINIMUM FIG. 12



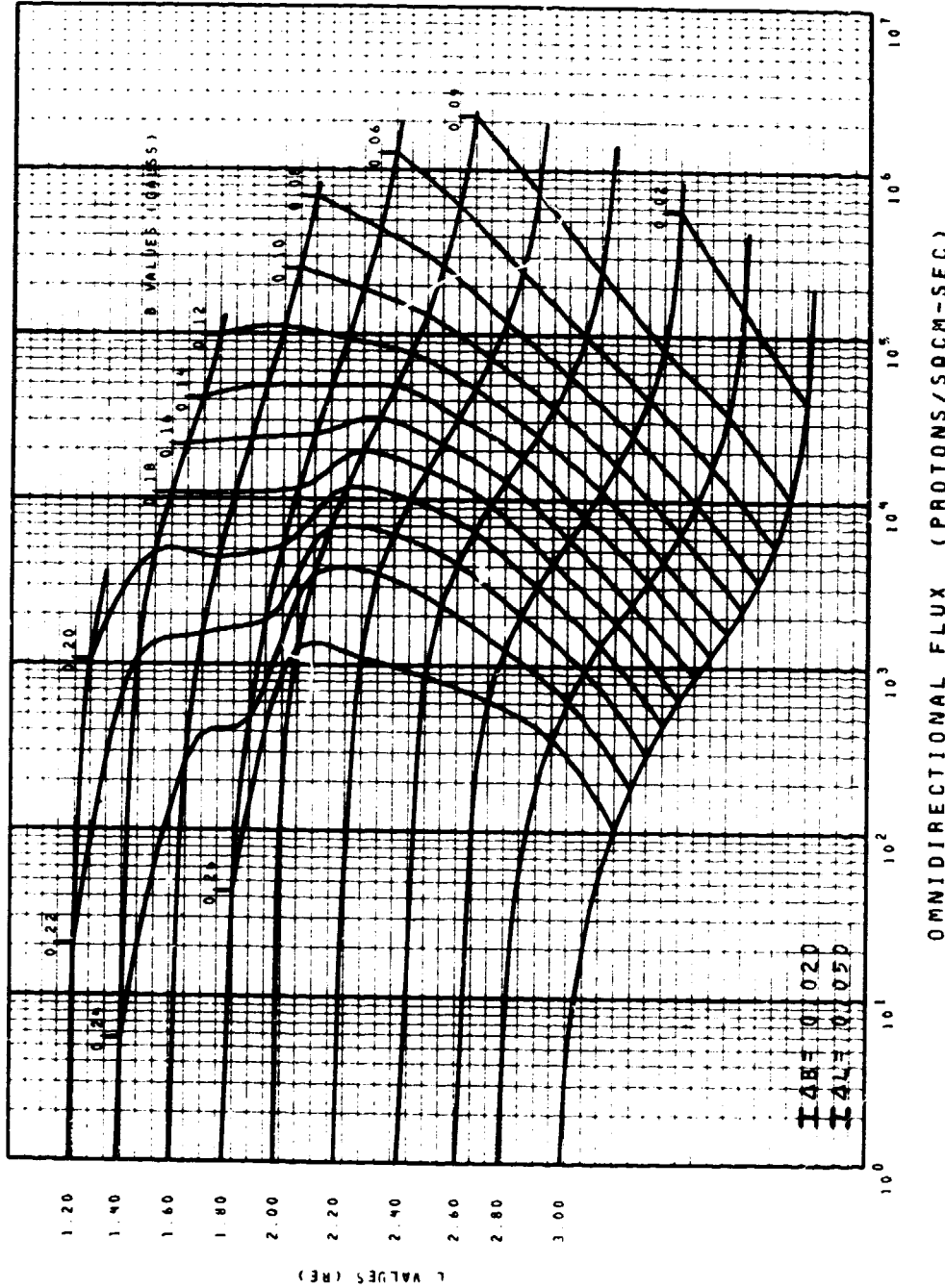
MODEL AP8 MIN FLUX DISTRIBUTIONS
 ENERGY = 1.0 MEV
 SOLAR MINIMUM FIG. 13



MODEL AP8 MIN FLUX DISTRIBUTIONS
 ENERGY = 2.0 MEV
 SOLAR MINIMUM FIG. 14



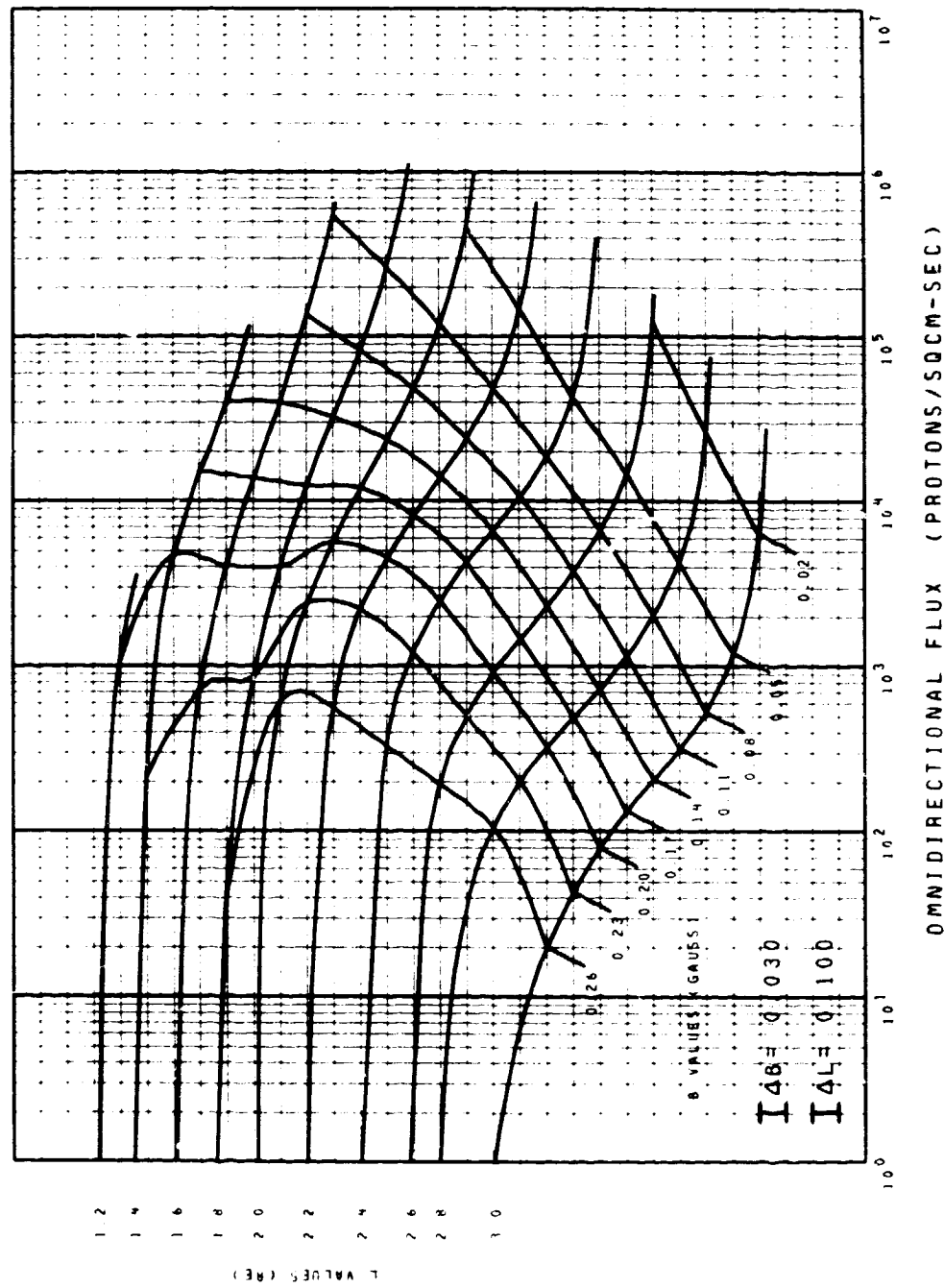
MODEL AP8 MIN FLUX DISTRIBUTIONS
 ENERGY = 4.0 MEV
 SOLAR MINIMUM FIG. 15



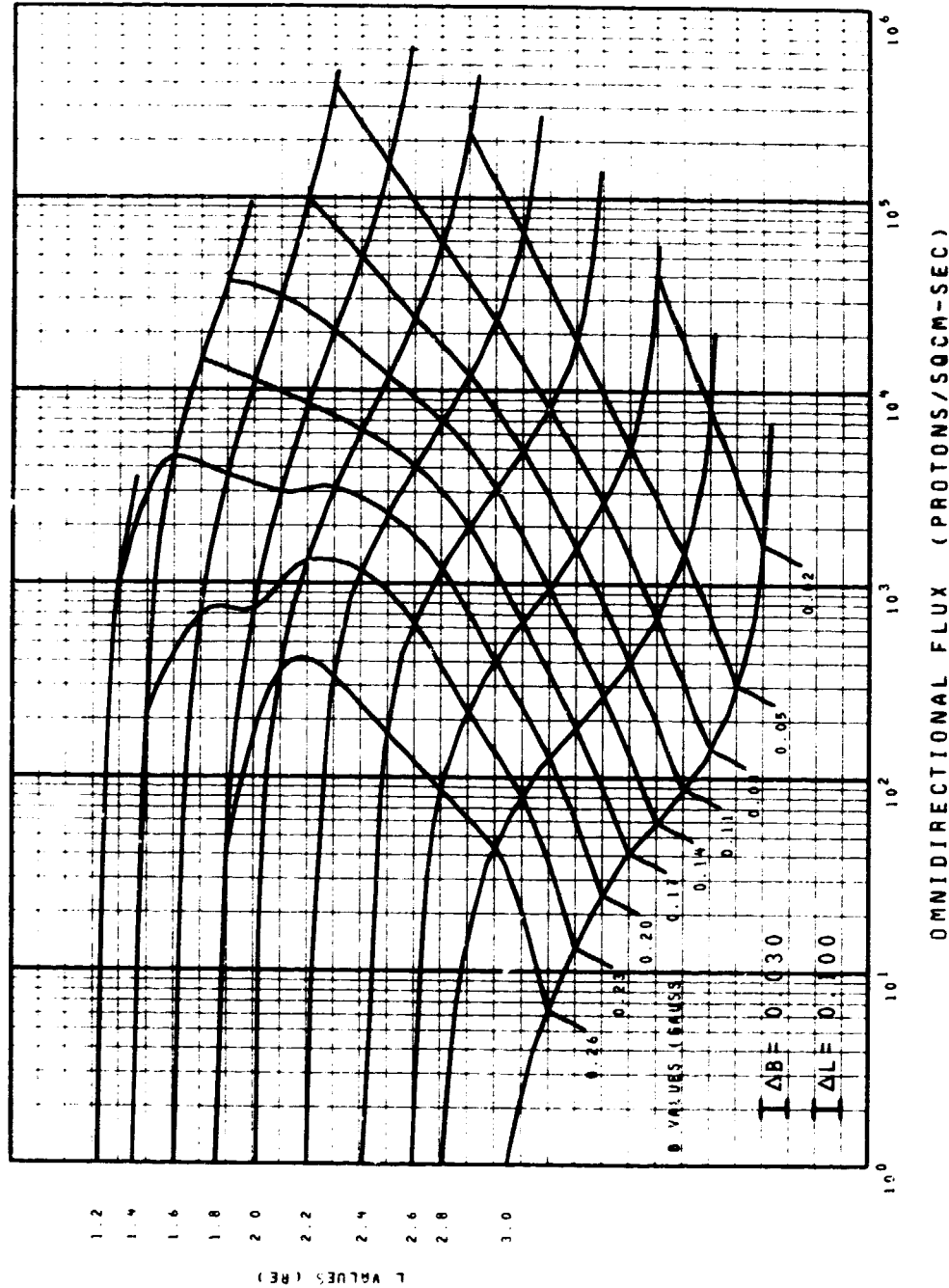
MODEL AP8 MIN FLUX DISTRIBUTIONS

ENERGY = 6.0 MEV

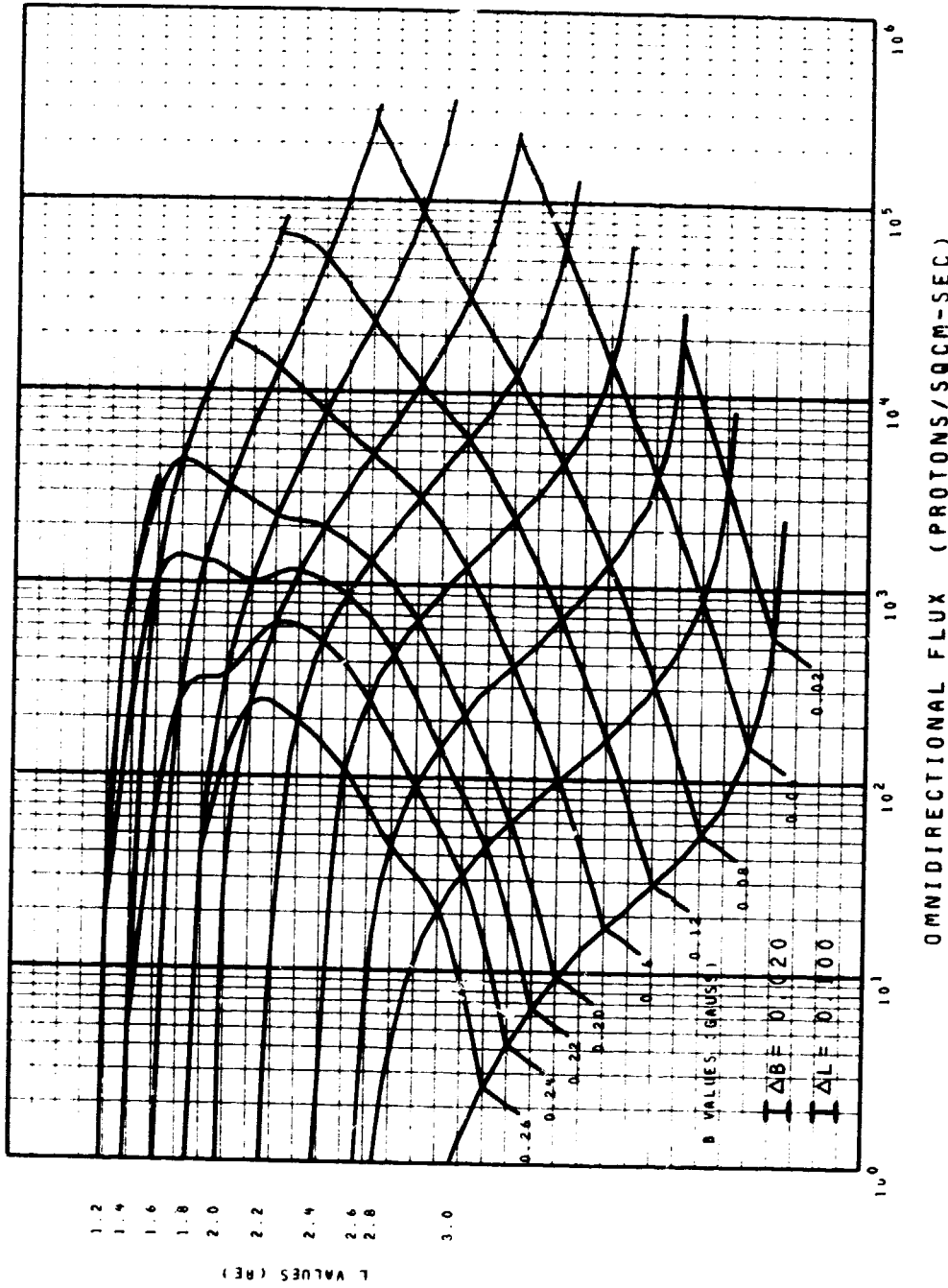
SOLAR MINIMUM FIG. 16



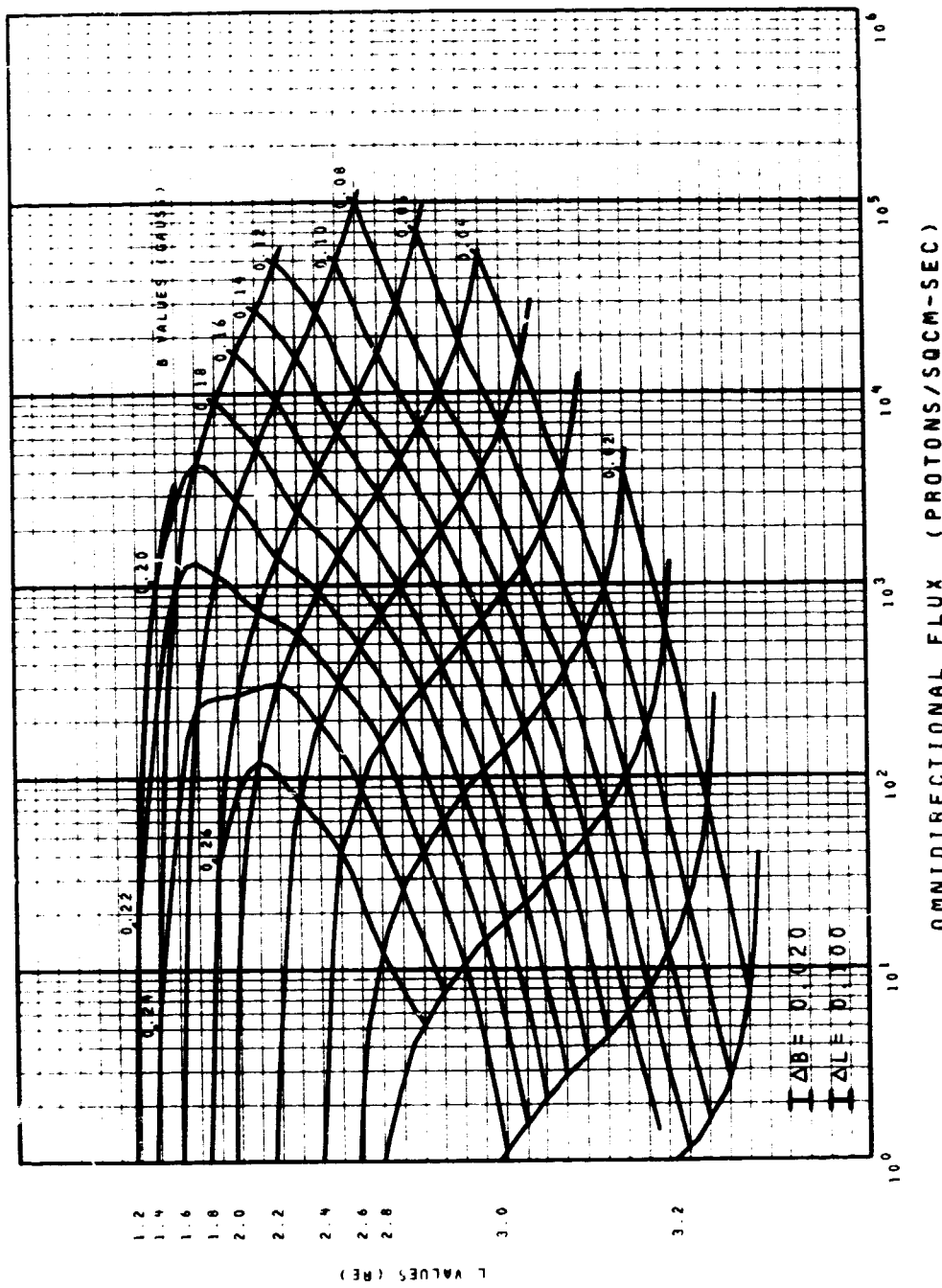
MODEL AP8 MIN FLUX DISTRIBUTIONS
 ENERGY = 8.0 MEV
 SOLAR MINIMUM FIG. 17



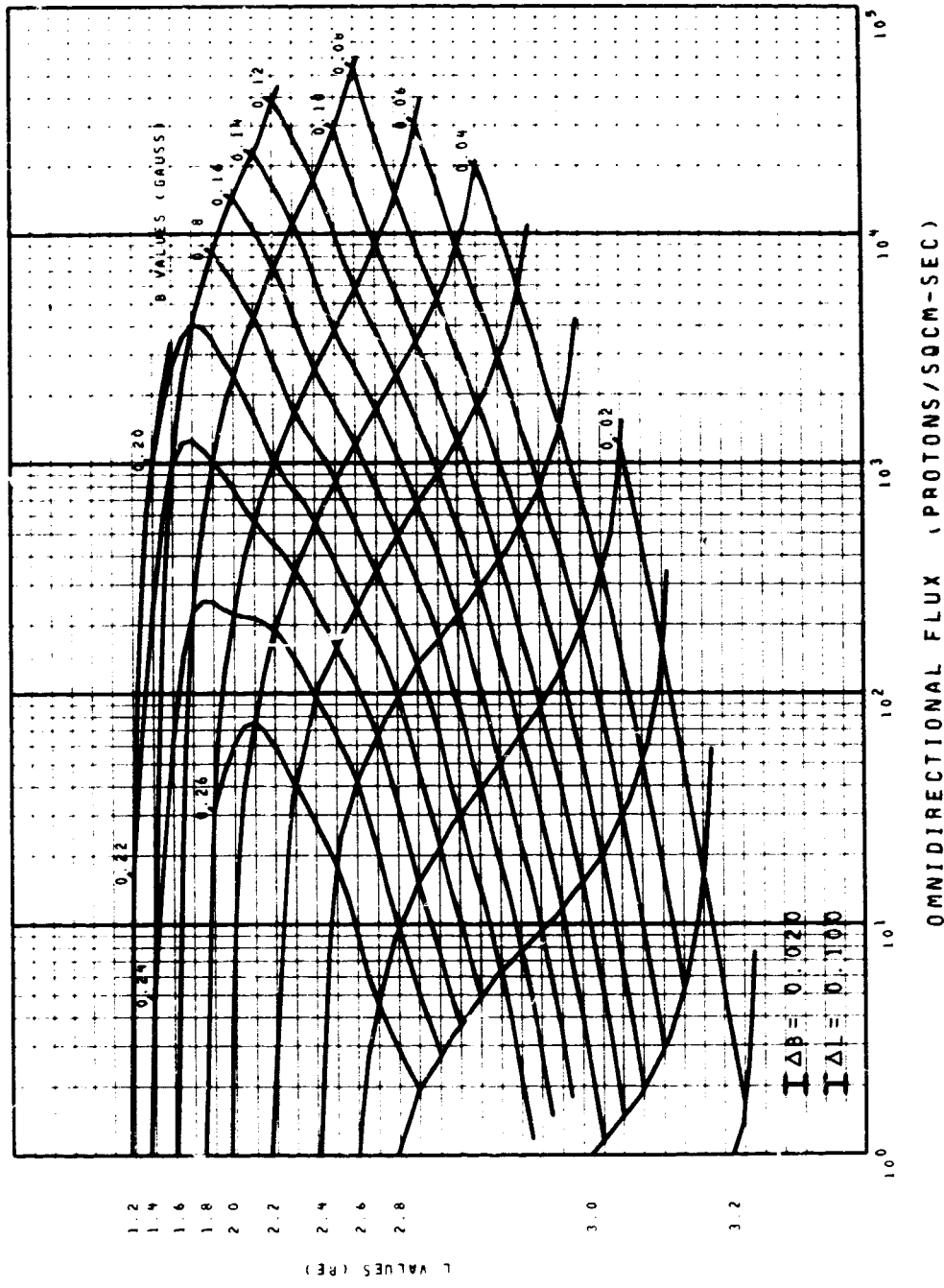
MODEL AP8 MIN FLUX DISTRIBUTIONS
 ENERGY = 10. MEV
 SOLAR MINIMUM FIG. 18



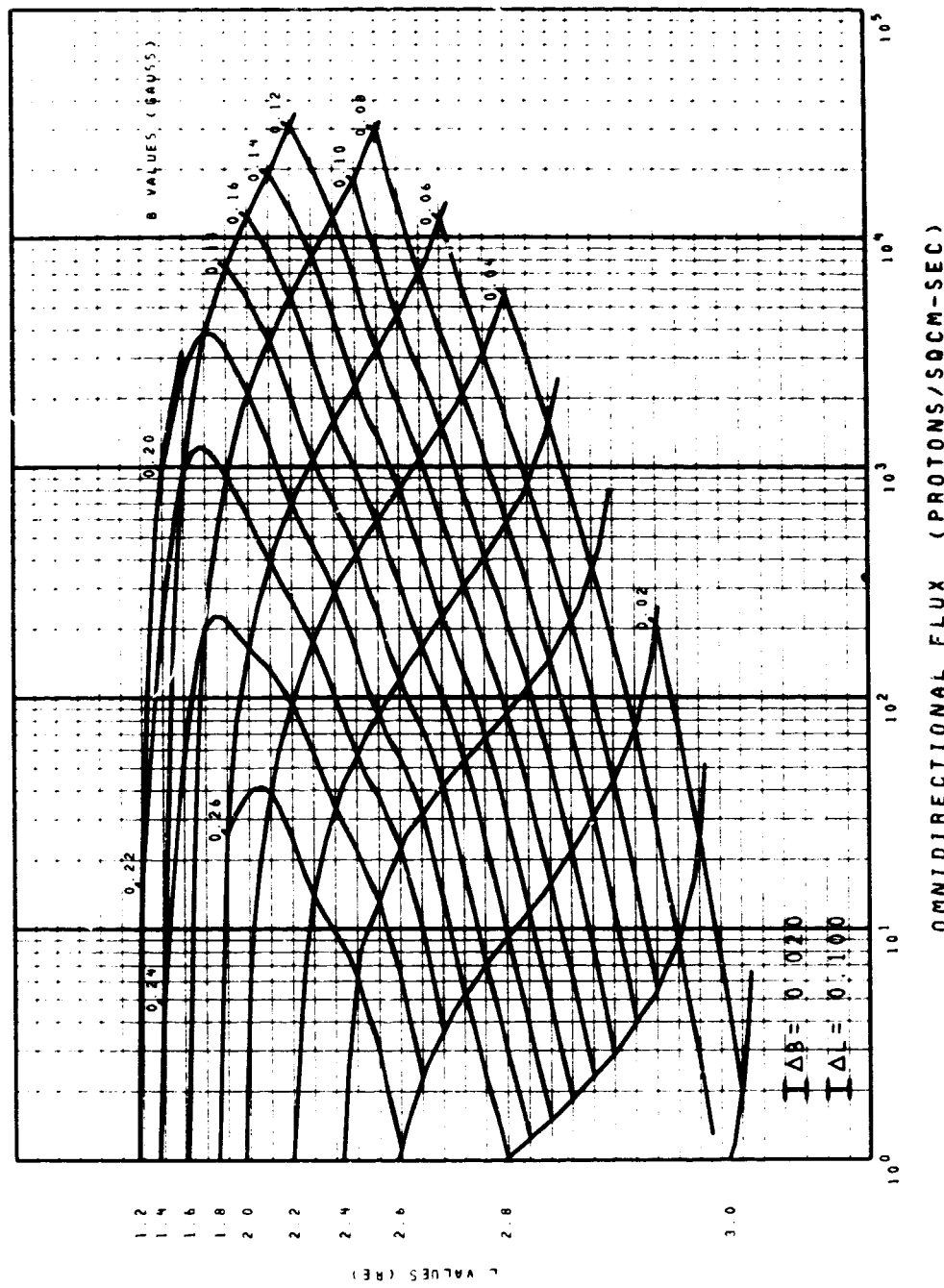
MODEL AP8 MIN FLUX DISTRIBUTIONS
ENERGY = 15. MEV
SOLAR MINIMUM FIG. 19



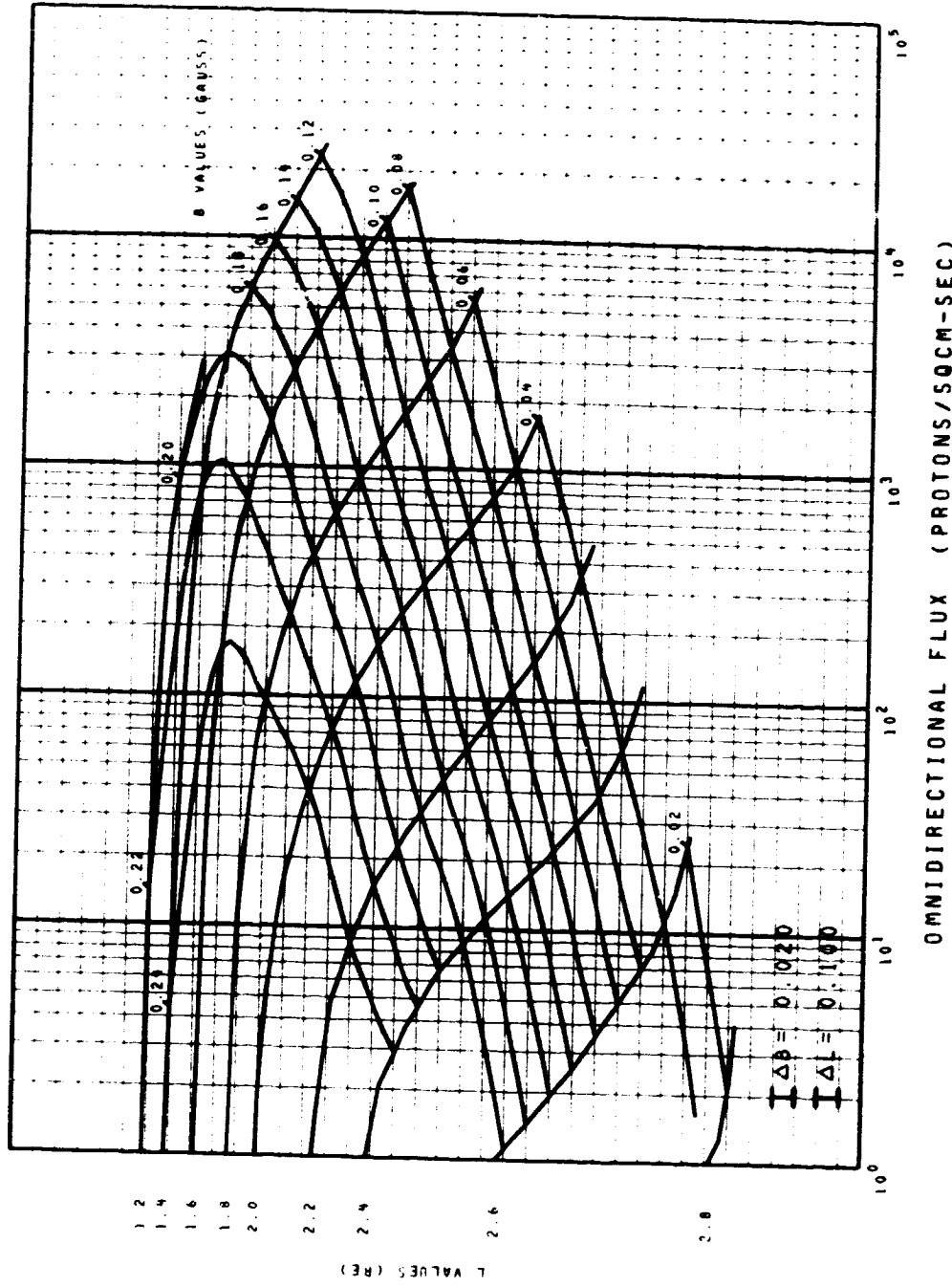
MODEL AP8 MIN FLUX DISTRIBUTIONS
 ENERGY = 20. MEV
 SOLAR MINIMUM FIG. 20



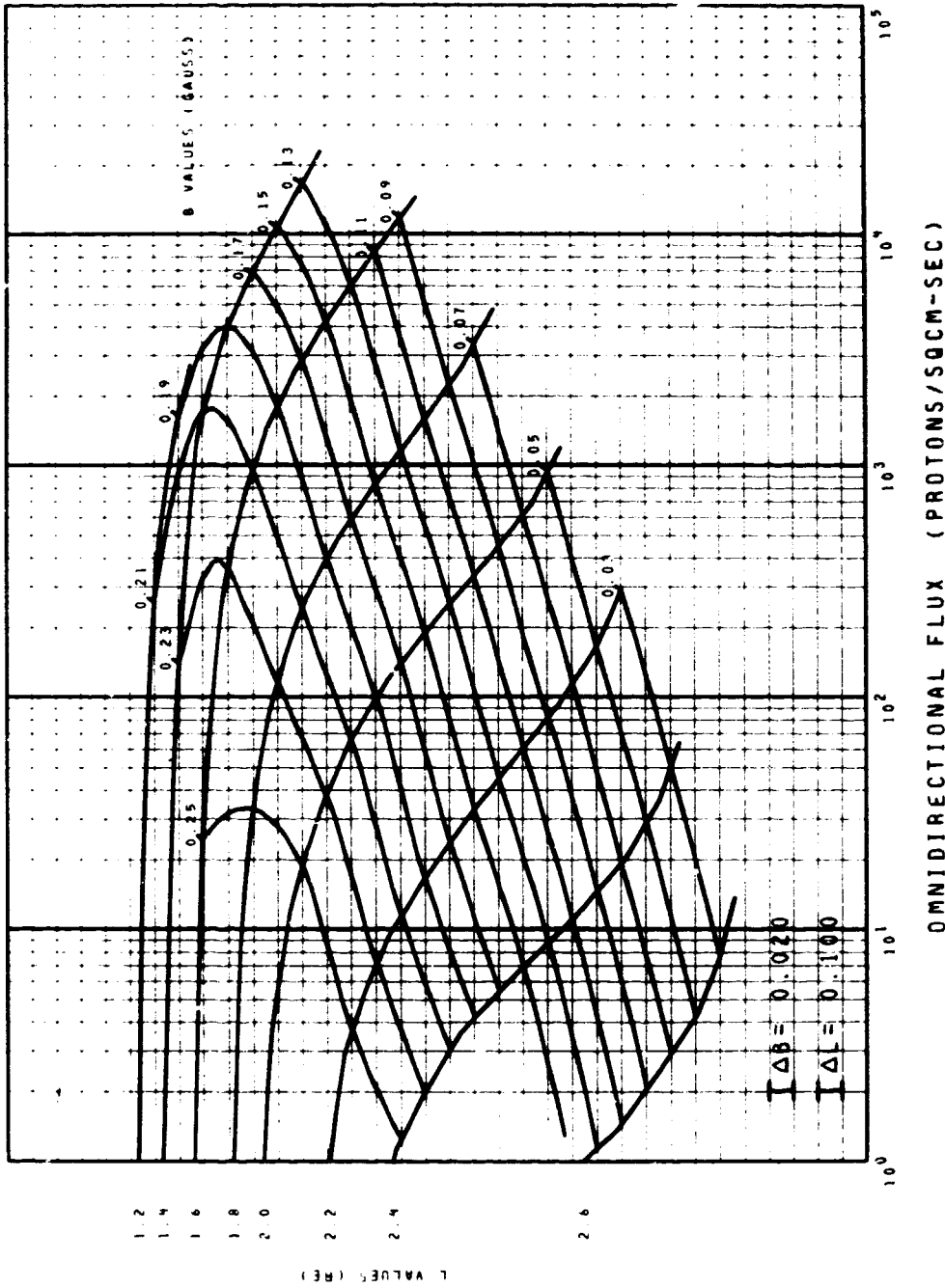
MODEL AP8 MIN FLUX DISTRIBUTIONS
 ENERGY = 30. MEV
 SOLAR MINIMUM FIG. 21



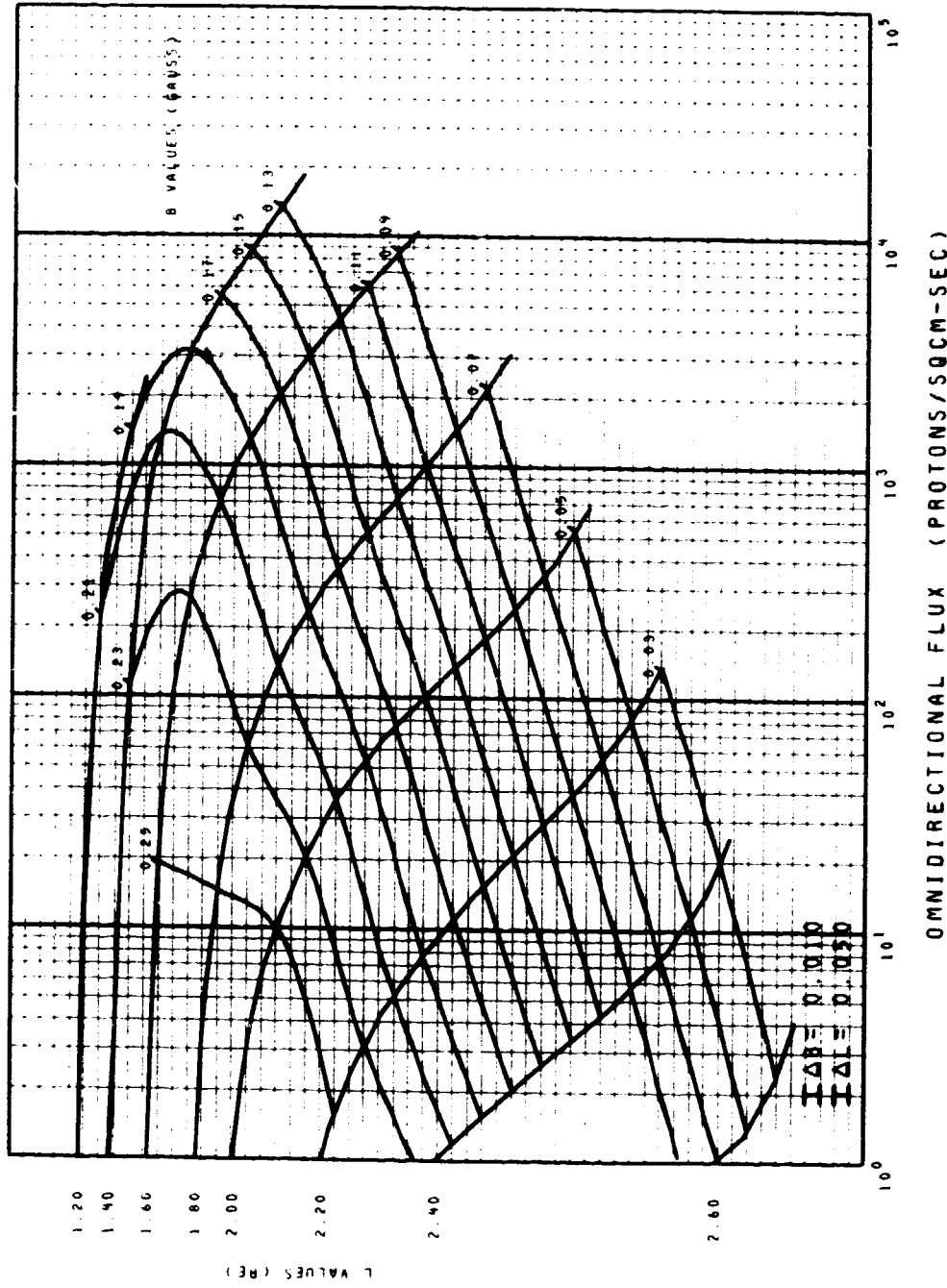
MODEL AP8 MIN FLUX DISTRIBUTIONS
 ENERGY = 50. MEV
 SOLAR MINIMUM FIG. 22



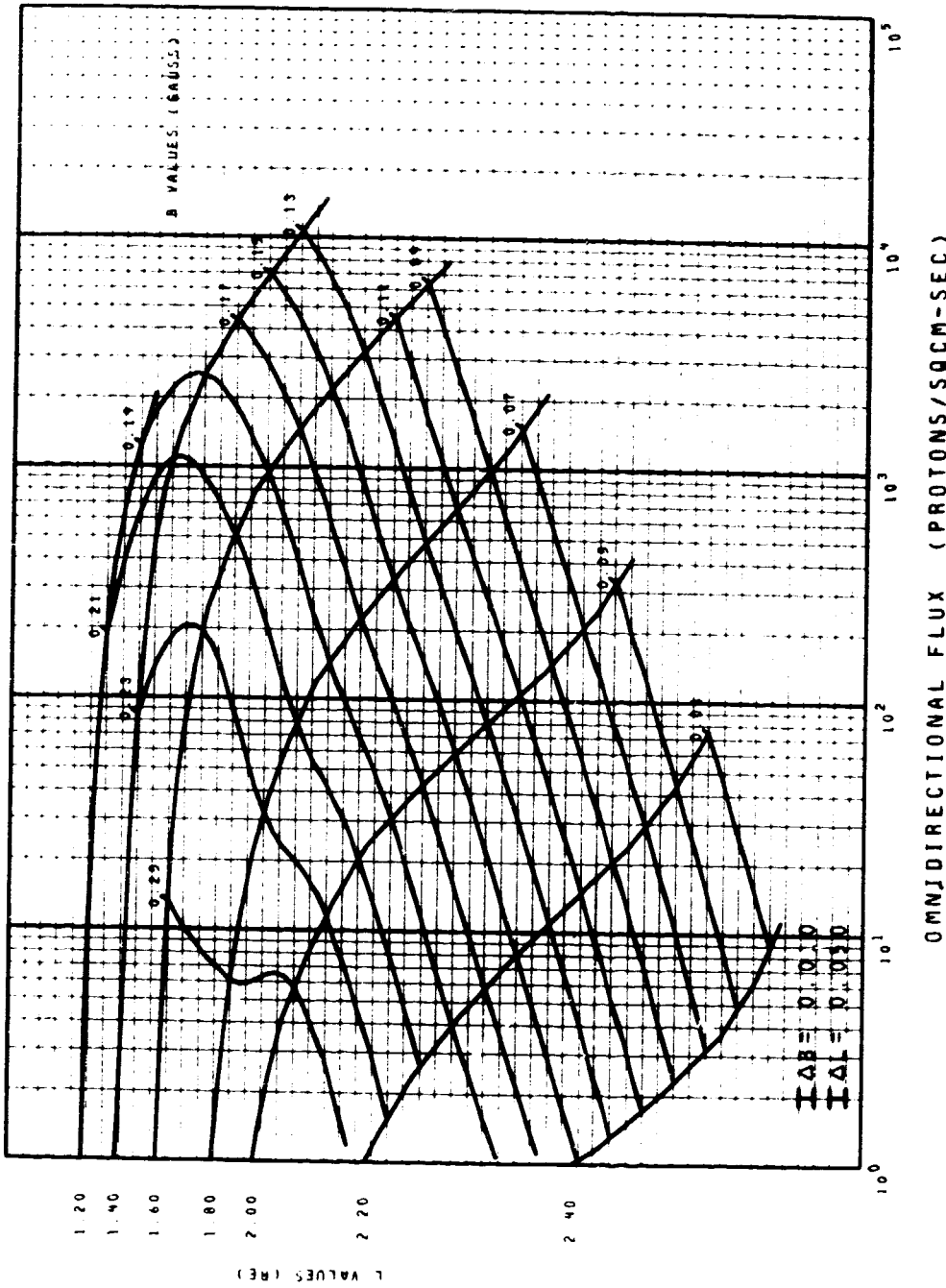
MODEL AP8 MIN FLUX DISTRIBUTIONS
 ENERGY = 60. MEV
 SOLAR MINIMUM FIG. 23



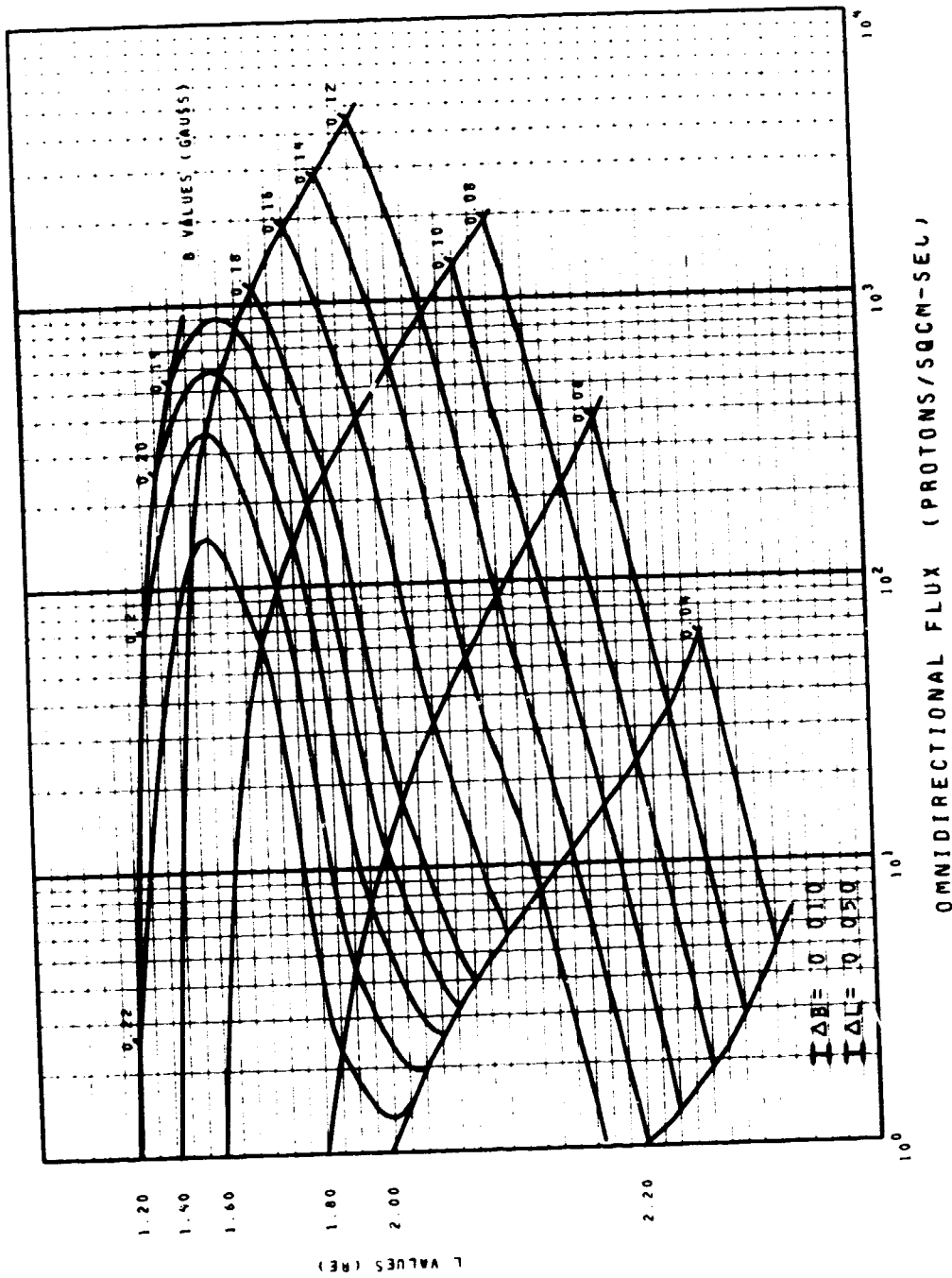
MODEL AP8 MIN FLUX DISTRIBUTIONS
 ENERGY = 80. MEV
 SOLAR MINIMUM FIG. 24



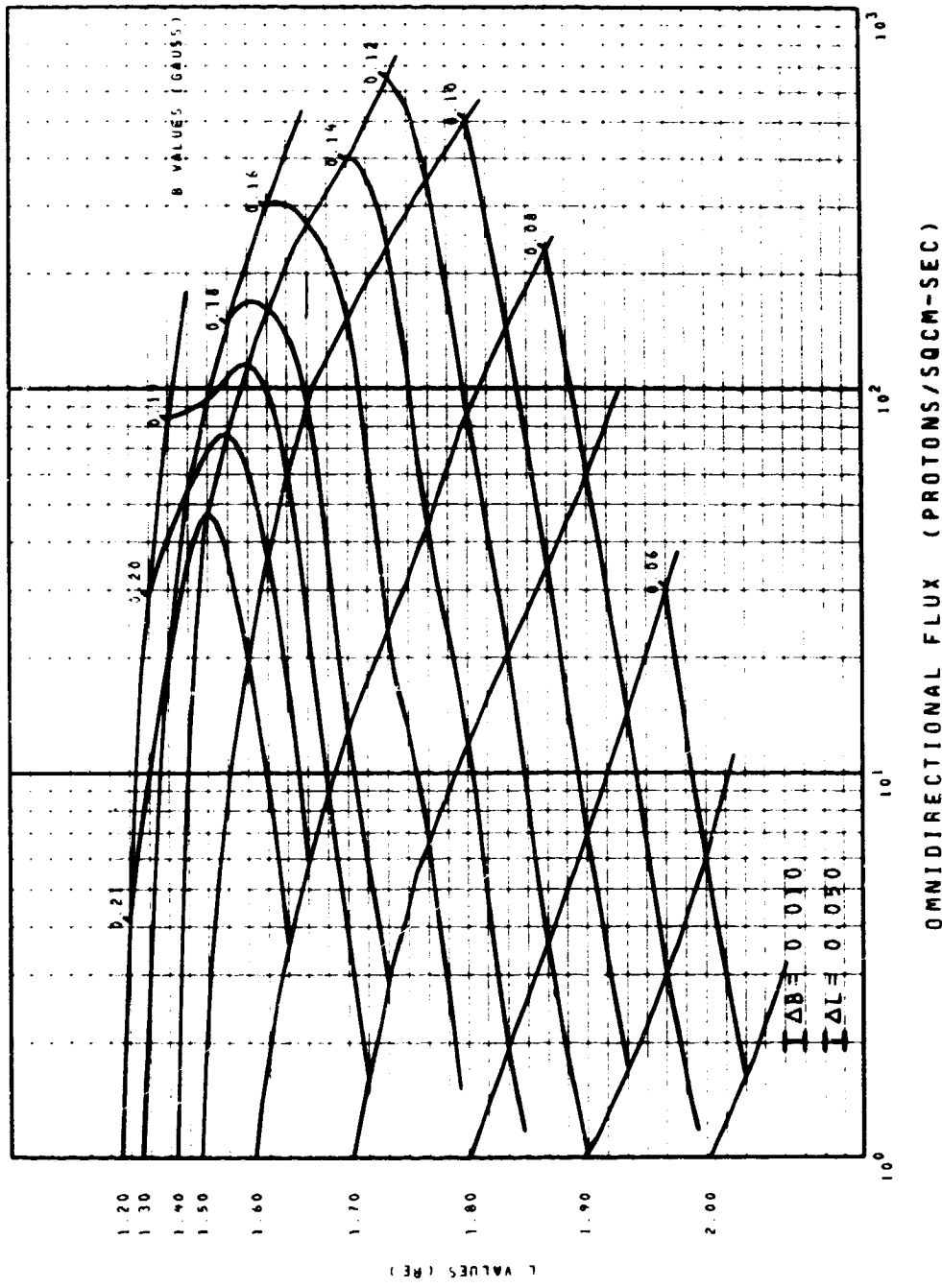
MODEL AP8 MIN FLUX DISTRIBUTIONS
 ENERGY=100. MEV
 SOLAR MINIMUM FIG. 25



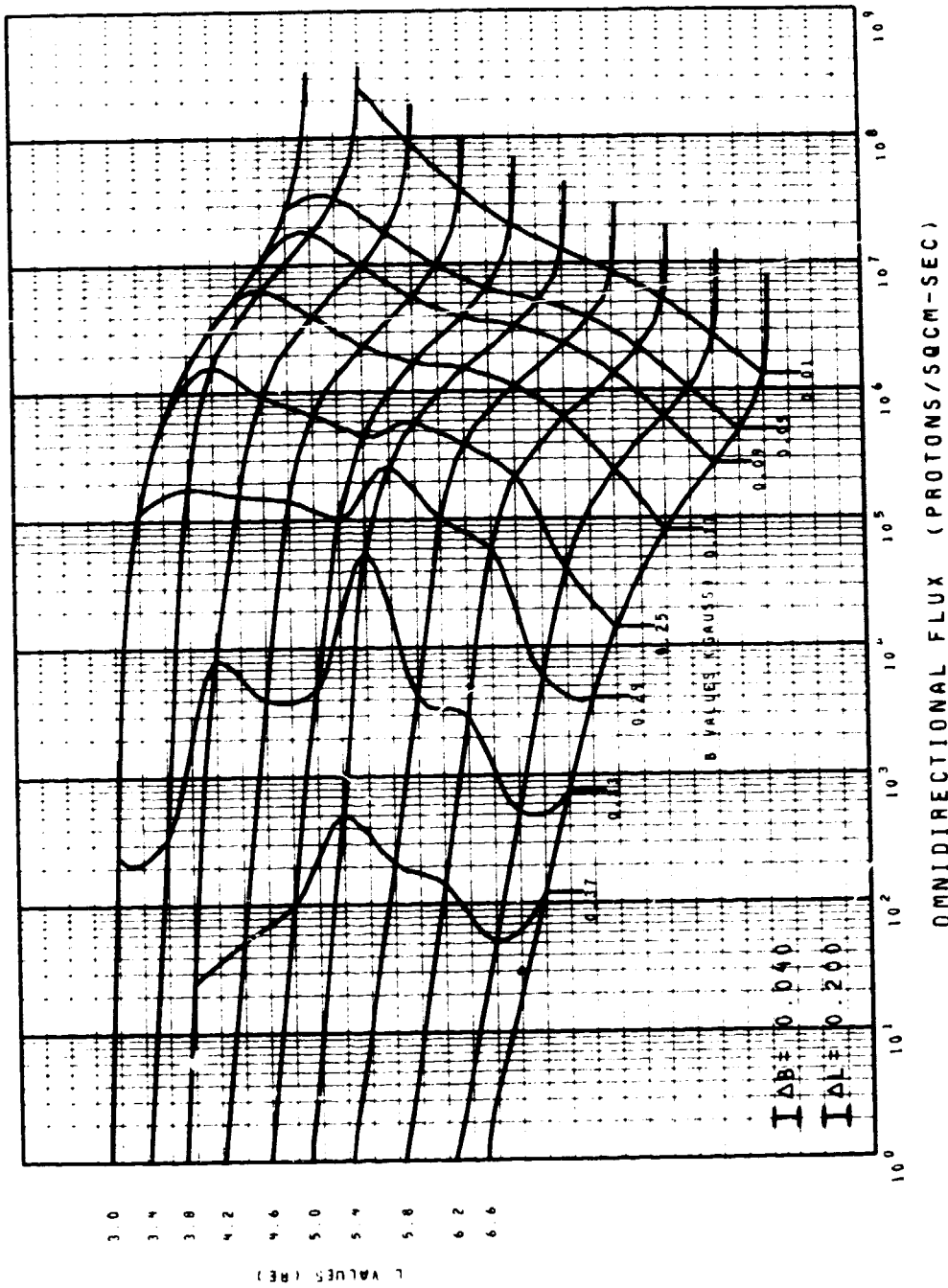
MODEL AP8 MIN FLUX DISTRIBUTIONS
 ENERGY = 200. MEV
 SOLAR MINIMUM FIG. 26



MODEL AP8 MIN FLUX DISTRIBUTIONS
 ENERGY = 400. MEV
 SOLAR MINIMUM FIG. 27

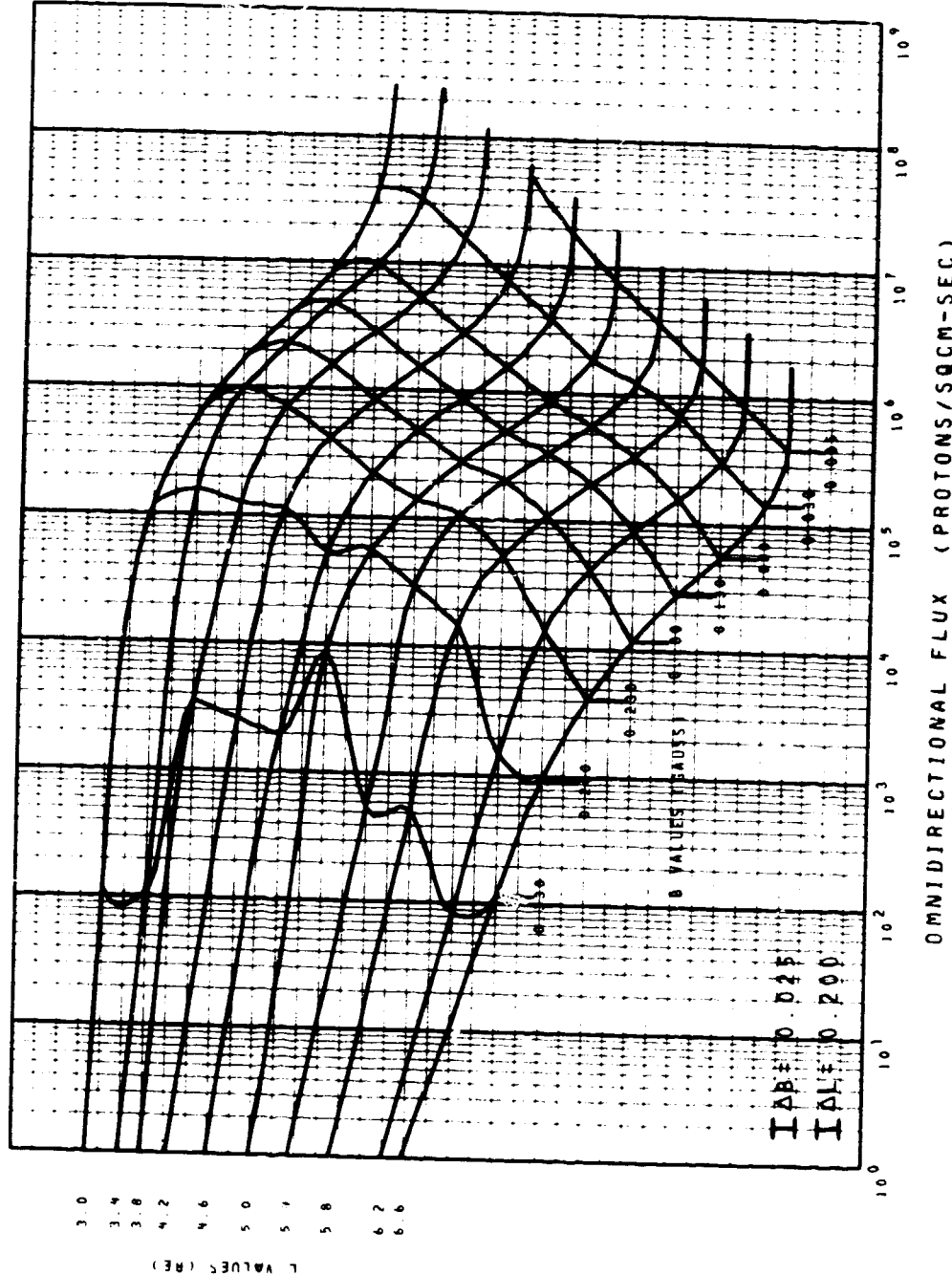


MODEL AP8 MIN FLUX DISTRIBUTIONS
ENERGY = 0.1 MEV
SOLAR MINIMUM FIG. 23

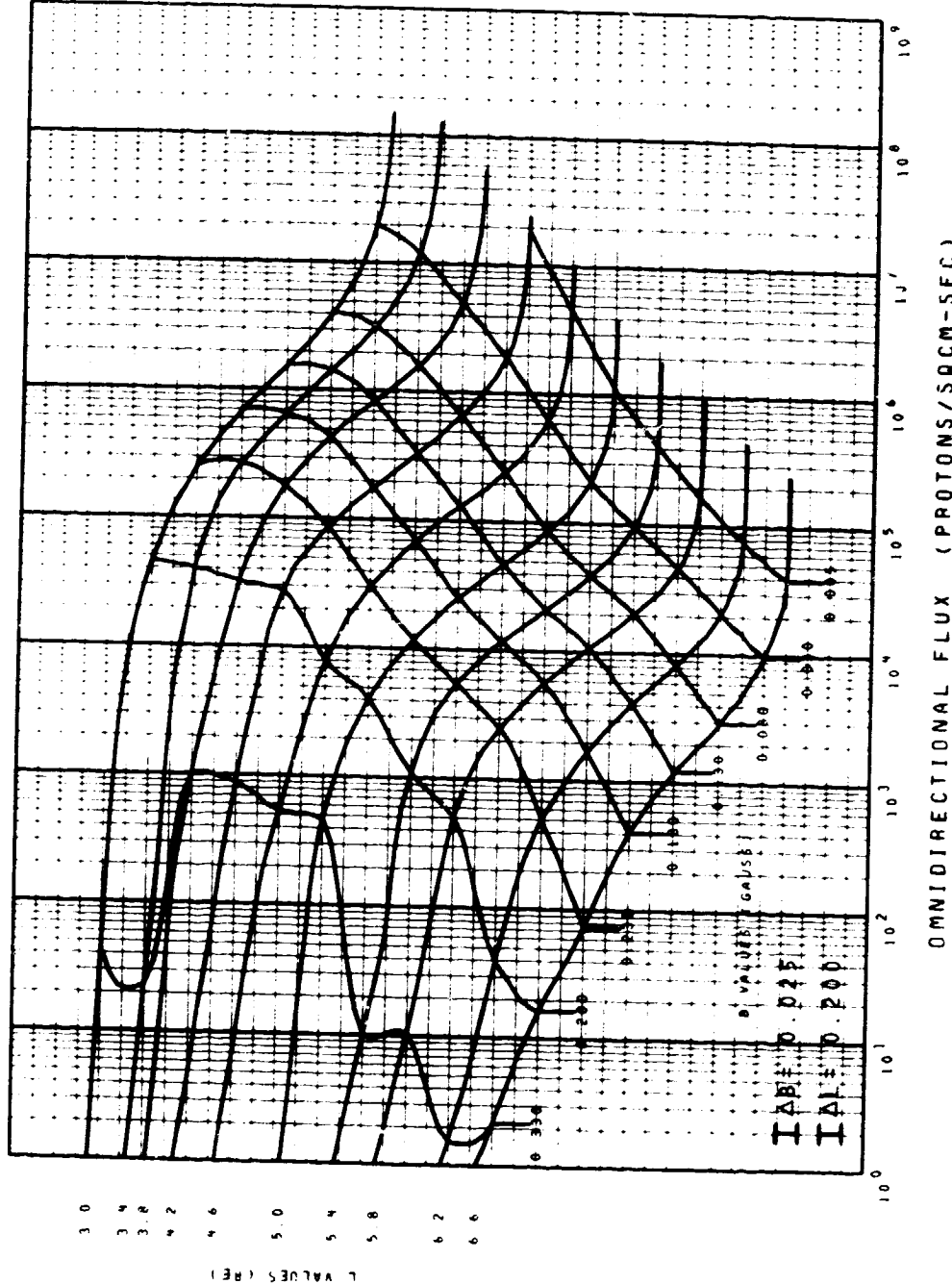


REPRODUCIBILITY OF FIGURE
MARGINAL PAGE IS POOR

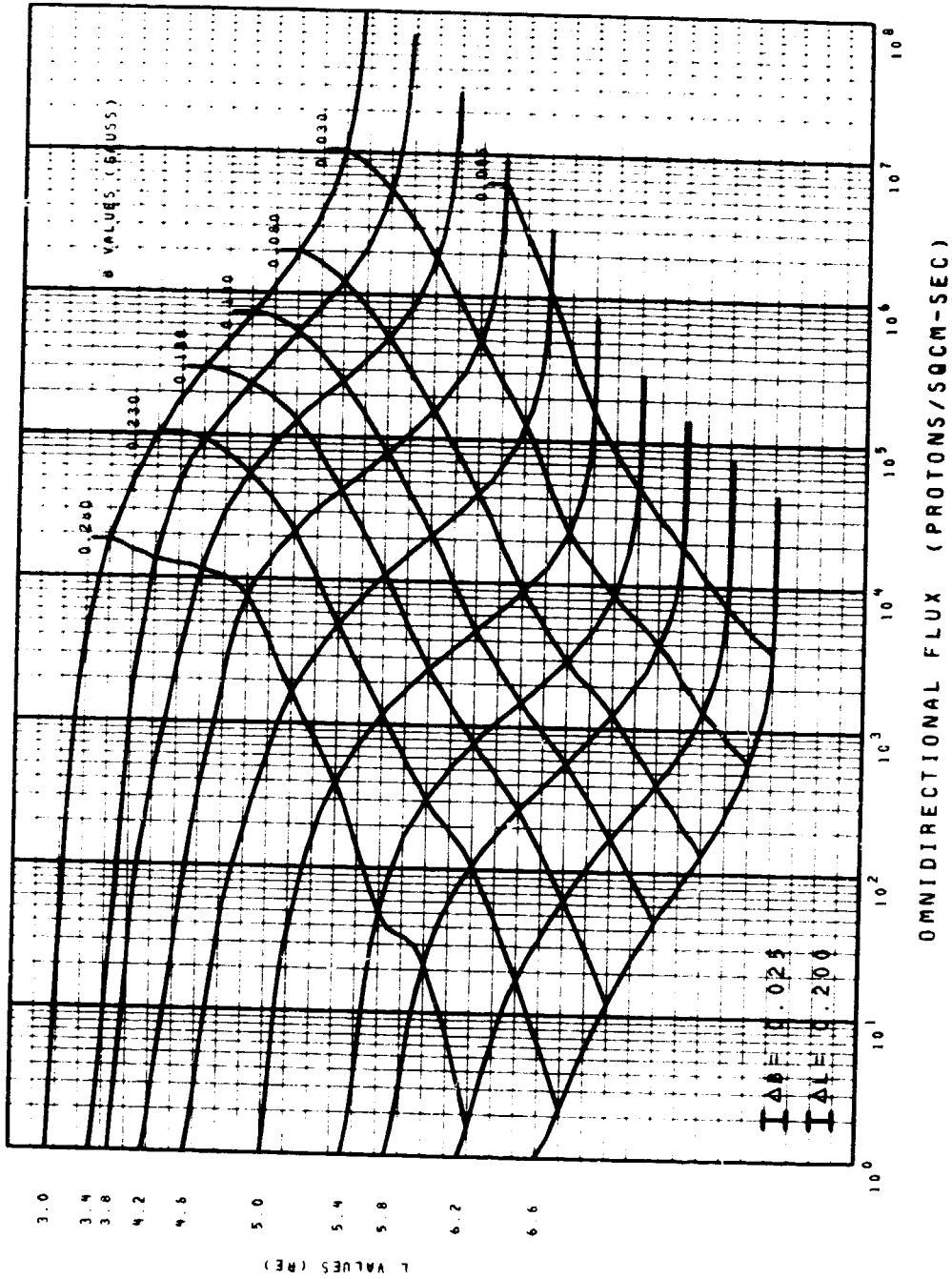
MODEL APP MIN FLUX DISTRIBUTIONS
 ENERGY = 0.2 MEV
 SOLAR MINIMUM FIG. 29



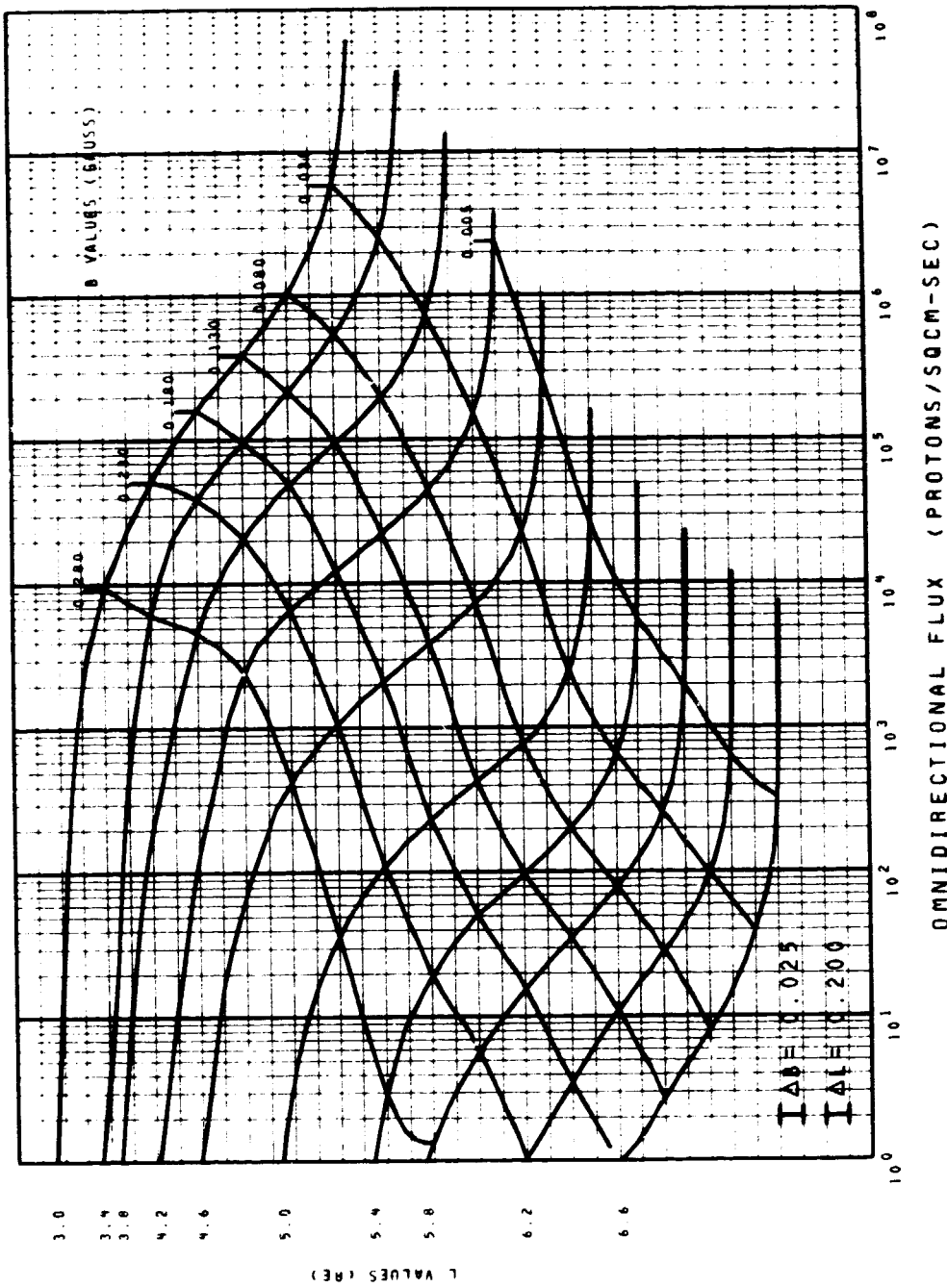
MODEL APP MIN FLUX DISTRIBUTIONS
 ENERGY = 0.4 MEV
 SOLAR MINIMUM FIG. 30



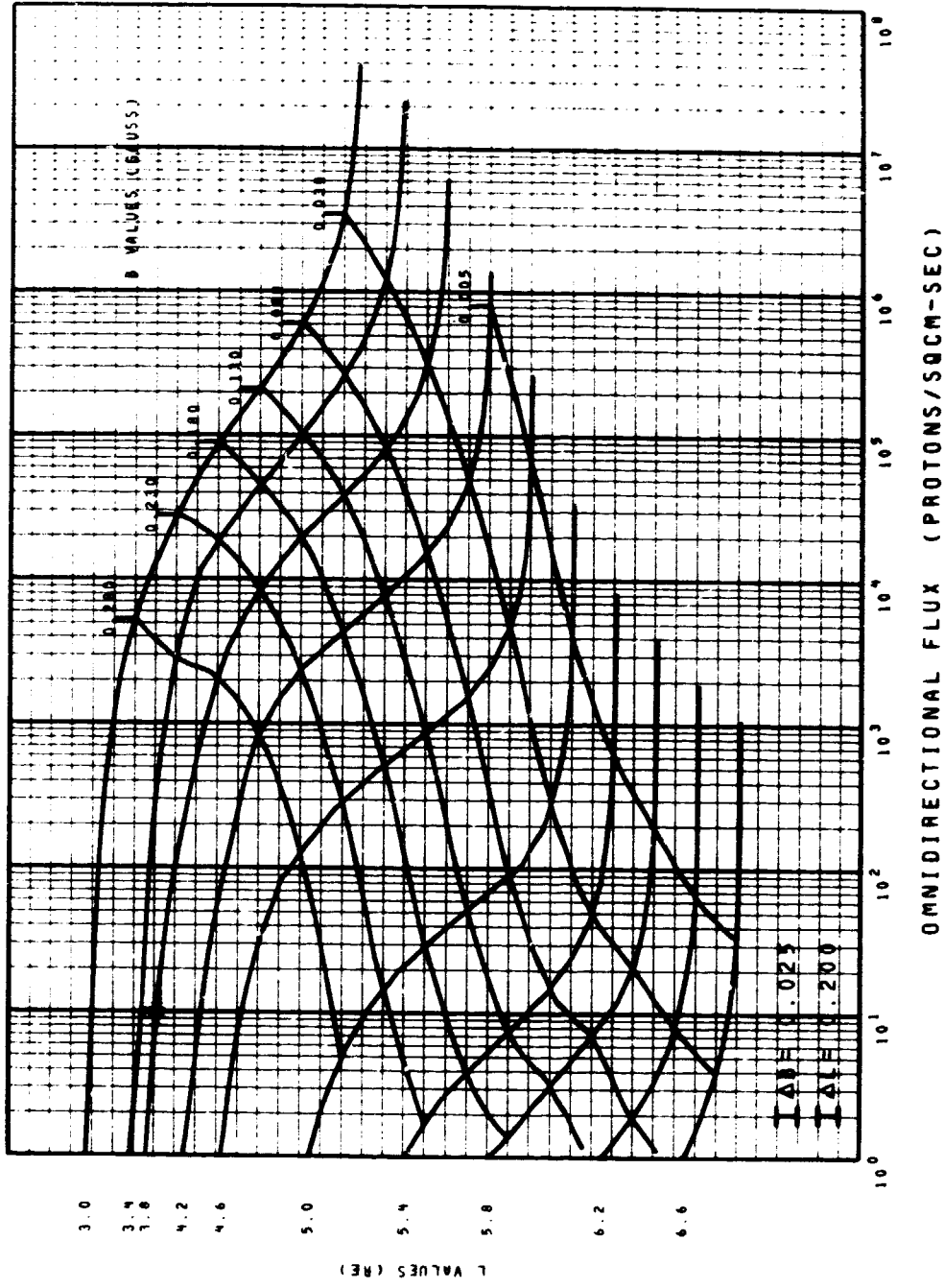
MODEL AP8 MIN FLUX DISTRIBUTIONS
 ENERGY = 0.6 MEV
 SOLAR MINIMUM FIG. 31



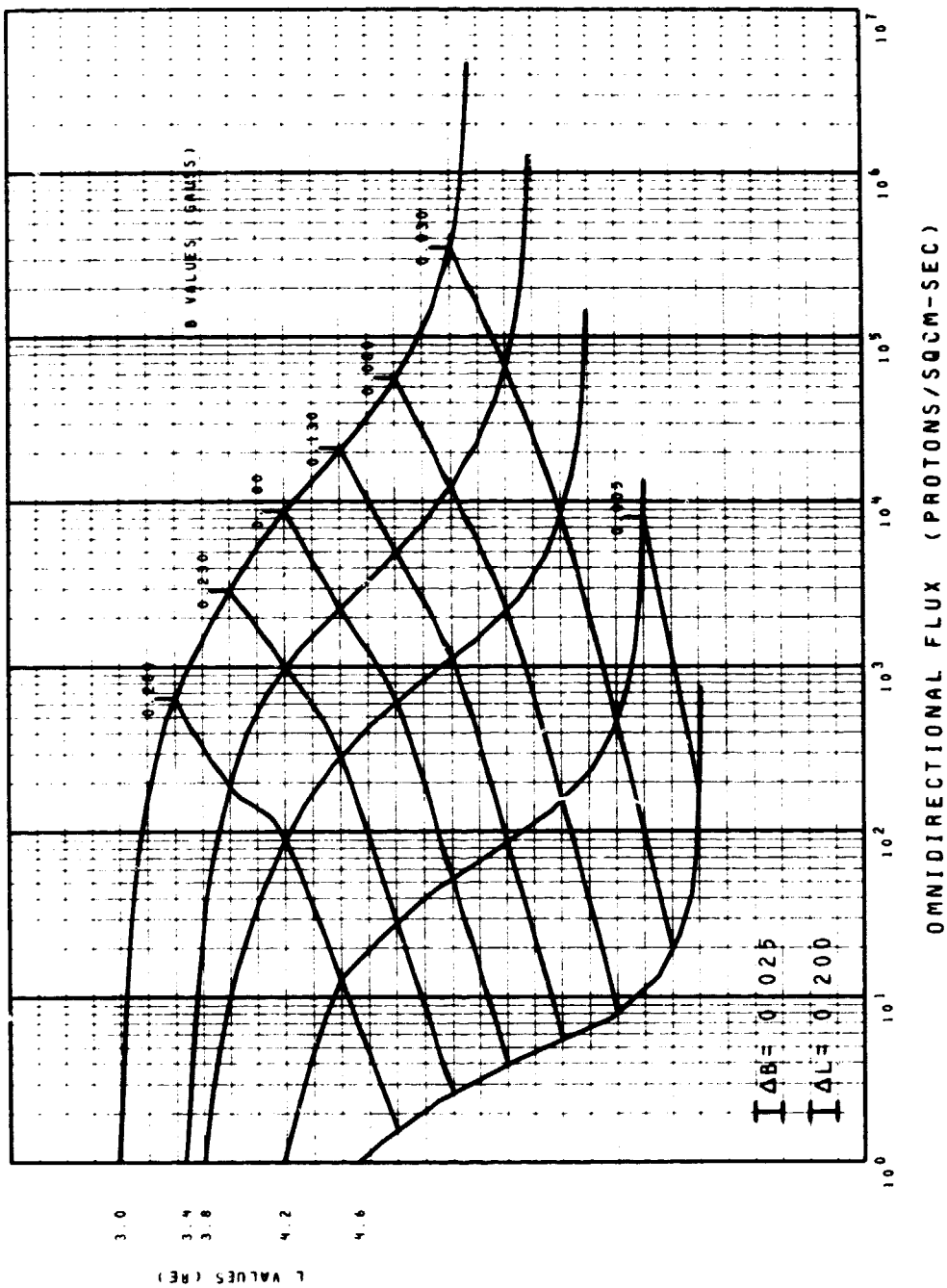
MODEL AP8 MIN FLUX DISTRIBUTIONS
 ENERGY = 0.8 MEV
 SOLAR MINIMUM FIG. 32



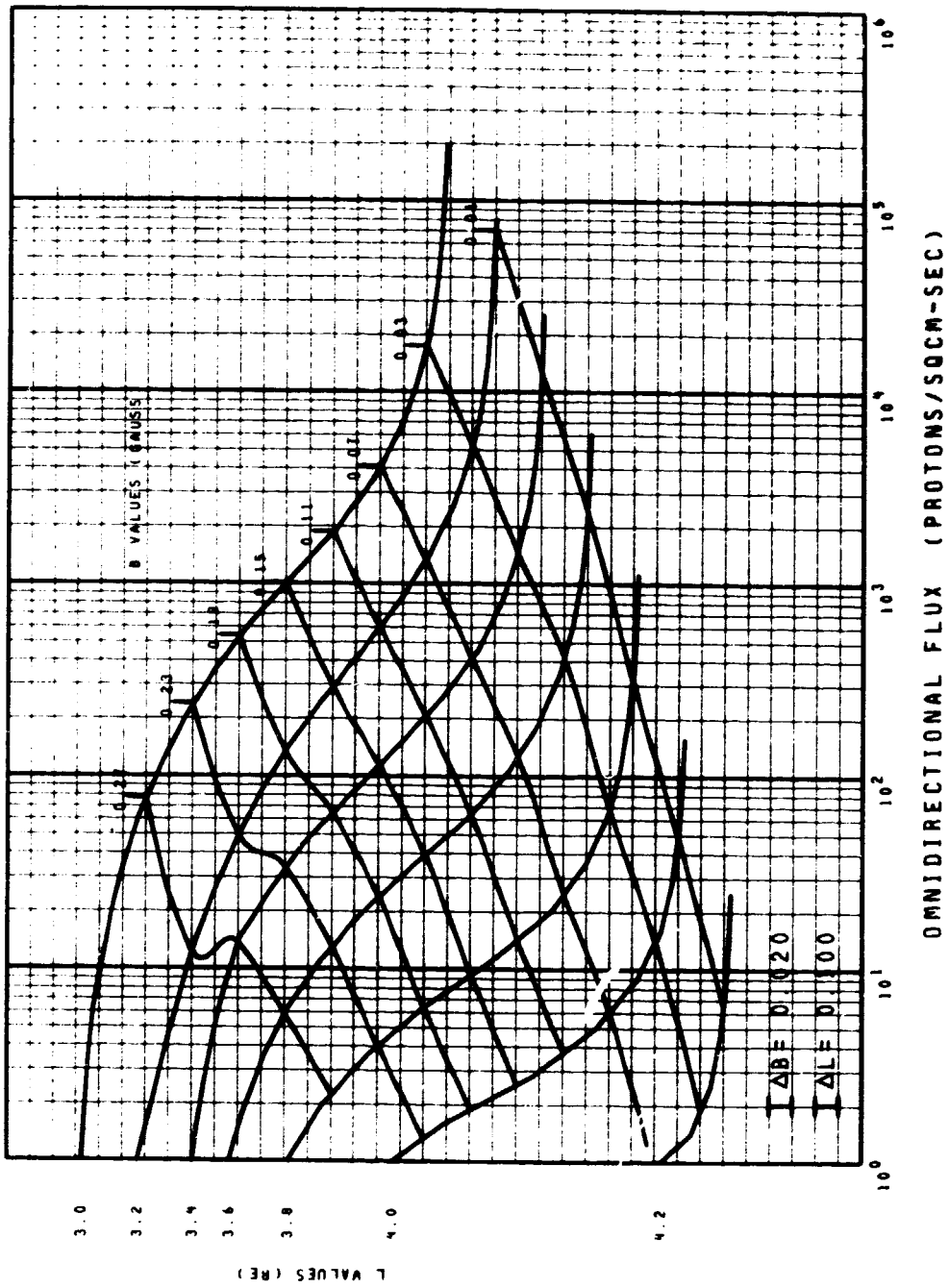
MODEL AP8 MIN FLUX DISTRIBUTIONS
ENERGY = 1.0 MeV
SOLAR MINIMUM FIG. 33



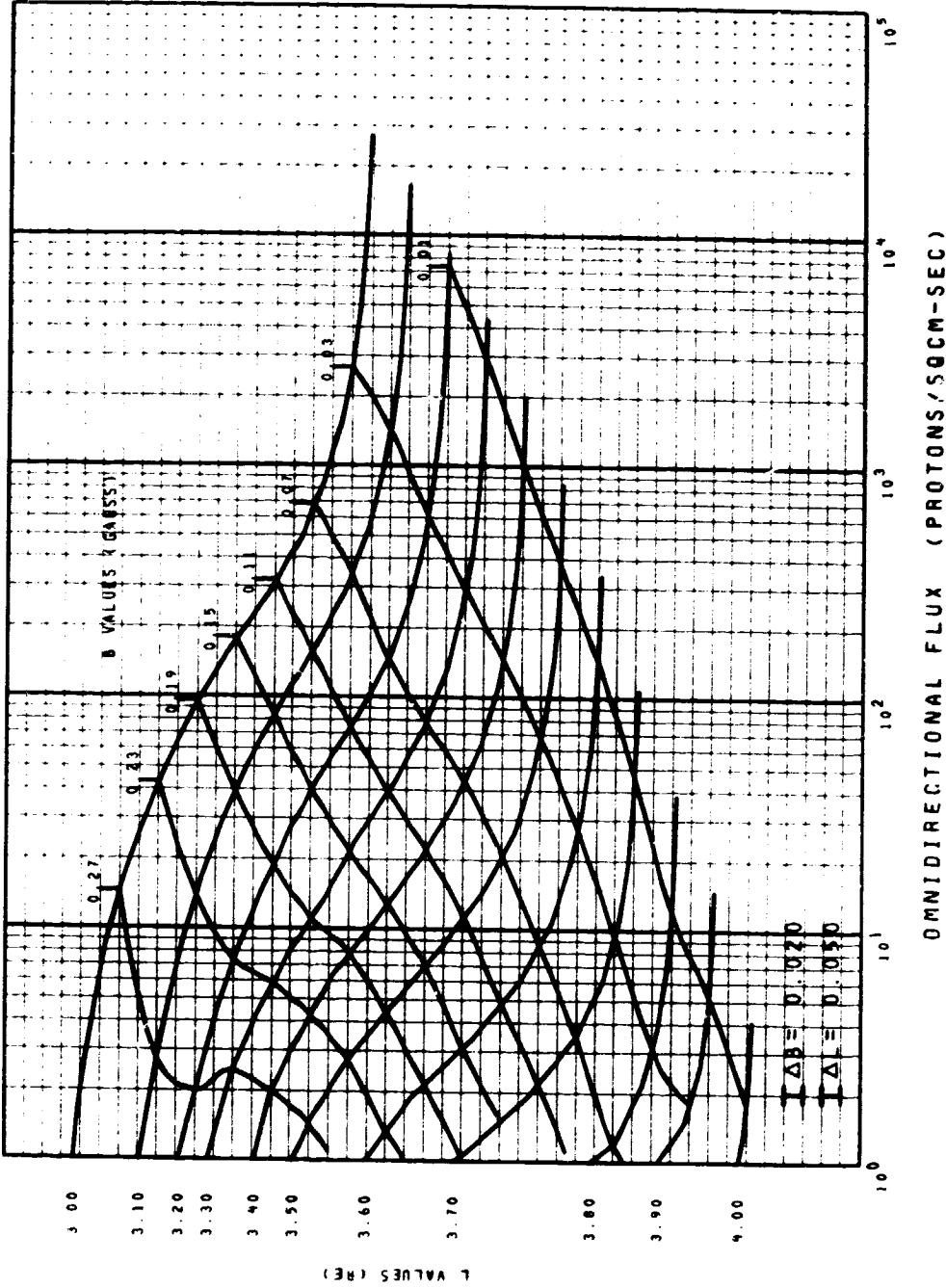
MODEL RP8 MIN FLUX DISTRIBUTIONS
ENERGY = 2.0 MEV
SOLAR MINIMUM FIG. 34



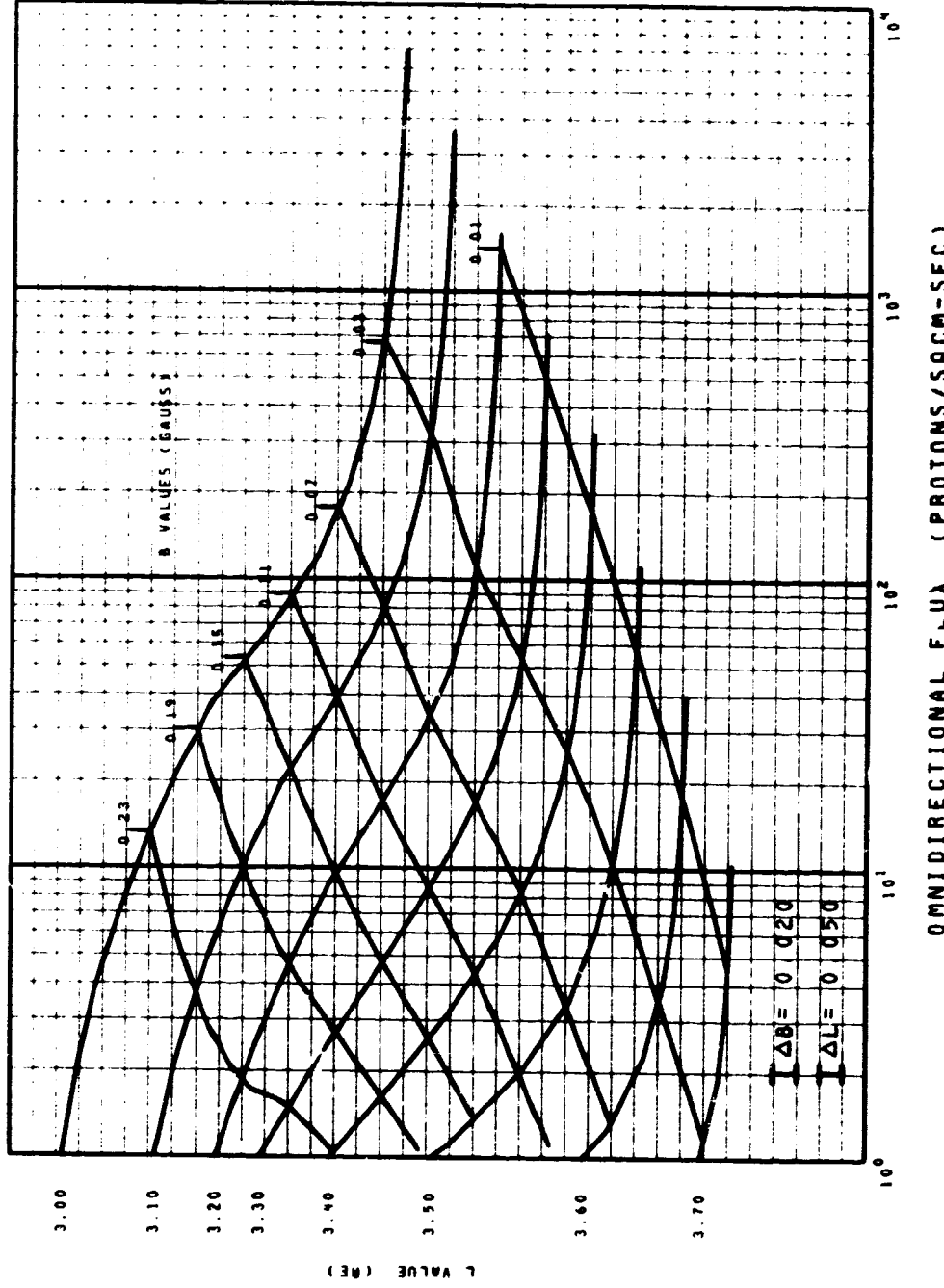
MODEL AP8 MIN FLUX DISTRIBUTIONS
 ENERGY = 4.0 MEV
 SOLAR MINIMUM FIG. 35



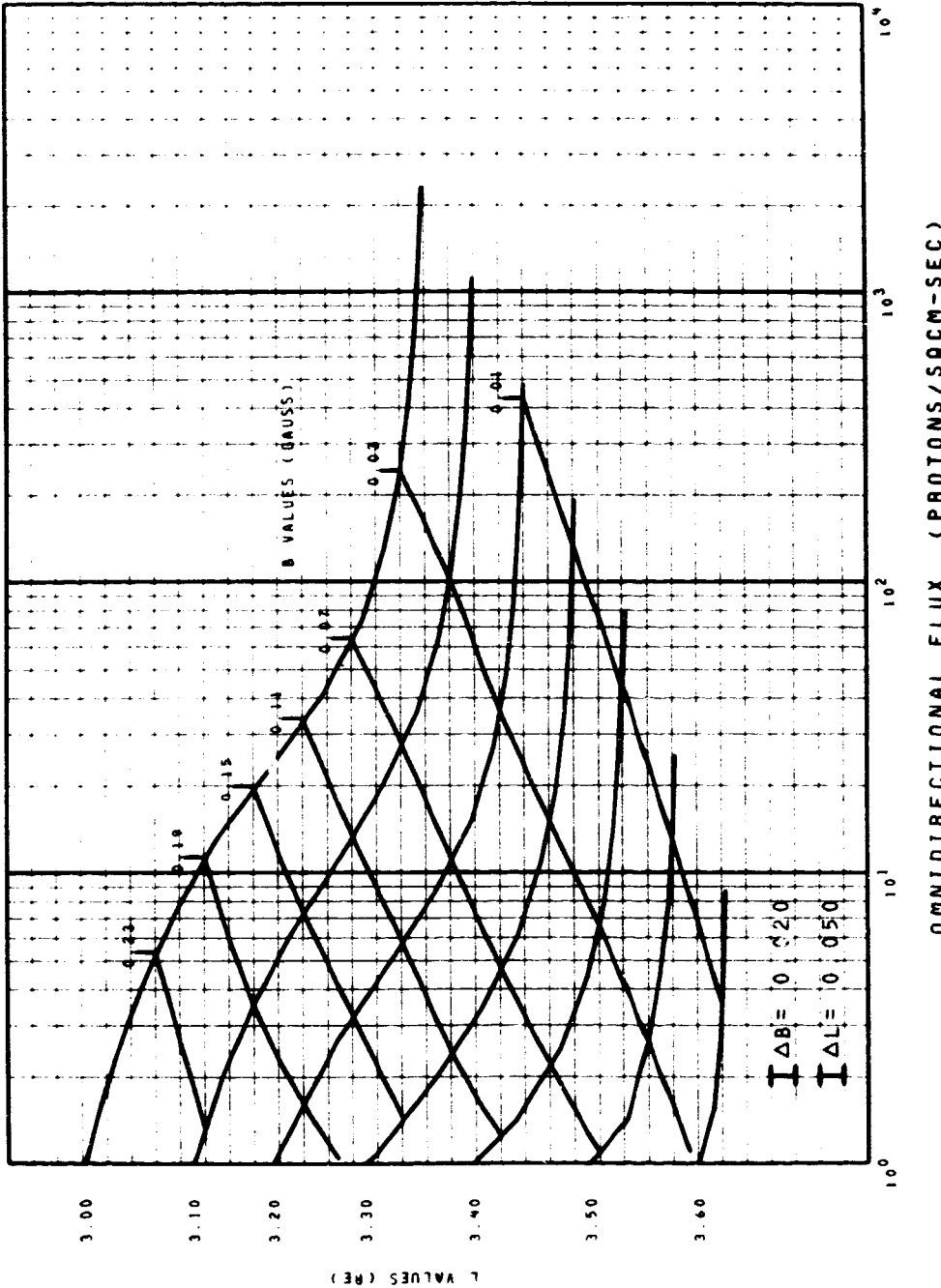
MODEL AP8 MIN FLUX DISTRIBUTIONS
 ENERGY = 6.0 MEV
 SOLAR MINIMUM FIG. 36



MODEL AP8 MIN FLUX DISTRIBUTIONS
ENERGY = 8.0 MEV
SOLAR MINIMUM FIG. 37

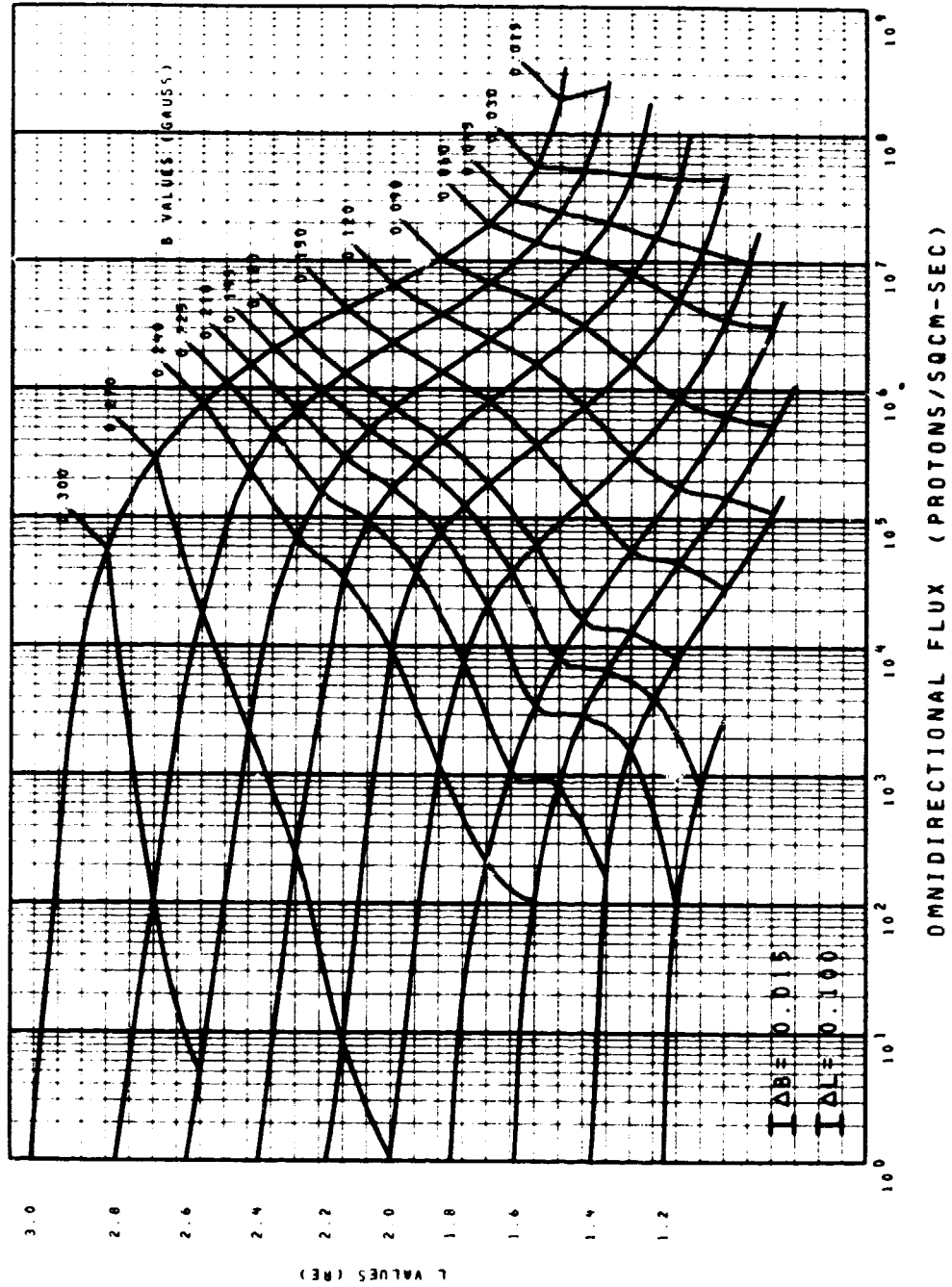


MODEL AP8 MIN FLUX DISTRIBUTIONS
 ENERGY = 10. MEV
 SOLAR MINIMUM FIG. 38

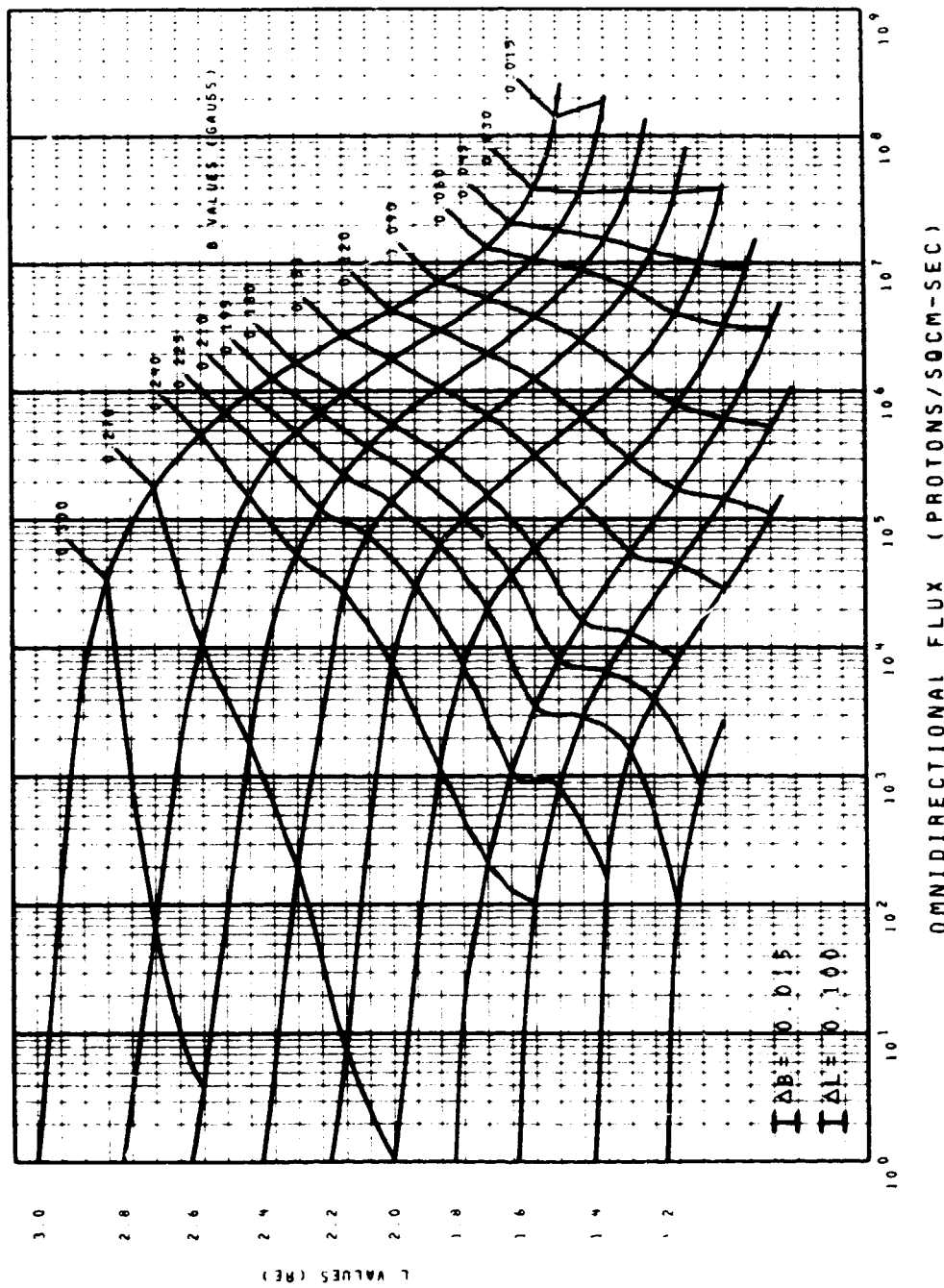


REPRODUCIBILITY OF THE
ORIGINAL PAGE IS POOR

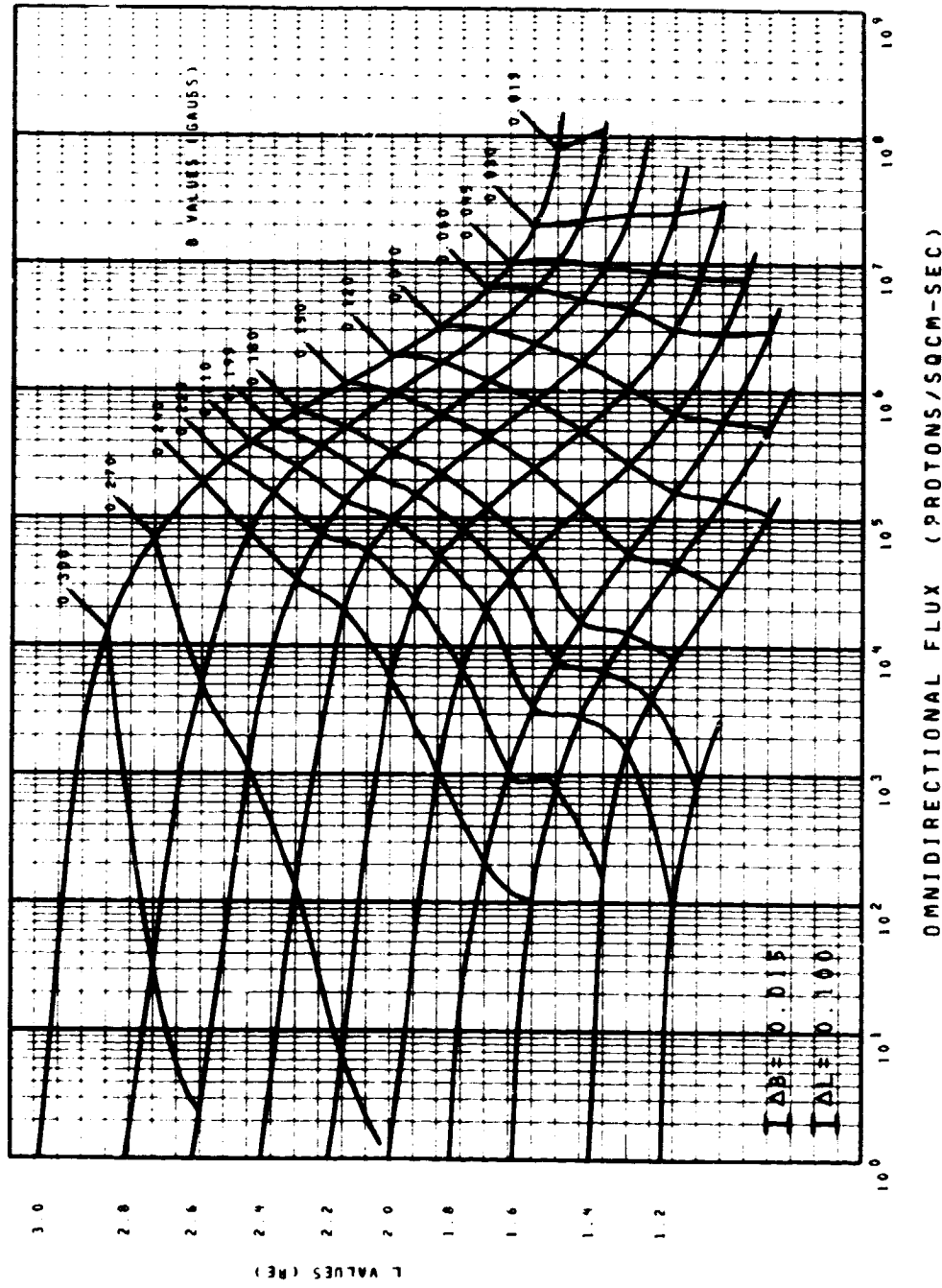
MODEL AP8 MAX FLUX DISTRIBUTIONS
 ENERGY = 0.1 MEV
 SOLAR MAXIMUM FIG. 39



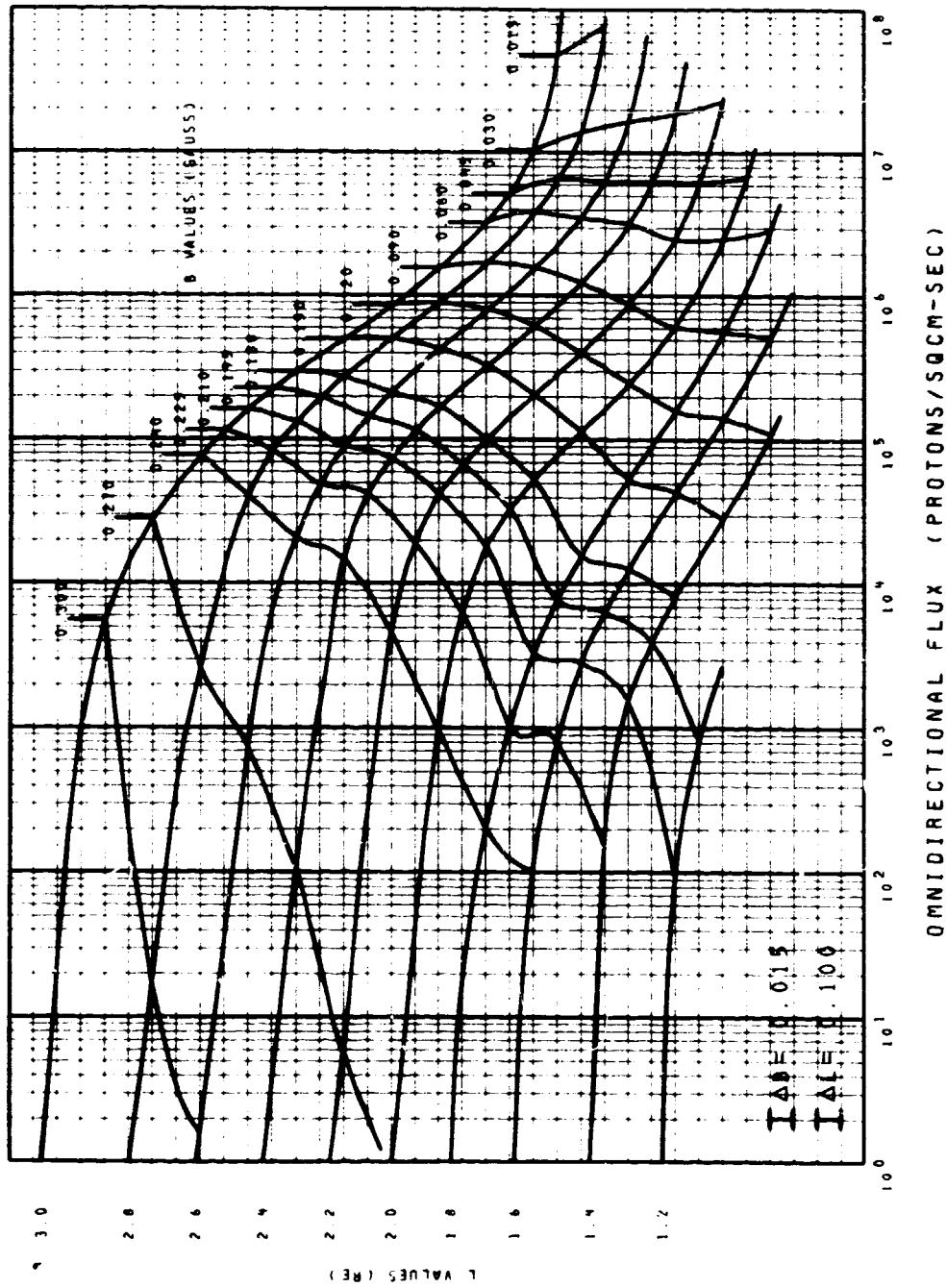
MODEL AP8 MAX FLUX DISTRIBUTIONS
 ENERGY = 0.2 MEV
 SOLAR MAXIMUM FIG. 40



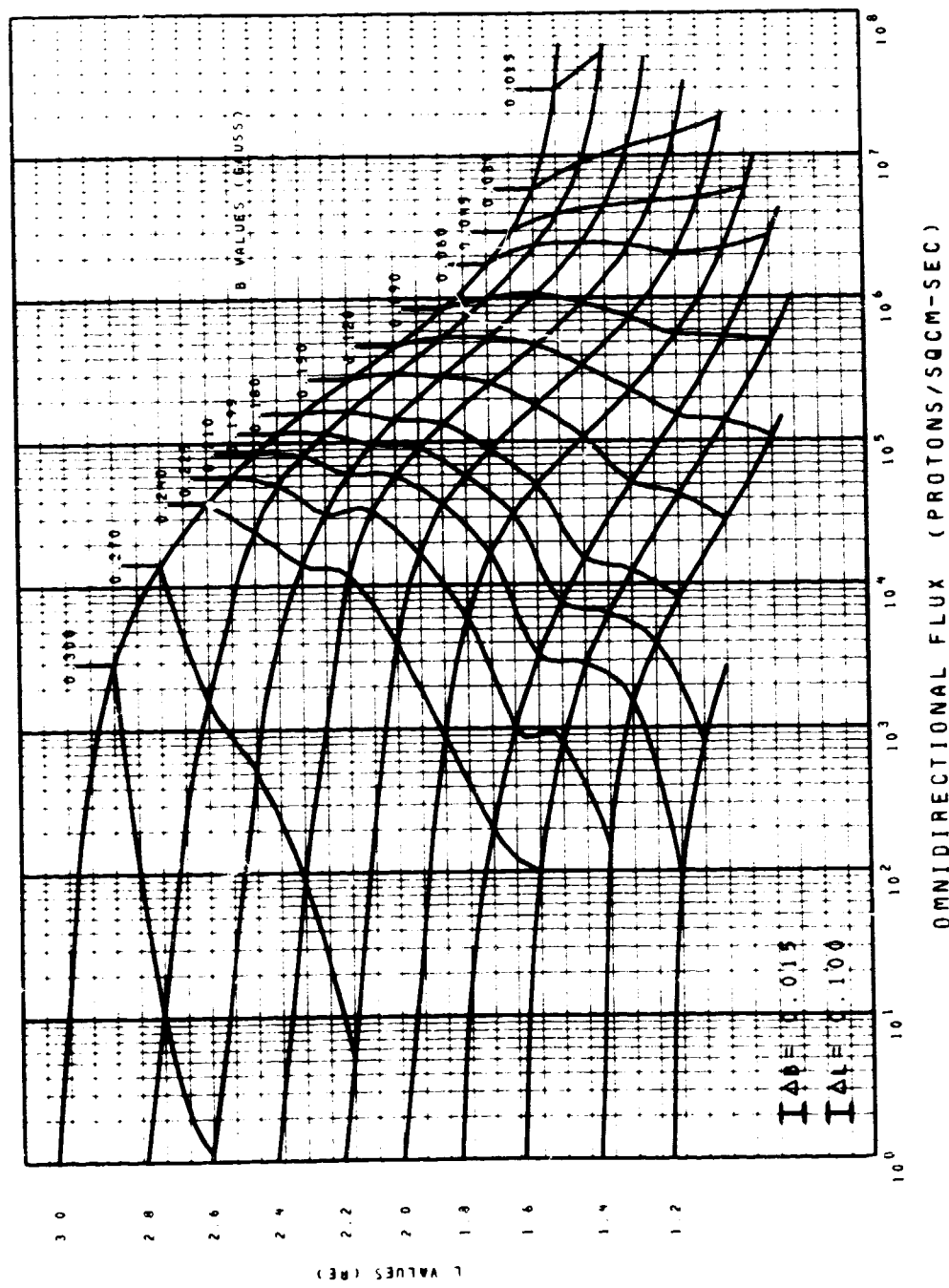
MODEL AP8 MAX FLUX DISTRIBUTIONS
 ENERGY = 0.4 MEV
 SOLAR MAXIMUM FIG. 41



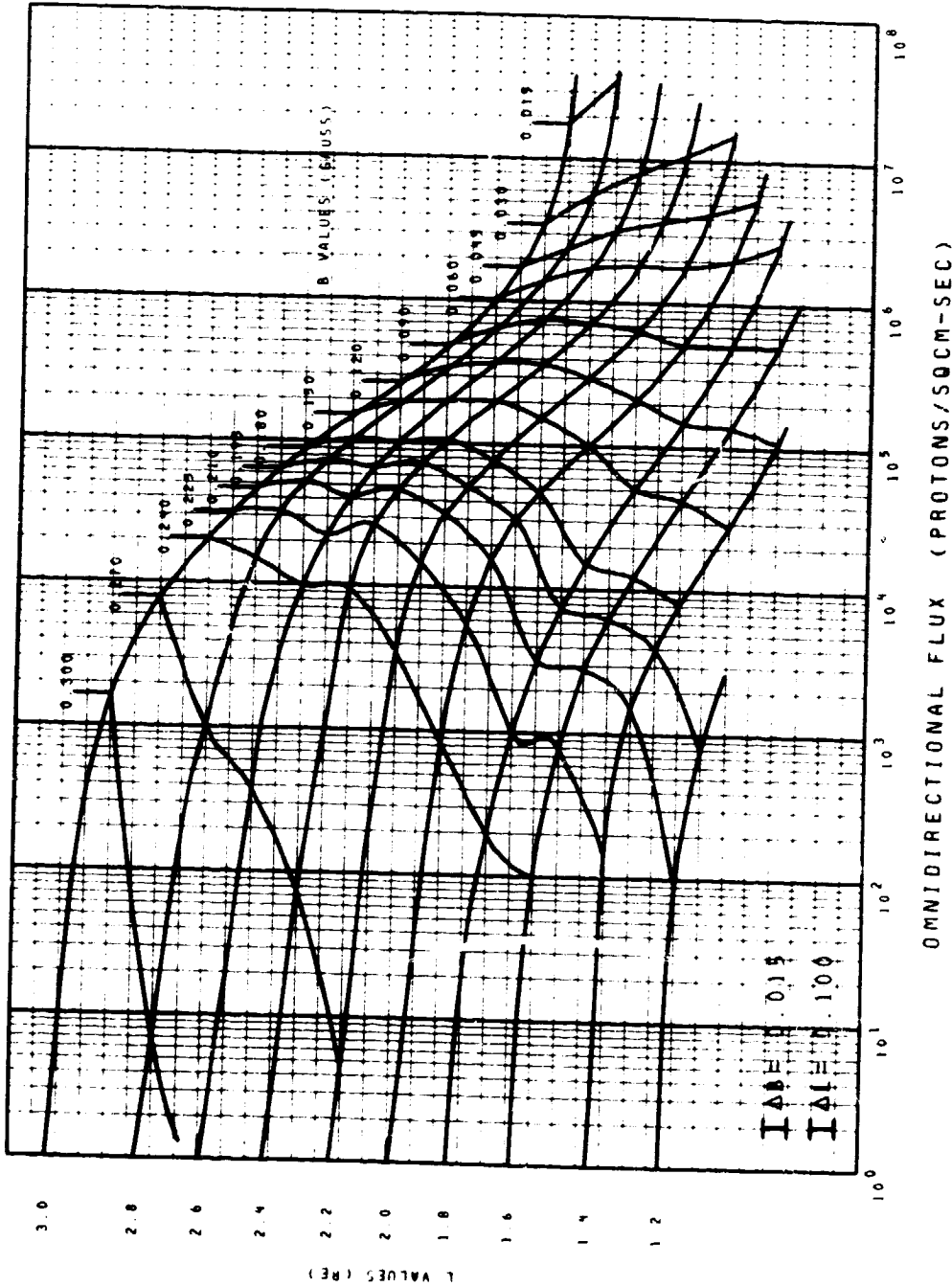
MODEL AP8 MAX FLUX DISTRIBUTIONS
 ENERGY = 0.6 MEV
 SOLAR MAXIMUM FIG. 42



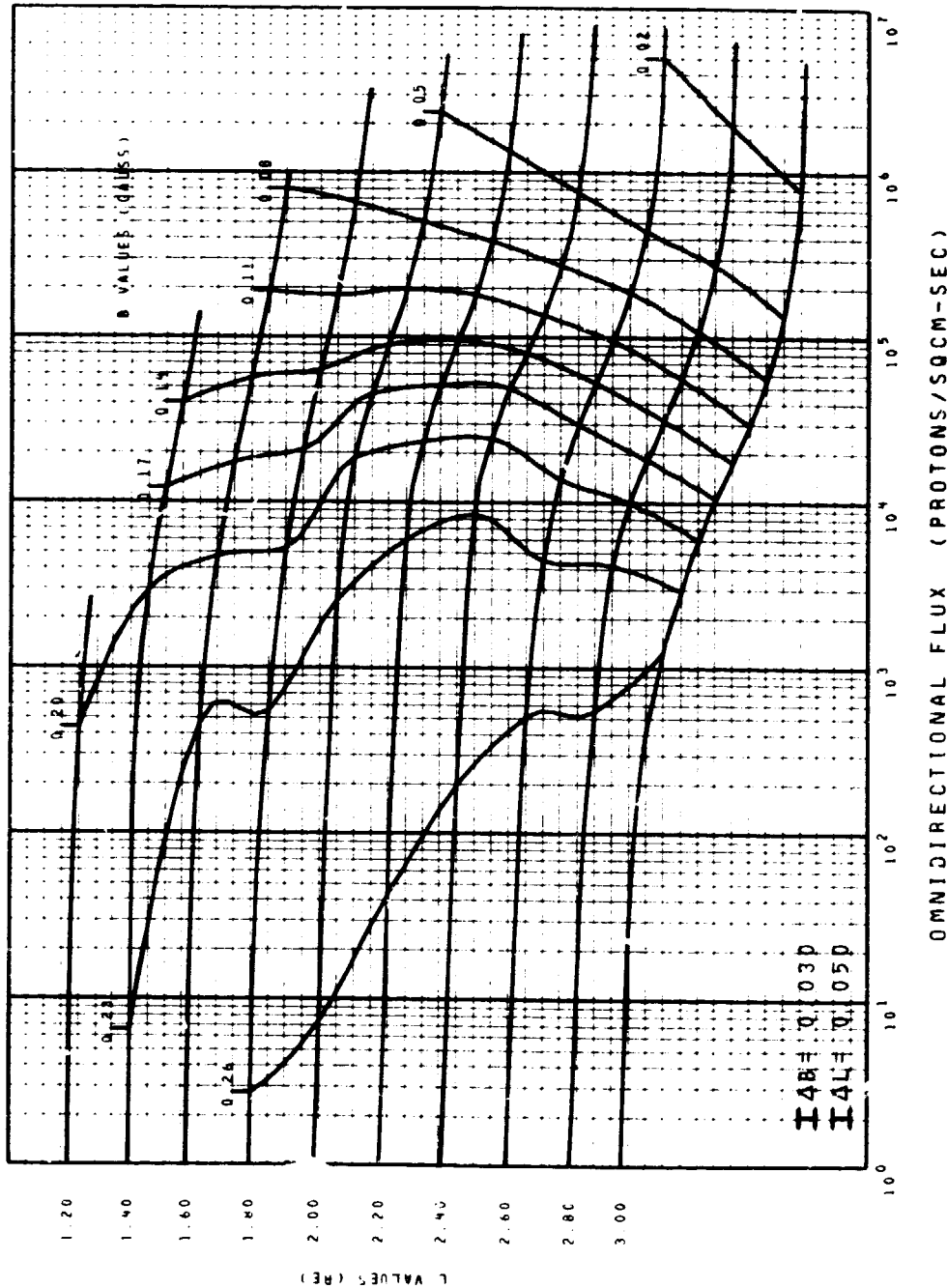
MODEL AP8 MAX FLUX DISTRIBUTIONS
 ENERGY = 0.8 MEV
 SOLAR MAXIMUM FIG. 43



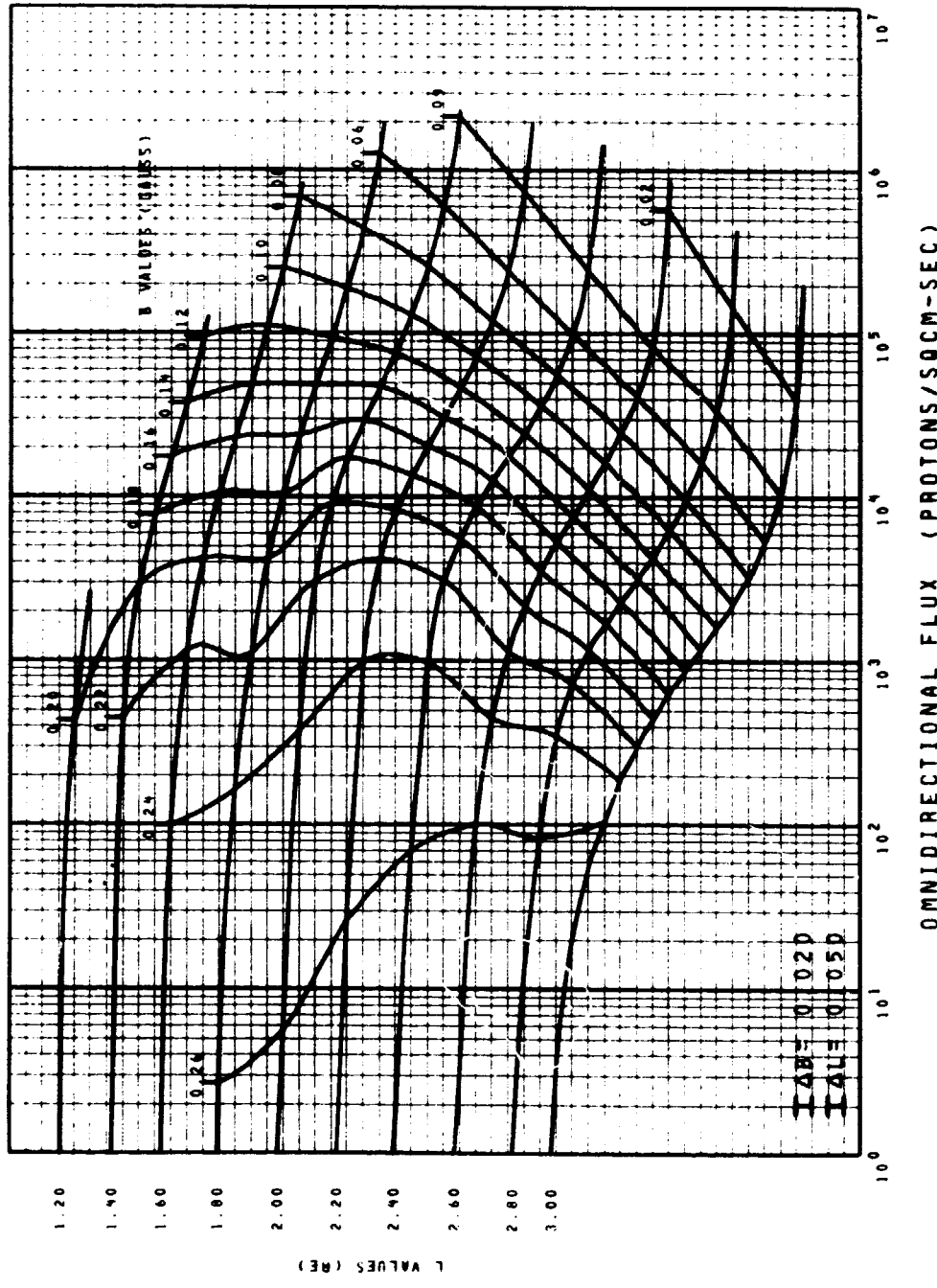
MODEL AP8 MAX FLUX DISTRIBUTIONS
 ENERGY = 1.0 MeV
 SOLAR MAXIMUM FIG. 44



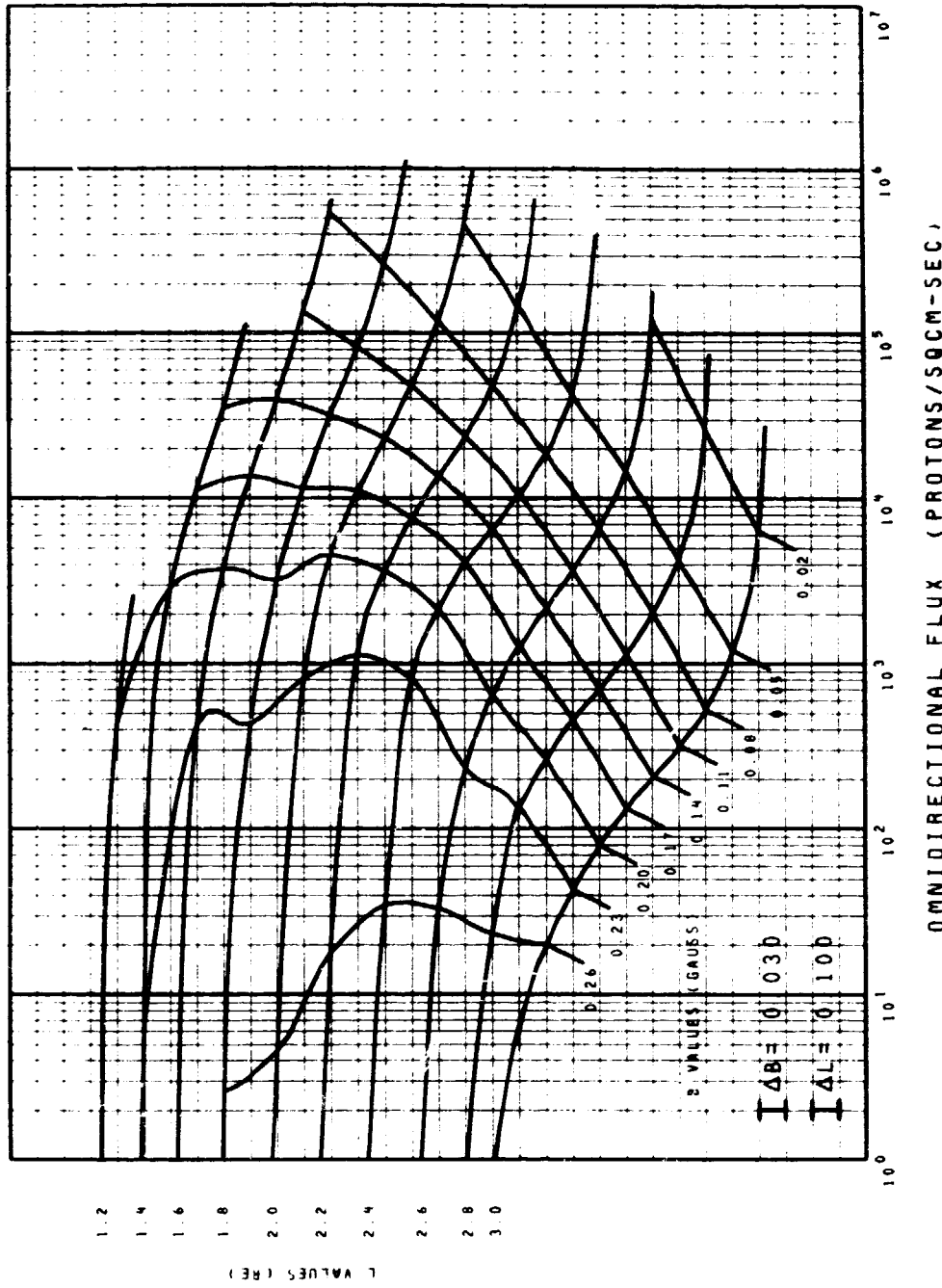
MODEL AP8 MAX FLUX DISTRIBUTIONS
 ENERGY = 2.0 MEV
 SOLAR MAXIMUM FIG. 45



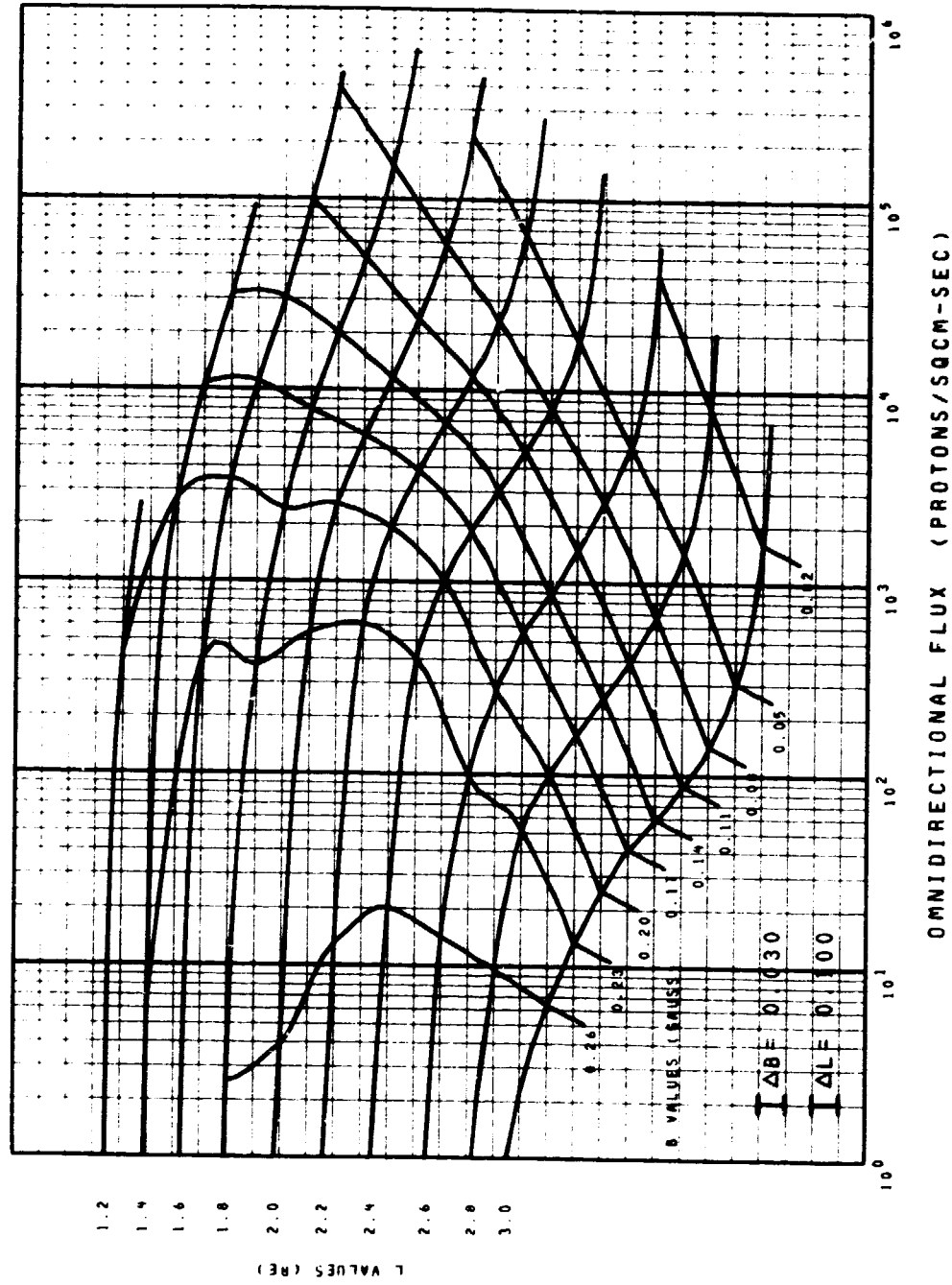
MODEL AP8 MAX FLUX DISTRIBUTIONS
ENERGY = 4.0 MEV
SOLAR MAXIMUM FIG. 46



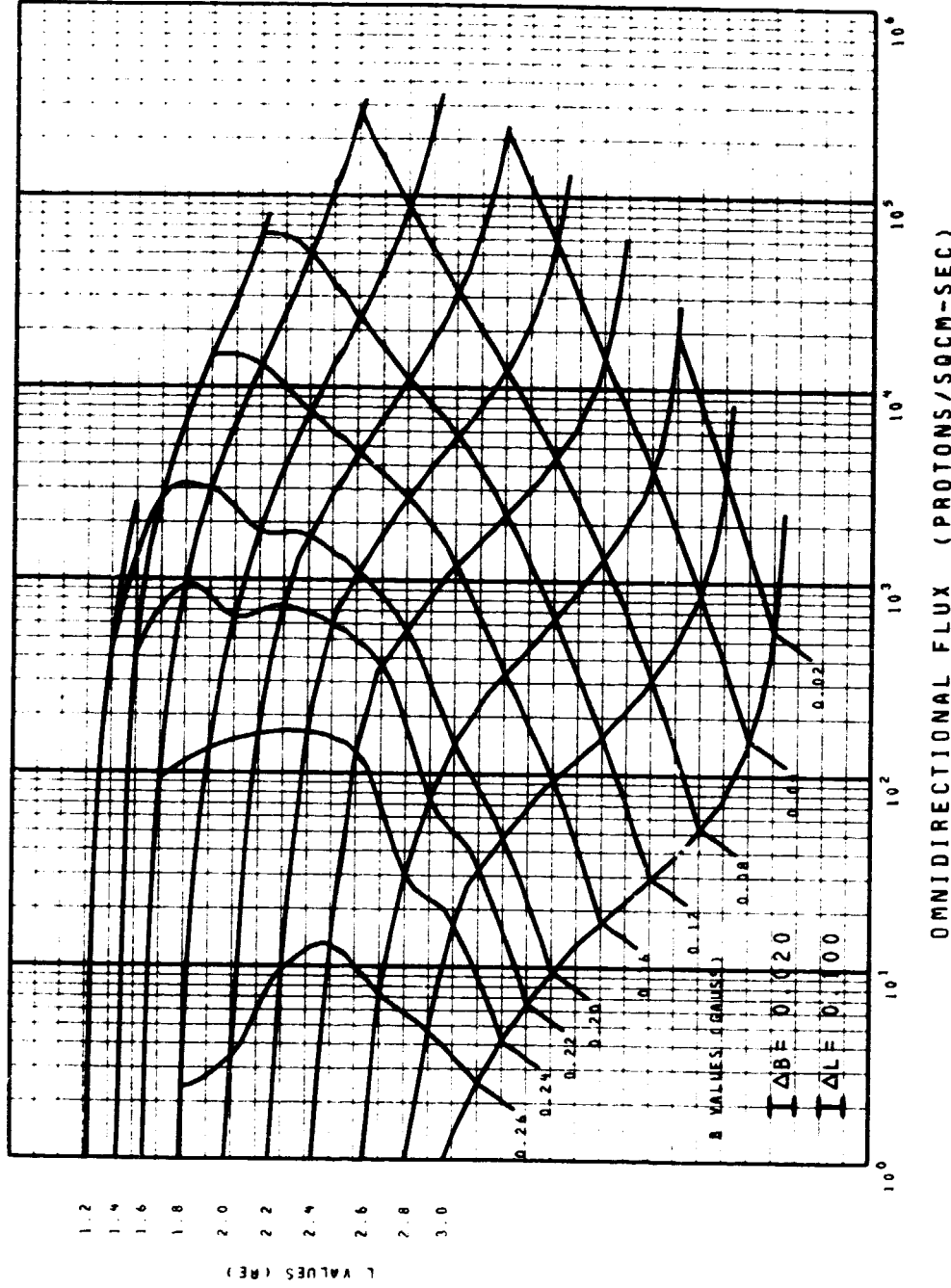
MODEL A P8 MAX FLUX DISTRIBUTIONS
 ENERGY = 6.0 MEV
 SOLAR MAXIMUM FIG. 47



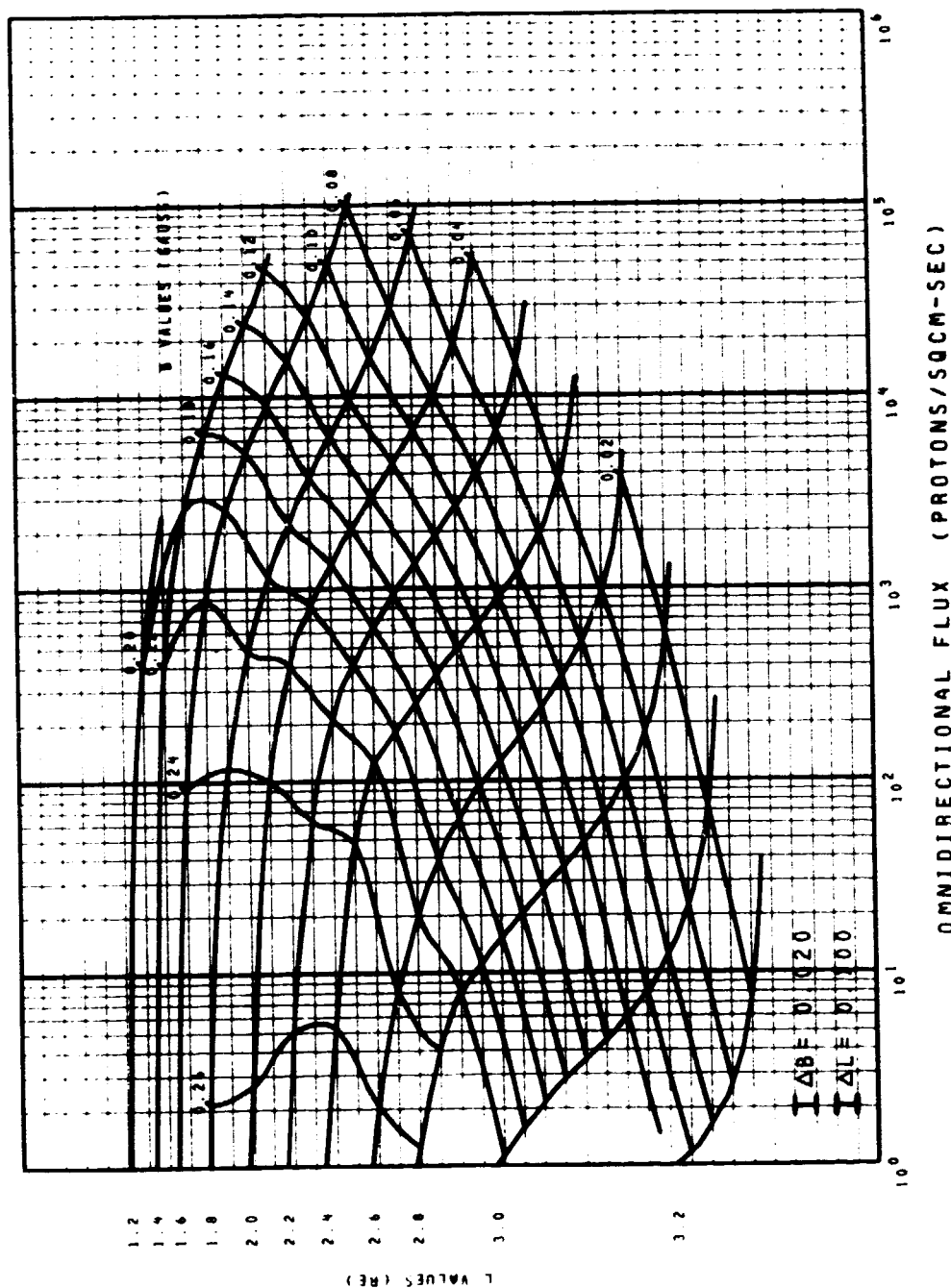
MODEL AP8 MAX FLUX DISTRIBUTIONS
 ENERGY = 8.0 MEV
 SOLAR MAXIMUM FIG. 48



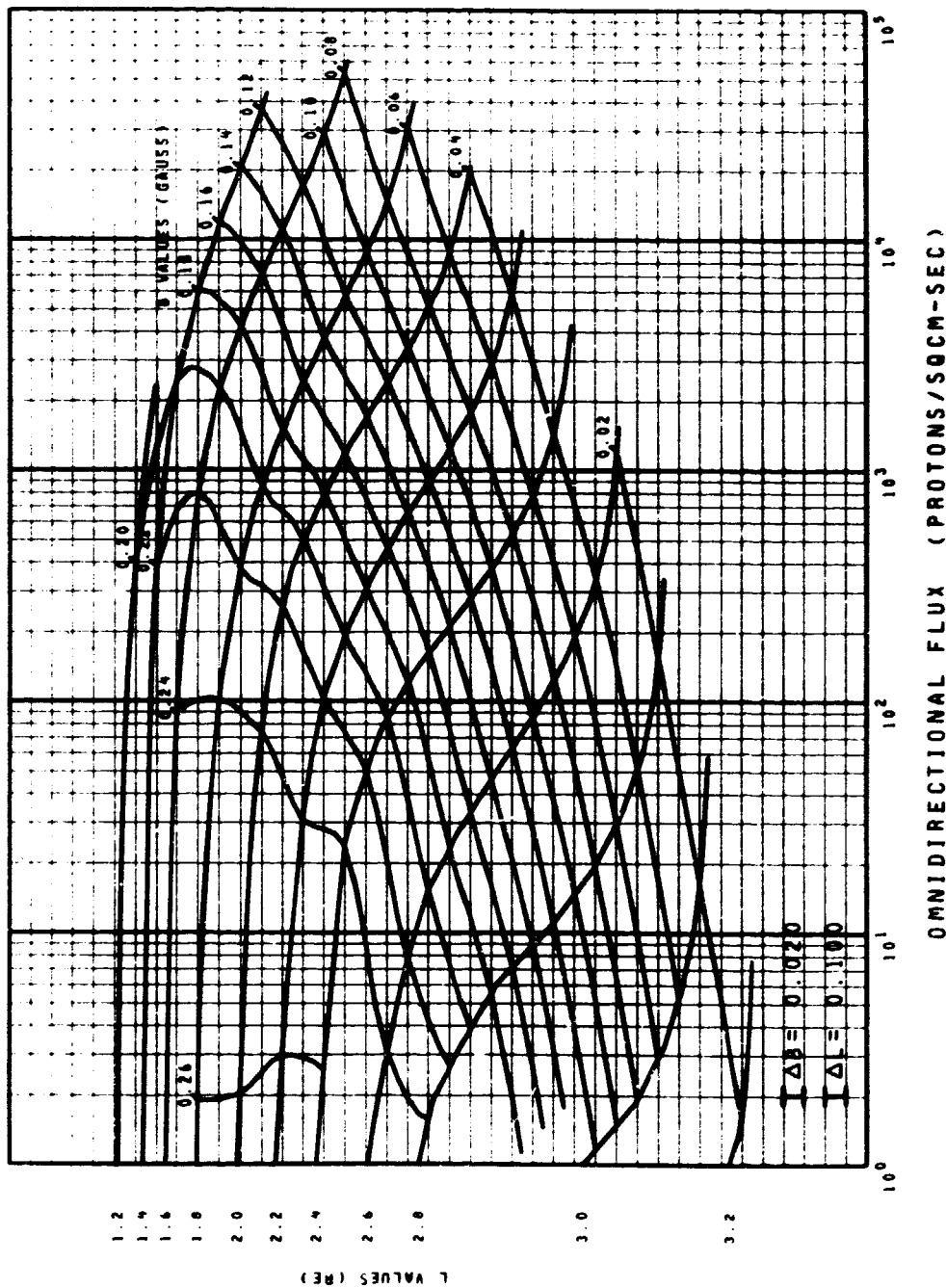
MODEL AP8 MAX FLUX DISTRIBUTIONS
 ENERGY = 10. MEV
 SOLAR MAXIMUM FIG. 49



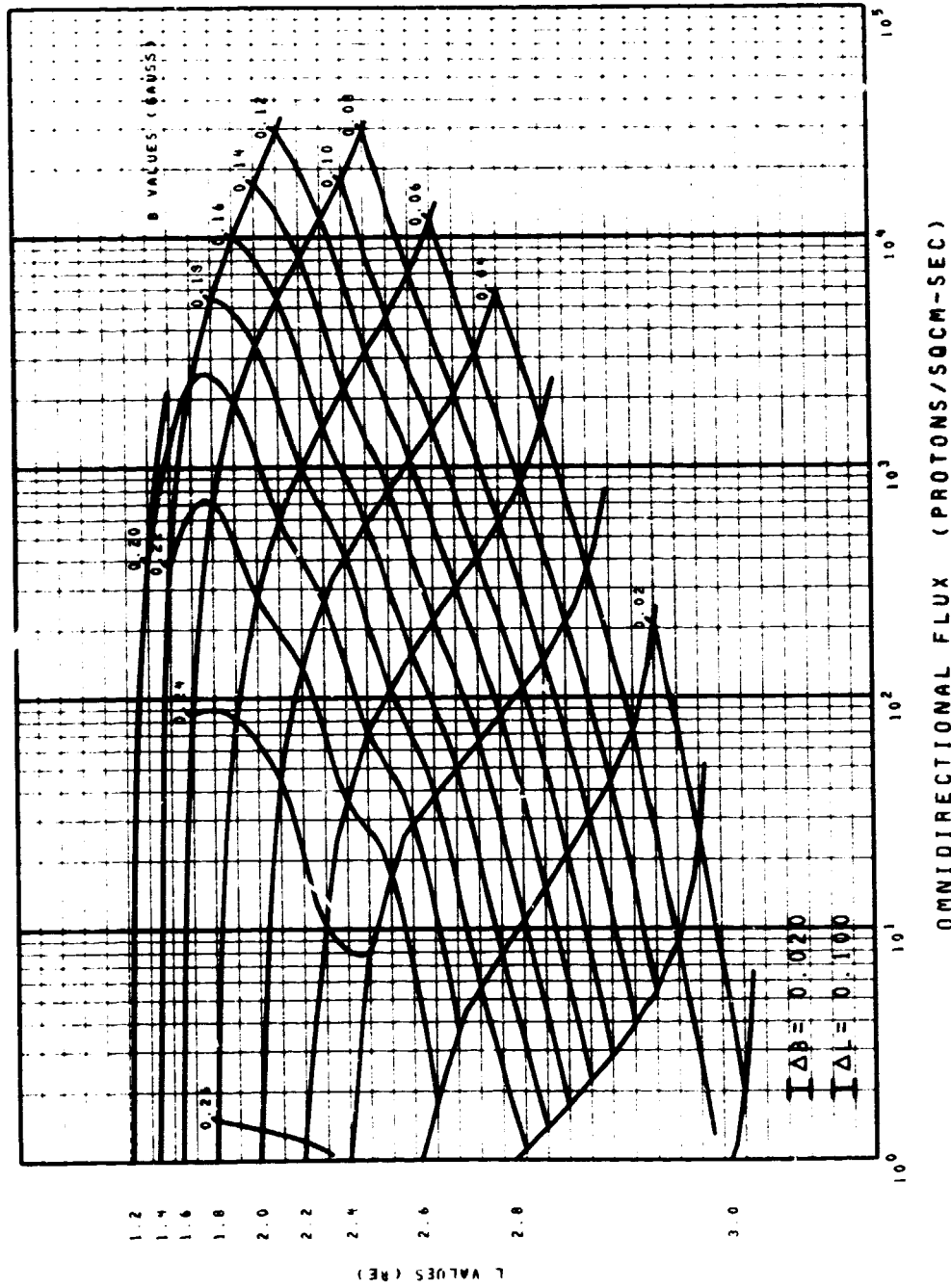
MODEL AP8 MAX FLUX DISTRIBUTIONS
 ENERGY = 15. MEV
 SOLAR MAXIMUM FIG. 50



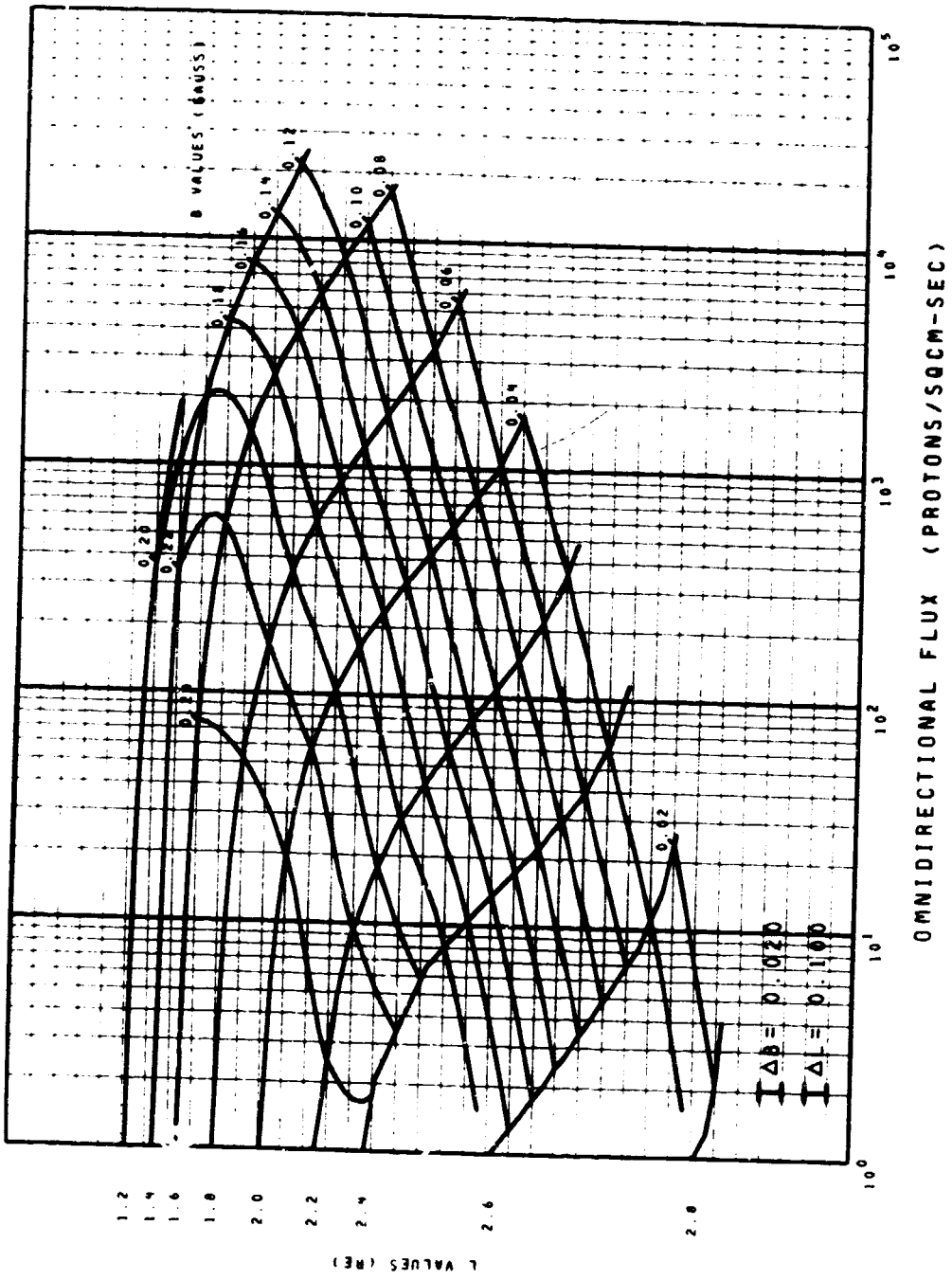
MODEL AP8 MAX FLUX DISTRIBUTIONS
 ENERGY = 20. MEV
 SOLAR MAXIMUM FIG. 51



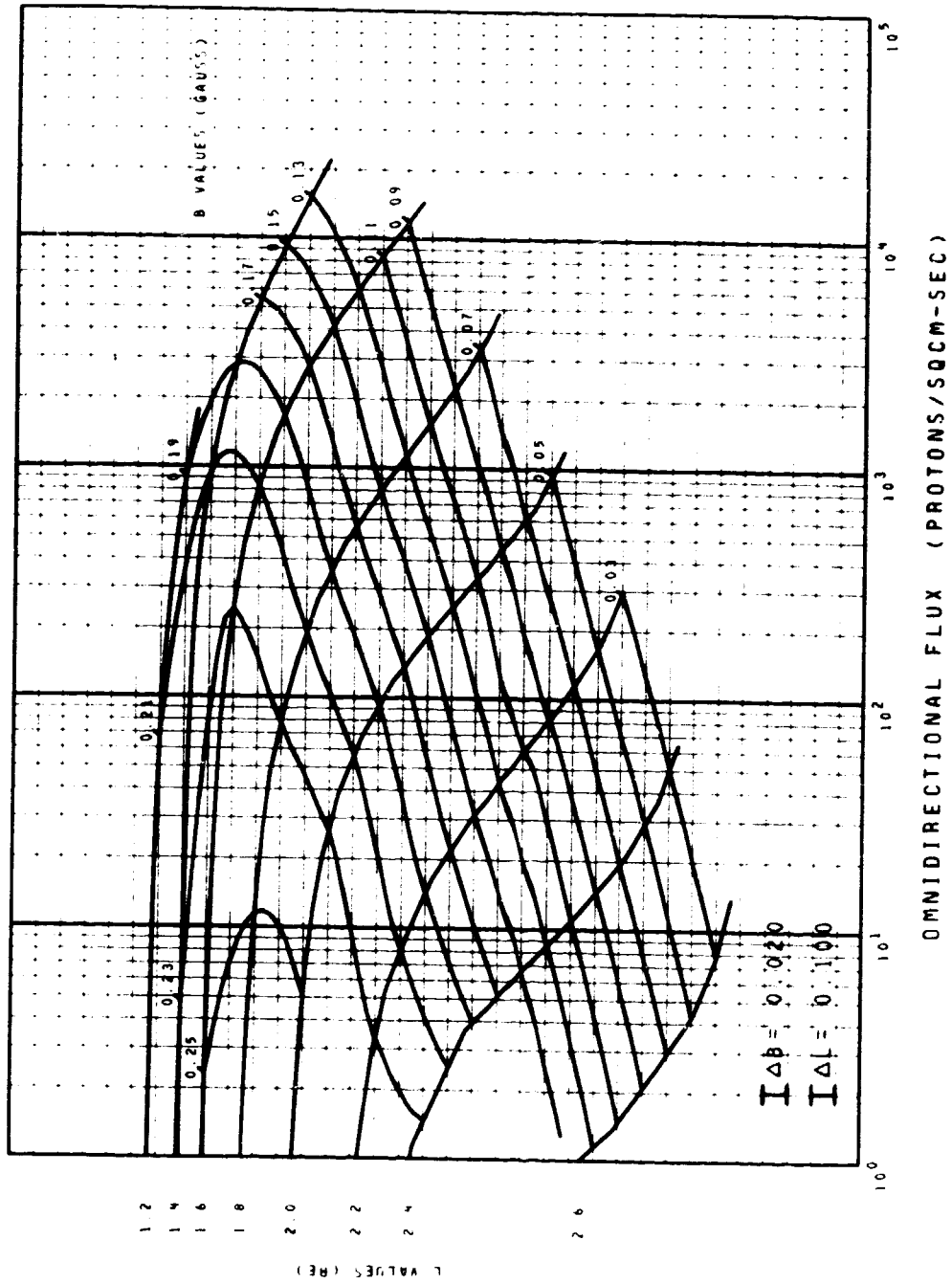
MODEL APO MAX FLUX DISTRIBUTIONS
ENERGY = 30. MEV
SOLAR MAXIMUM FIG. 52



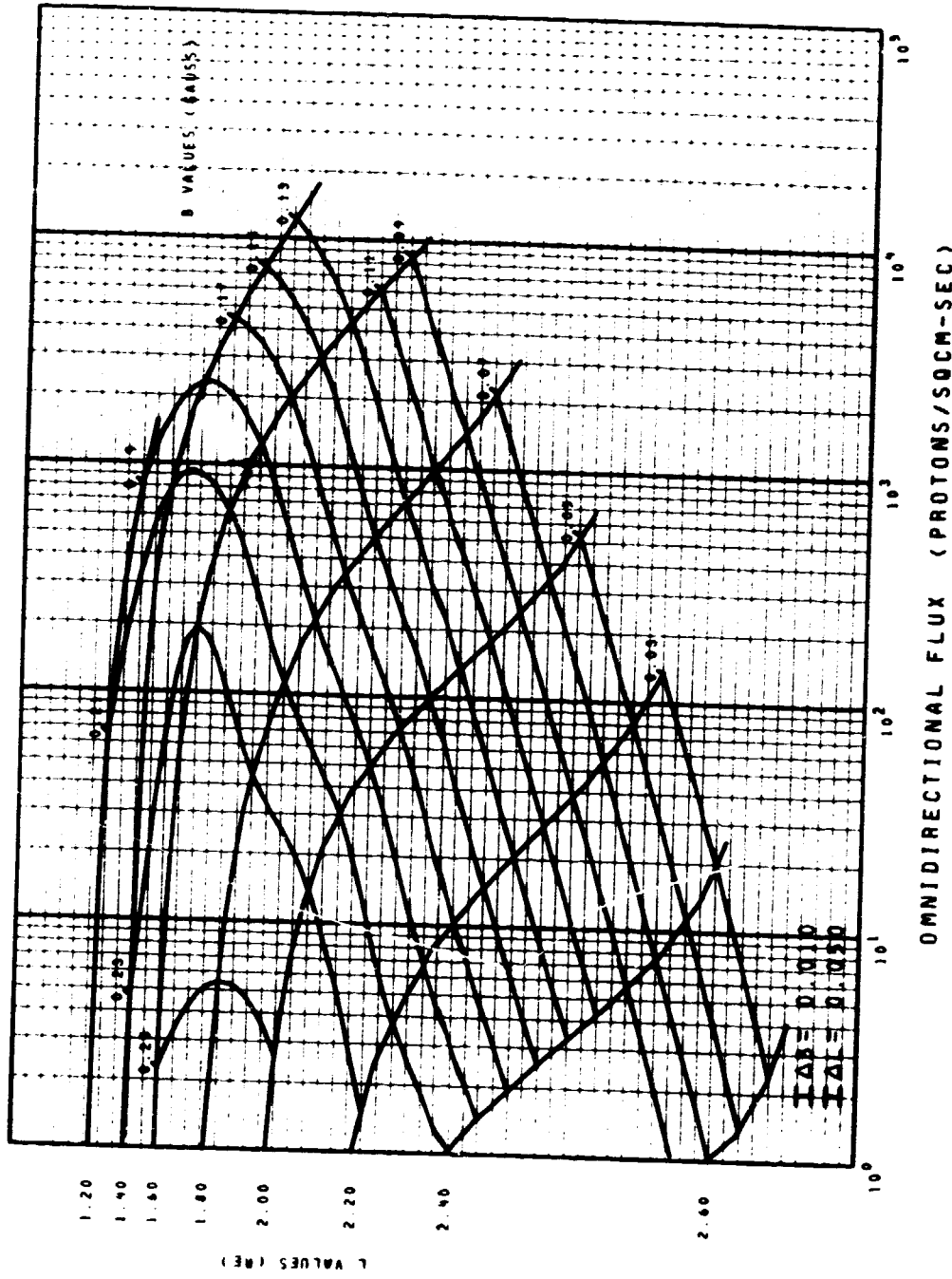
MODEL APP MAX FLUX DISTRIBUTIONS
 ENERGY = 50. MEV
 SOLAR MAXIMUM FIG. 53



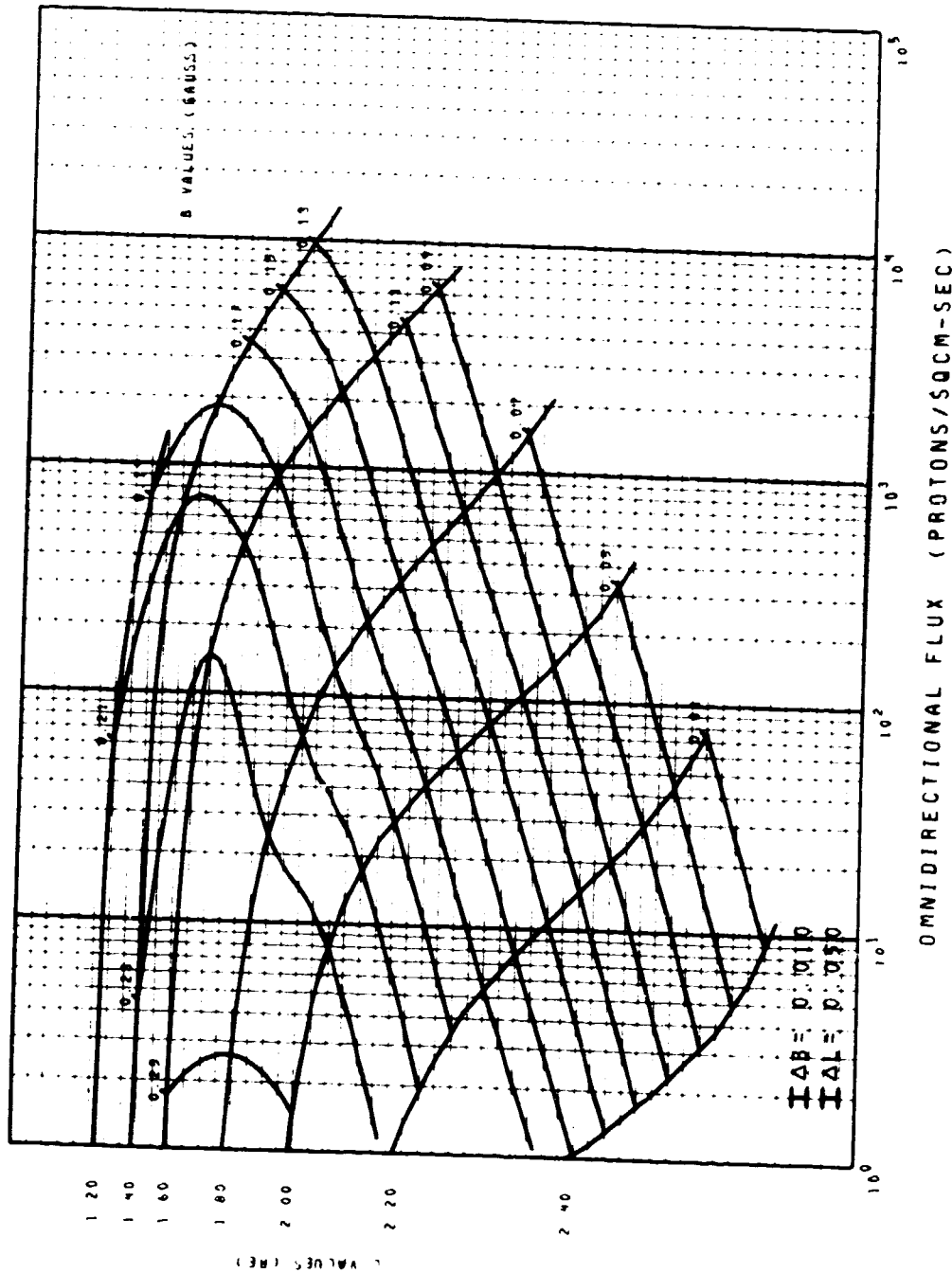
MODEL AP8 MAX FLUX DISTRIBUTIONS
 ENERGY = 60. MEV
 SOLAR MAXIMUM FIG. 54



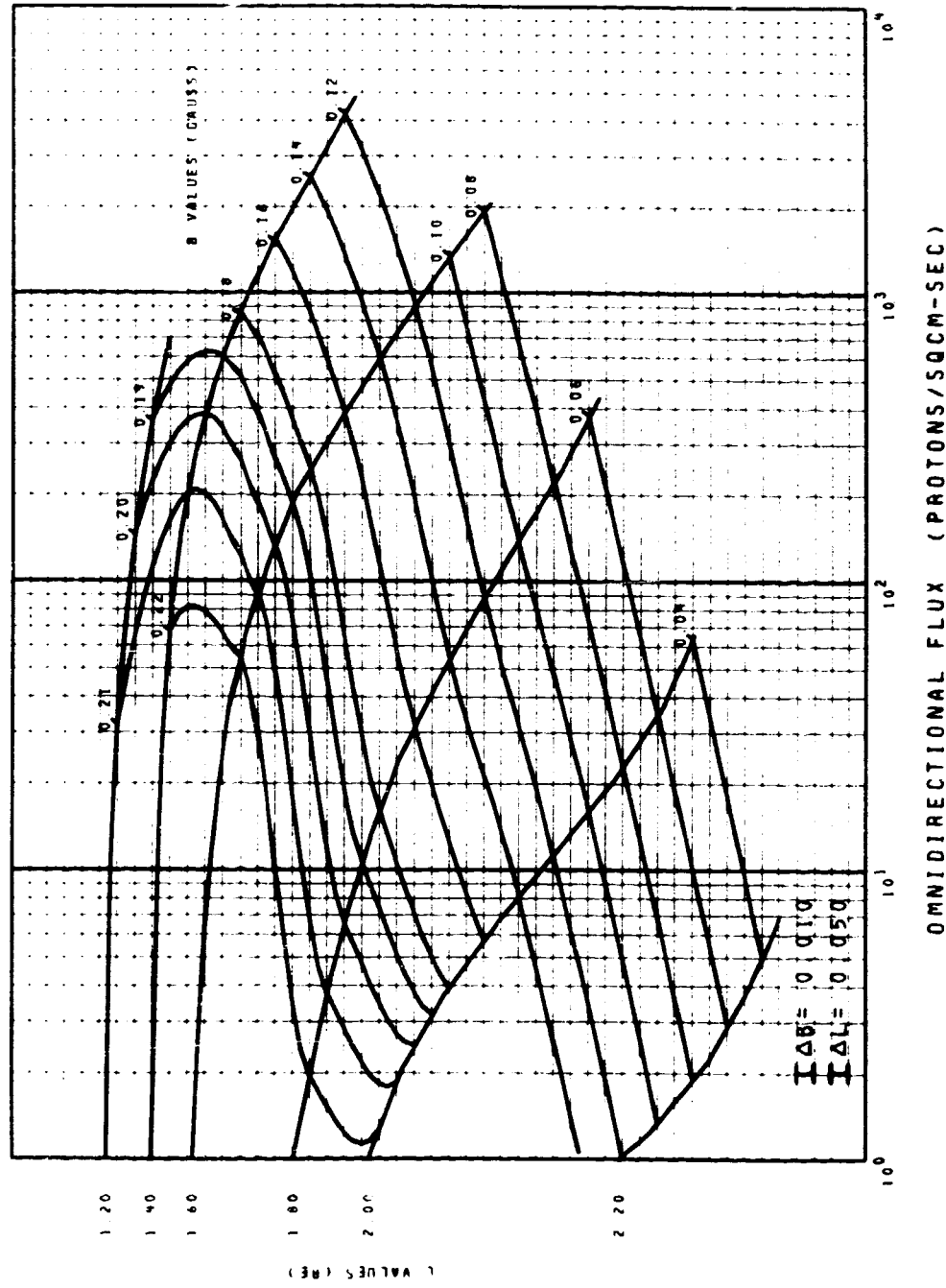
MODEL APO MAX FLUX DISTRIBUTIONS
 ENERGY = 80. MEV
 SOLAR MAXIMUM FIG. 55



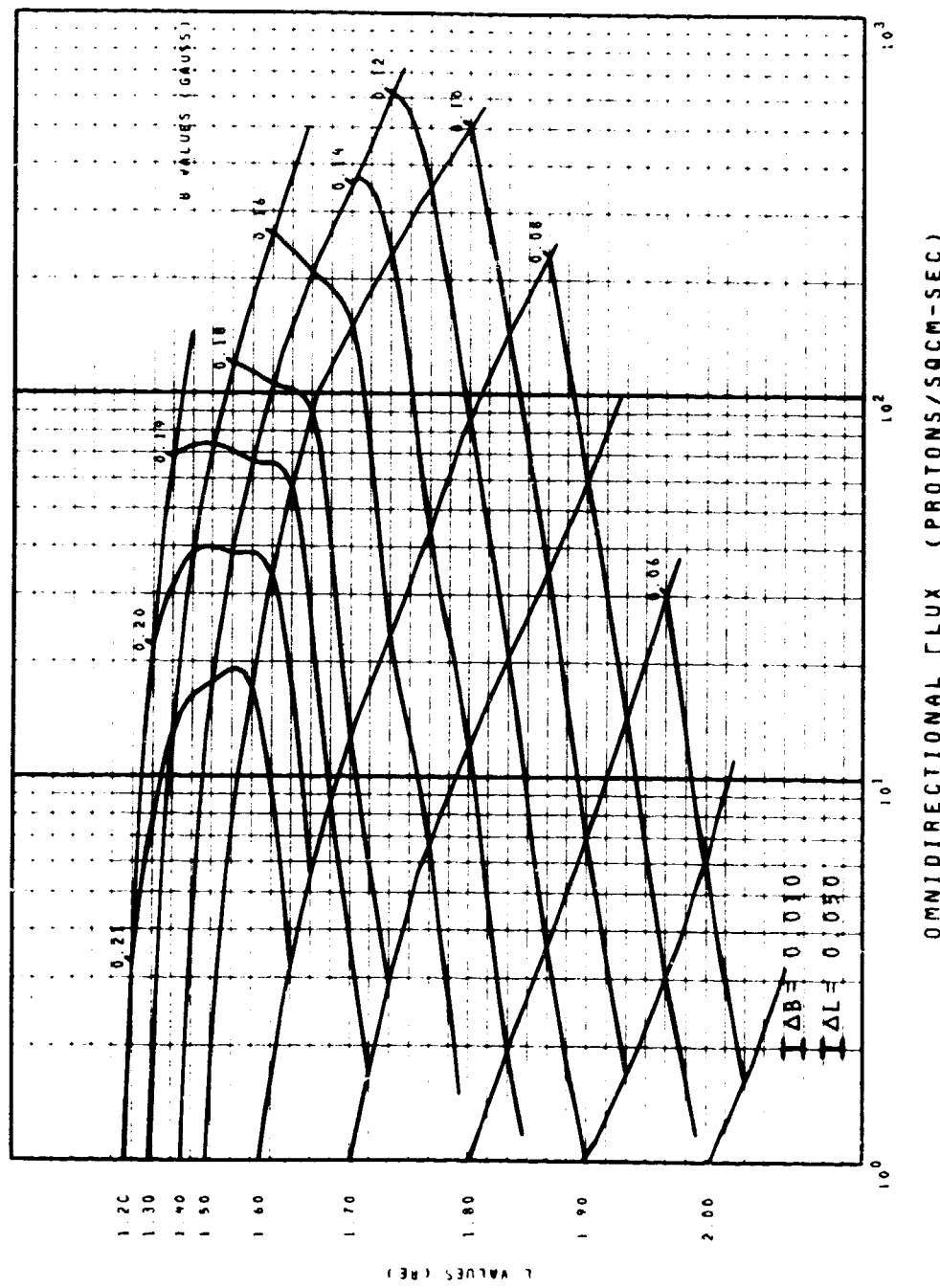
DEL APP MAX FLUX DISTRIBUTIONS
ENERGY=100. MEV
SOLAR MAXIMUM FIG. 56



MODEL AP8 MAX FLUX DISTRIBUTIONS
 ENERGY = 200. MEV
 SOLAR MAXIMUM FIG. 57



MODEL AP8 MAX FLUX DISTRIBUTIONS
 ENERGY=400. MEV
 SOLAR MAXIMUM FIG. 58



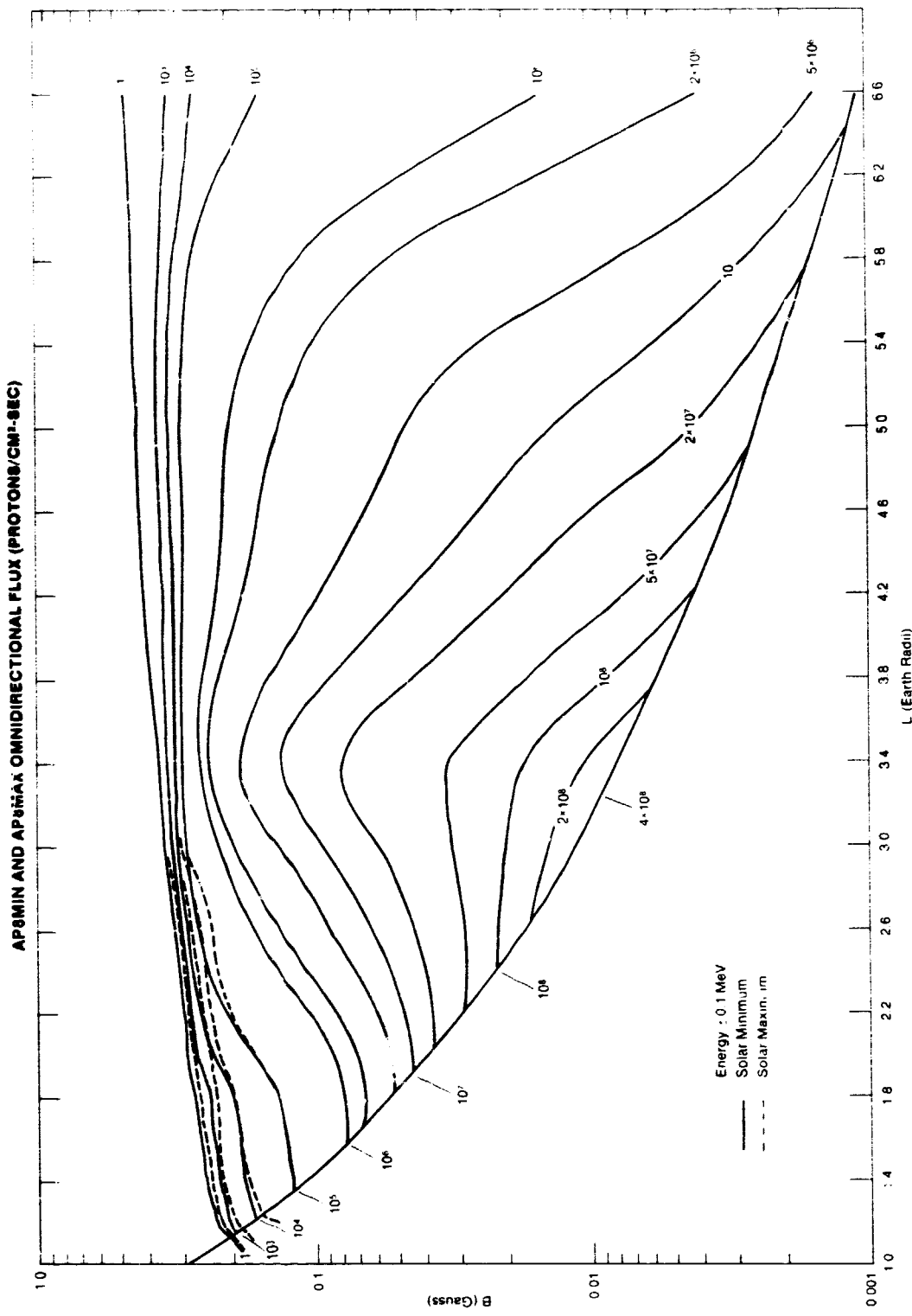


Figure 59. Ap8W_Y and Ap8W_{B-L} Plot of Constant Intensity Flux Contours with an energy of 0.1 MeV.

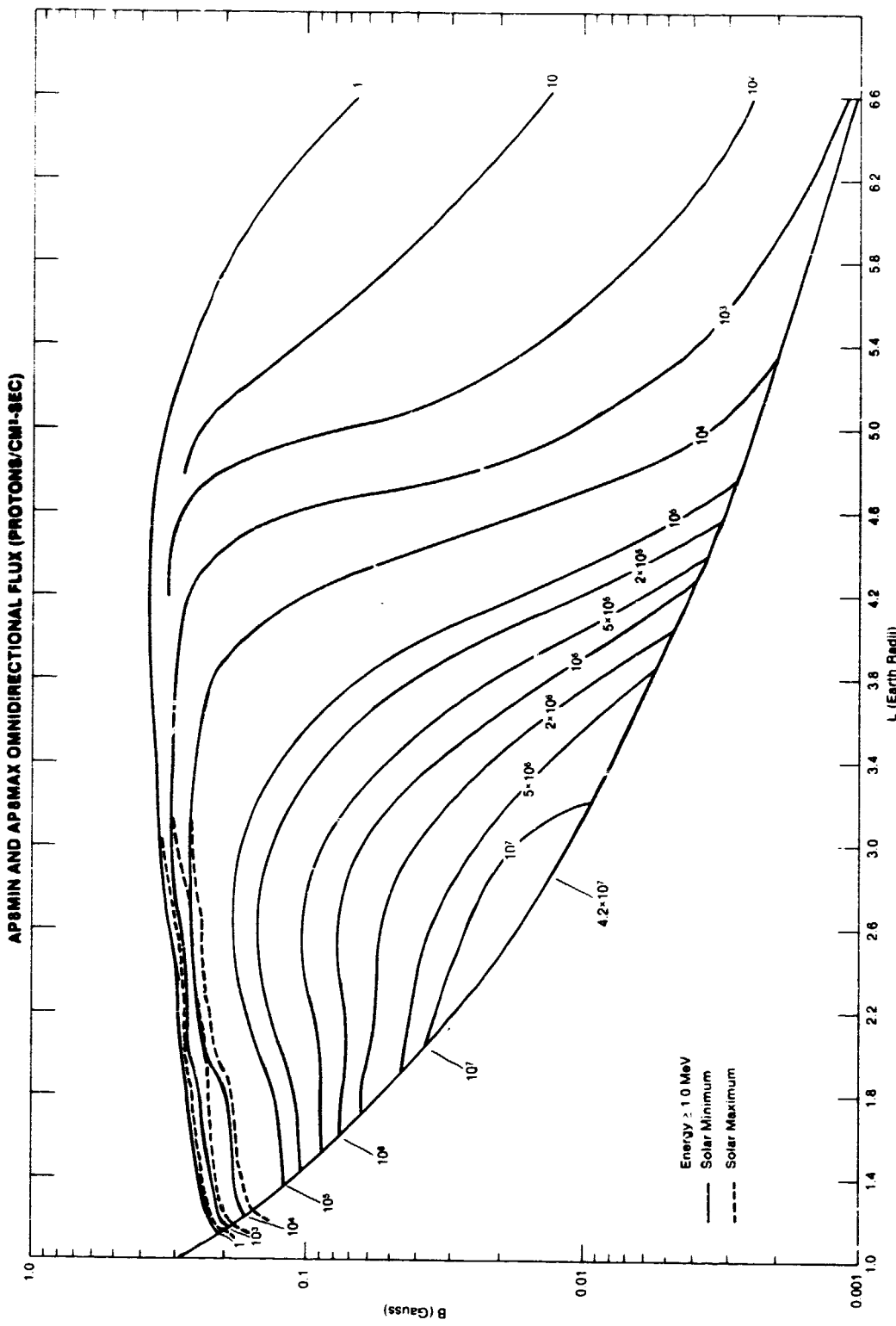


Figure 60. AP8MIN and AP8MAX B-L Plot of Constant Intensity Flux Contours with an Energy of
1.0 MeV

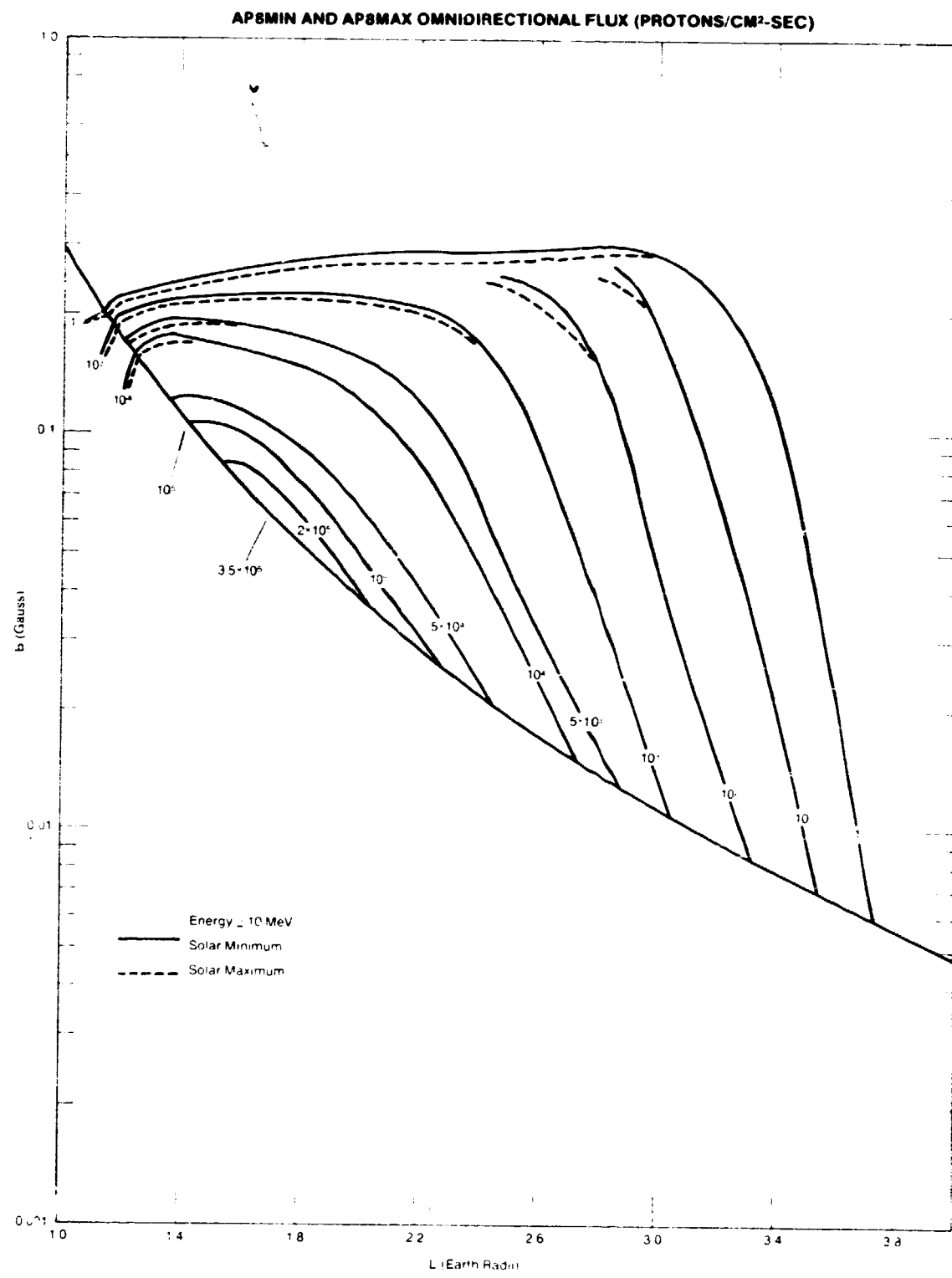


Figure 61. AP8MIN and AP8MAX B-L Plot of Constant Intensity Flux Contours with an Energy of > 10 MeV

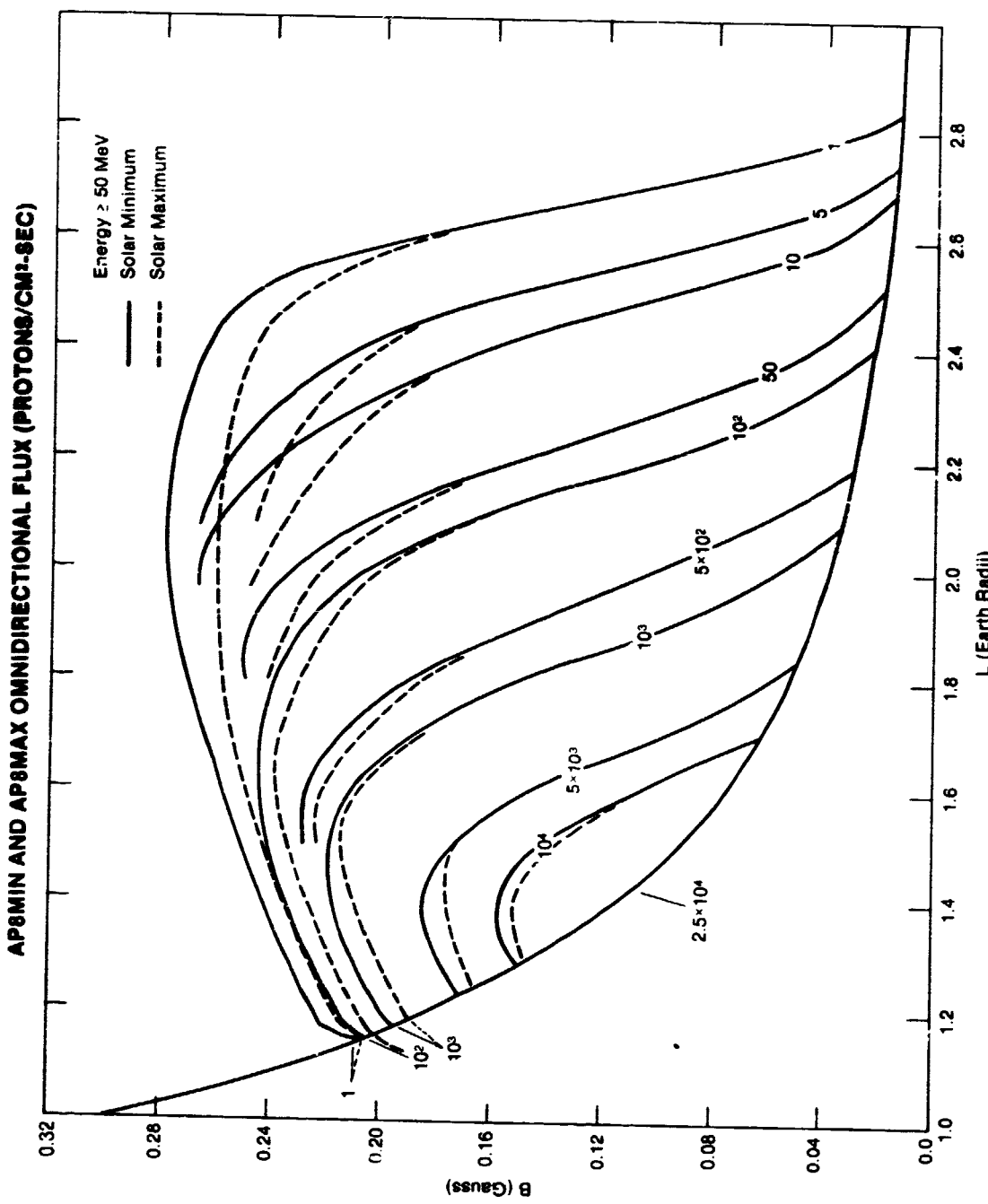


Figure 62. AP8MIN and AP8MAX B-L Plot of Constant Intensity Flux Contours with an Energy of ≥ 50 MeV

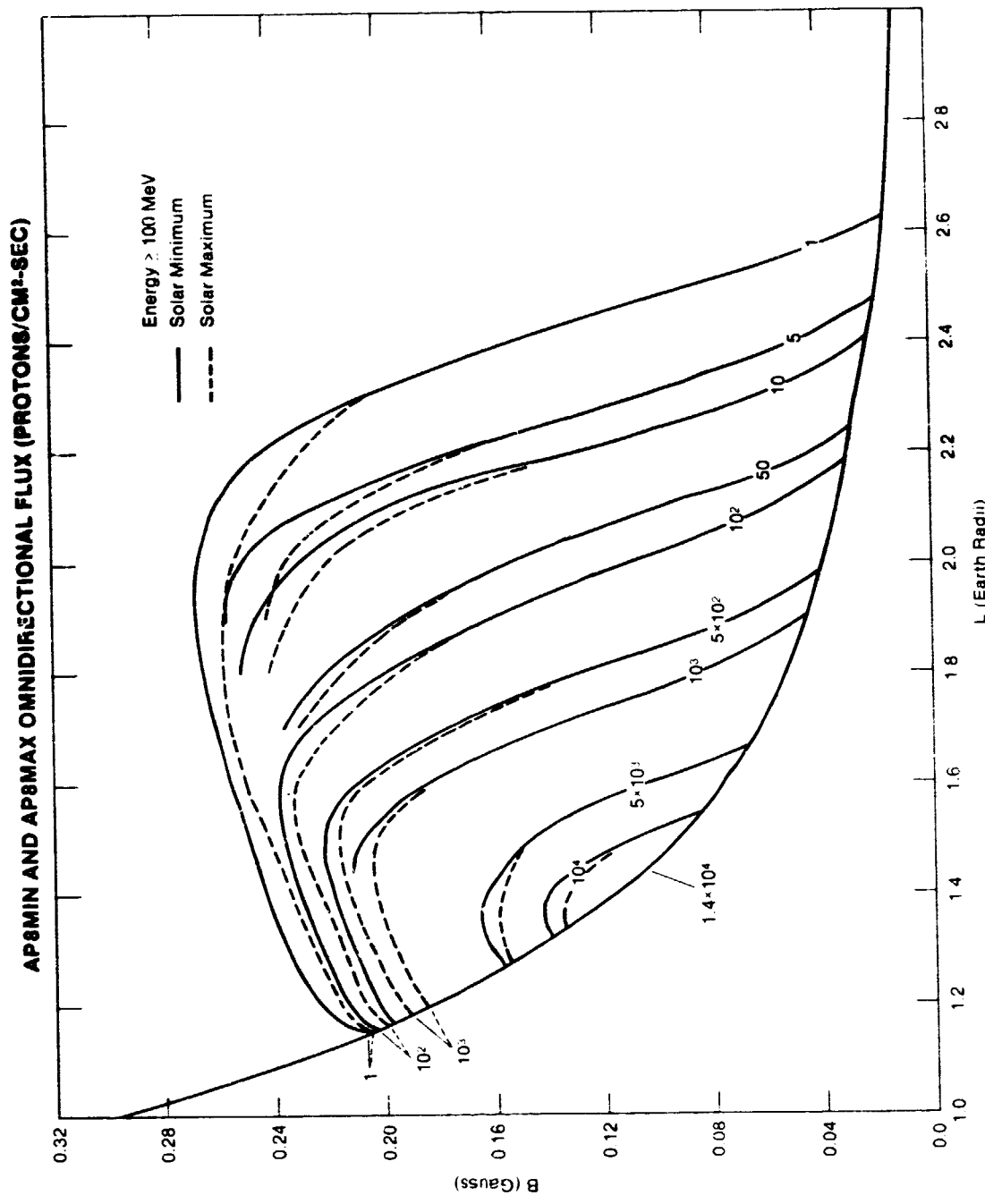


Figure 63. AP8MIN and AP8MAX OMNIDIRECTIONAL FLUX (PROTONS/CM²-SEC)

Figure 63, AP8MIN and AP8MAX 3-1. Plot of Constant Intensity Flux Contours with an Energy of
100 MeV

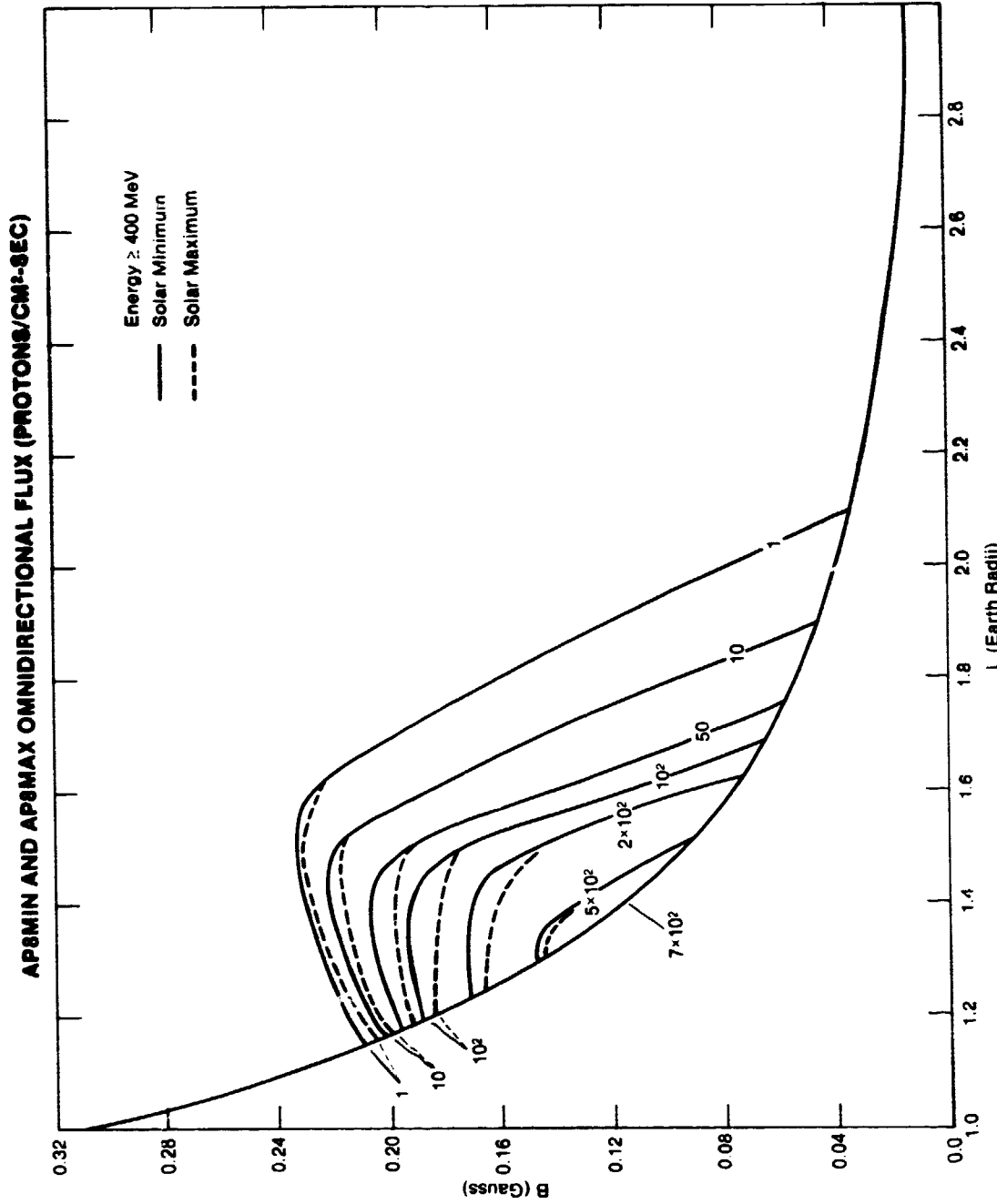


Figure 64. AP8'IN and AP8'MAX B-1 Plot of Constant Intensity Flux Contours with an energy of ≥ 400 MeV

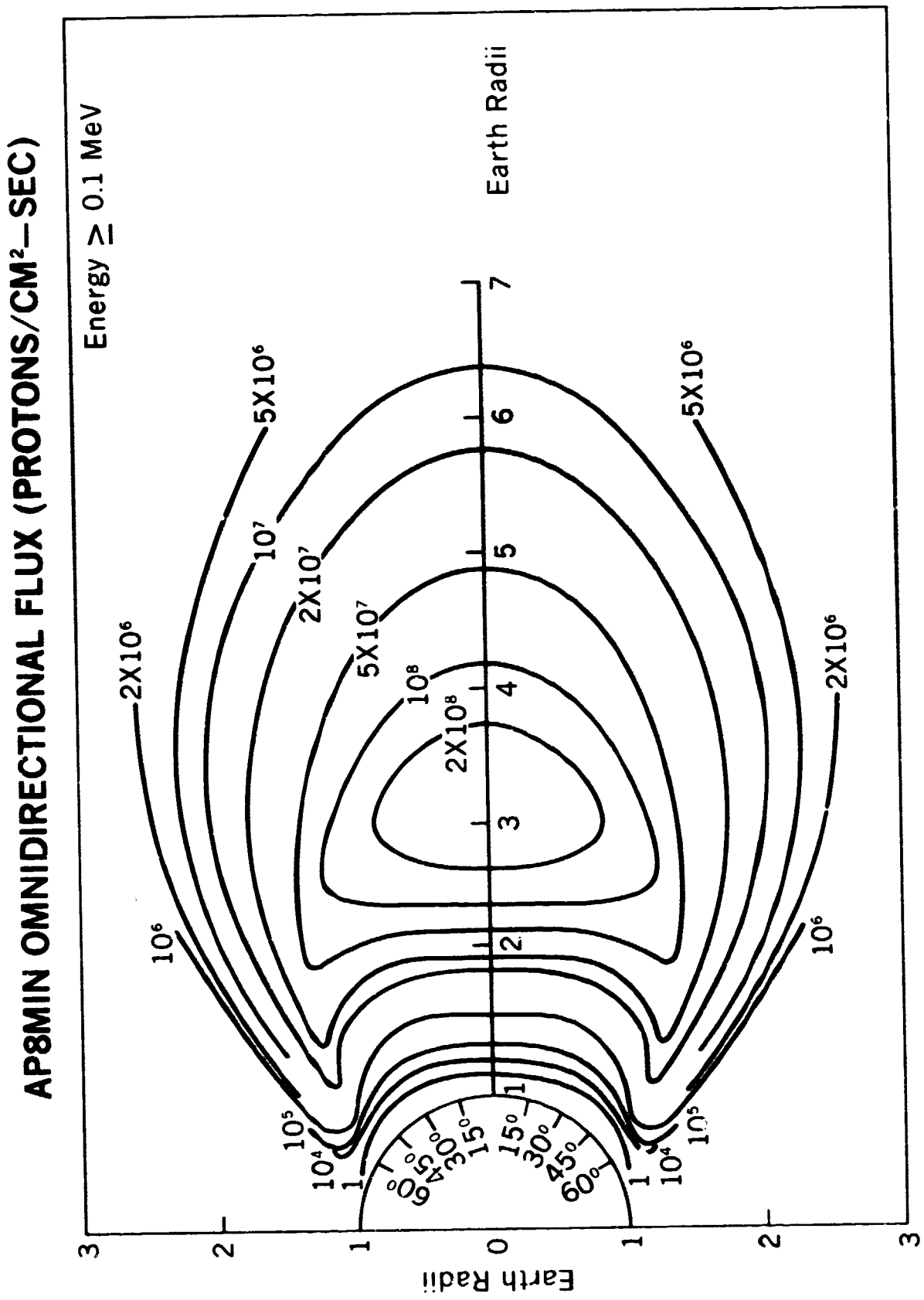


Figure 65. APWVN R- λ Plot of Constant Intensity Flux Contours with an Energy of ≥ 0.1 MeV

AP8MIN OMNIDIRECTIONAL FLUX (PROTONS/CM²-SEC)

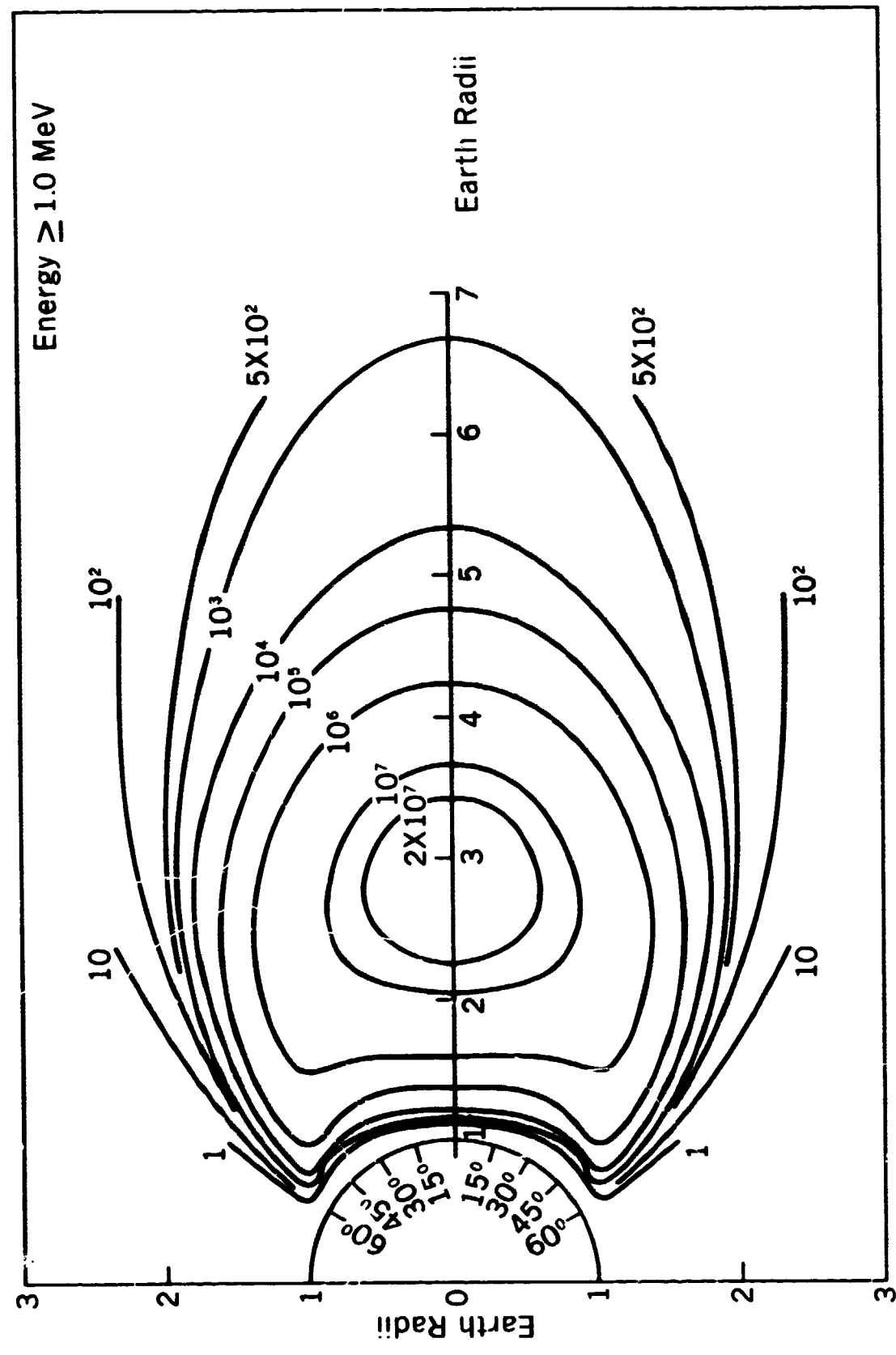


Figure 66. AP8MIN R-λ Plot of Constant Intensity Flux Contours with an Energy of ≥ 1.0 MeV

AP8MIN OMNIDIRECTIONAL FLUX (PROTONS/CM²-SEC)

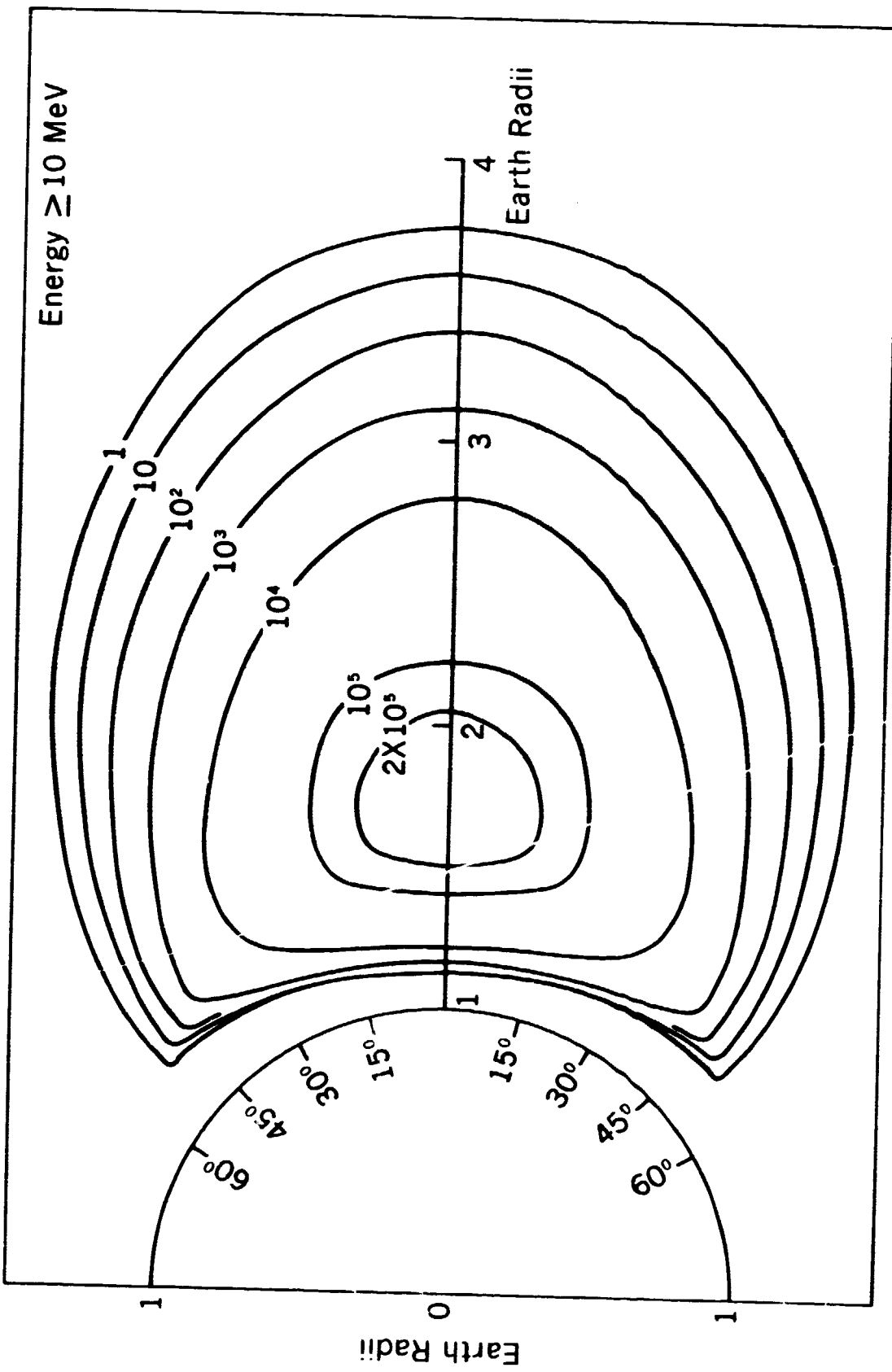


Figure 67. AP8MIN R-λ Plot of Constant Intensity Flux Contours with an Energy of ≥ 10 MeV

AP8MIN OMNIDIRECTIONAL FLUX (PROTONS/CM²-SEC)

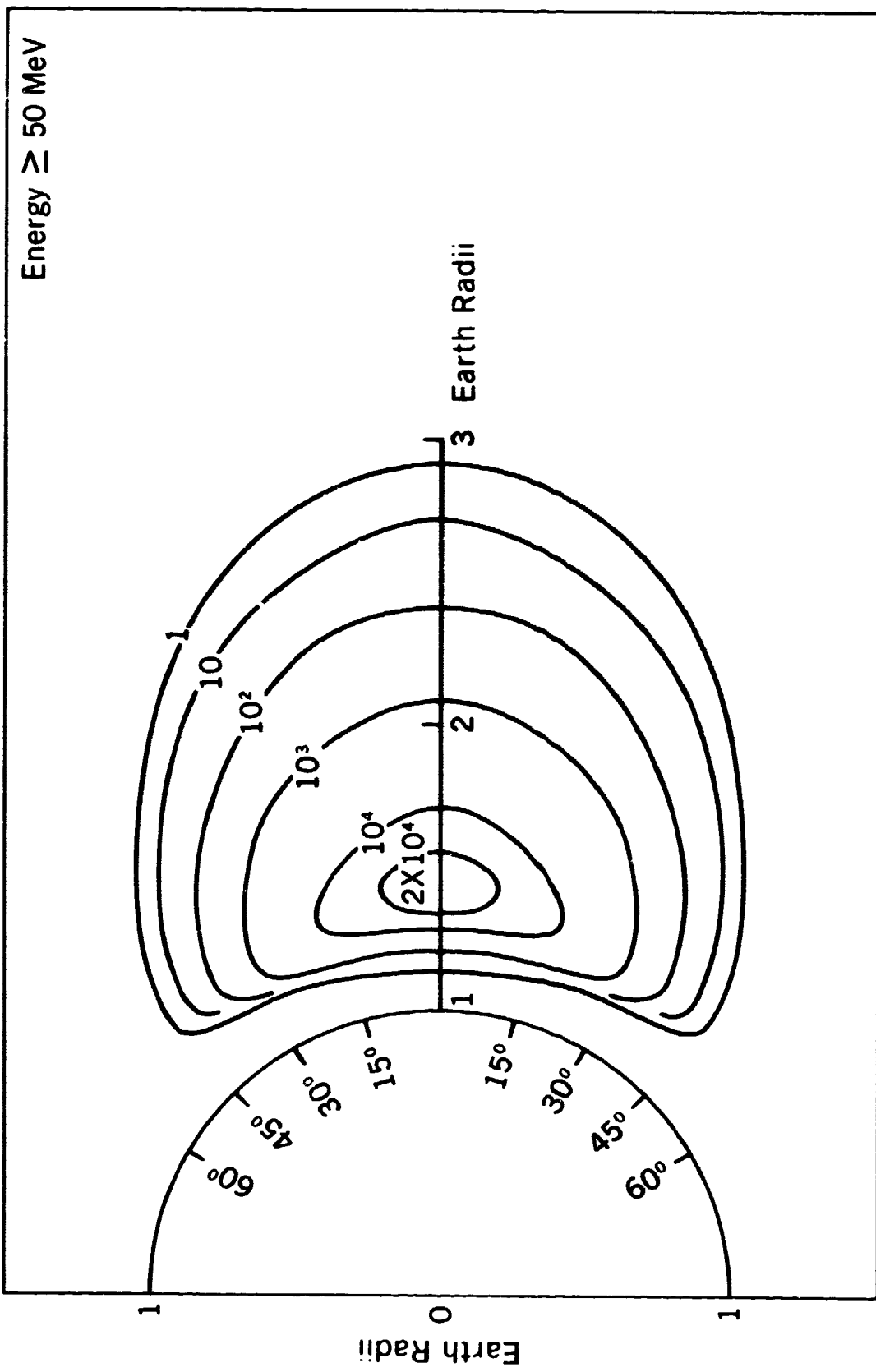


Figure 68. AP8MIN R- λ Plot of Constant Intensity Flux Contours with an Energy of ≥ 50 MeV

APP8MIN OMNIDIRECTIONAL FLUX (PROTONS/CM²-SEC)

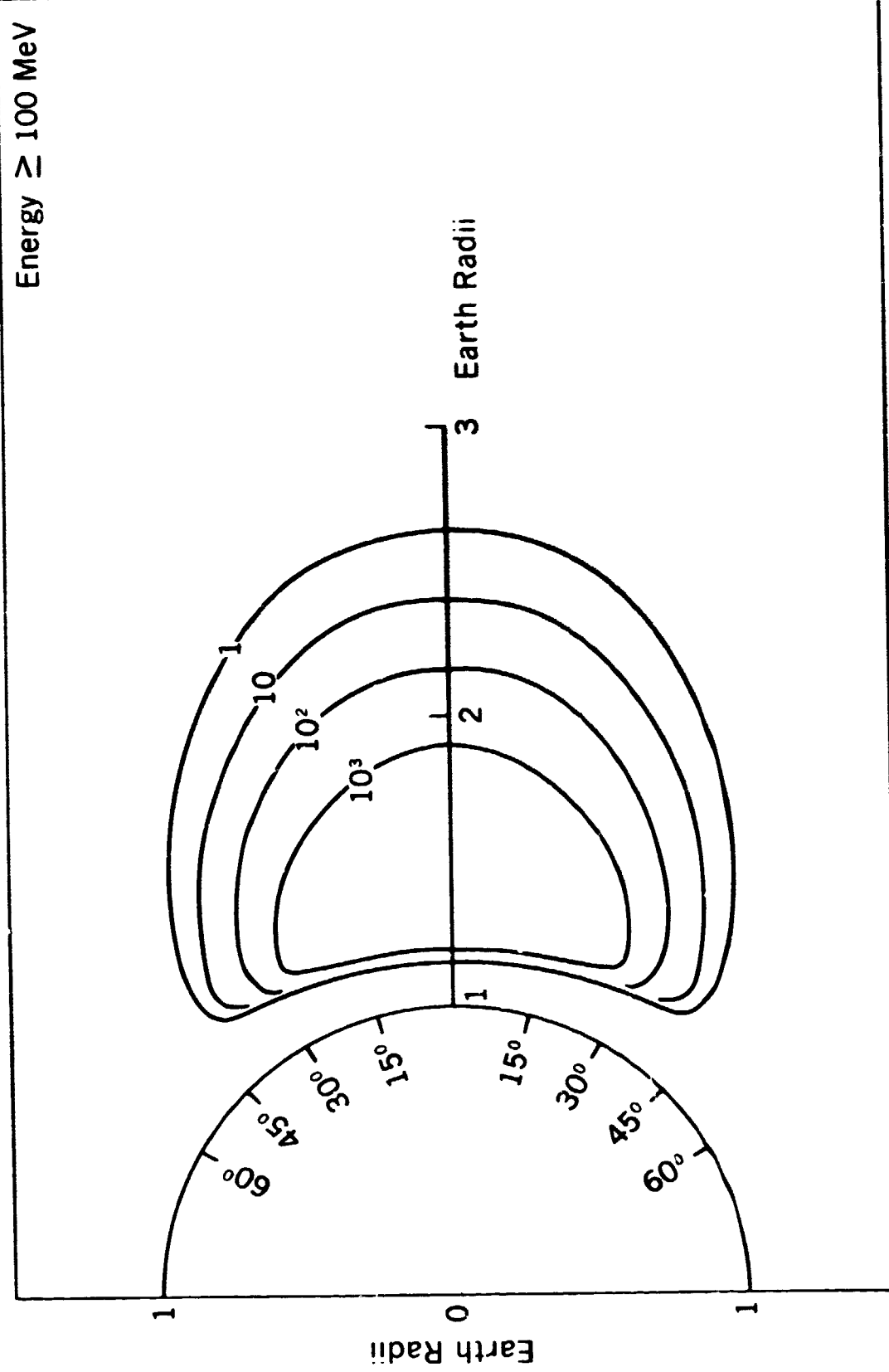


Figure 69. AP8MIN R- λ Plot of Constant Intensity Flux Contours with an Energy of ≥ 100 MeV

AP8MIN OMNIDIRECTIONAL FLUX (PROTONS/CM²-SEC)

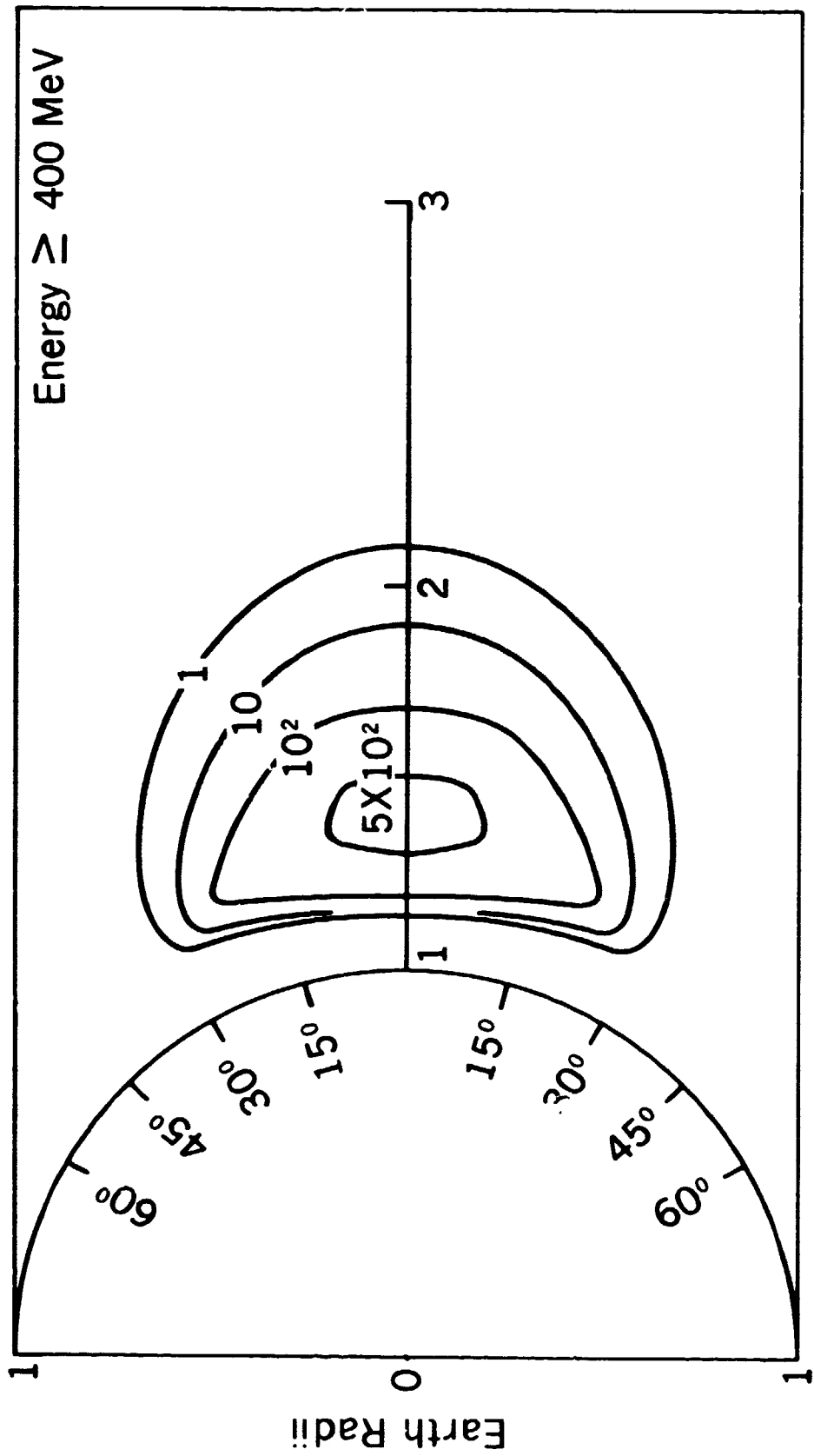


Figure 70. VGPIN R-λ plot of constant Intensity Flux Contours with an Energy of \geq 400 Mev

AP8MIN EQUATORIAL OMNIDIRECTIONAL RADIAL PROFILES

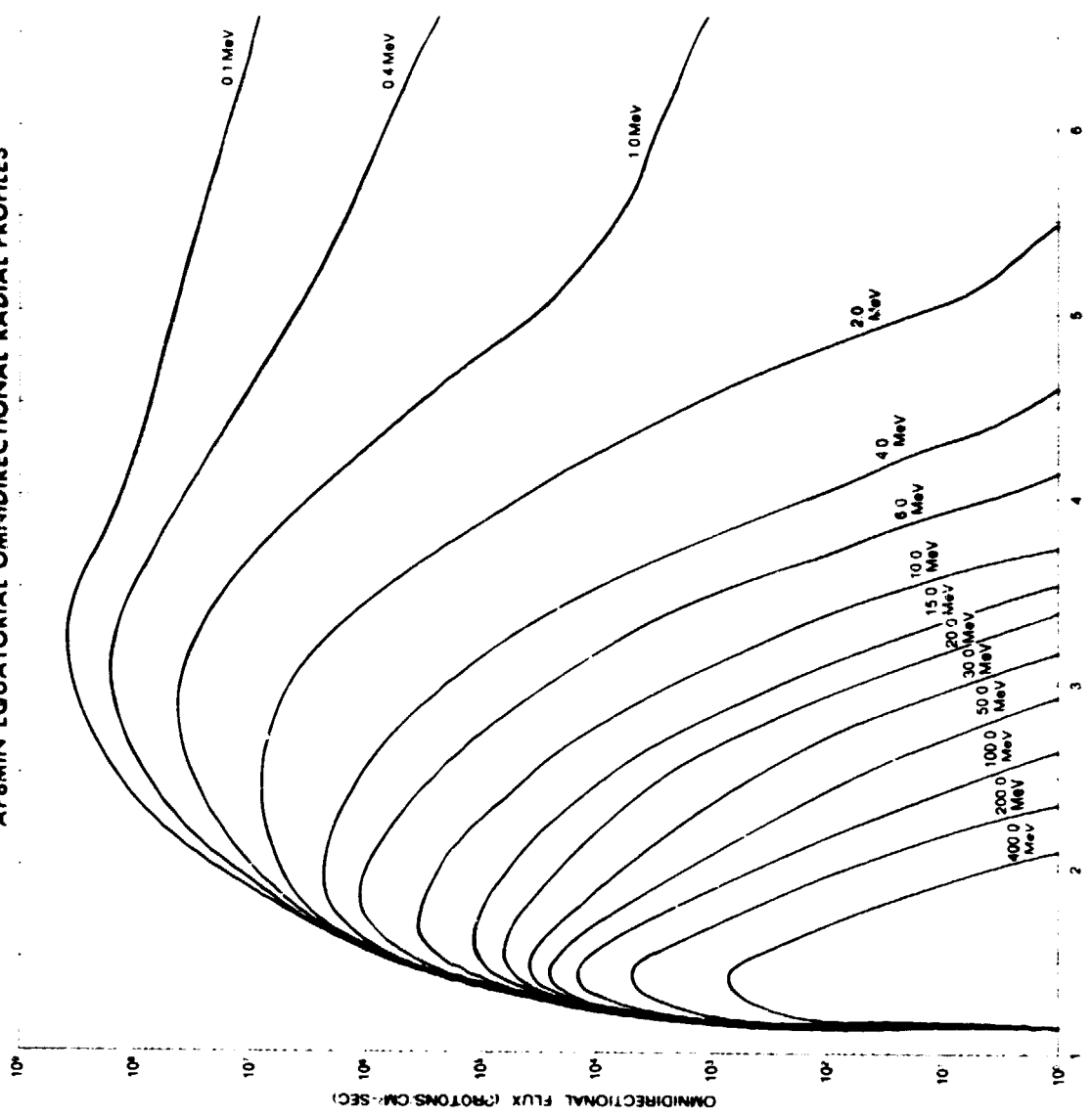
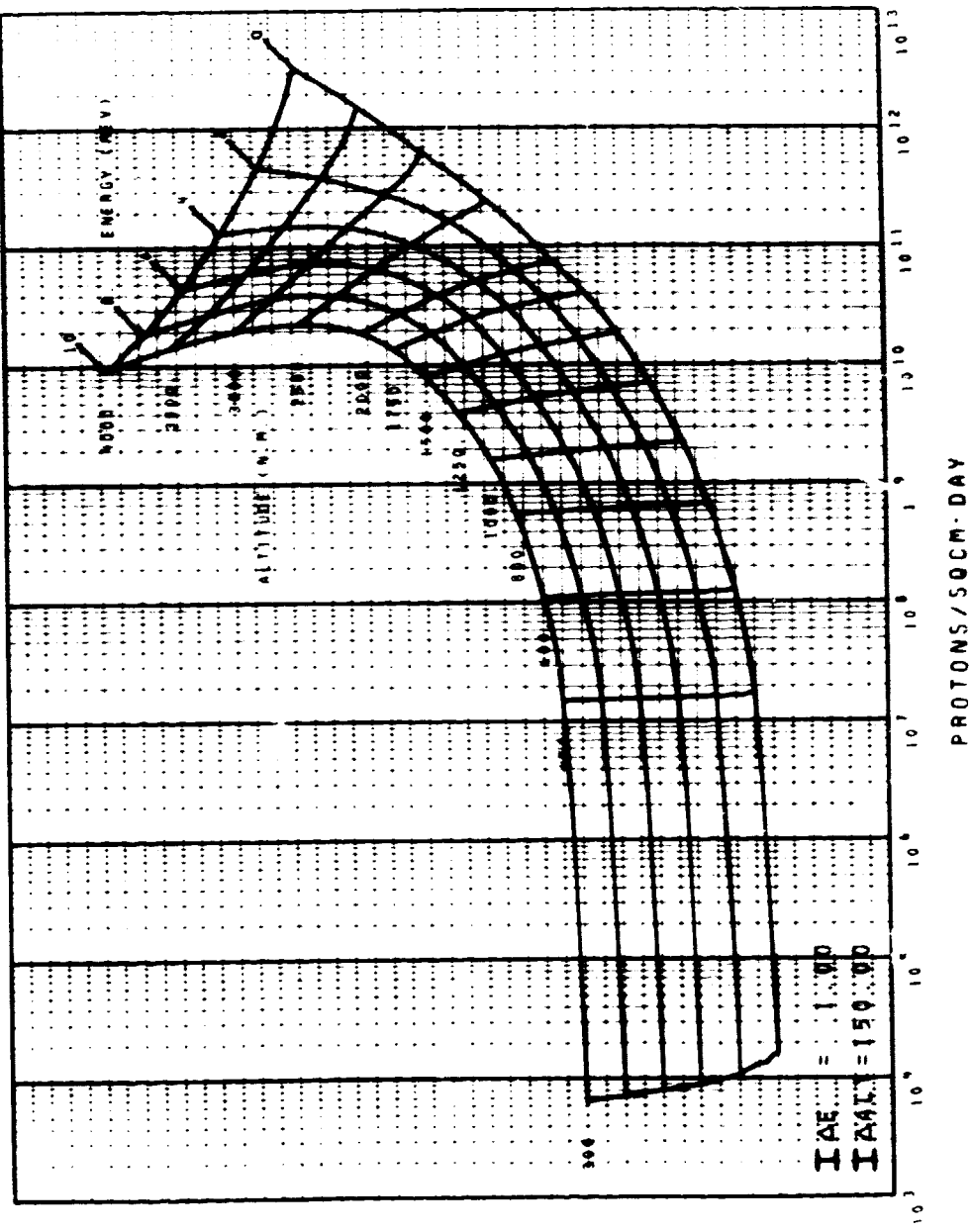
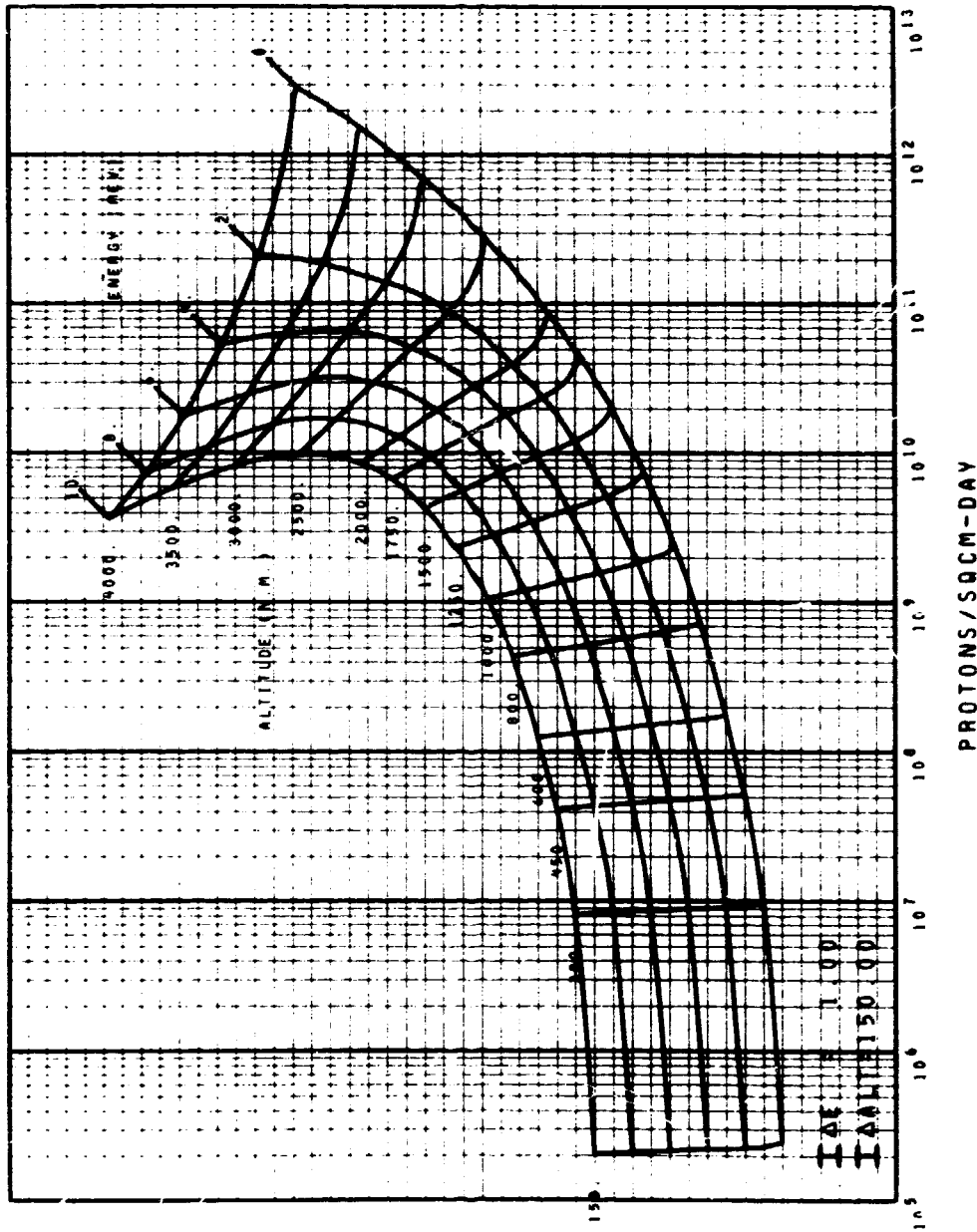


Figure 71. AP8MIN Equatorial Radial Profiles with Energies between 0.1 and 400 MeV

ORBITAL INTEGRATION MAP 300 TO 4000 N.M.
 CIRCULAR ORBIT 0 DEGREE INCLINATION
 APP MIN SOLAR MINIMUM PROTONS ENERGY LE 10 MEV FIG. 72

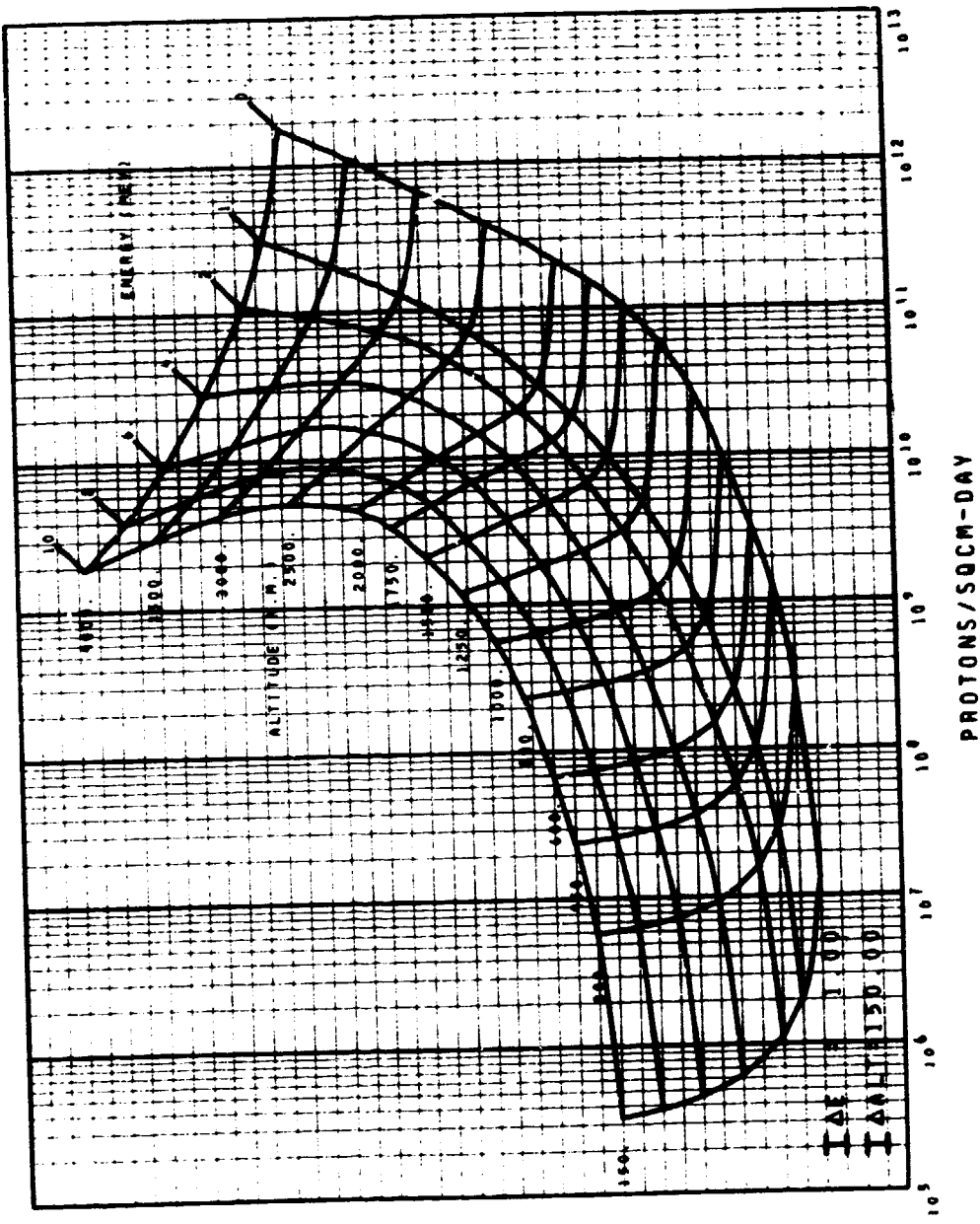


ORBITAL INTEGRATION MAP 150 TO 4000 N.M.
CIRCULAR ORBIT 30 DEGREE INCLINATION
AP 8 MIN SOLAR MINIMUM PROTONS ENERGY LE 10 MEV FIG. 73

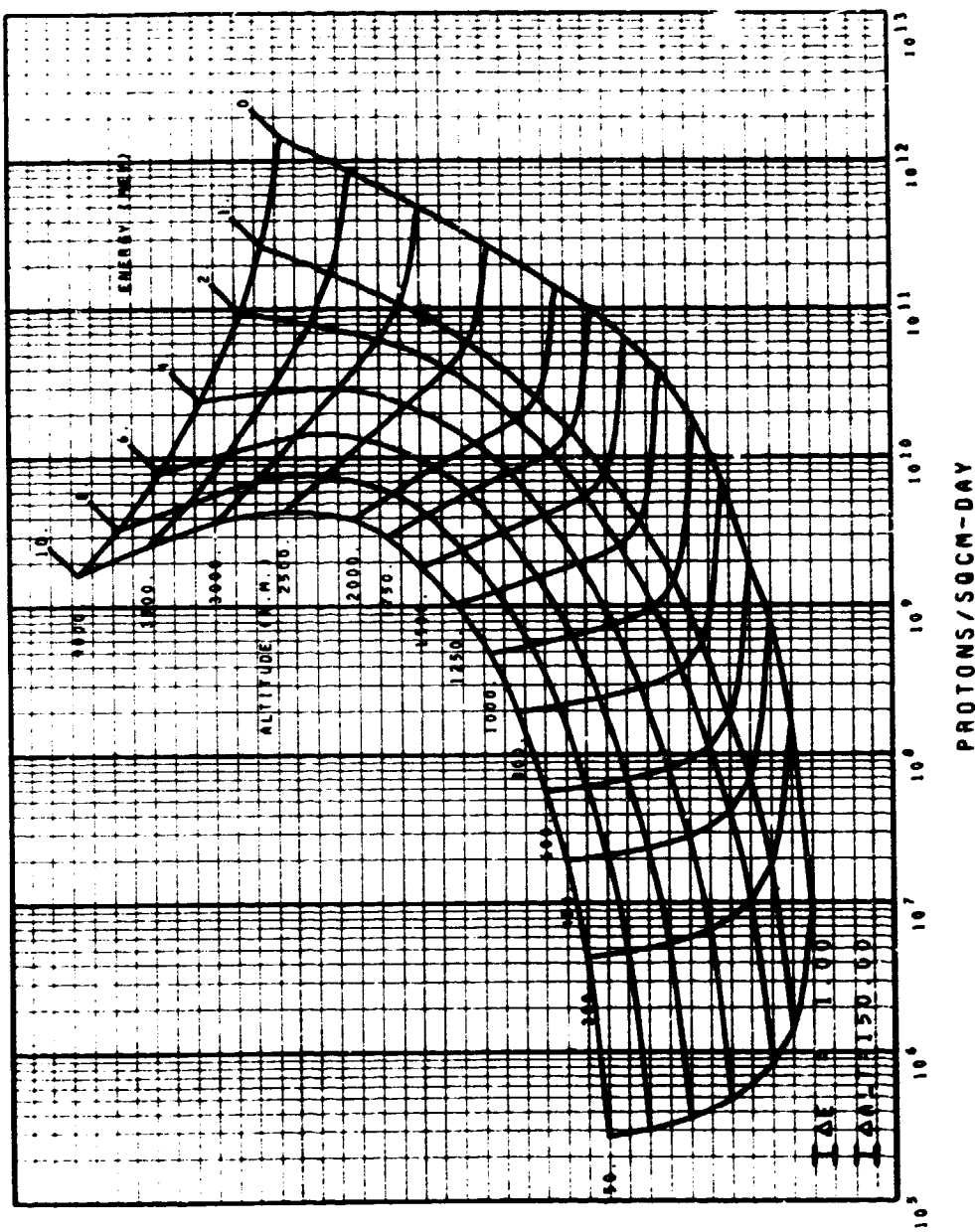


C-2

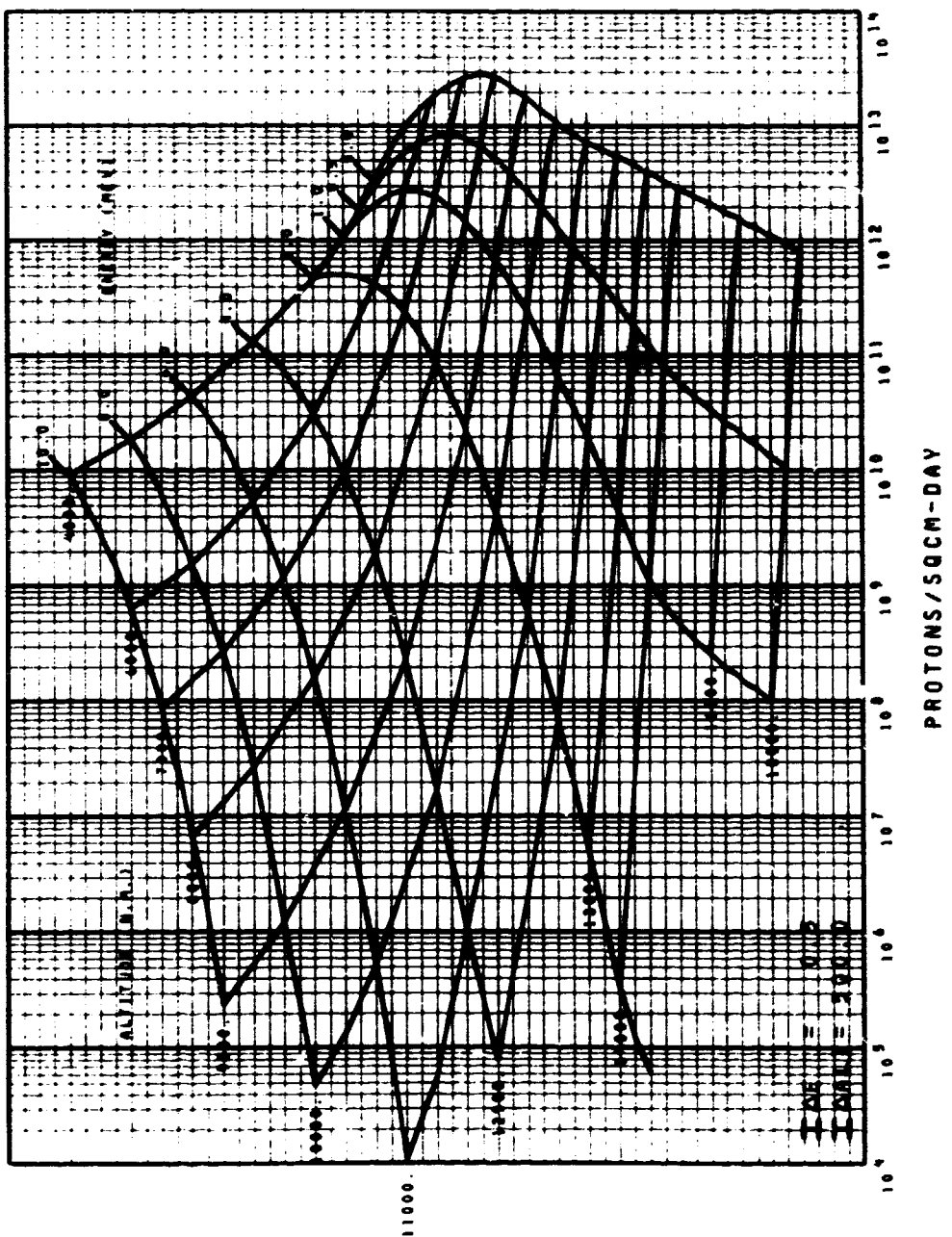
ORBITAL INTEGRATION MAP 150 TO 4000 N.M.
 CIRCULAR ORBIT 60 DEGREE INCLINATION
 AP8 MIN SOLAR MINIMUM PROTONS ENERGY LE 10 MEV FIG. 74



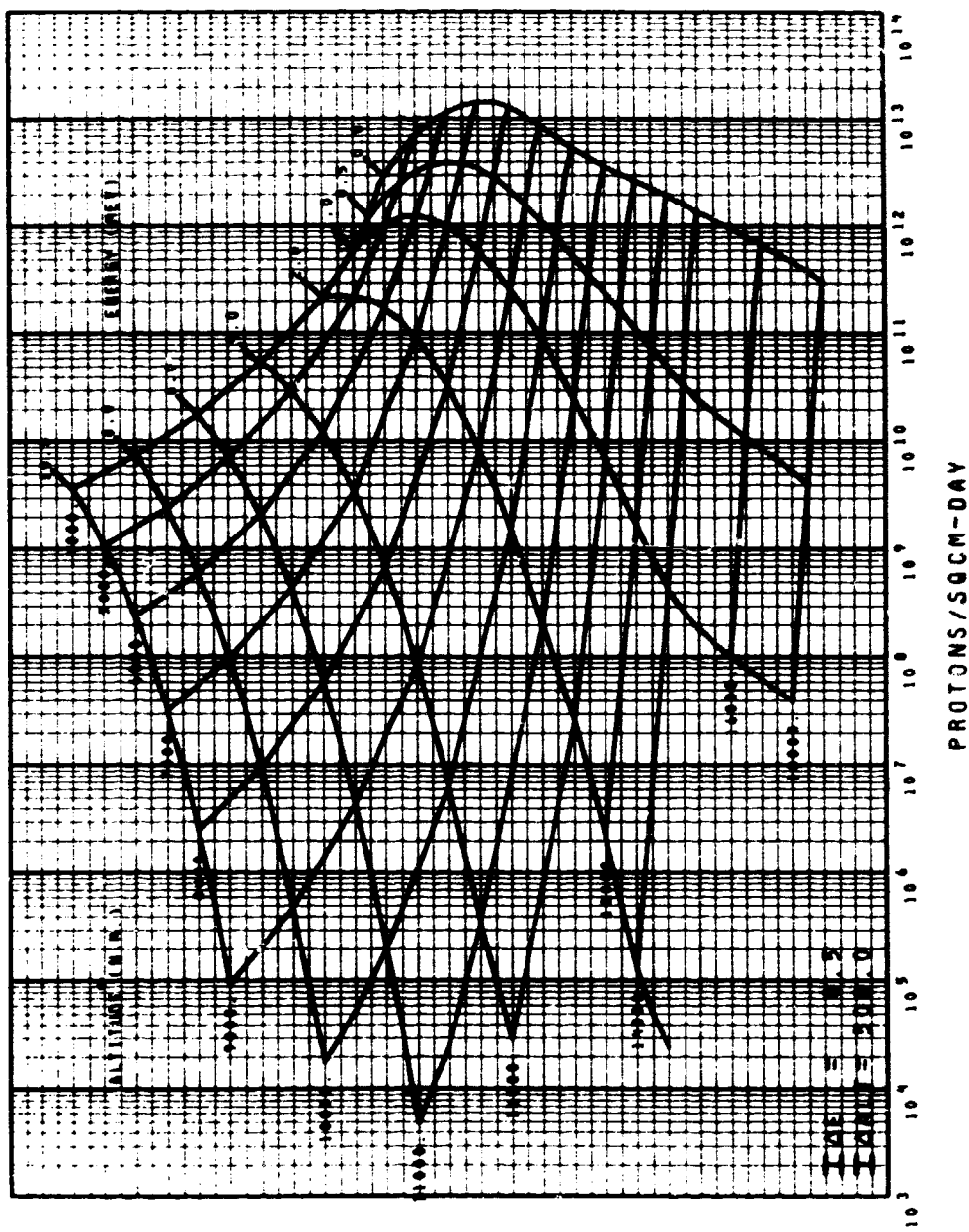
ORBITAL INTEGRATION MAP 150 TO 4000 N.M.
CIRCULAR ORBIT 90 DEGREE INCLINATION
AP 8 MIN SOLAR MINIMUM PROTONS ENERGY LE 10 MEV FIG. 75



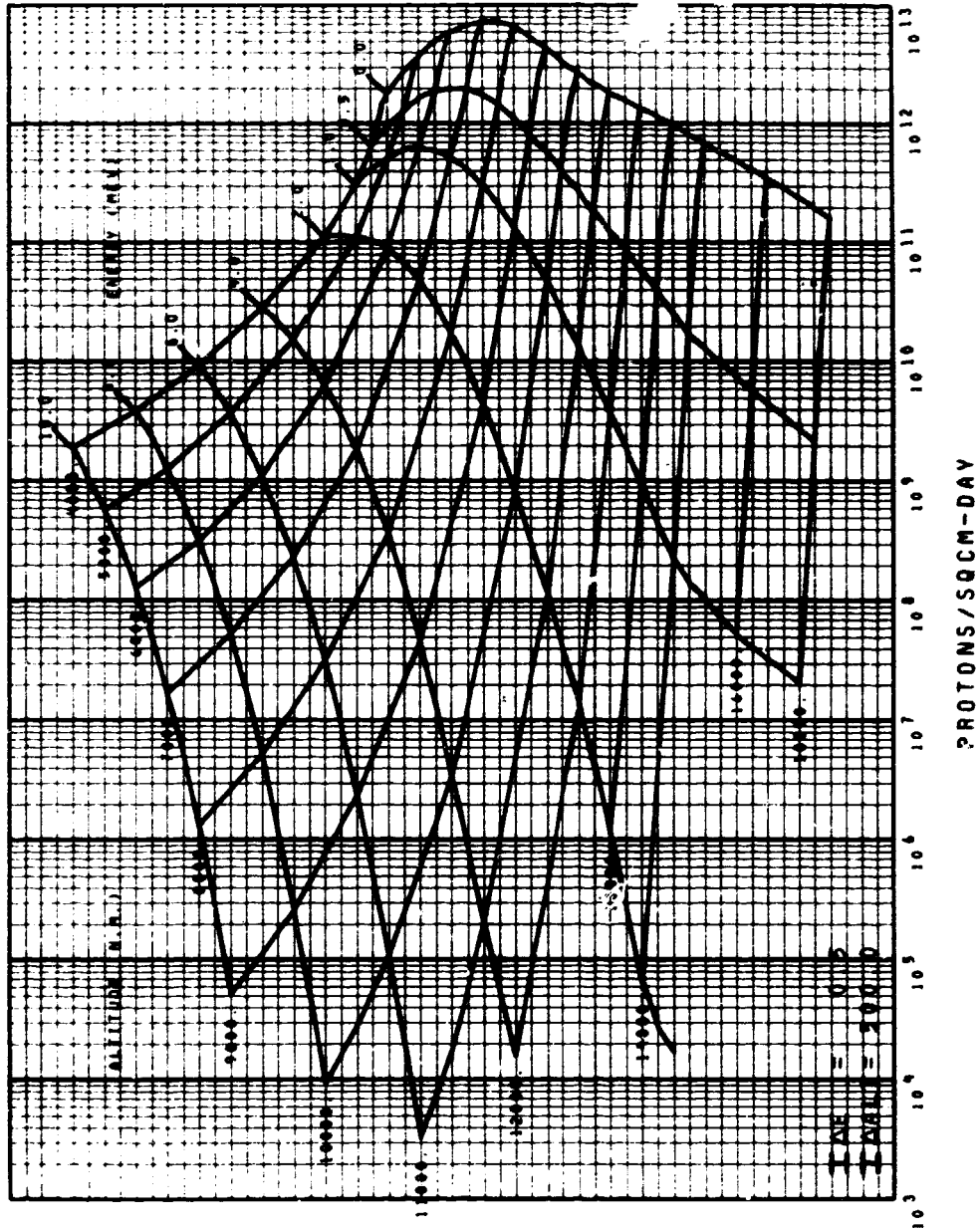
ORBITAL INTEGRATION MAP 4000 TO 18000 N.M.
CIRCULAR ORBIT 0 DEGREE INCLINATION
AP8 MIN SOLAR MINIMUM PROTONS ENERGY LE 10 MEV FIG. 76



ORBITAL INTEGRATION MAP 4000 TO 10000 N.M.
CIRCULAR ORBIT 30 DEGREE INCLINATION
AP 8 MIN SOLAR MINIMUM PROTONS ENERGY LE 10 MEV FIG. 77



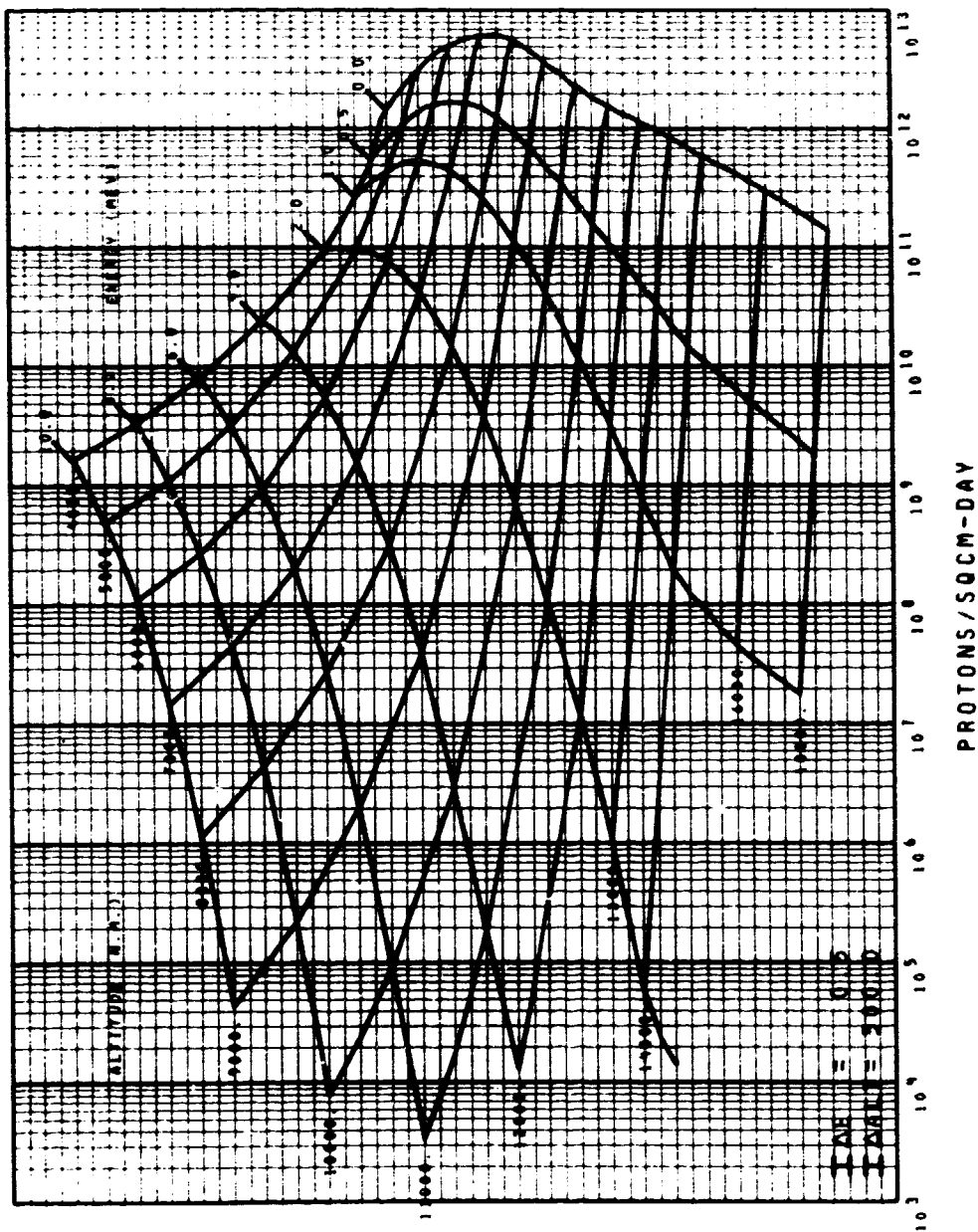
ORBITAL INTEGRATION MAP 4000 TO 18000 N.M.
CIRCULAR ORBIT 60 DEGREE INCLINATION
AP8 MIN SOLAR MINIMUM PROTONS ENERGY LE 10 MEV FIG. 78



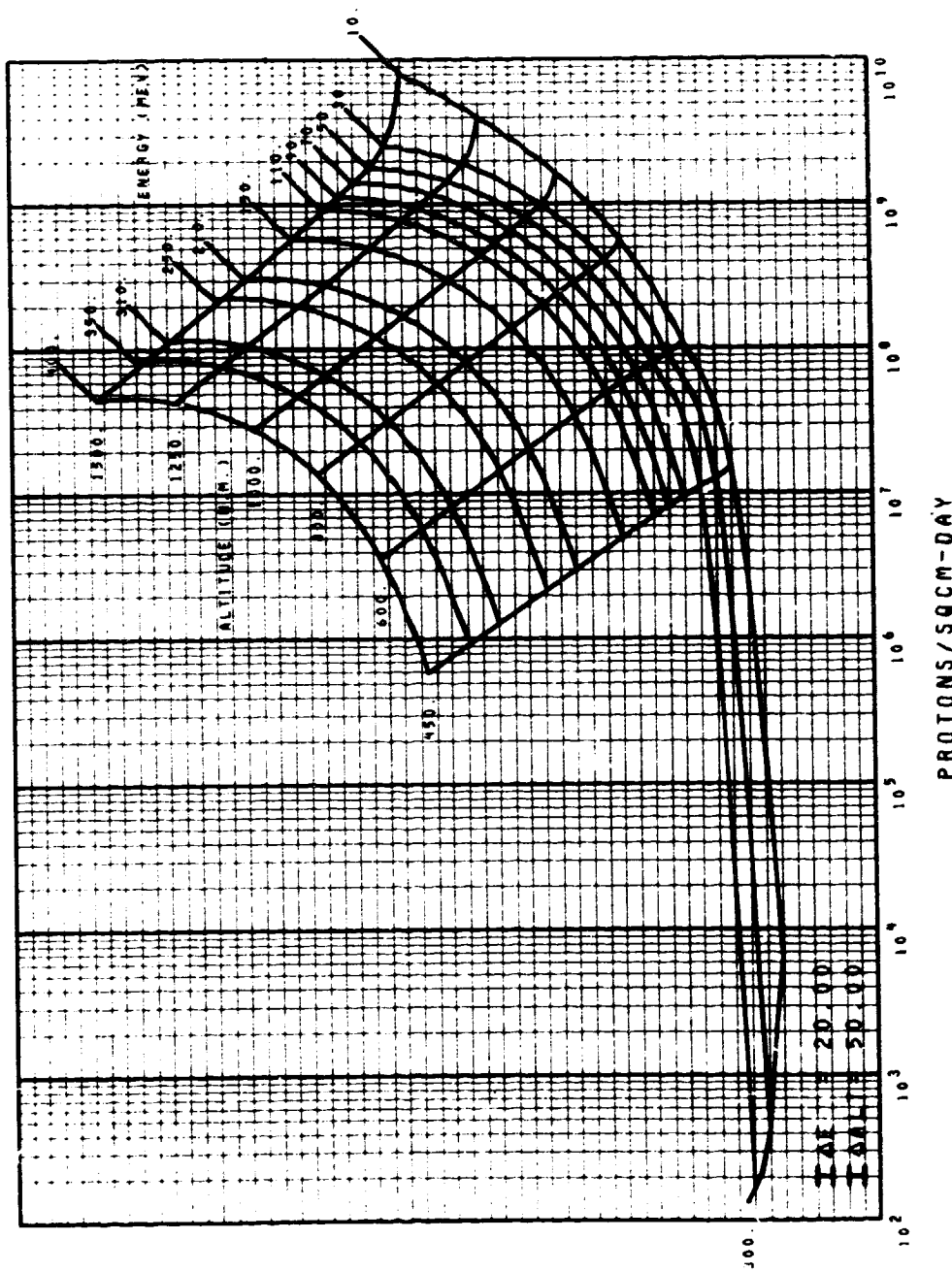
100

REPRODUCIBILITY OF THE
ORIGINAL PAGE IS POOR

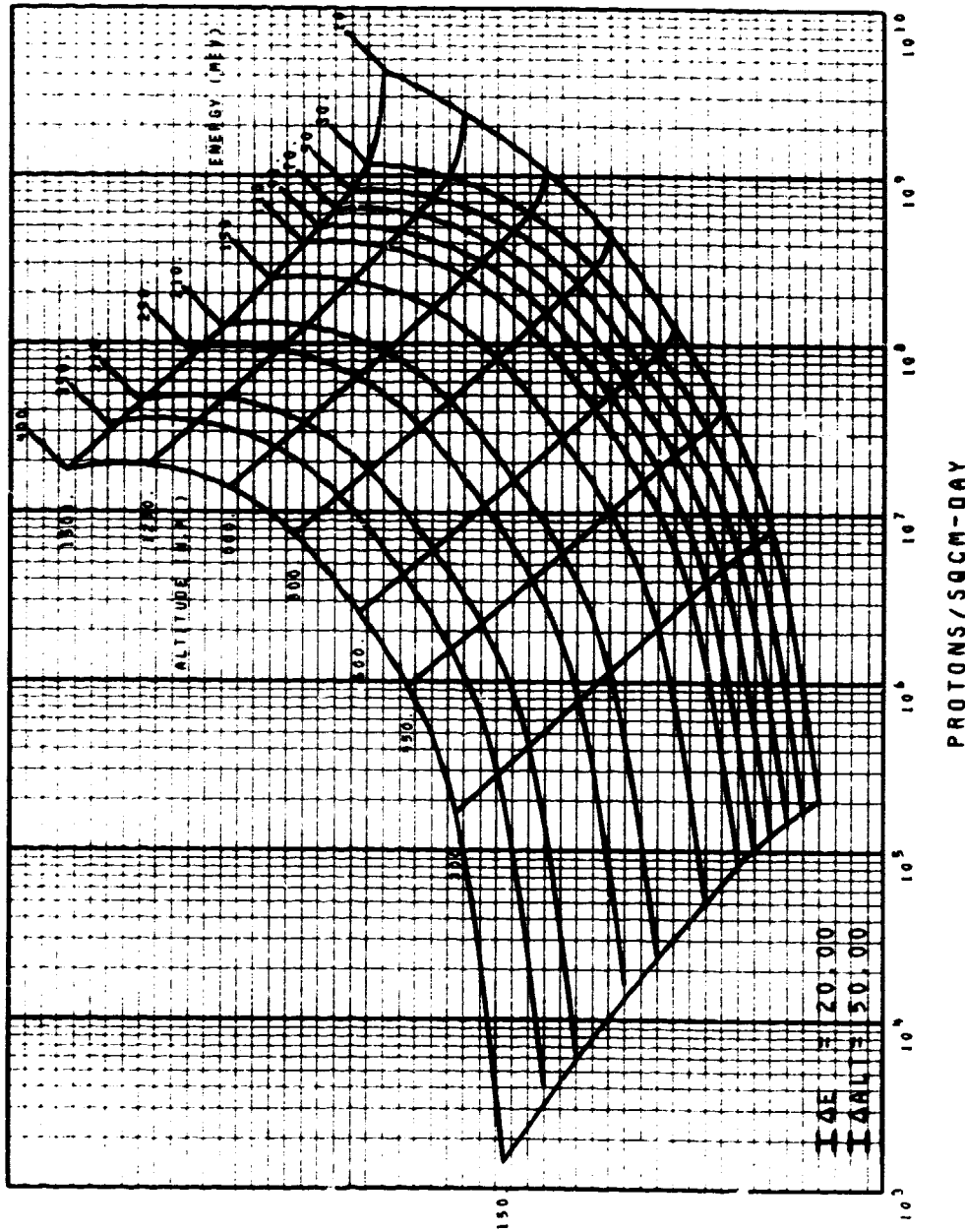
ORBITAL INTEGRATION MAP 4000 TO 18000 N.M.
CIRCULAR ORBIT 90 DEGREE INCLINATION
AP8 MIN SOLAR MINIMUM PROTONS ENERGY LE 10 MEV FIG. 79



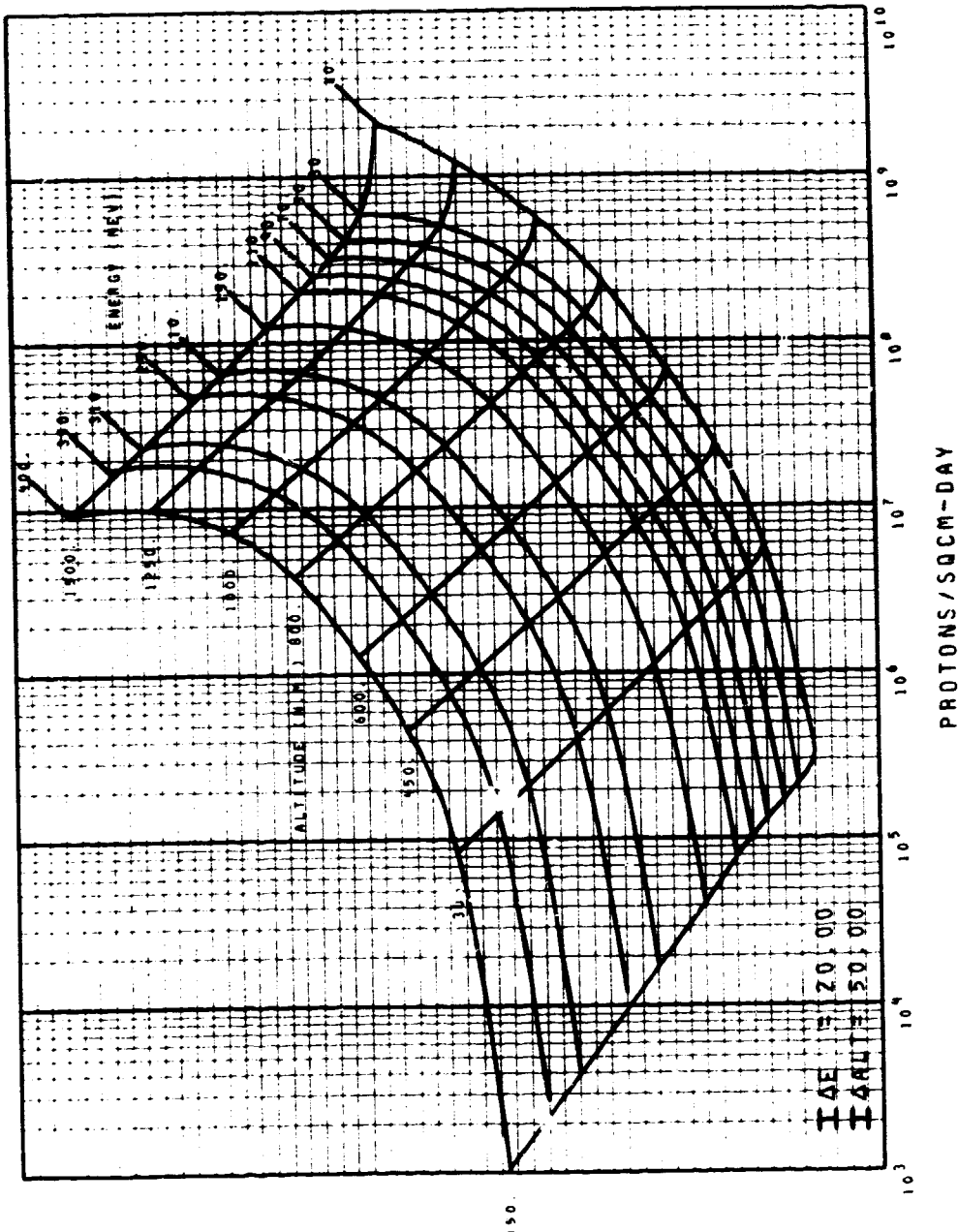
ORBITAL INTEGRATION MAPP 300 TO 1500 N.M.
 CIRCULAR ORBIT 0 DEGREE INCLINATION
 APR 8 MIN SOLAR MINIMUM PROTONS ENERGY GE 10 MEV FIG. 80



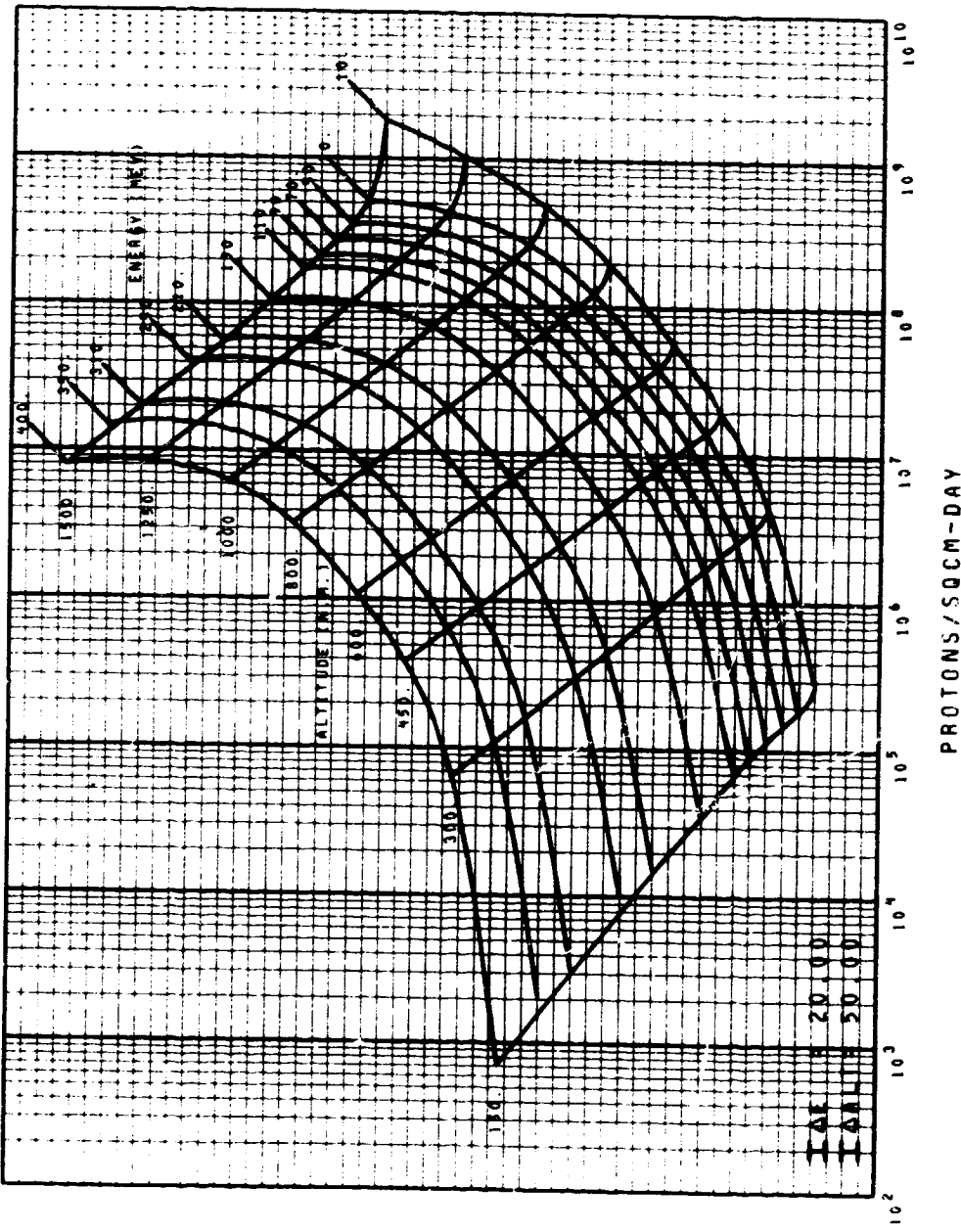
ORBITAL INTEGRATION MAP 150 TO 1500 N.M.
 CIRCULAR ORBIT 30 DEGREE INCLINATION
 APP IN SOLAR MINIMUM PROTONS ENERGY GE 10 MEV FIG. 81



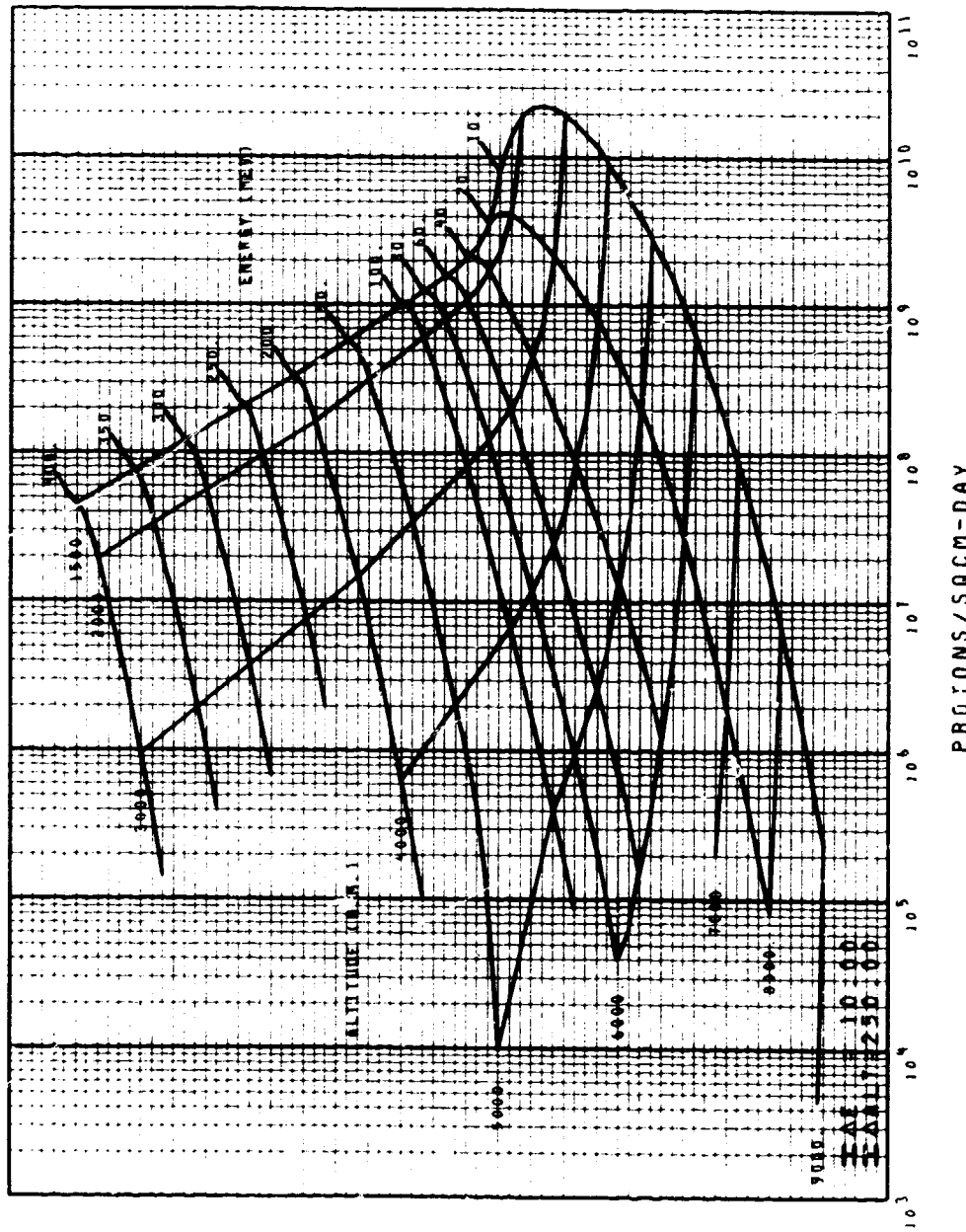
ORBITAL INTEGRATION MAP 150 TO 1500 N.M.
 CIRCULAR ORBIT 60 DEGREE INCLINATION
 AP8 MIN SOLAR MINIMUM PROTONS ENERGY GE 10 MEV FIG. 82



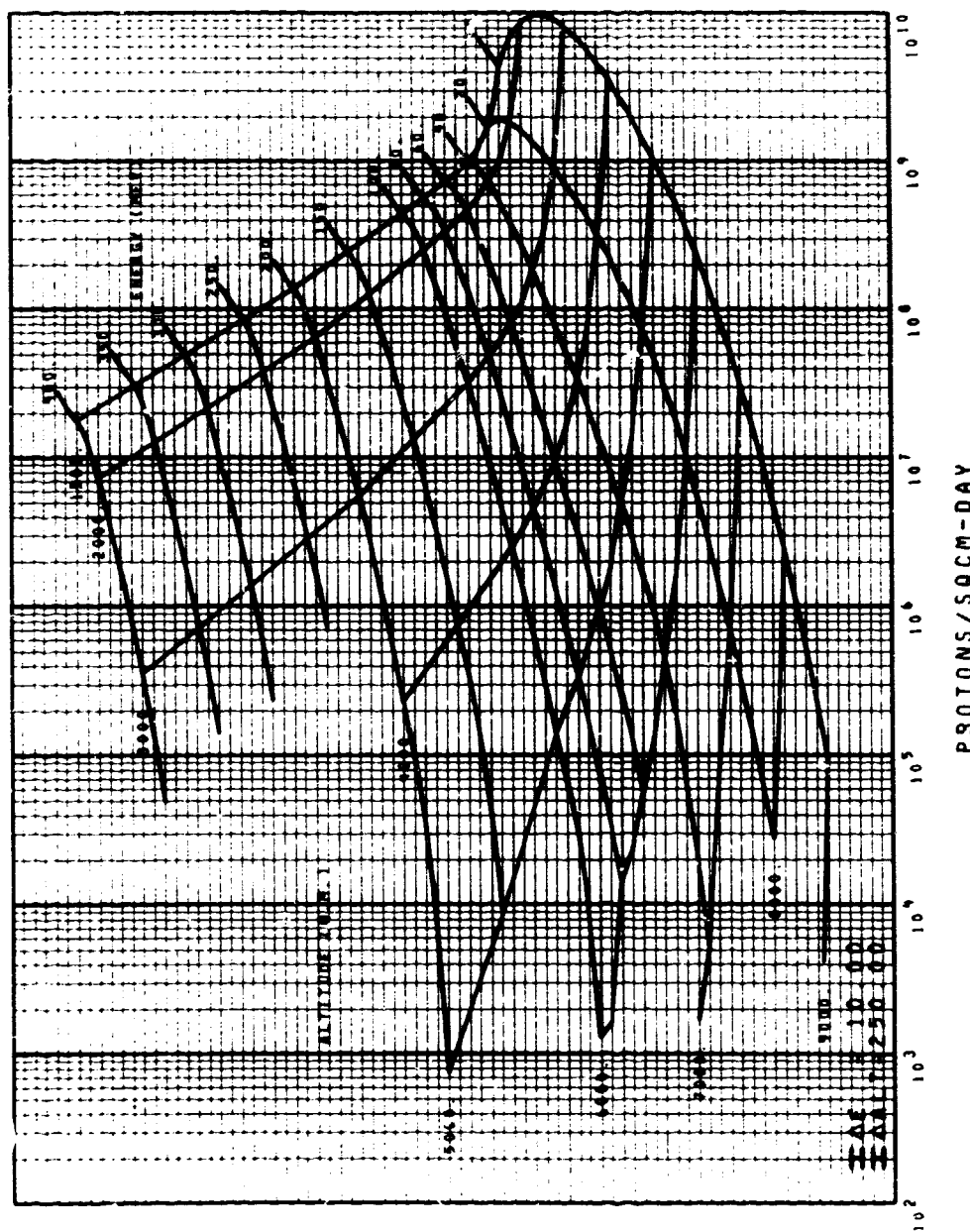
ORBITAL INTEGRATION MAP 150 TO 1500 N.M.
CIRCULAR ORBIT 90 DEGREE INCLINATION
APP 8 MIN SOLAR MINIMUM PROTONS ENERGY GE 10 MEV FIG. 83



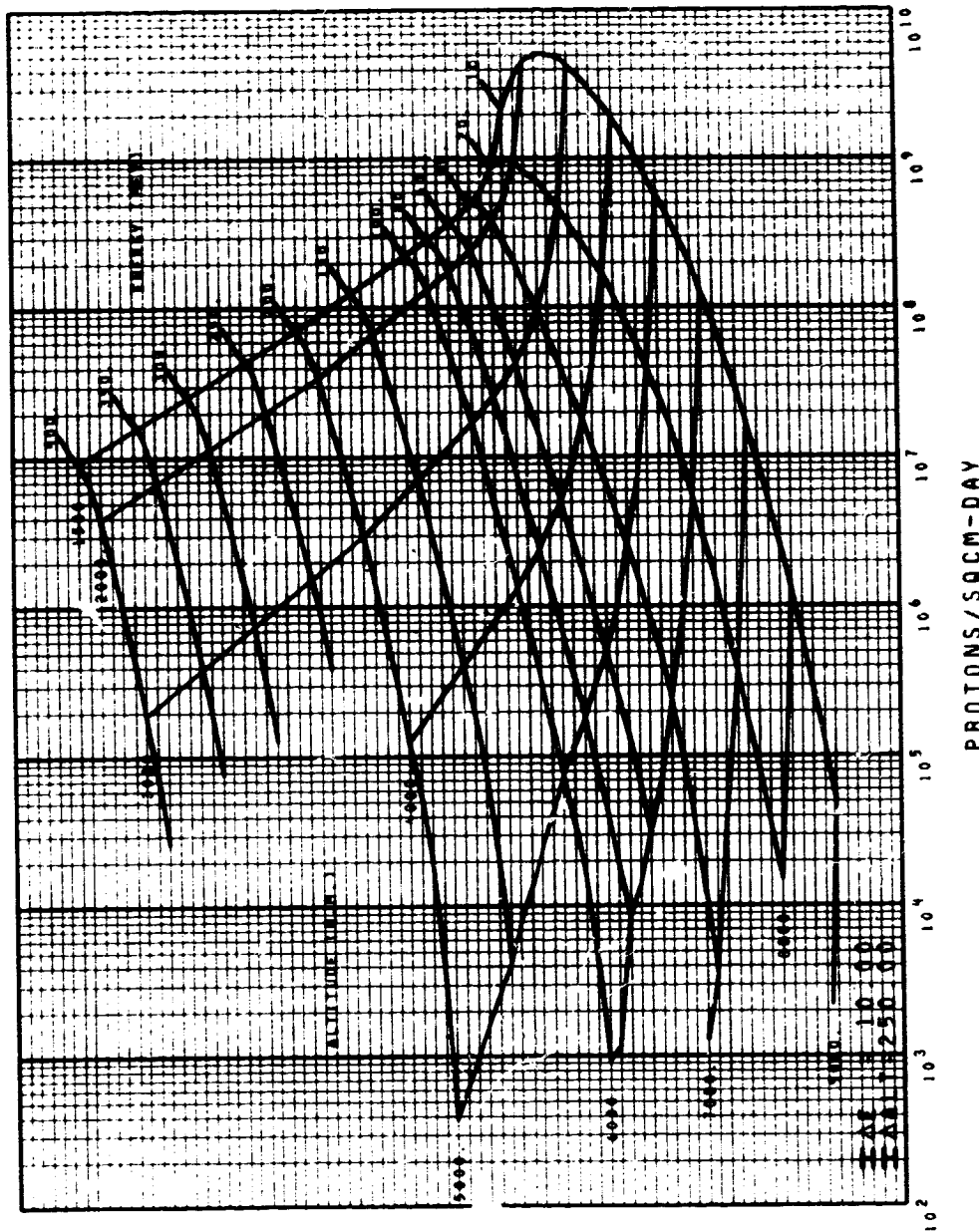
ORBITAL INTEGRATION MAP 1500 TO 9000 N.M.
CIRCULAR ORBIT 0 DEGREE INCLINATION
AP8 MIN SOLAR MINIMUM PROTONS ENERGY GE 10 MEV FIG. 84



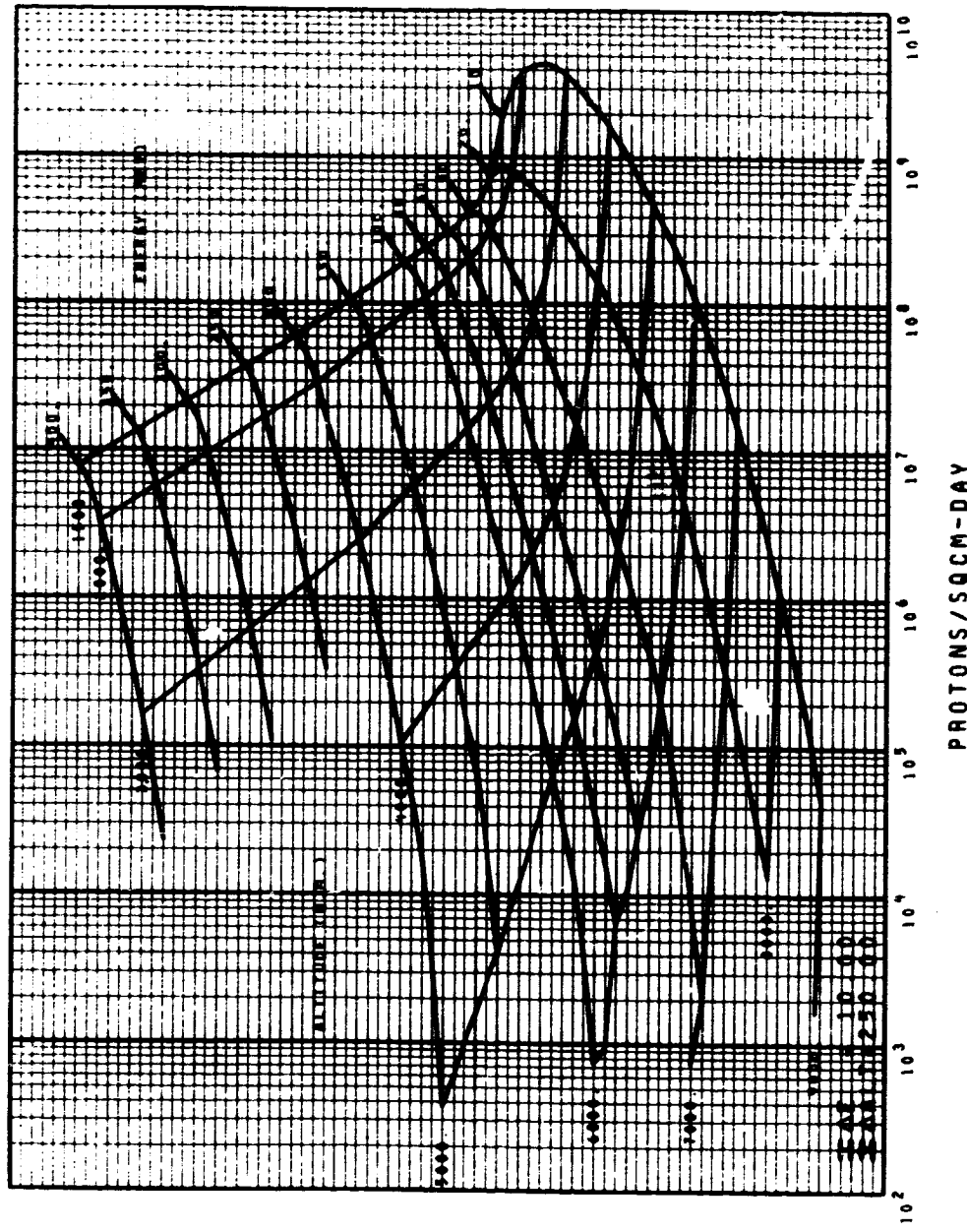
ORBITAL INTEGRATION MAP 1500 TO 9000 N.M.
CIRCULAR ORBIT 30 DEGREE INCLINATION
AP 8 MIN SOLAR MINIMUM PROTONS ENERGY GE 10 MEV FIG. 85



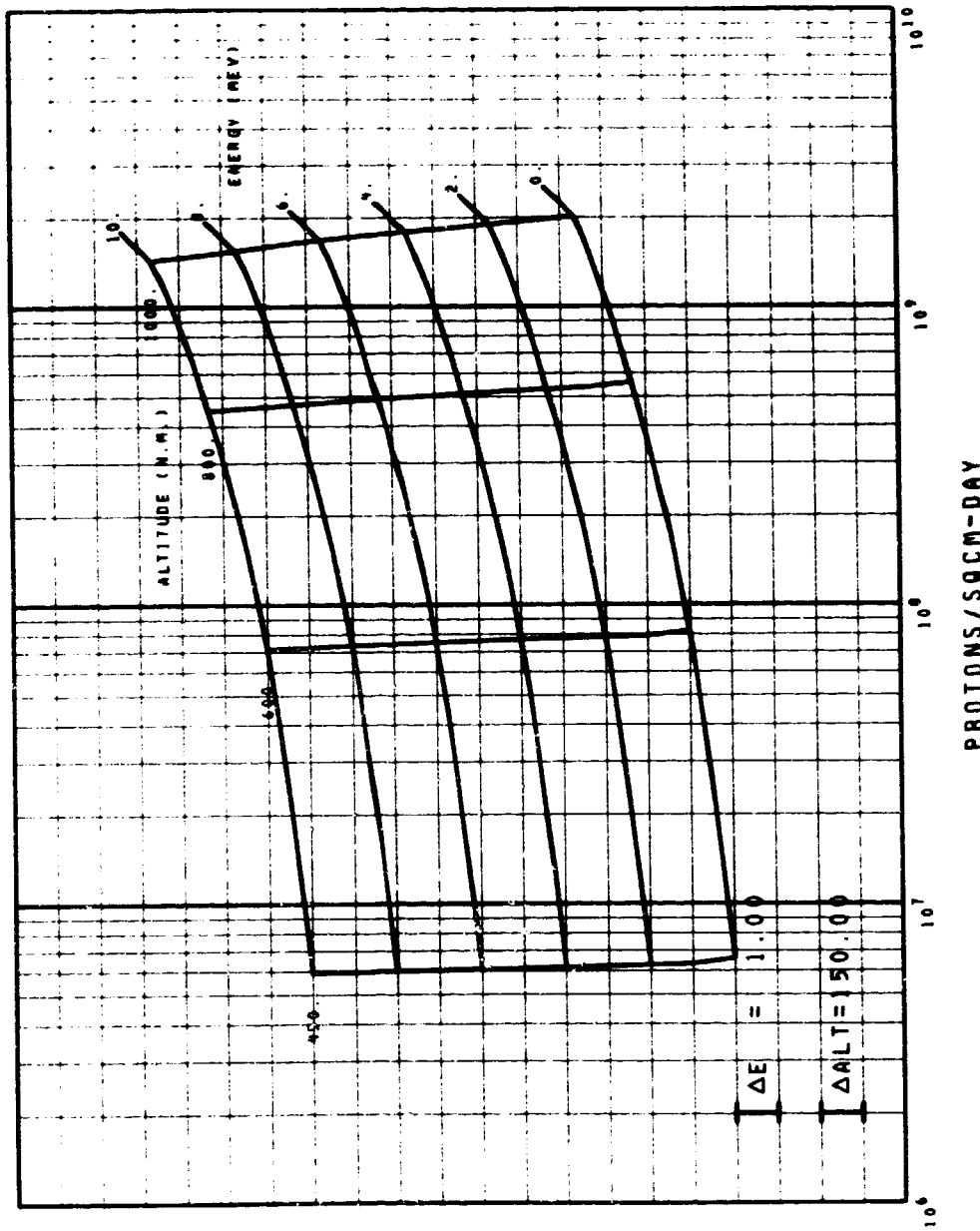
ORBITAL INTEGRATION MAP 1500 TO 9000 N.M.
CIRCULAR ORBIT 60 DEGREE INCLINATION
AP 8 MIN SOLAR MINIMUM PROTONS ENERGY GE 10 MEV FIG. 86



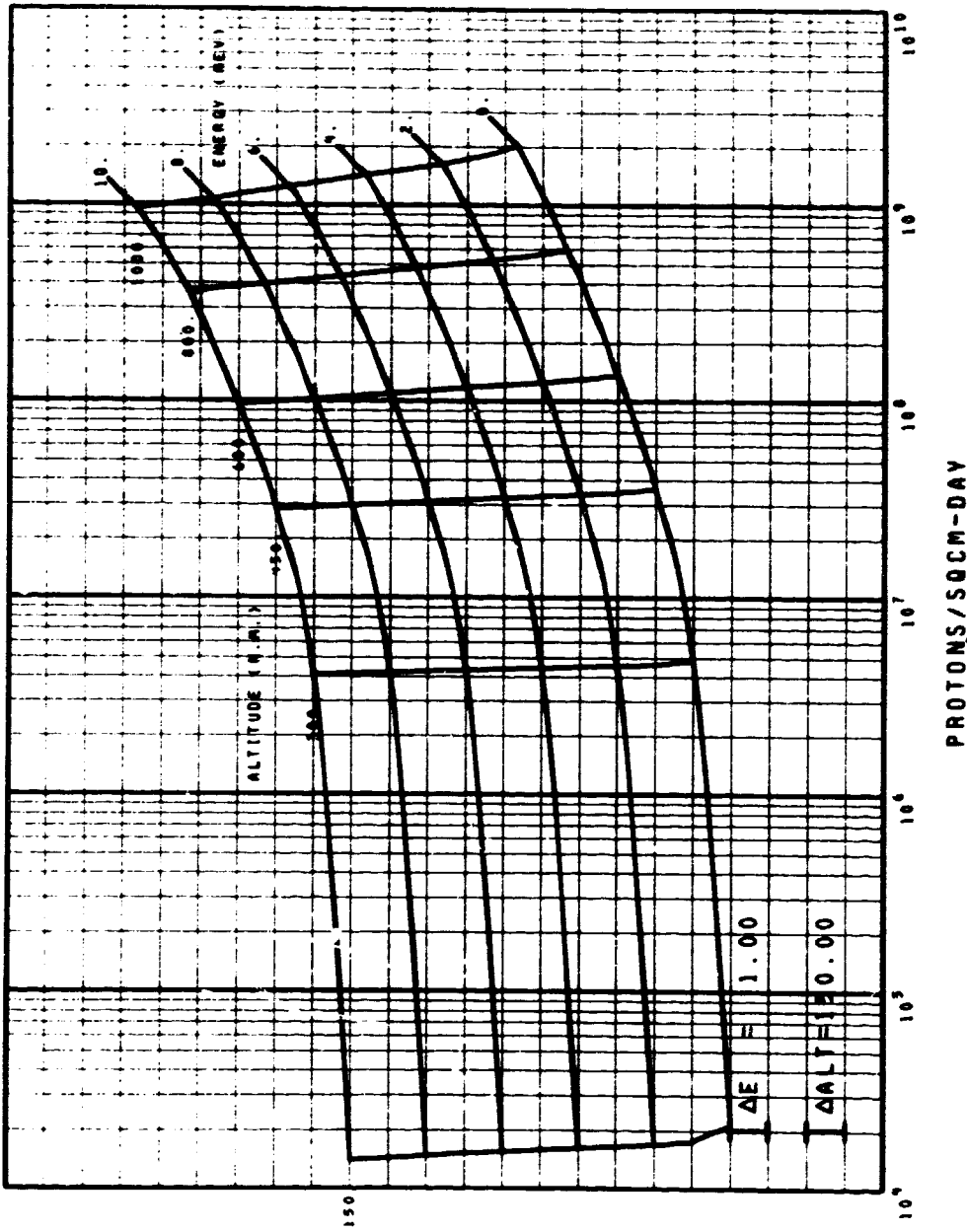
ORBITAL INTEGRATION MAP 1500 TO 9000 N.M.
CIRCULAR ORBIT 90 DEGREE INCLINATION
AP8 MIN SOLAR MINIMUM PROTONS ENERGY GE 10 MEV FIG. 87



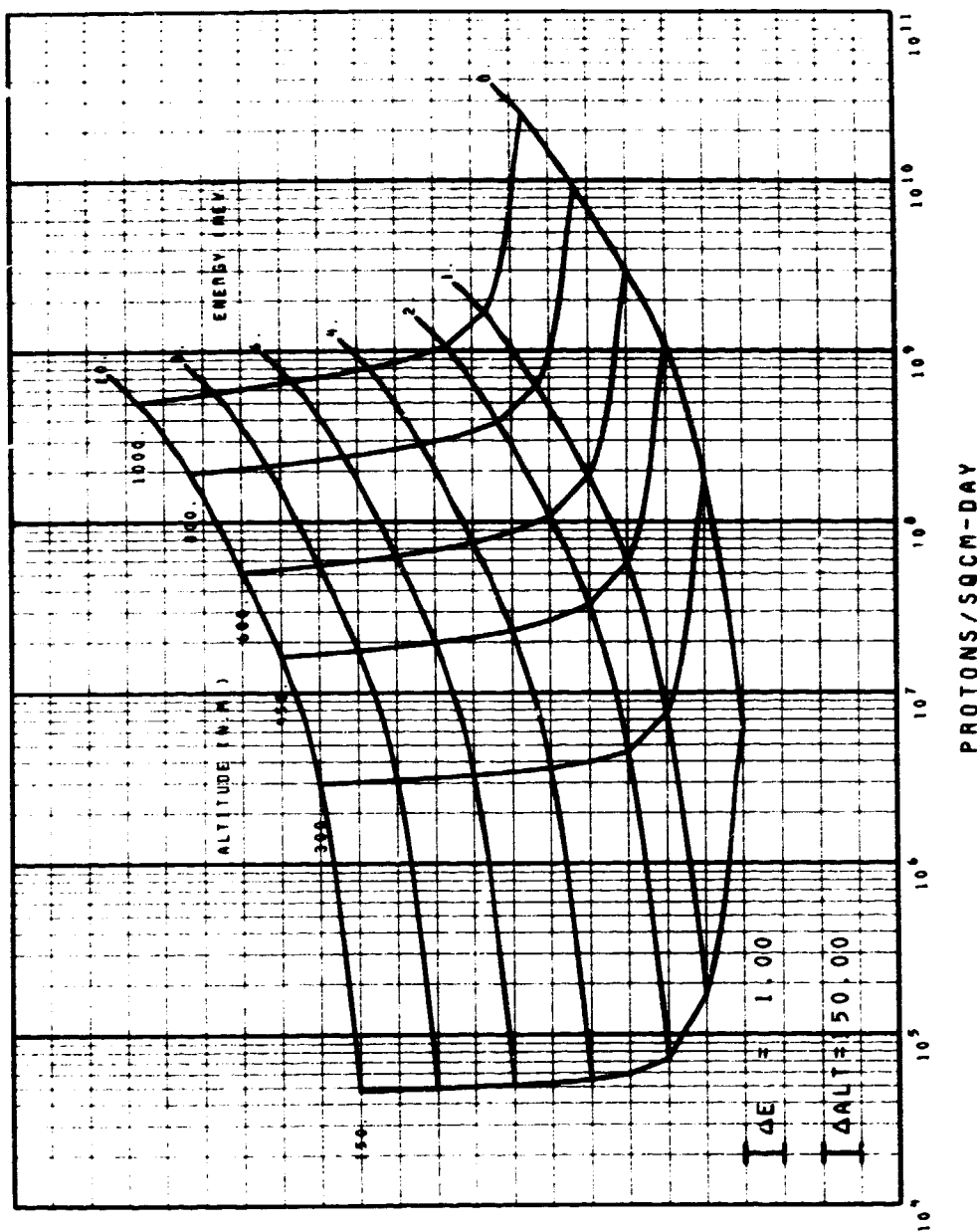
ORBITAL INTEGRATION MAP 450 TO 1000 N.M.
 CIRCULAR ORBIT 0 DEGREE INCLINATION
 APP 8 MAX SOLAR MAXIMUM PROTONS ENERGY LE 10 MEV FIG. 88



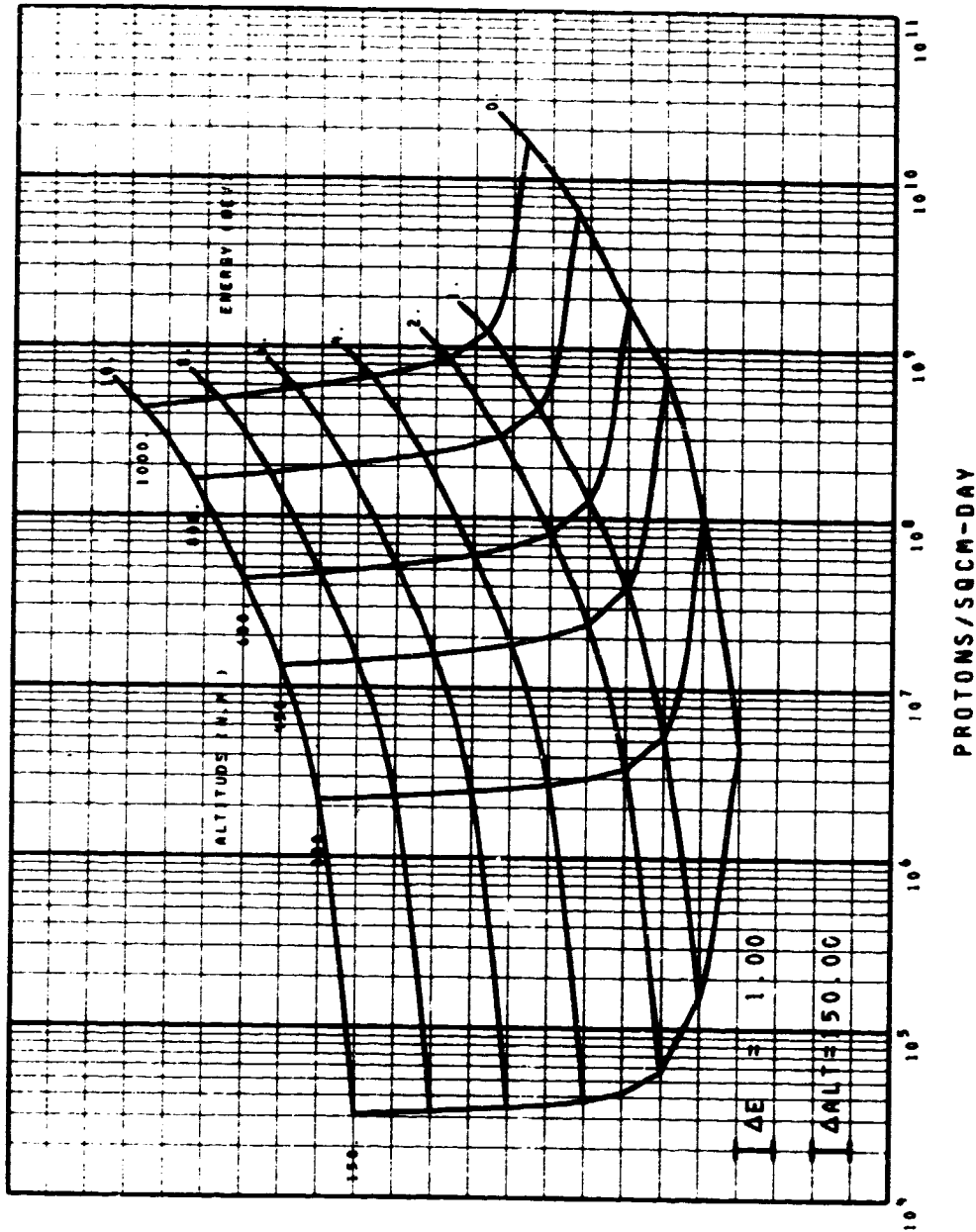
ORBITAL INTEGRATION MAP 150 TO 1000 N.M.
CIRCULAR ORBIT 30 DEGREE INCLINATION
AP8 MAX SOLAR MAXIMUM PROTONS ENERGY LE 10 MEV FIG. 89



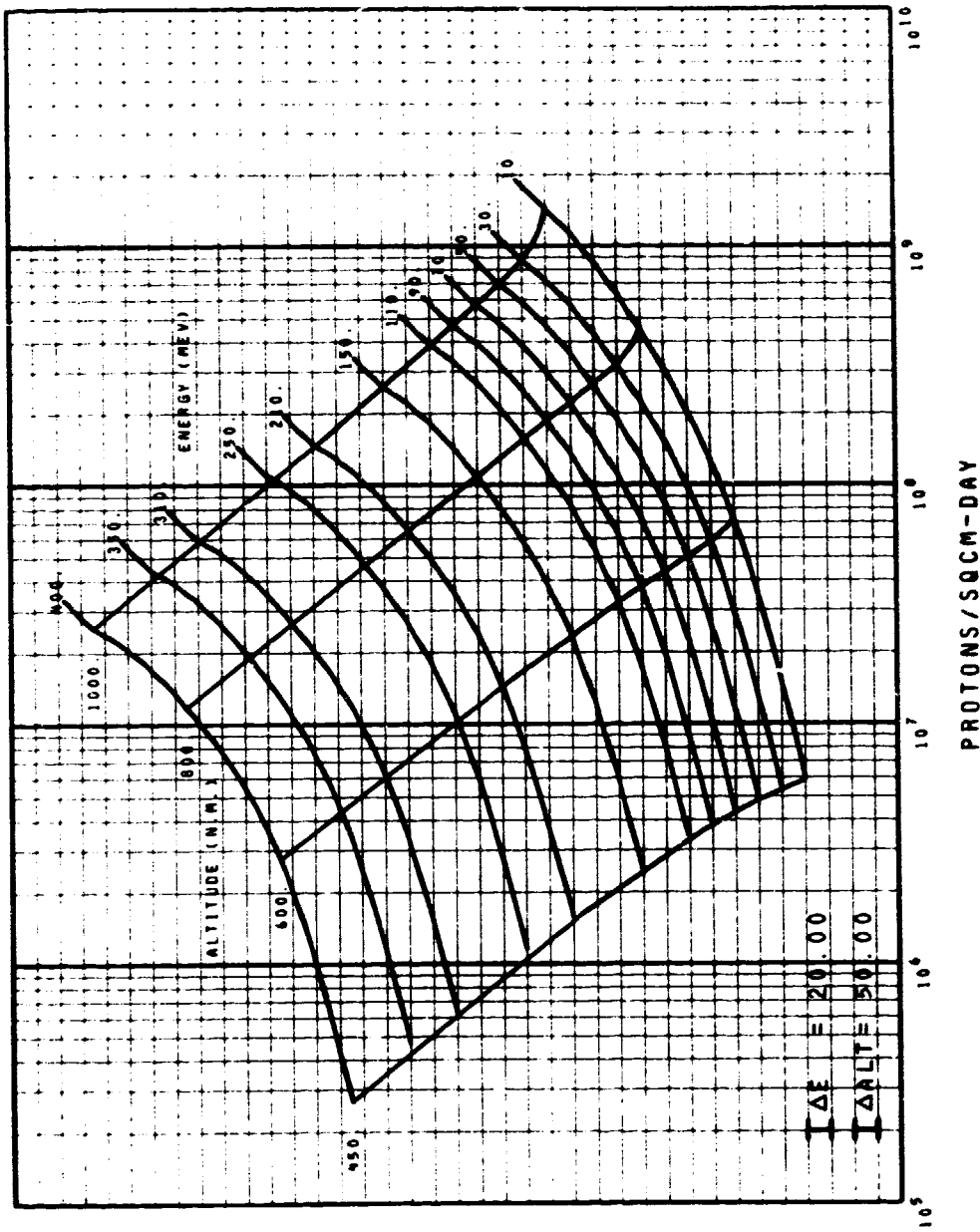
ORBITAL INTEGRATION MAP 150 TO 1000 N.M.
 CIRCULAR ORBIT 60 DEGREE INCLINATION
 APP 8 MAX SOLAR MAXIMUM PROTONS ENERGY LE 10 MEV FIG. 90



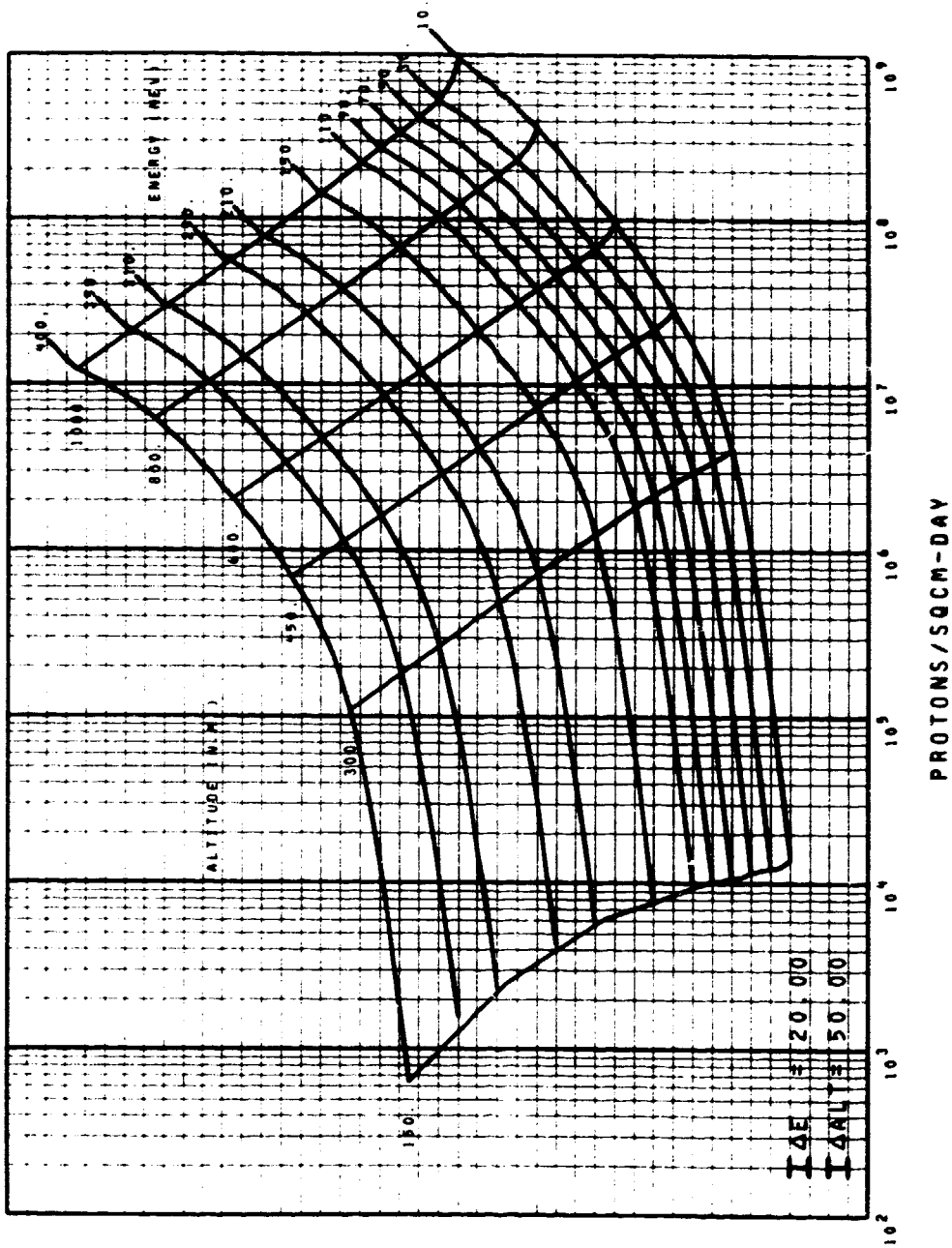
ORBITAL INTEGRATION MAP 150 TO 1000 N.M.
CIRCULAR ORBIT 90 DEGREE INCLINATION
AP8 MAX SOLAR MAXIMUM PROTONS ENERGY LE 10 MEV FIG. 91



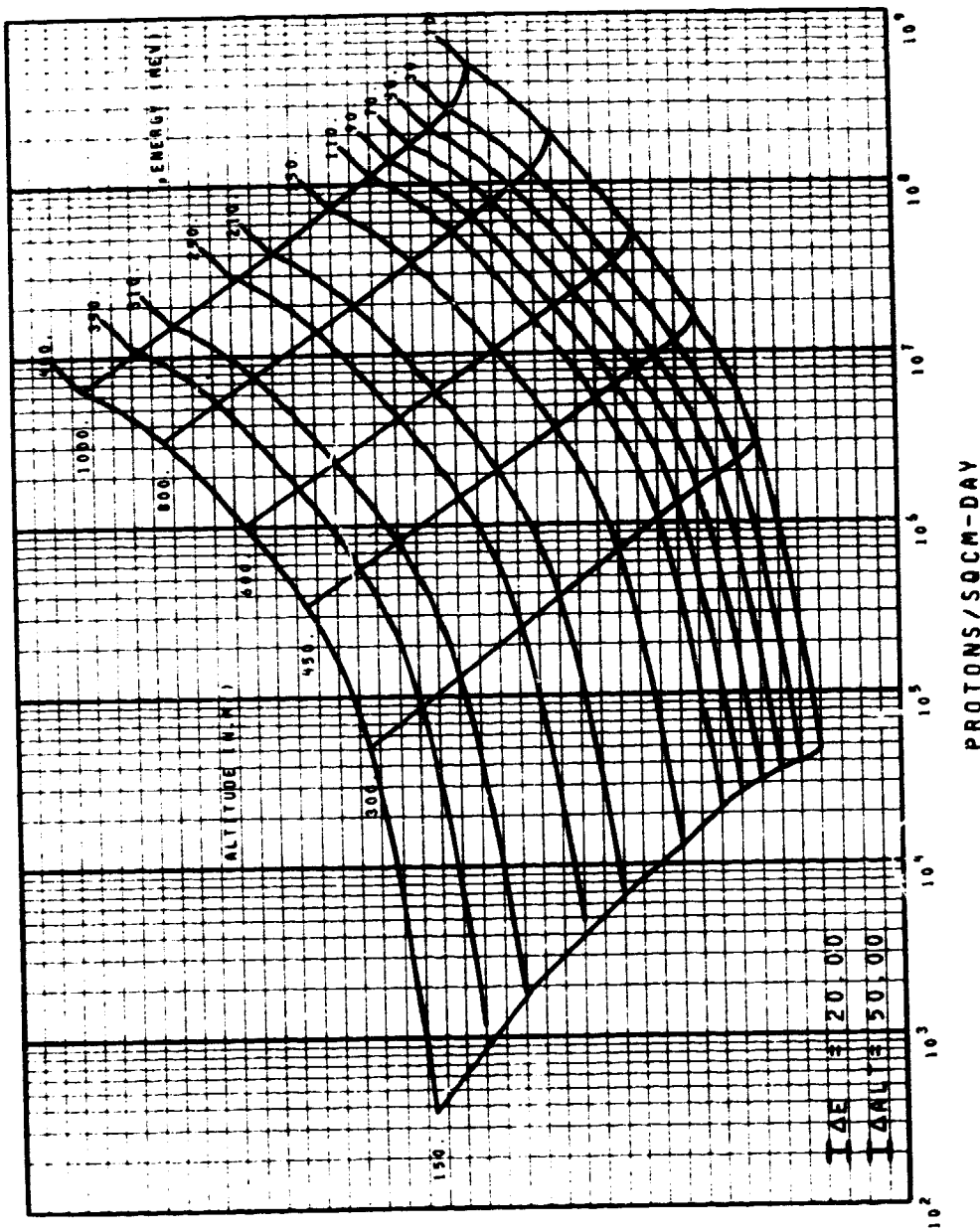
ORBITAL INTEGRATION MAP 450 TO 1000 N.M.
 CIRCULAR ORBIT 0 DEGREE INCLINATION
 APP MAX SOLAR MAXIMUM PROTONS ENERGY GE 10 MEV FIG. 92



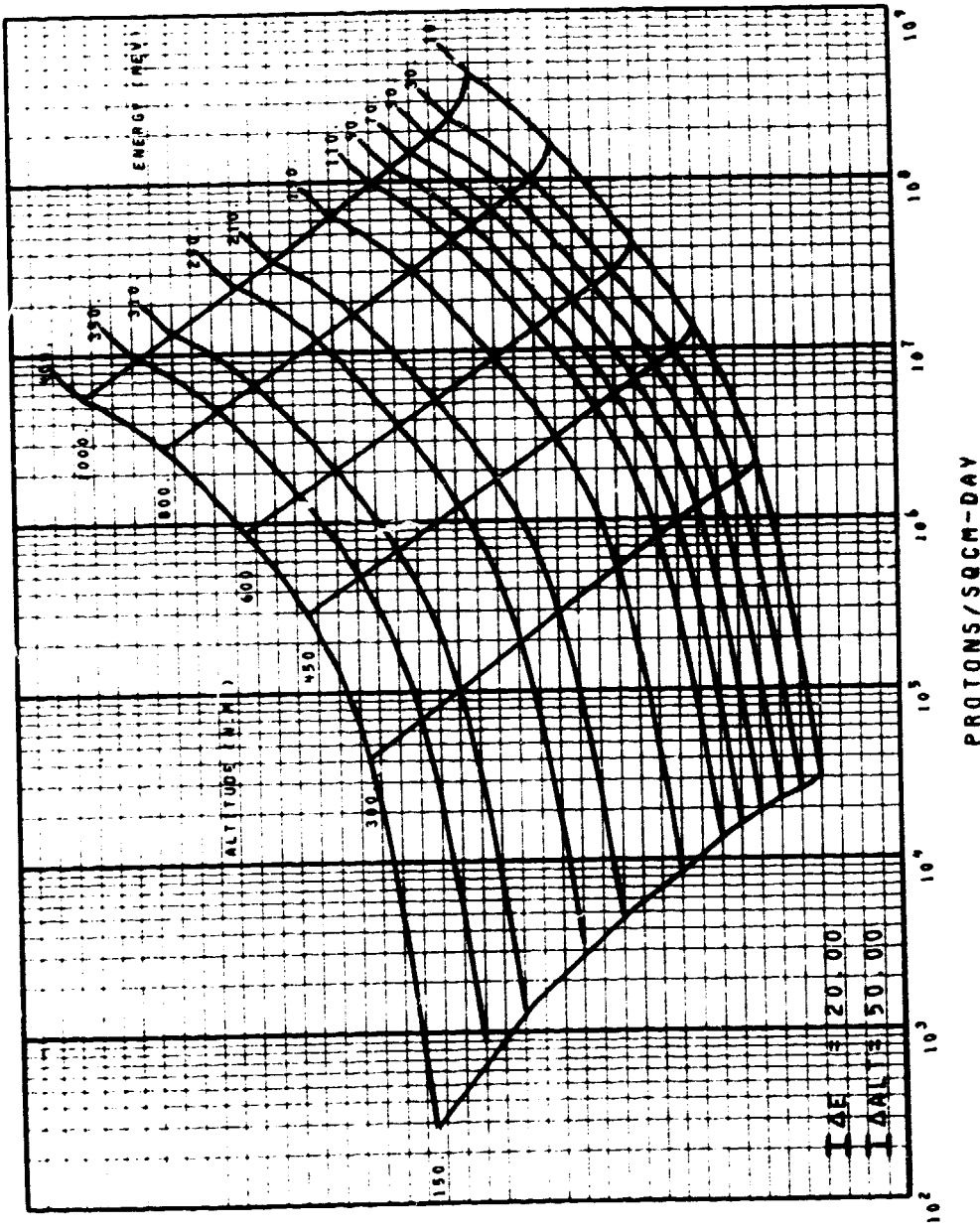
ORBITAL INTEGRATION MAP 150 TO 1000 N.M.
CIRCULAR ORBIT 30 DEGREE INCLINATION
AP & MAX SOLAR MAXIMUM PROTONS ENERGY GE 10 MEV FIG. 93



ORBITAL INTEGRATION MAP 150 TO 1000 N.M.
 CIRCULAR ORBIT 60 DEGREE INCLINATION
 APE MAX SOLAR MAXIMUM PROTONS ENERGY GE 10 MEV FIG. 94



ORBITAL INTEGRATION MAP 150 TO 1000 N.M.
 CIRCULAR ORBIT 90 DEGREE INCLINATION
 AP8 MAX SOLAR MAXIMUM PROTONS ENERGY GE 10 MEV FIG. 95



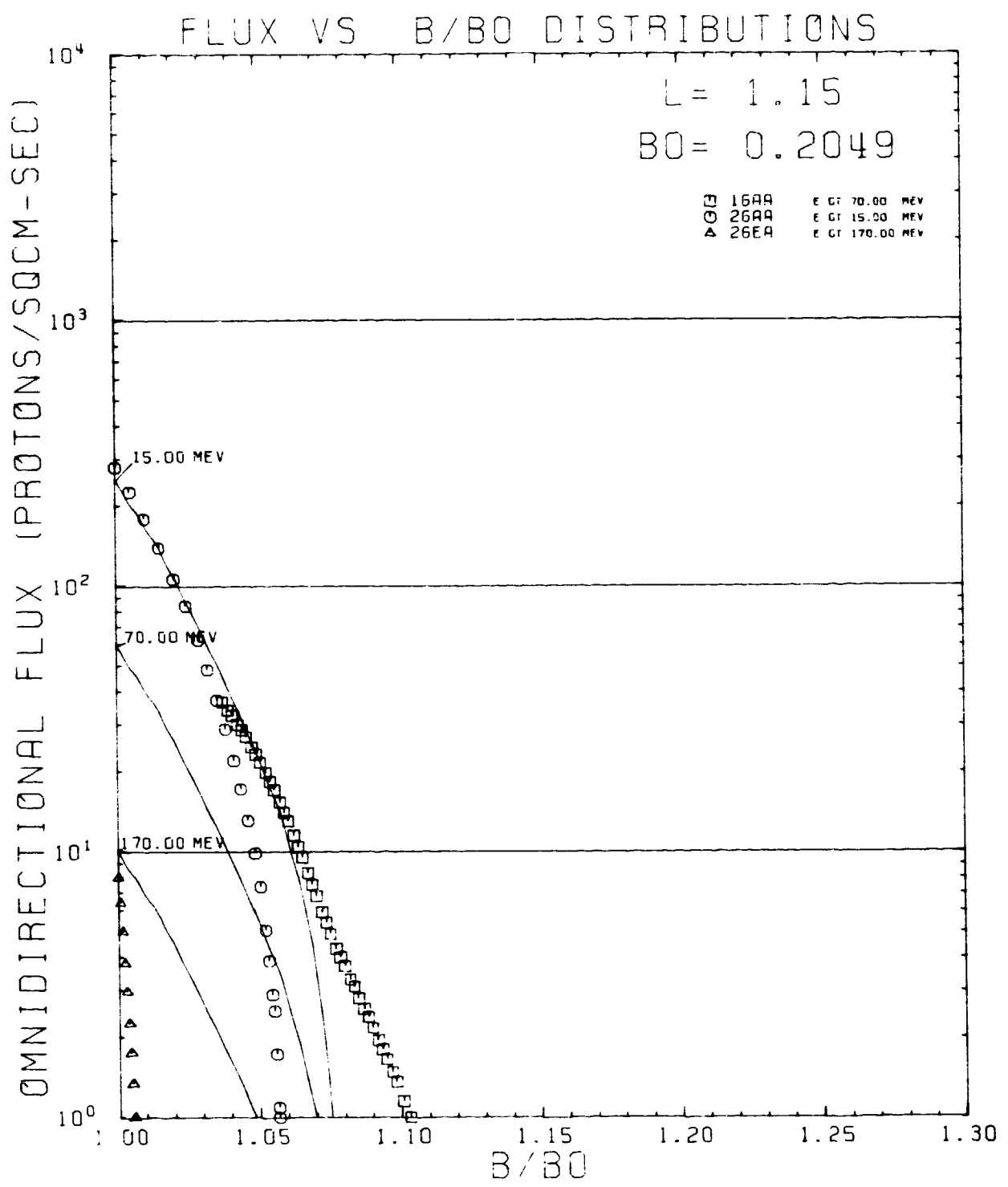


Figure 96. AP8MIN and Data Flux vs B/B_0 Comparison Plot for $L = 1.15$ RE

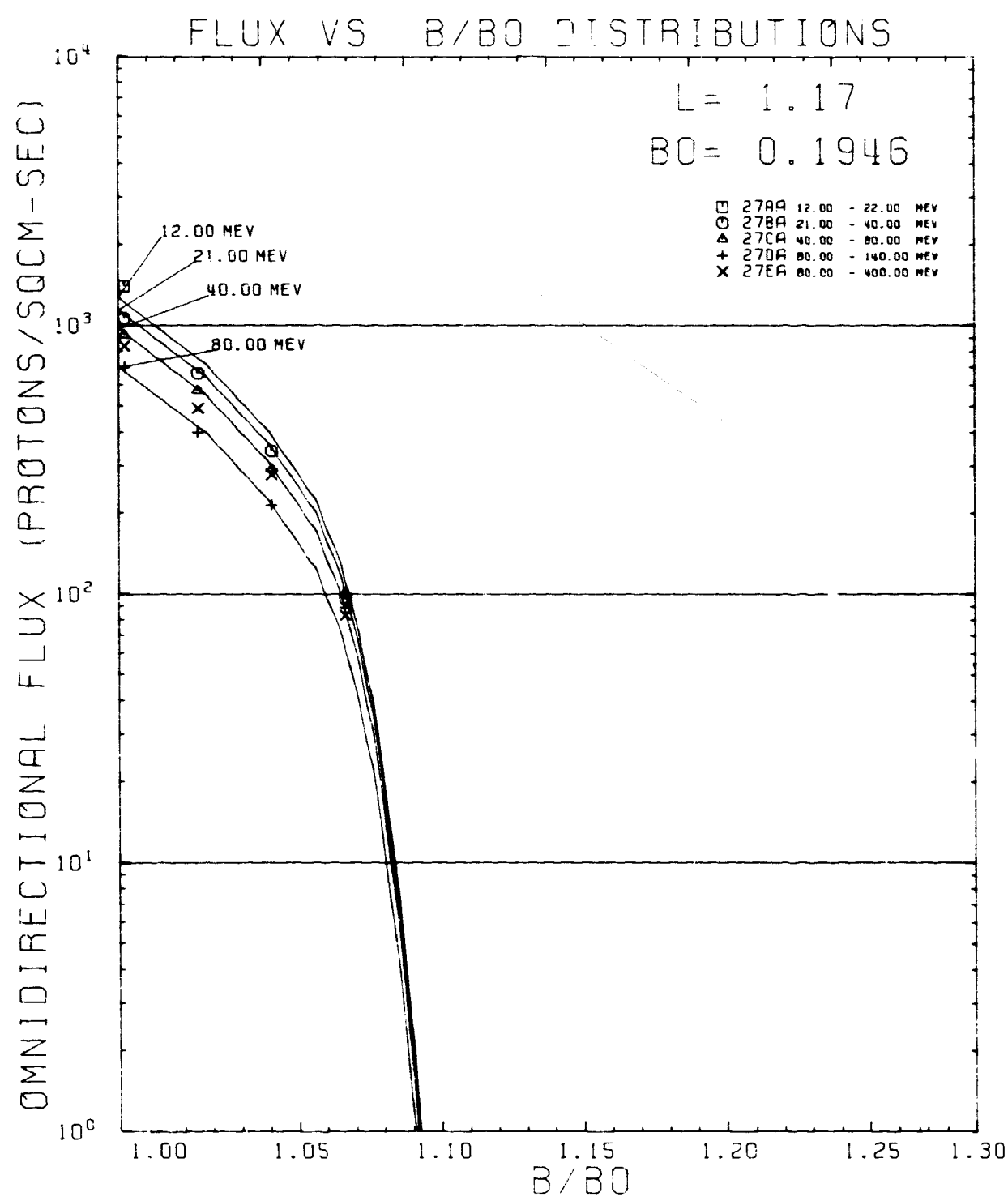


Figure 97. AP8MIN and Data Flux vs B/B_0 Comparison Plot for $L = 1.17$ RE

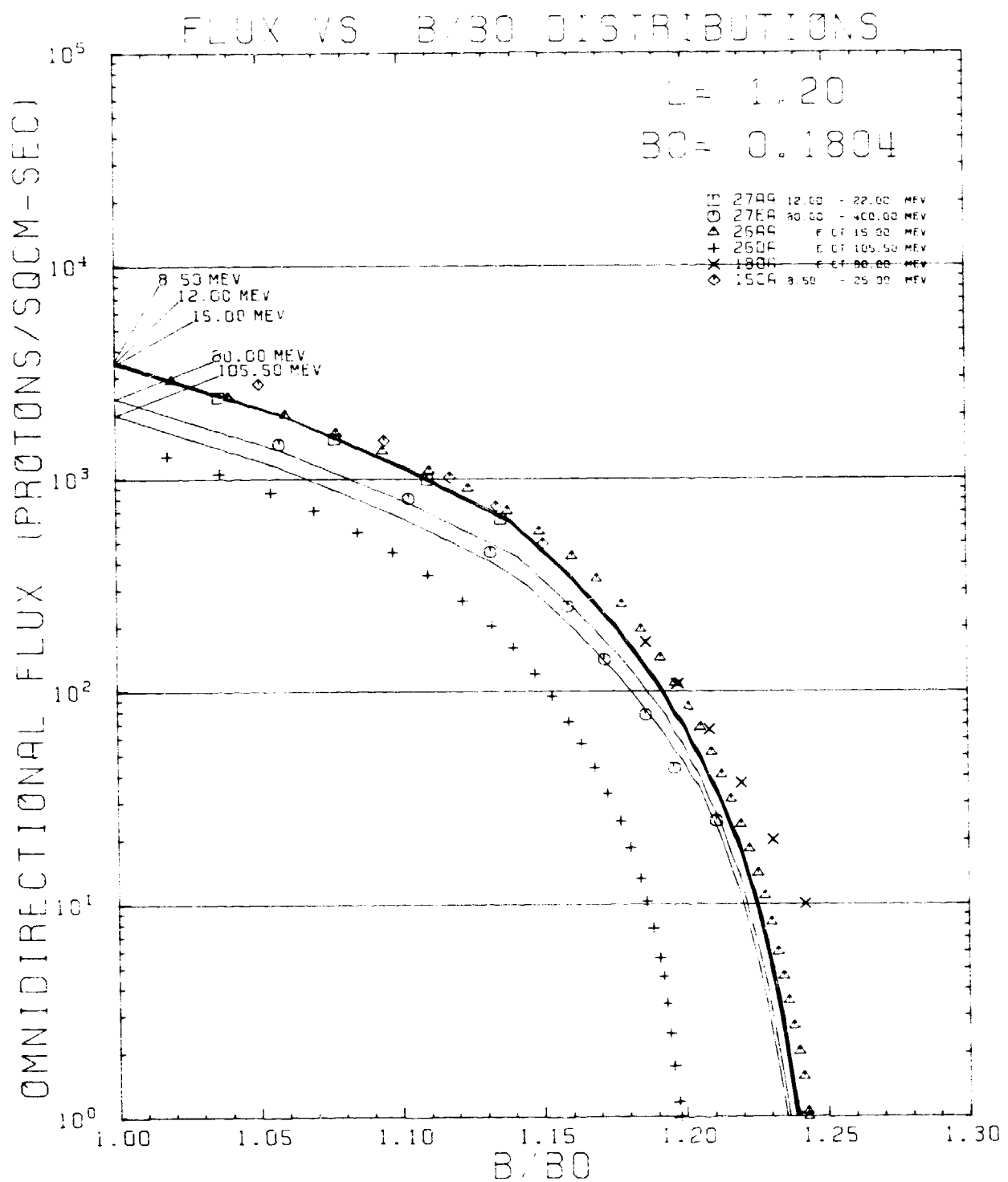


Figure 98. AP8MIN and Data Flux vs B/B_0 Comparison Plot for $L = 1.20 R_E$

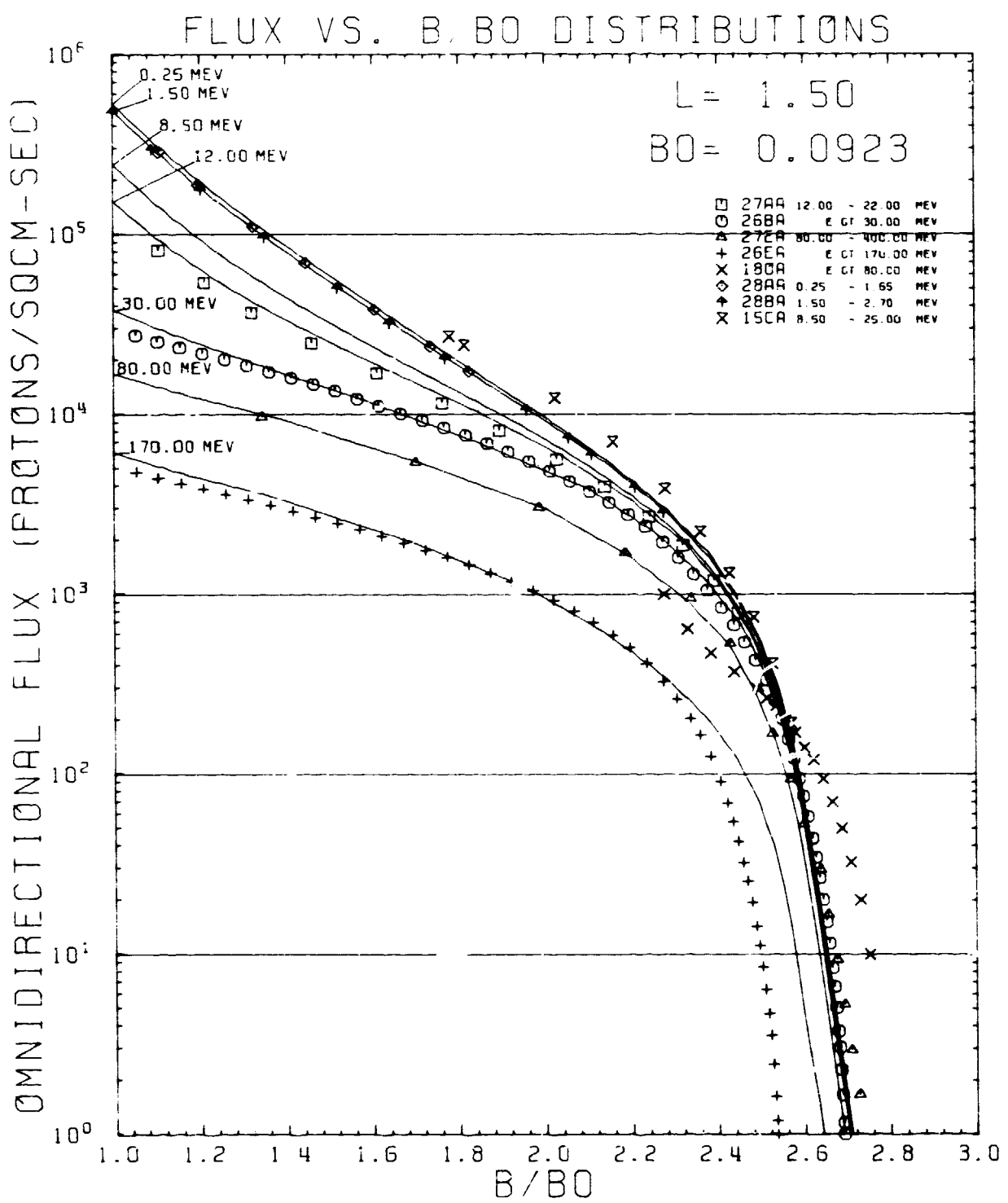


Figure 99. AP8MIN and Data Flux vs B/B_0 Comparison Plot for $L = 1.50 R_E$

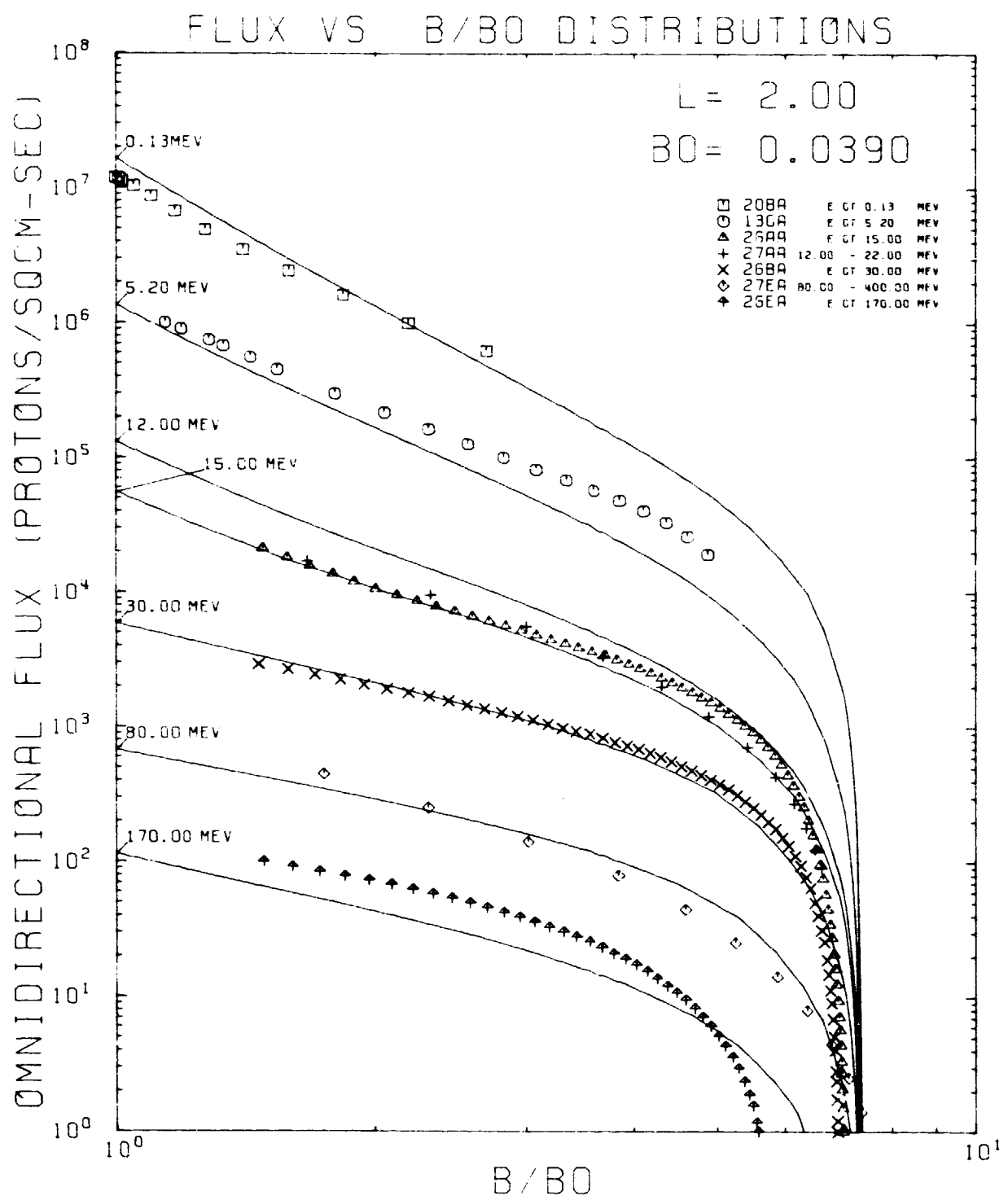


Figure 100. AP8MIN and Data Flux vs B/B_0 Comparison Plot for $L = 2.00 R_E$

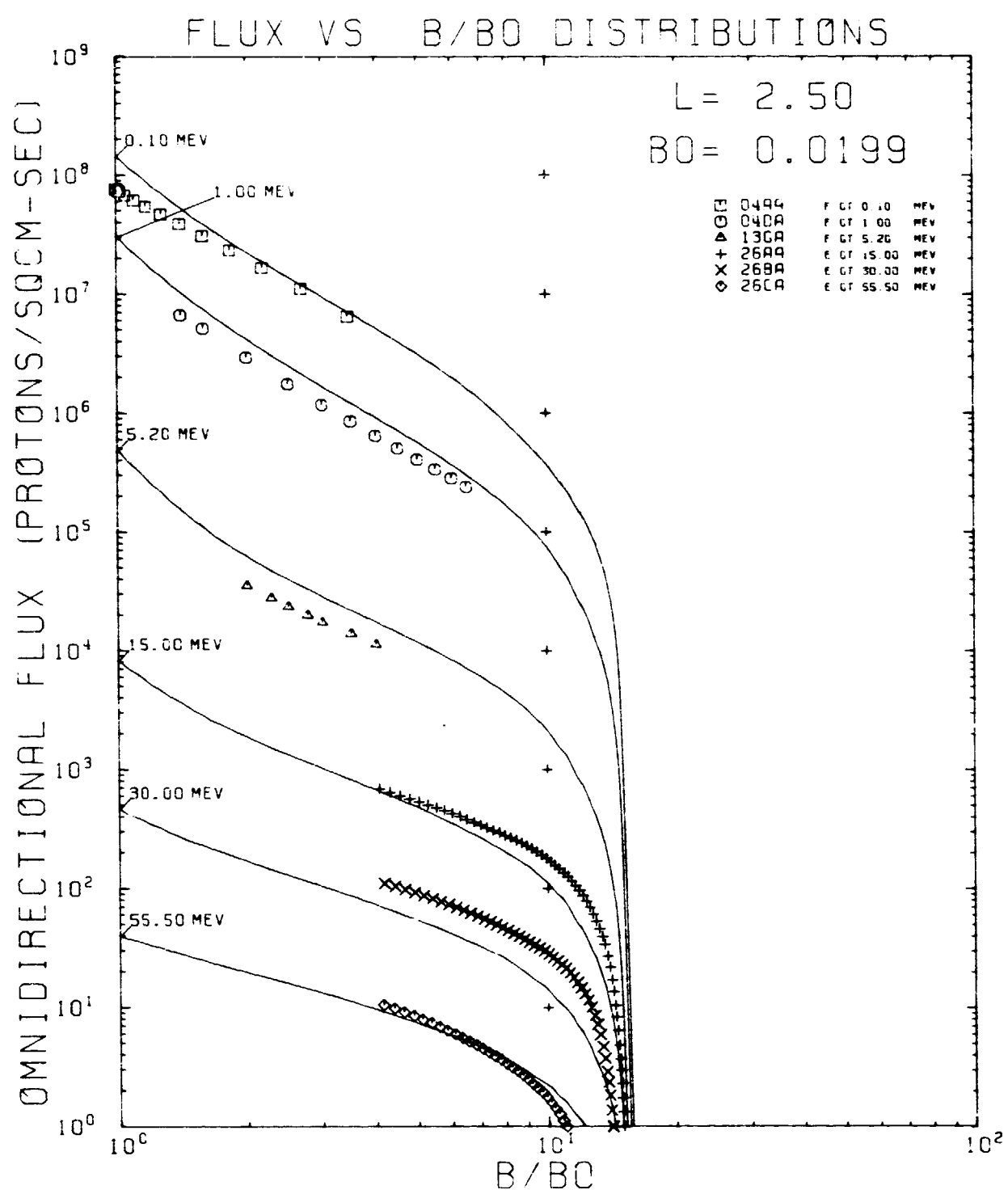


Figure 101. AP8MIN and Data Flux vs B/B_0 Comparison Plot for $L = 2.50$ RE

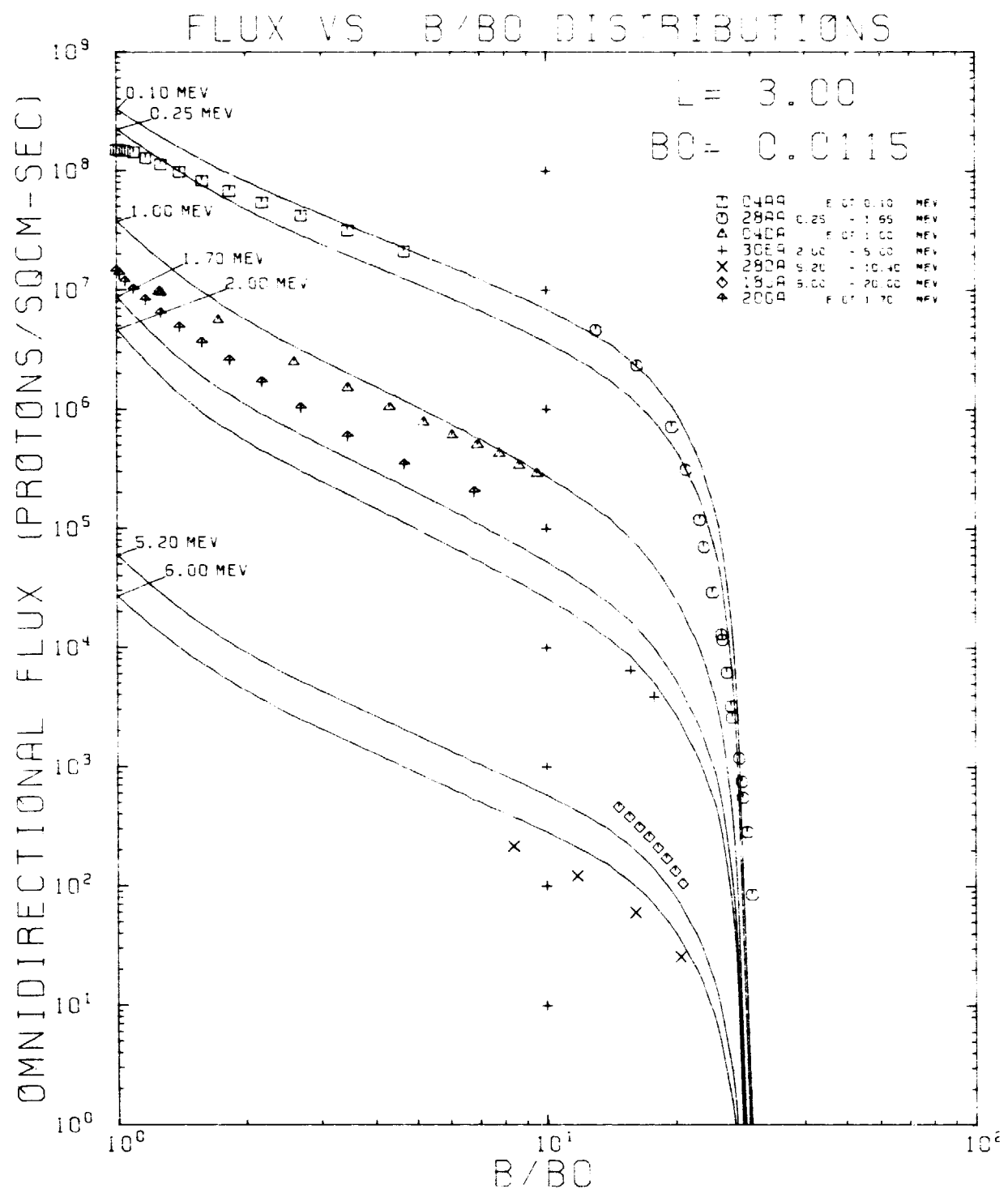


Figure 102. AP8MIN and Data Flux vs B/B₀ Comparison Plot for L = 3.00 RE

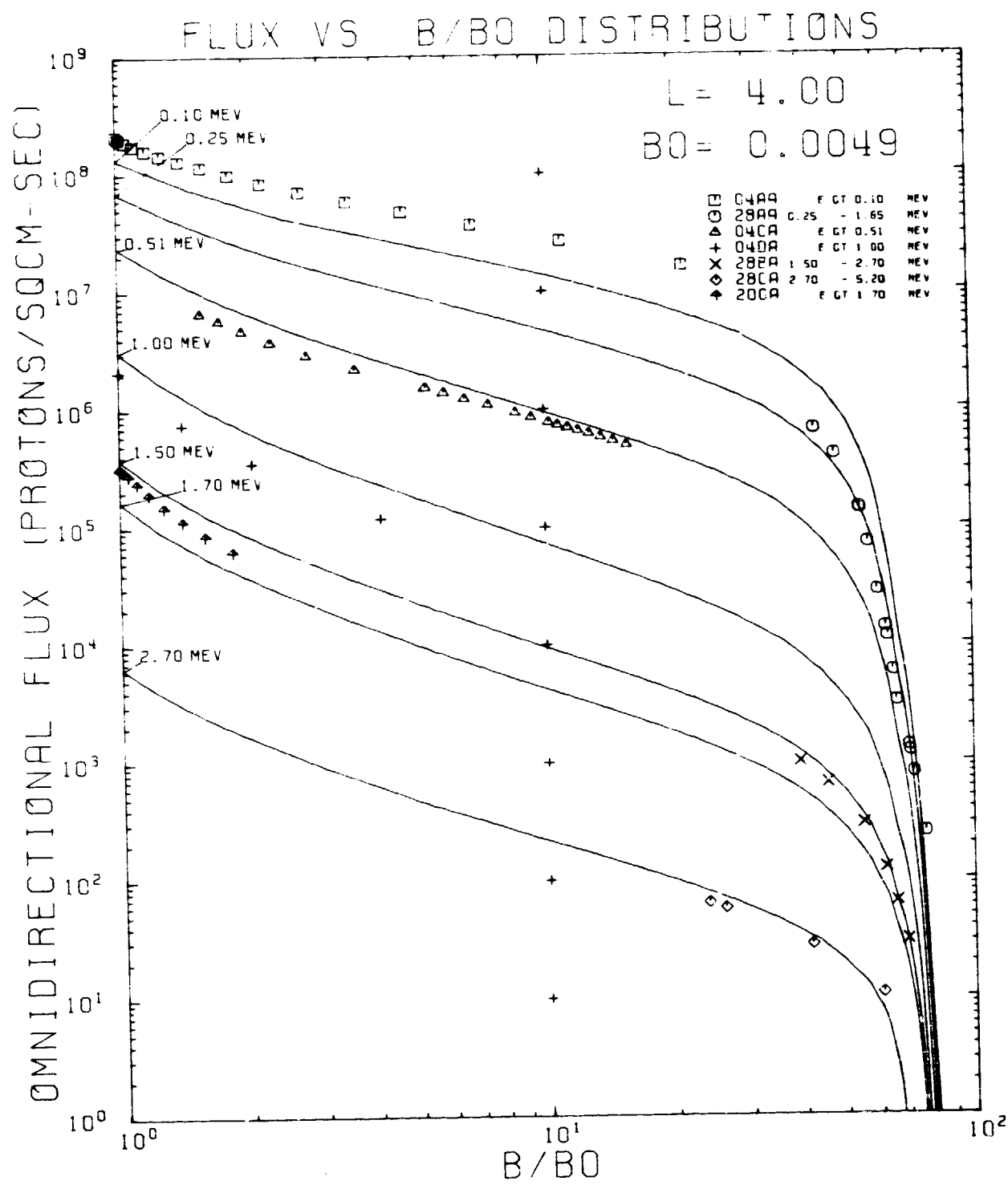


Figure 103. AP8MIN and Data Flux vs B/B_0 Comparison Plot for $L = 4.00 R_E$

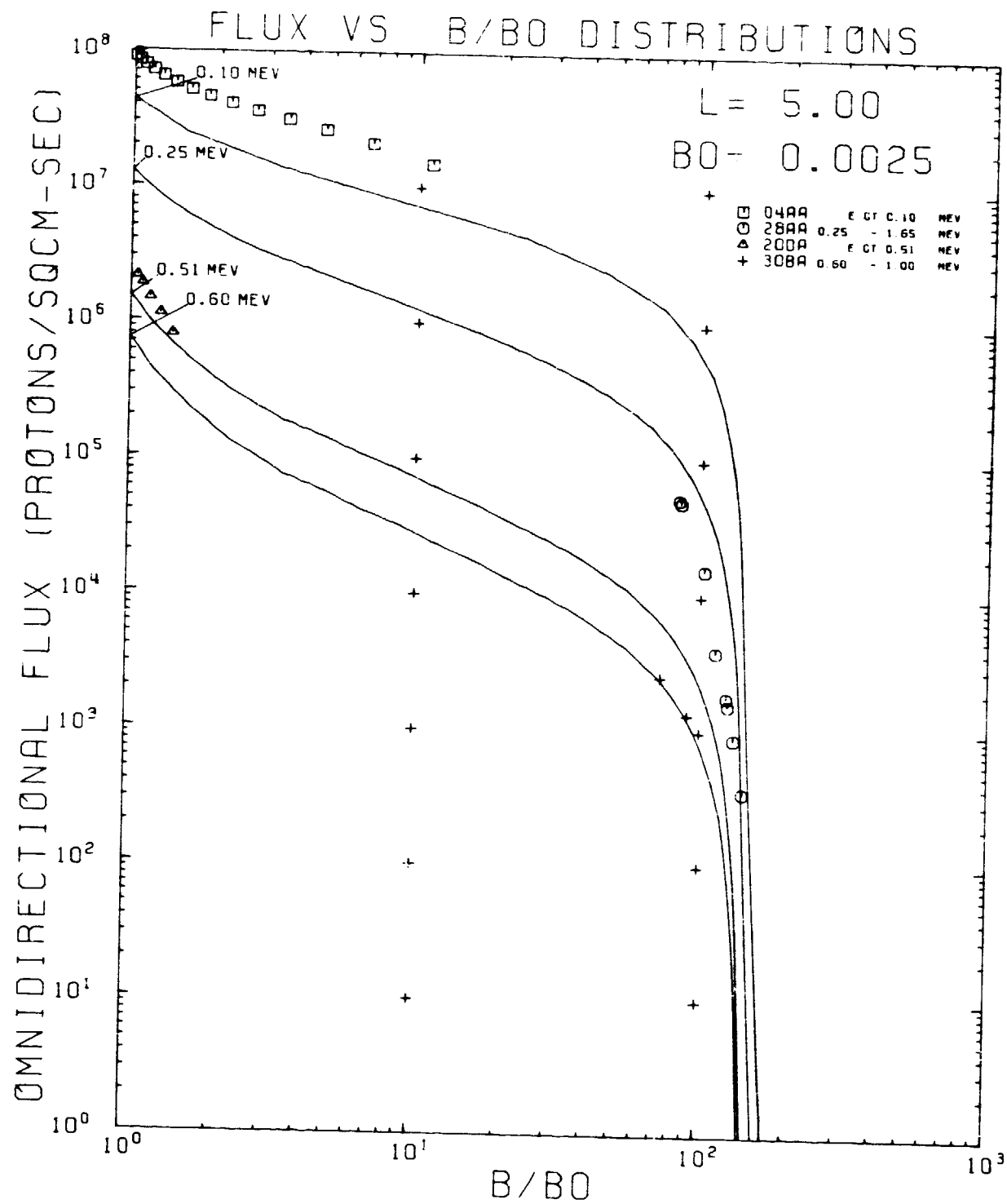


Figure 104. AP8MIN and Data Flux vs B/B_0 Comparison Plot for $L = 5.00$ RE

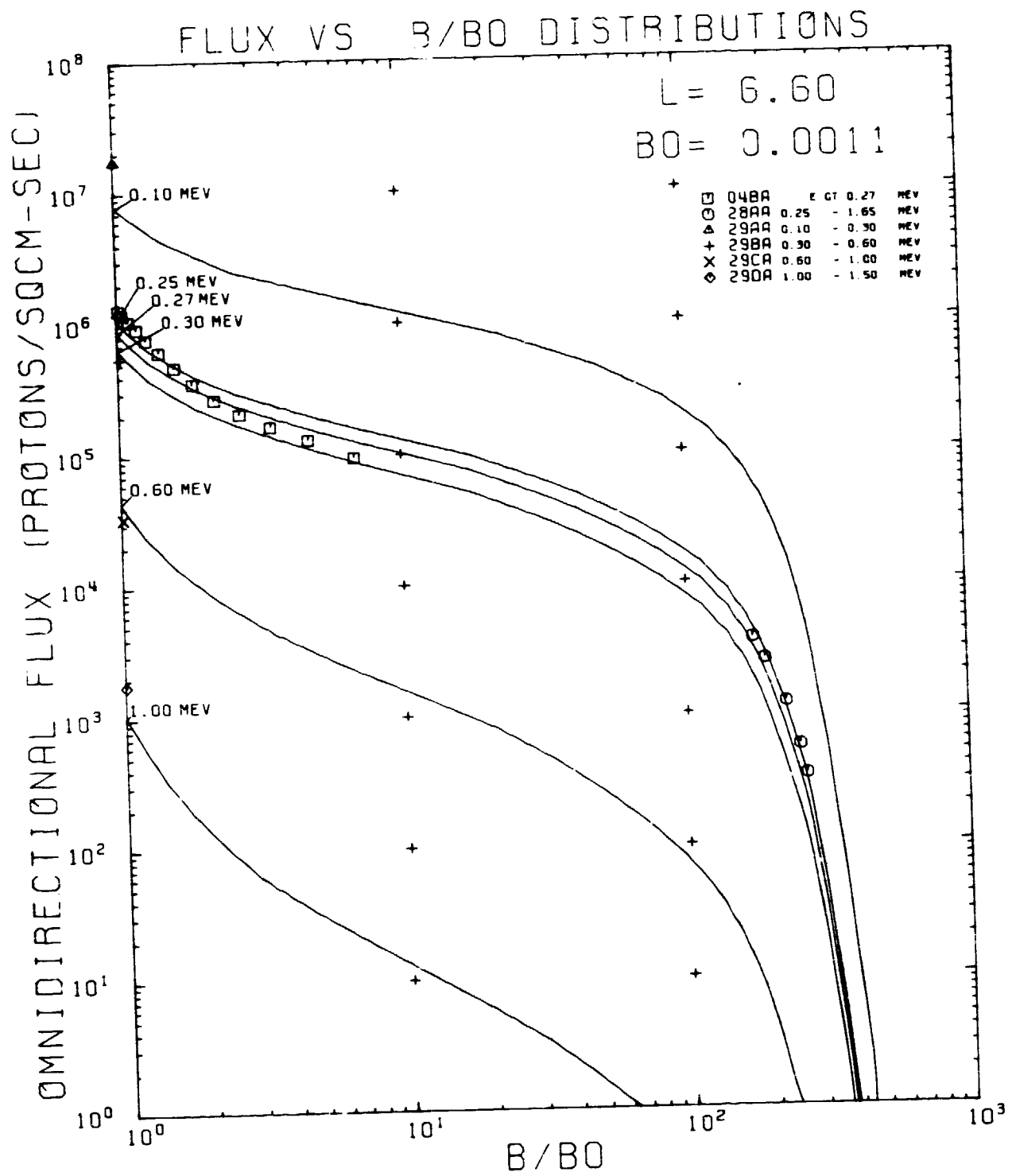


Figure 105. AP8MIN and Data Flux vs B/B_0 Comparison Plot for $L = 6.60$ RE

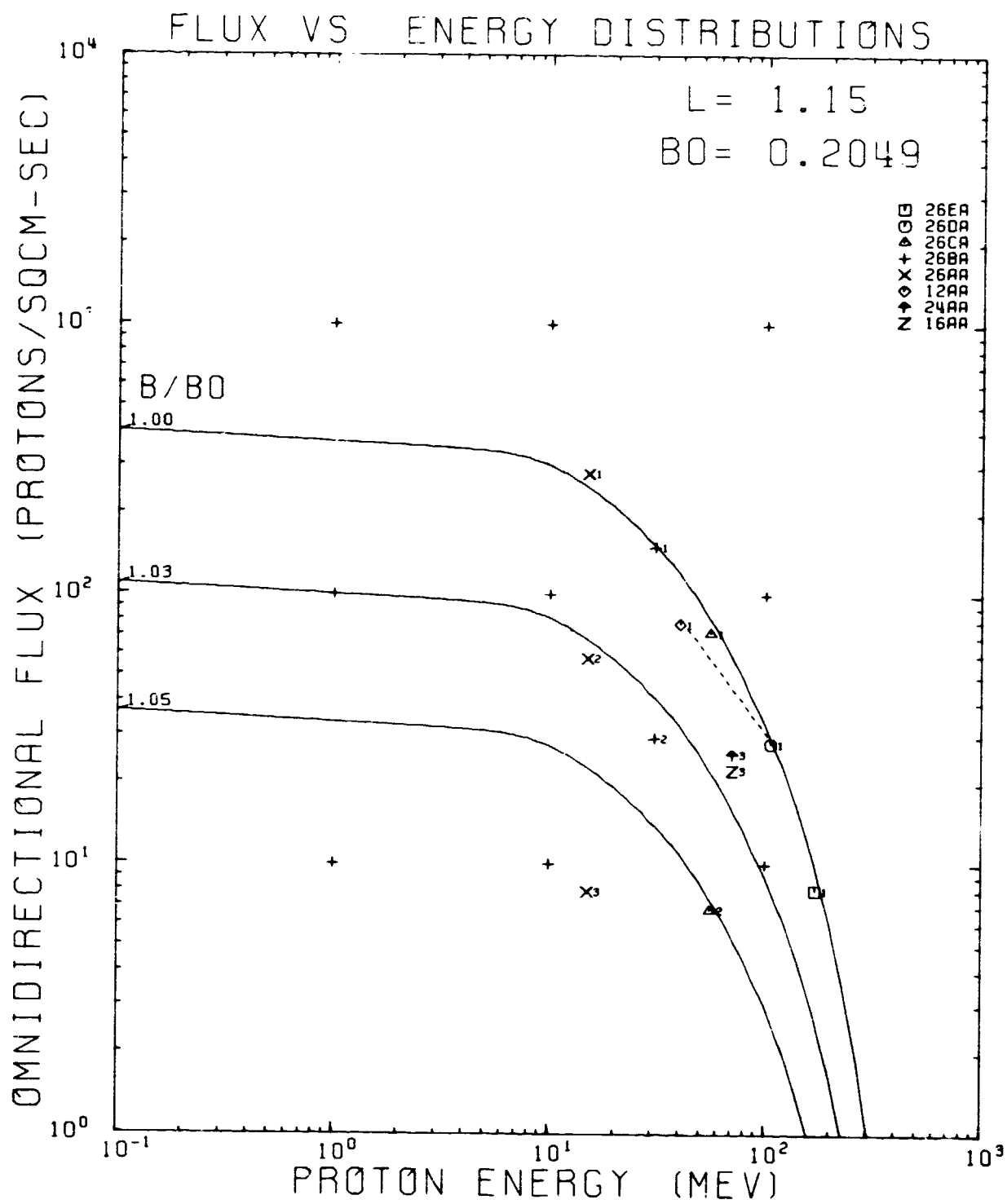


Figure 106. AP8MIN and Data Flux vs Energy Comparison Plot for $L = 1.15 R_E$

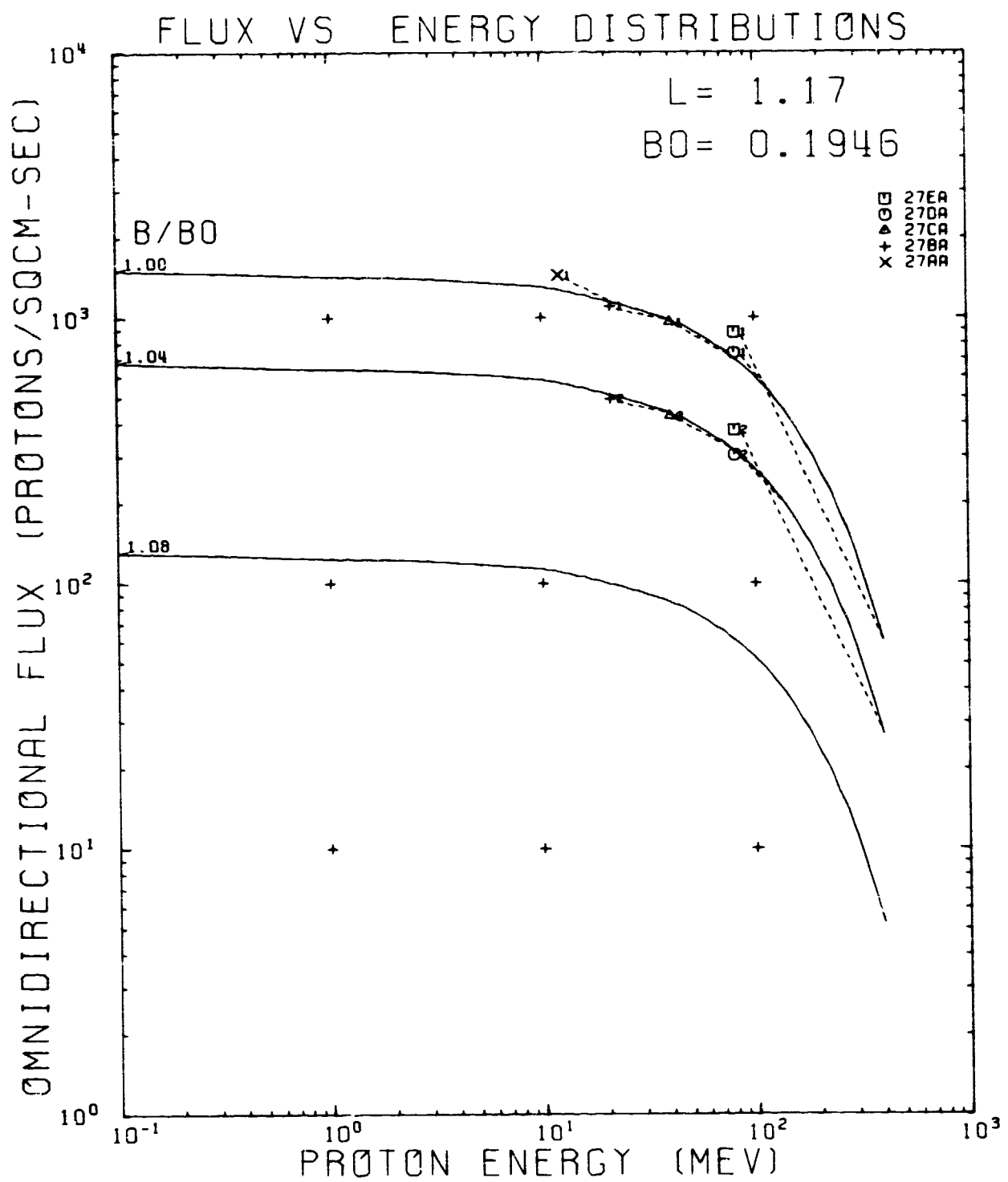


Figure 107. AP8MIN and Data Flux vs Energy Comparison Plot for $L = 1.17 R_E$

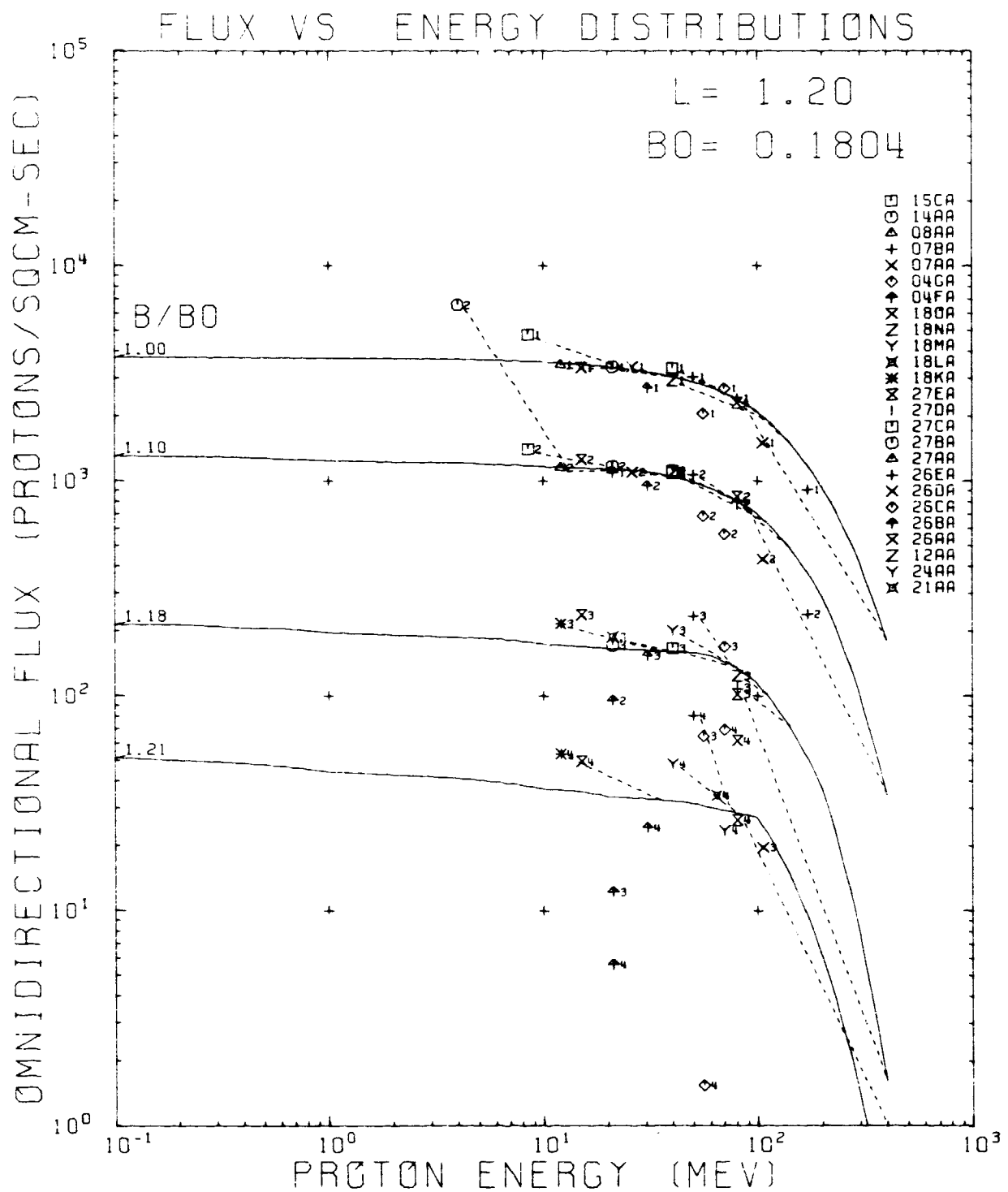


Figure 108. AP8MIN and Data Flux vs Energy Comparison Plot for $L = 1.20 R_E$

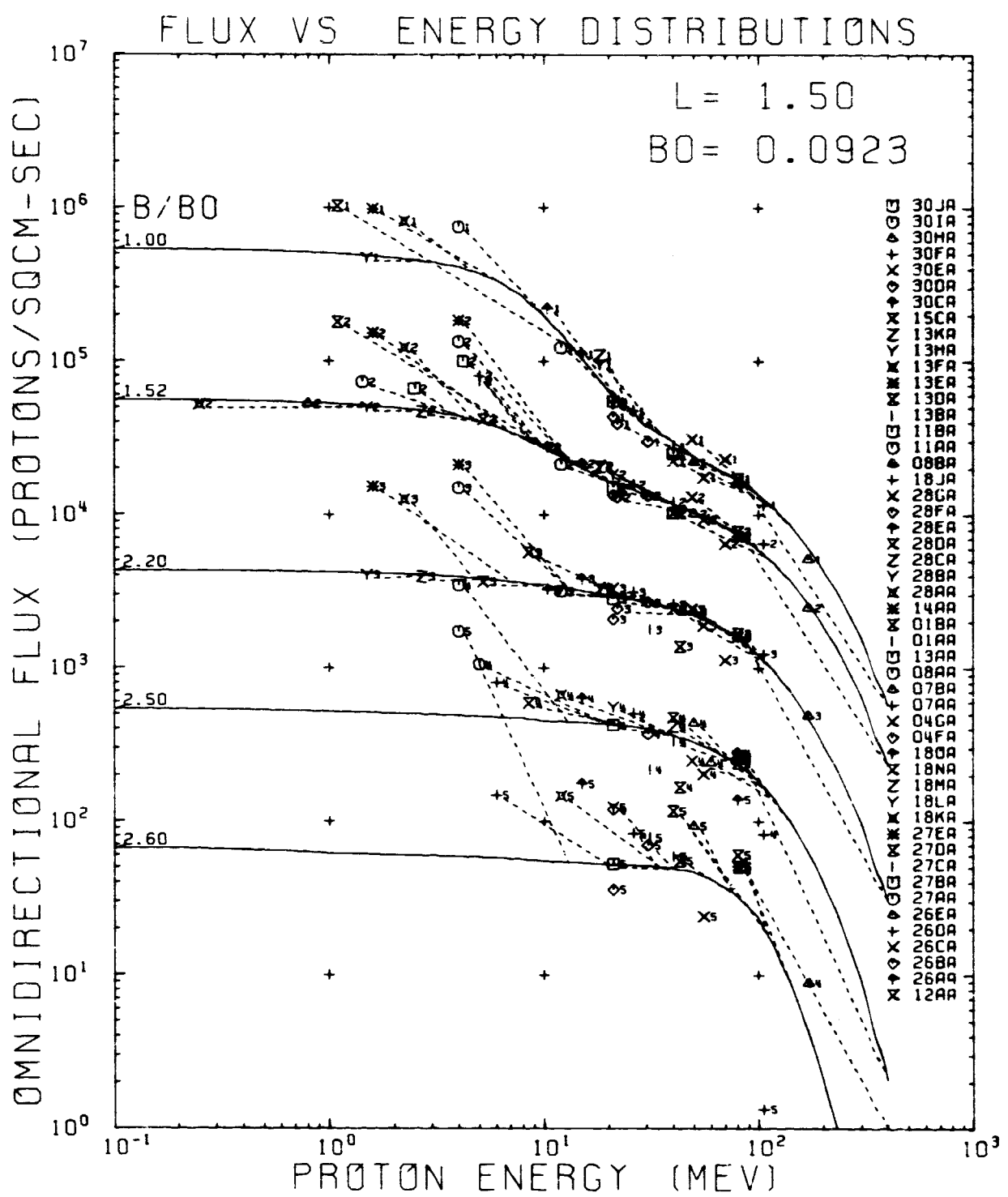


Figure 109. AP8MIN and Data Flux vs Energy Comparison Plot for $L = 1.50 R_E$

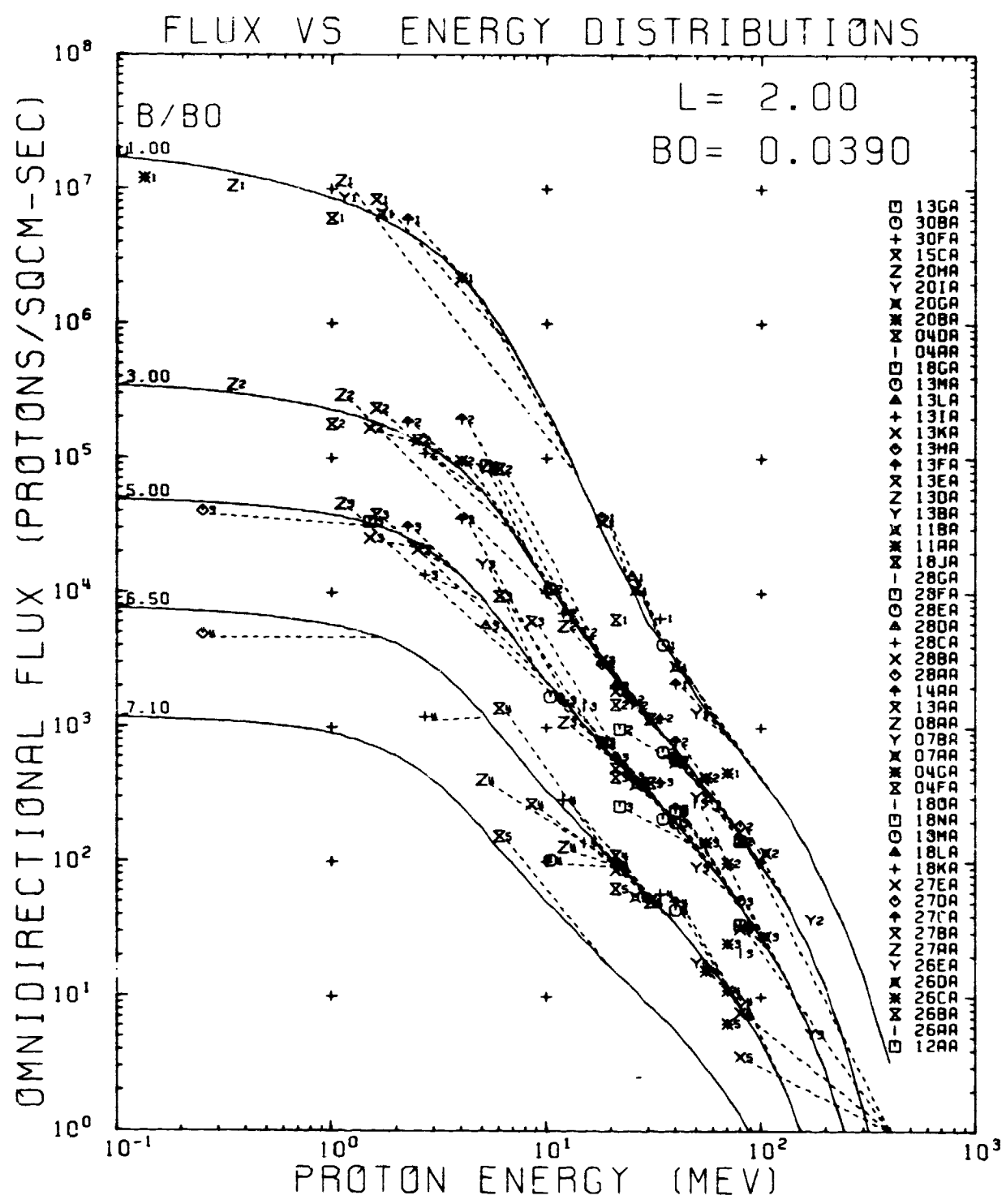


Figure 110. AP8MIN and Data Flux vs Energy Comparison Plot for $L = 2.00 R_E$

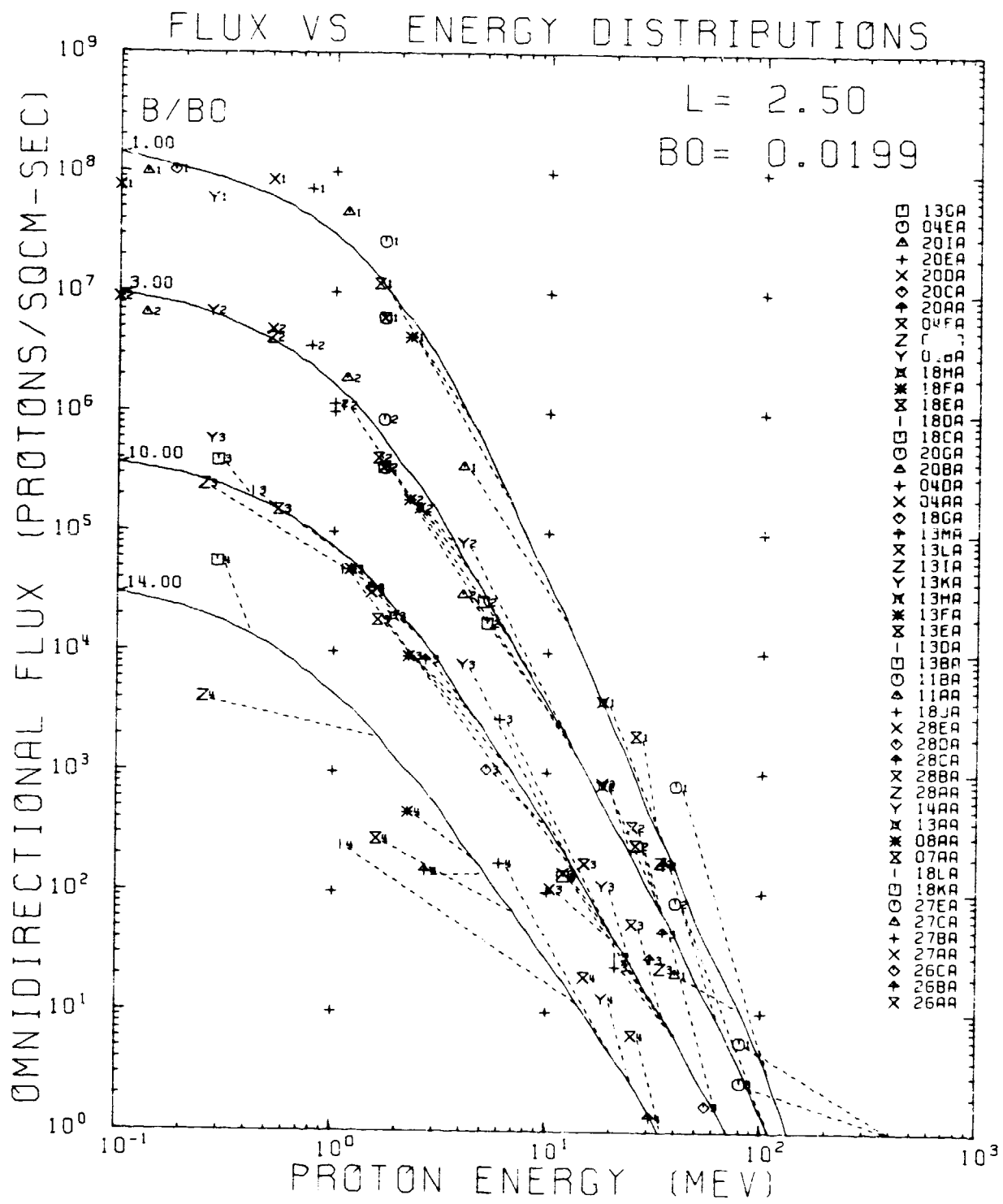


Figure 111. AP8MIN and Data Flux vs Energy Comparison Plot for $L = 2.50 R_E$

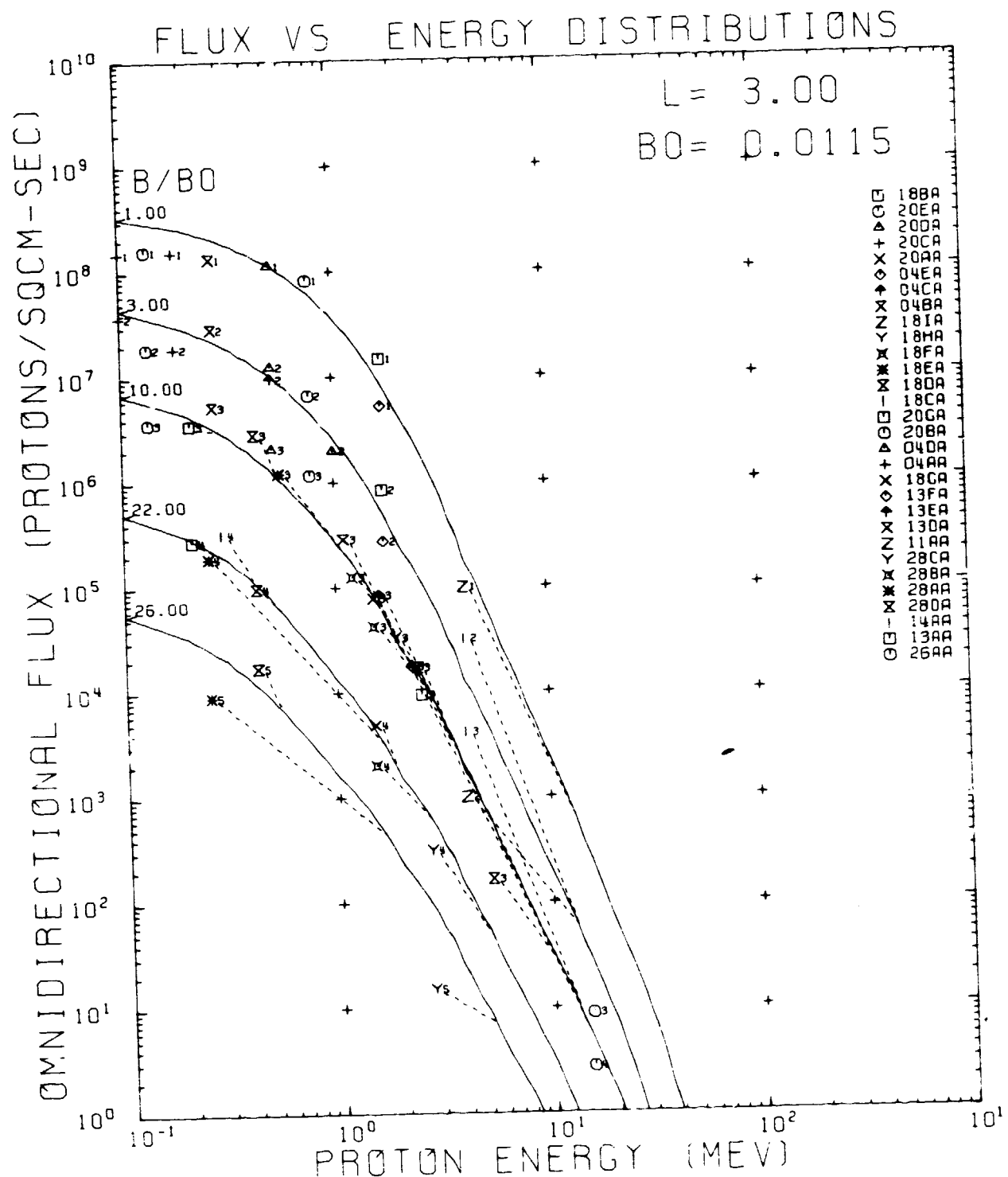


Figure 112. AP8MIN and Data Flux vs Energy Comparison Plot for $L = 3.00 R_E$

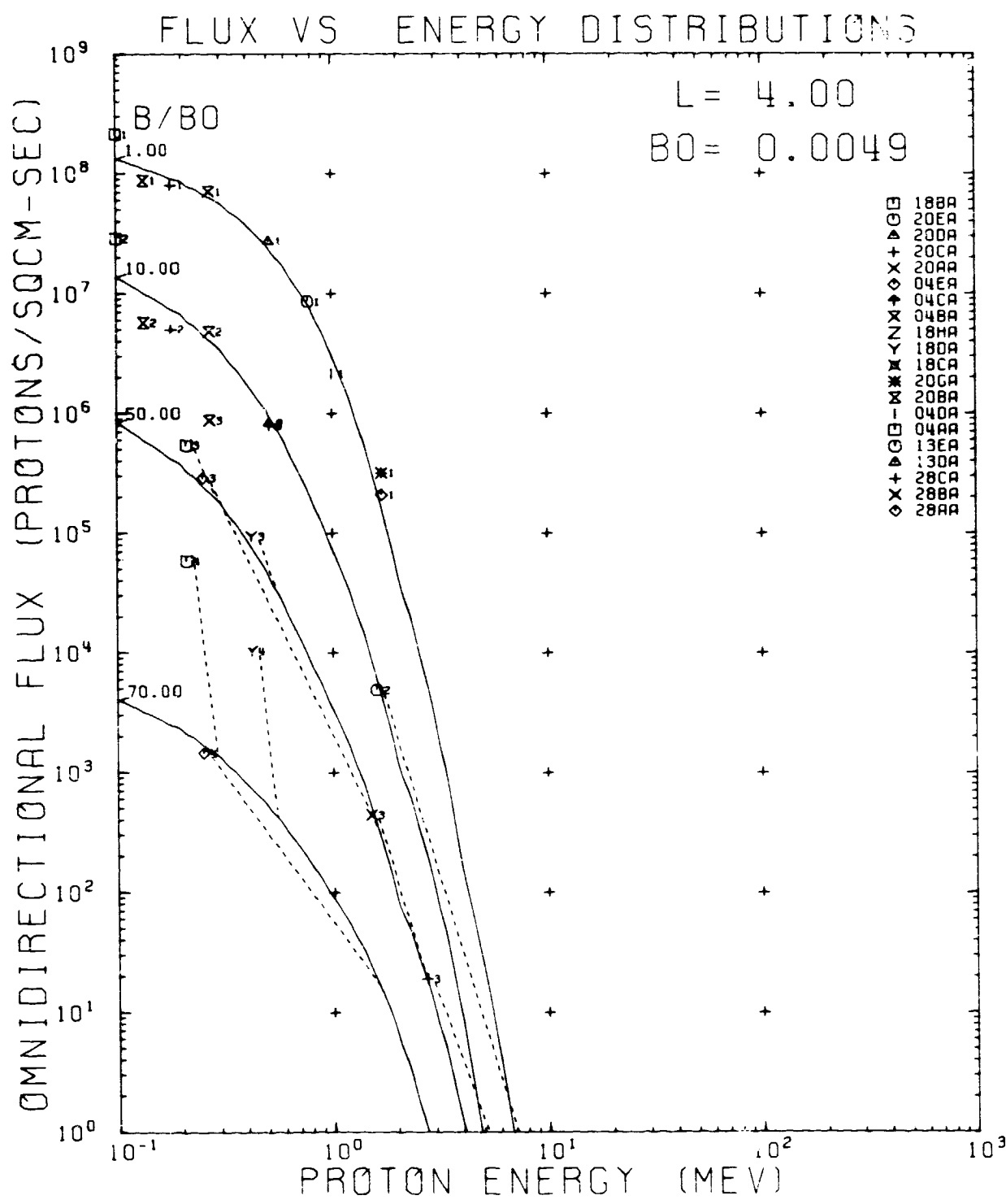


Figure 113. AP8MIN and Data Flux vs Energy Comparison Plot for $L = 4.00$ RE

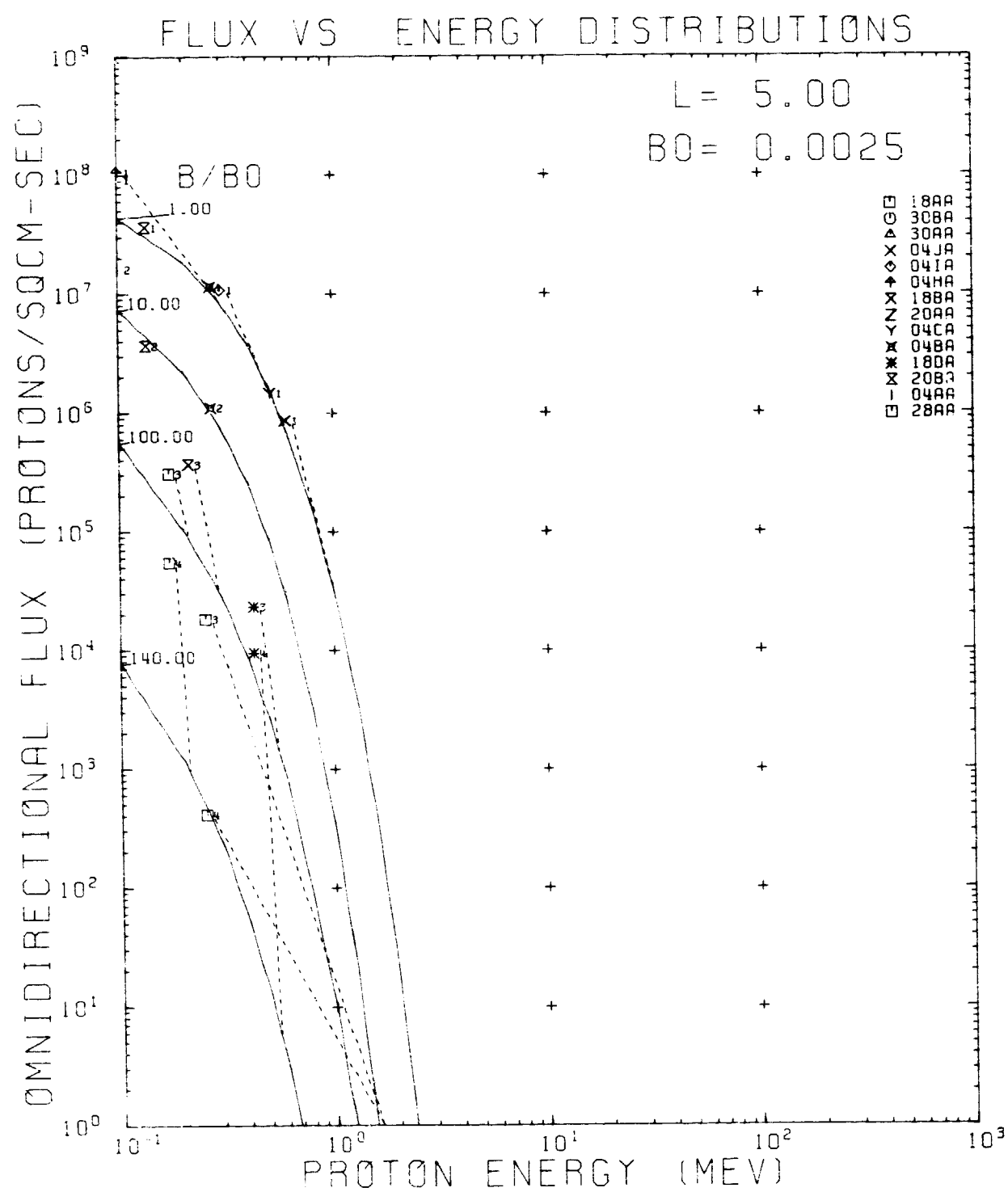


Figure 114. AP8MIN and Data Flux vs Energy Comparison Plot for $L = 5.00 R_E$

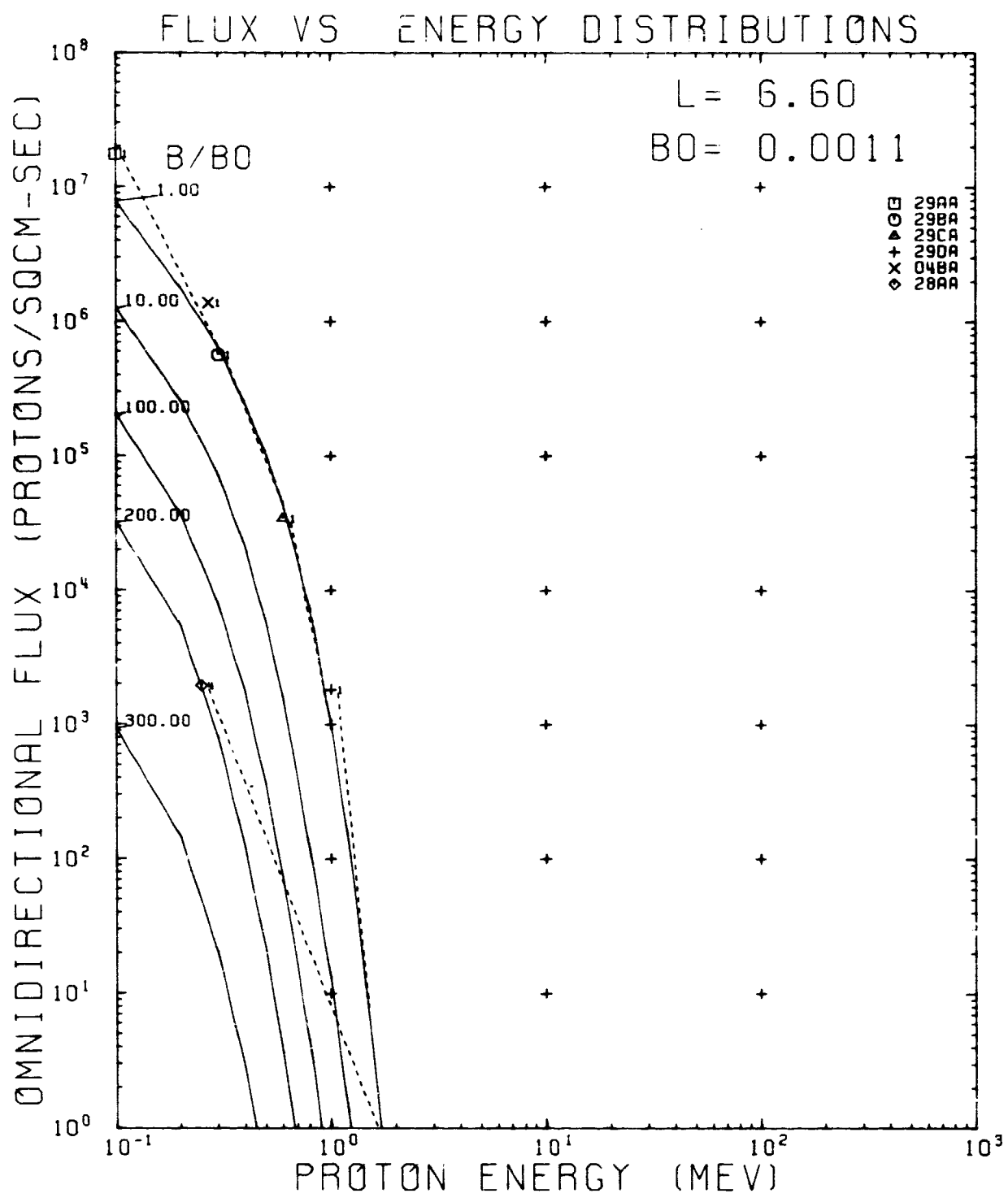


Figure 115. AP8MIN and Data Flux vs Energy Comparison Plot for $L = 6.60 R_E$

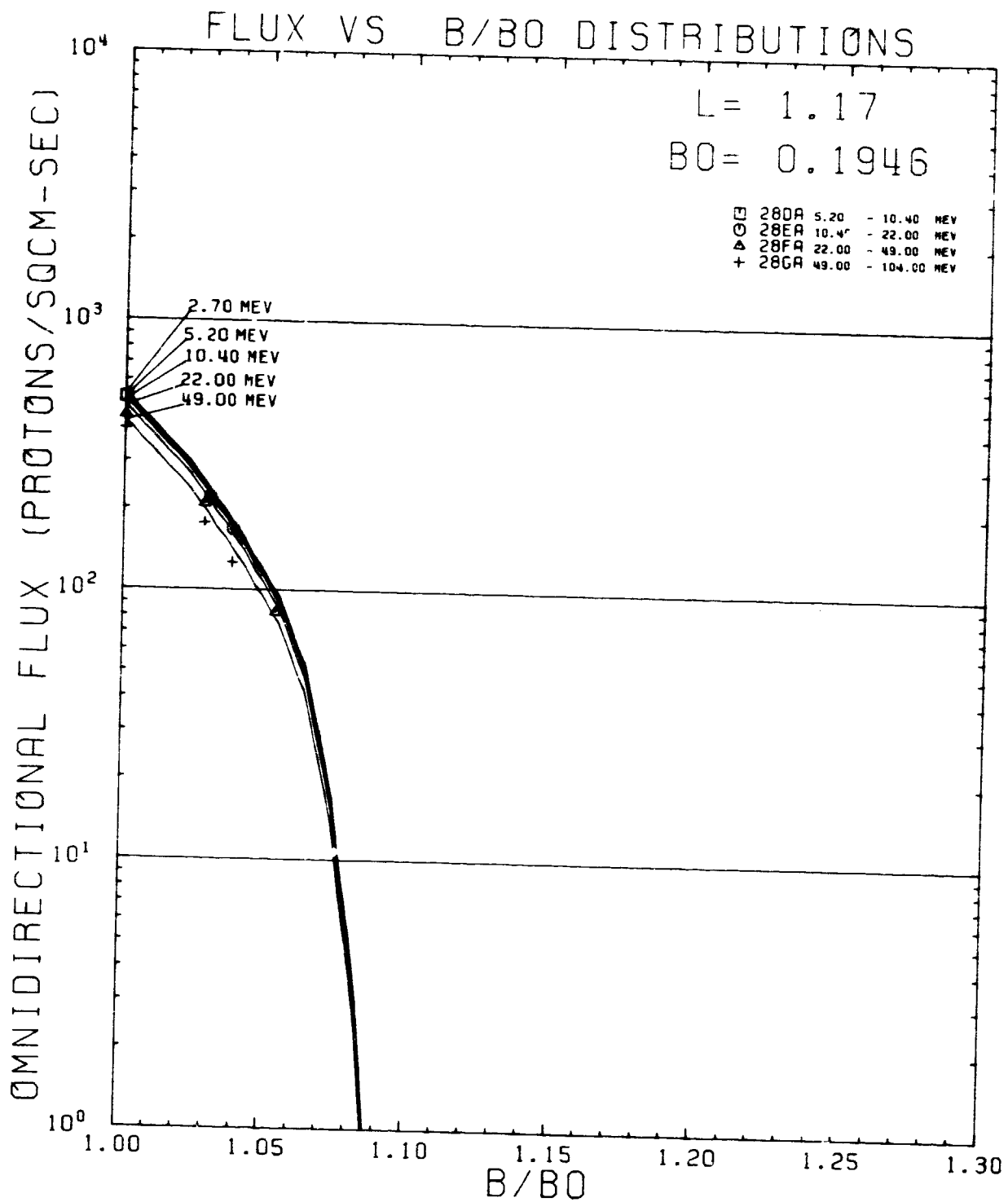


Figure 116. AP8MAX and Data Flux vs B/B_0 Comparison Plot for $L = 1.17 R_E$

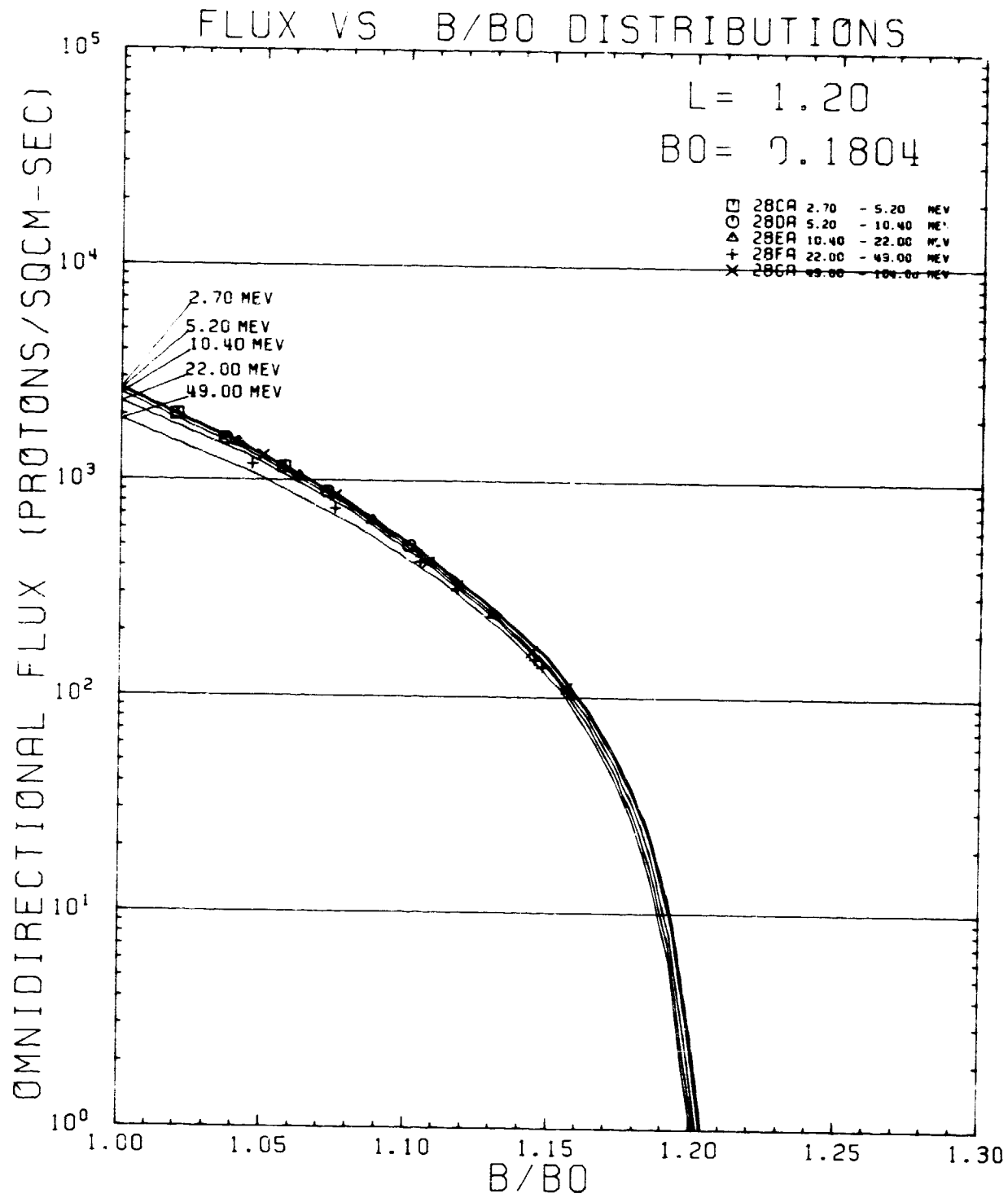


Figure 117. AP8MAX and Data Flux vs B/B_0 Comparison Plot for $L = 1.20 R_E$

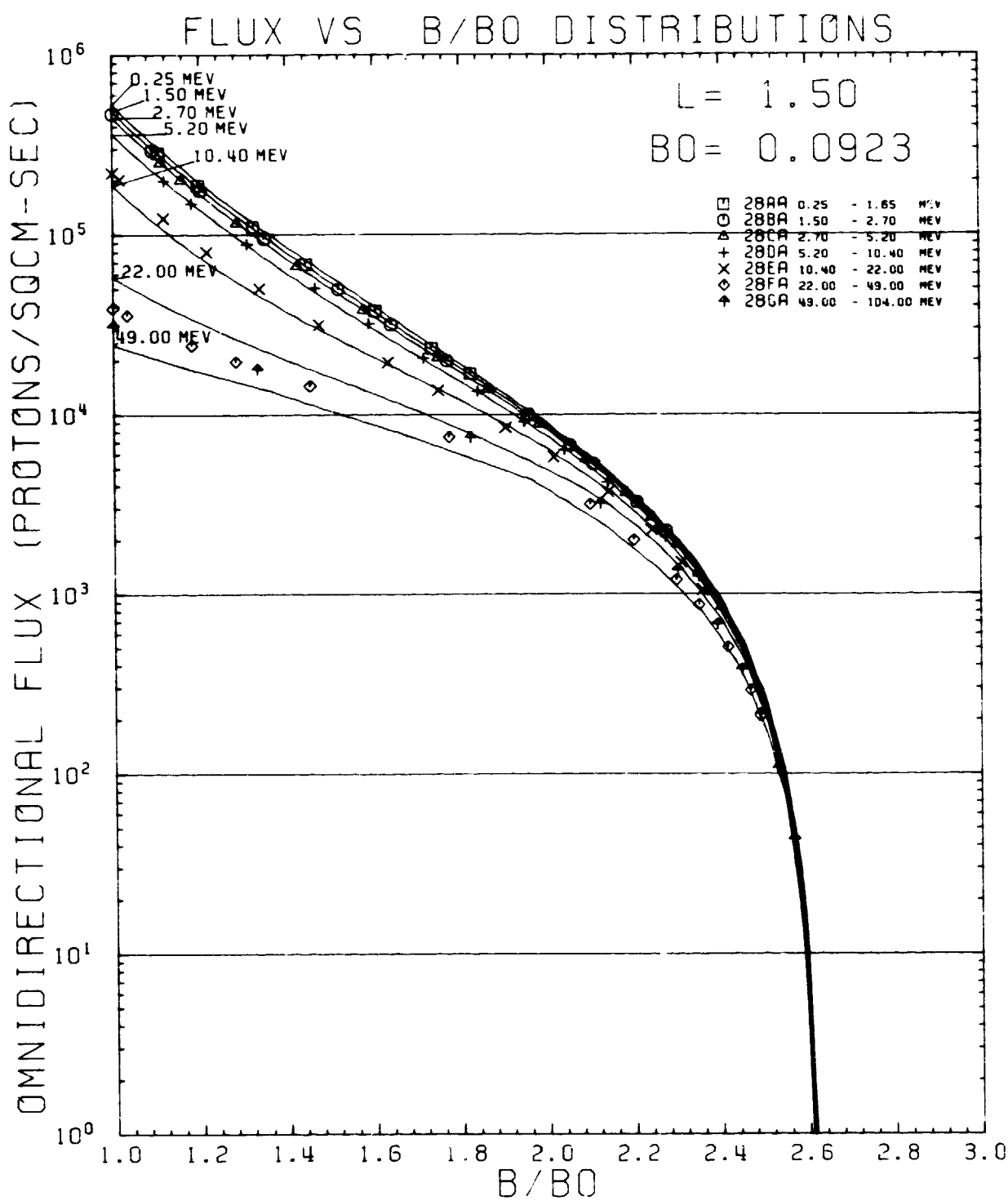


Figure 118. AP8MAX and Data Flux vs B/B_0 Comparison Plot for $L = 1.50 R_E$

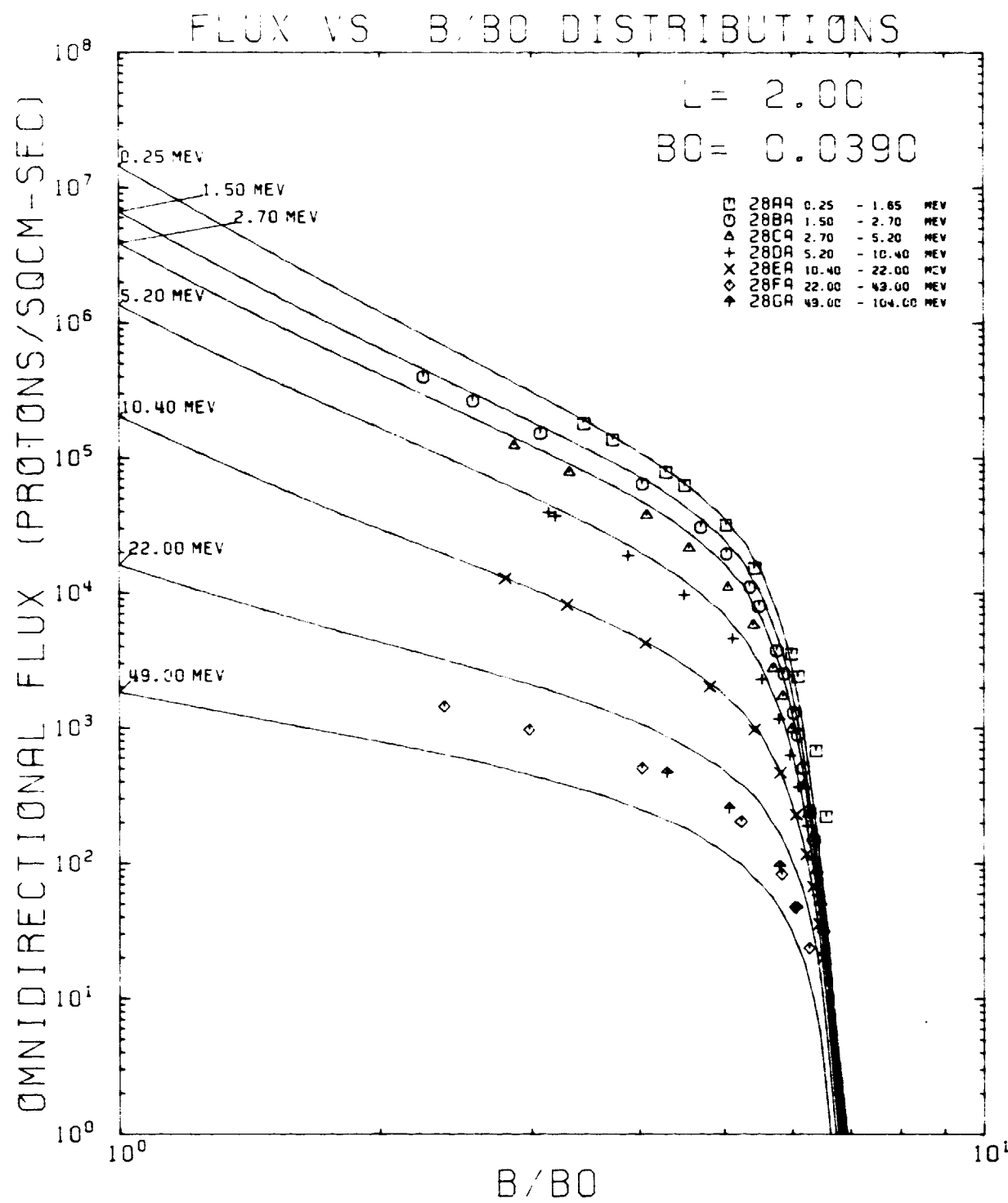


Figure 119. AP8MAX and Data Flux vs B/B_0 Comparison Plot for $L = 2.00$ RE

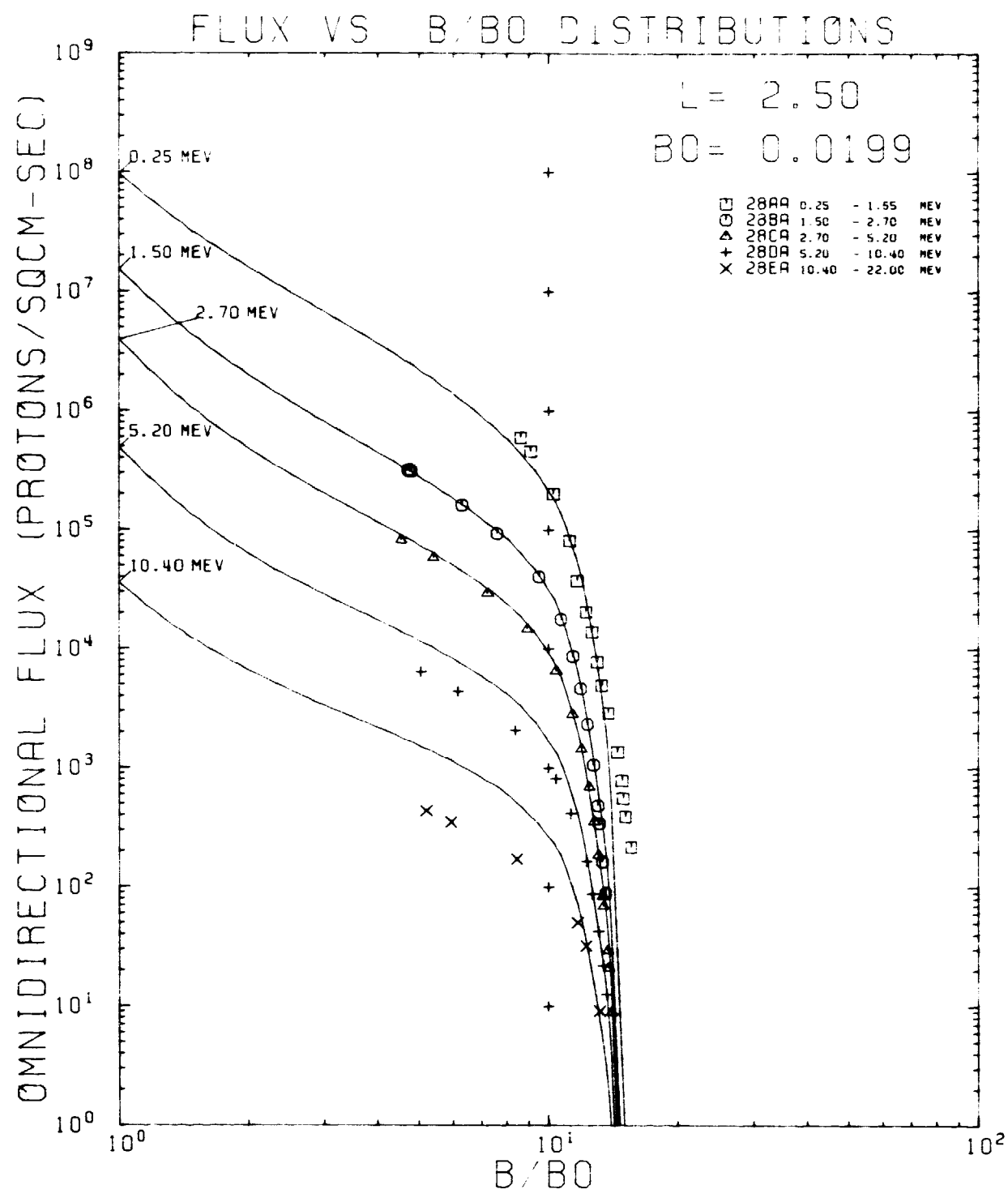


Figure 120. AP8MAX and Data Flux vs B/B_0 Comparison Plot for $L = 2.50 R_E$

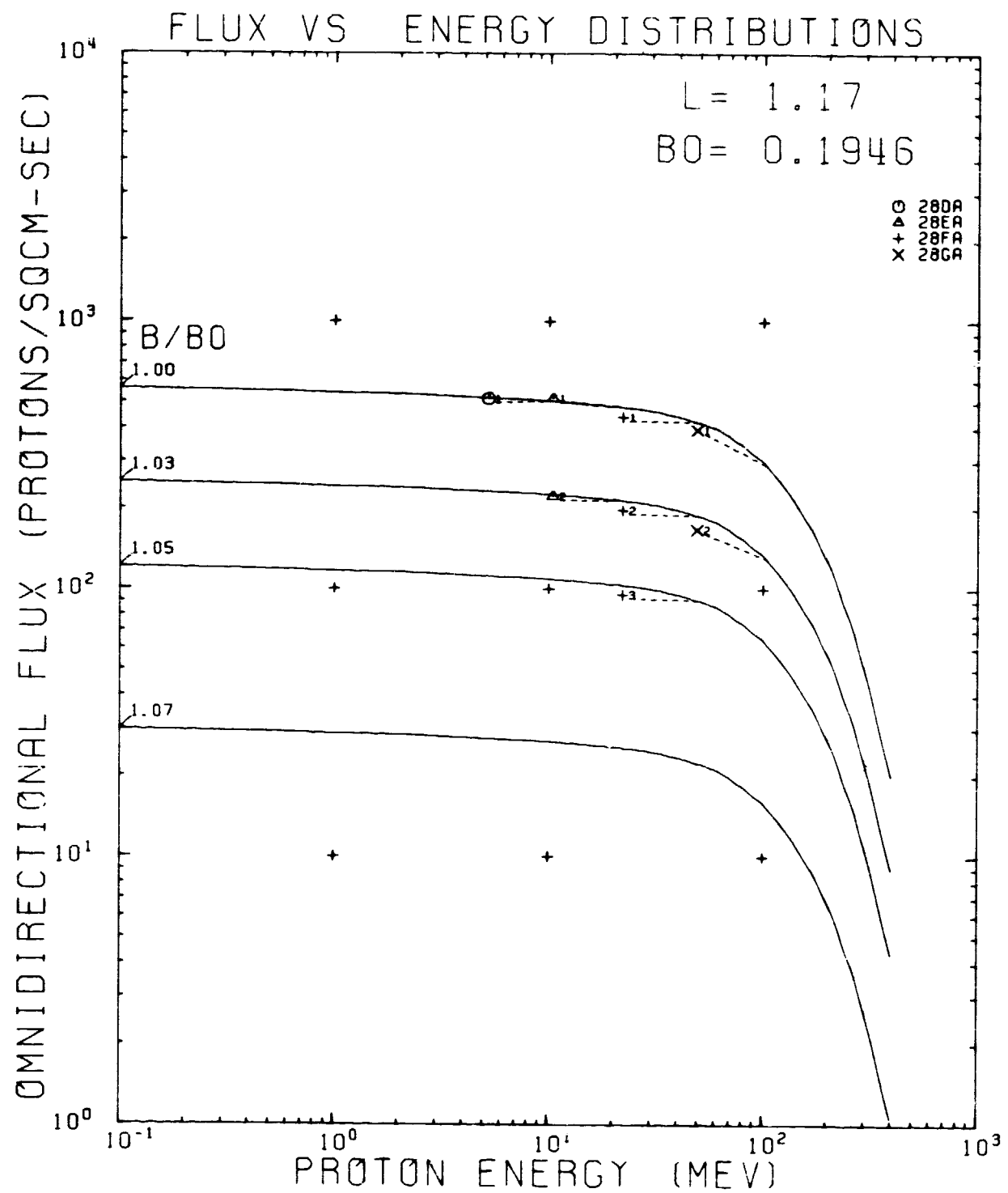


Figure 121. AP8MAX and Data Flux vs Energy Comparison Plot for $L = 1.17 R_E$

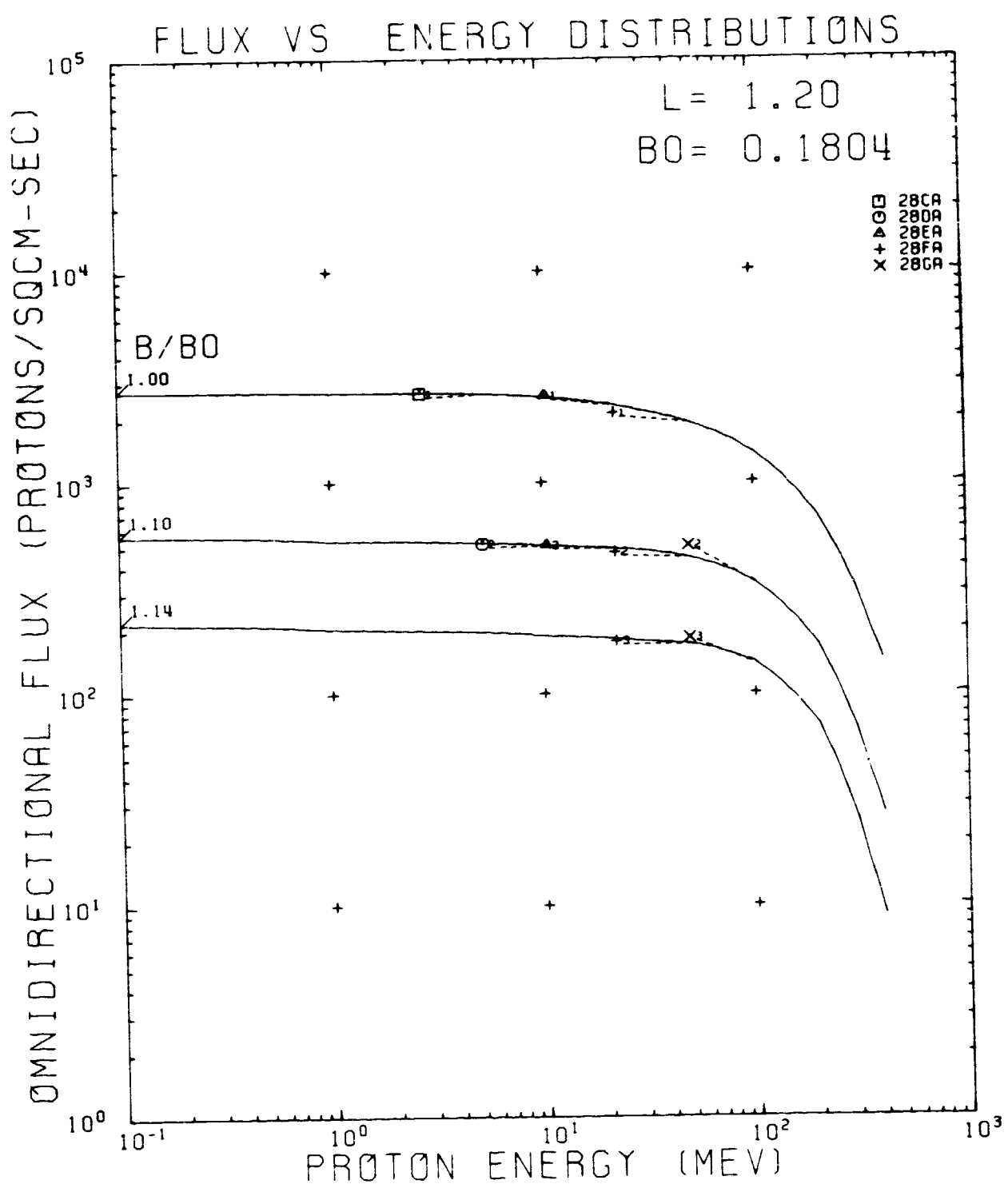


Figure 122. AP8MAX and Data Flux vs Energy Comparison Plot for $L = 1.20 R_E$

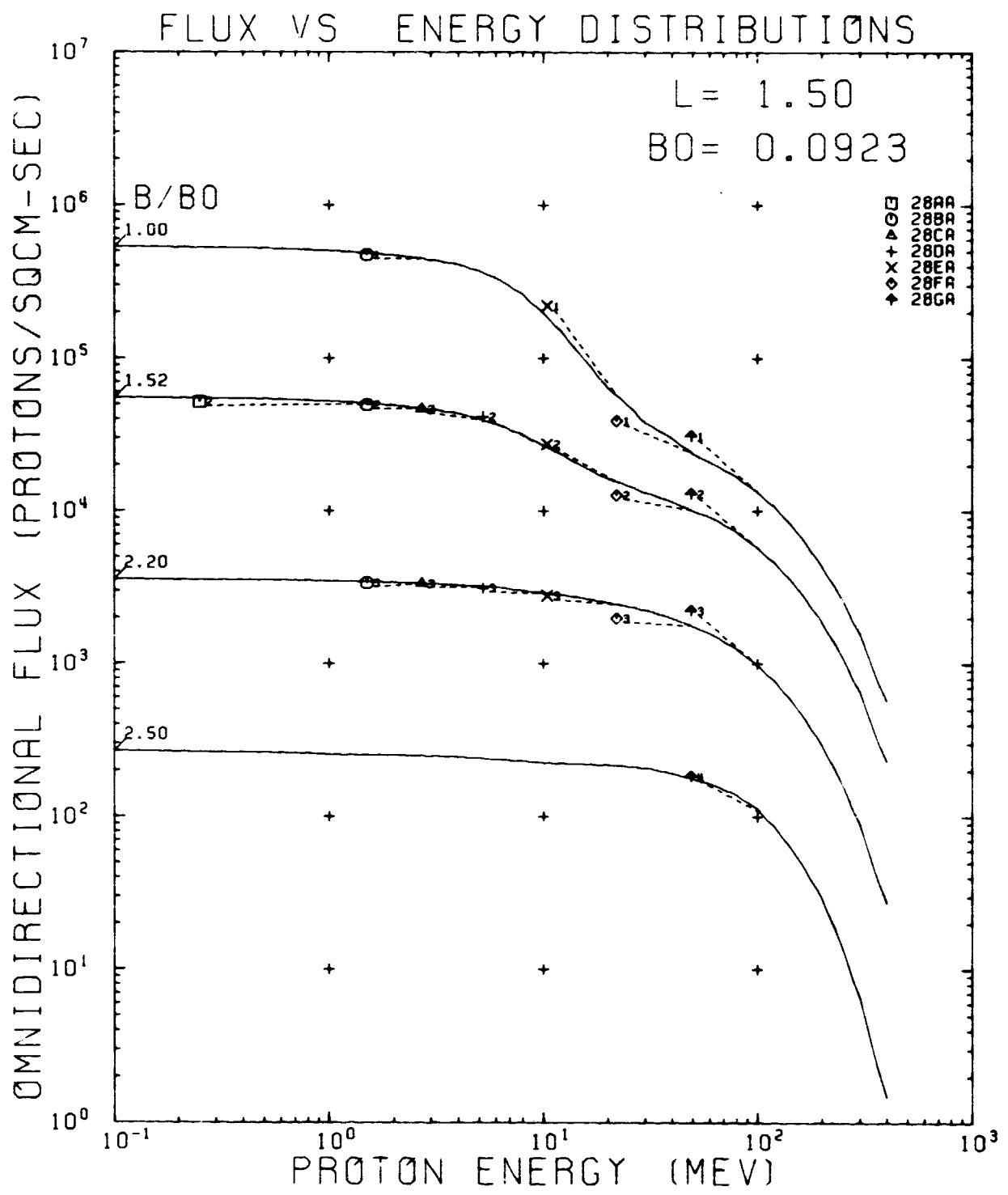


Figure 123. AP8MAX and Data Flux vs Energy Comparison Plot for $L = 1.50 R_E$

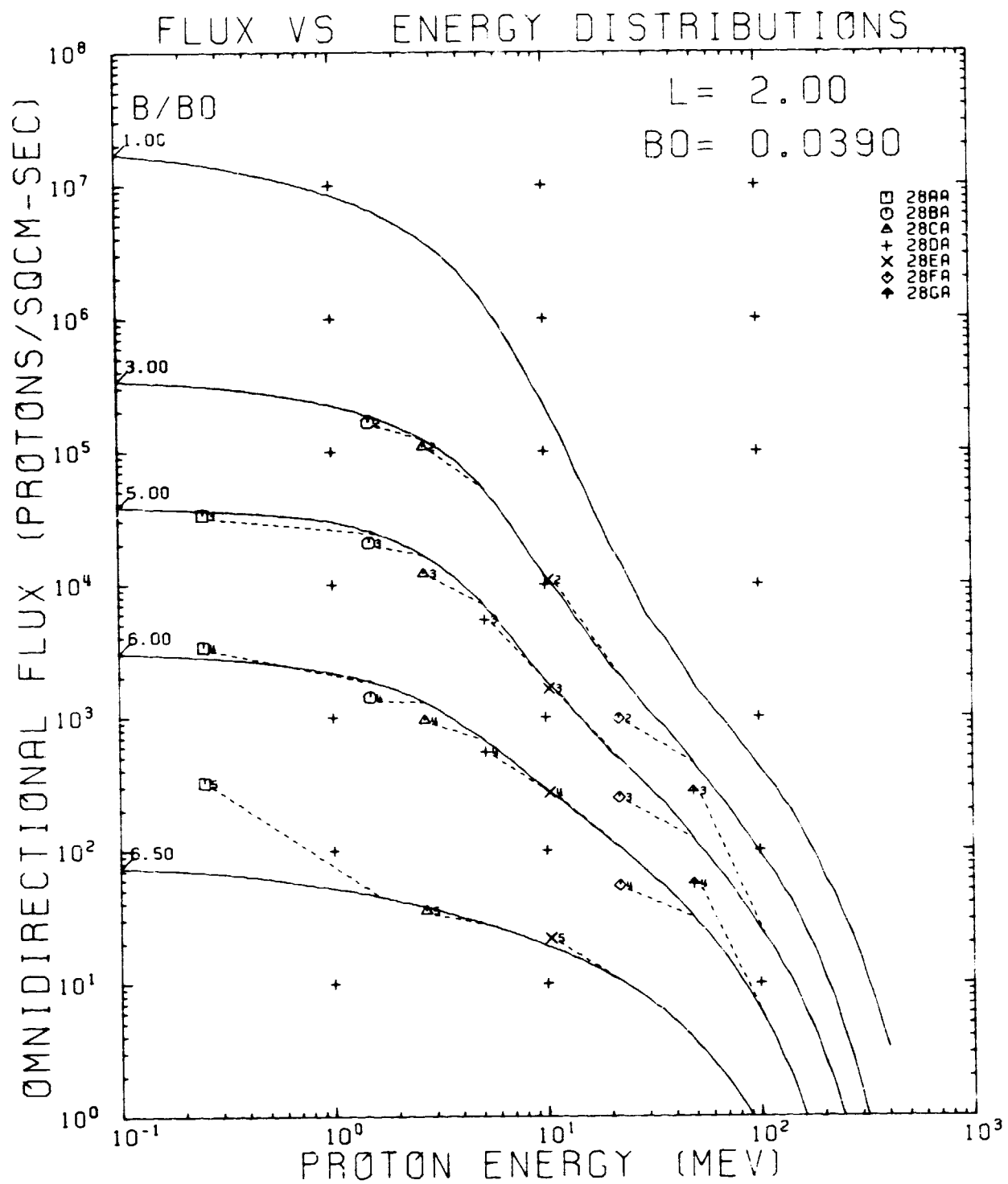


Figure 124. AP8MAX and Data Flux vs Energy Comparison Plot for $L = 2.00 R_E$

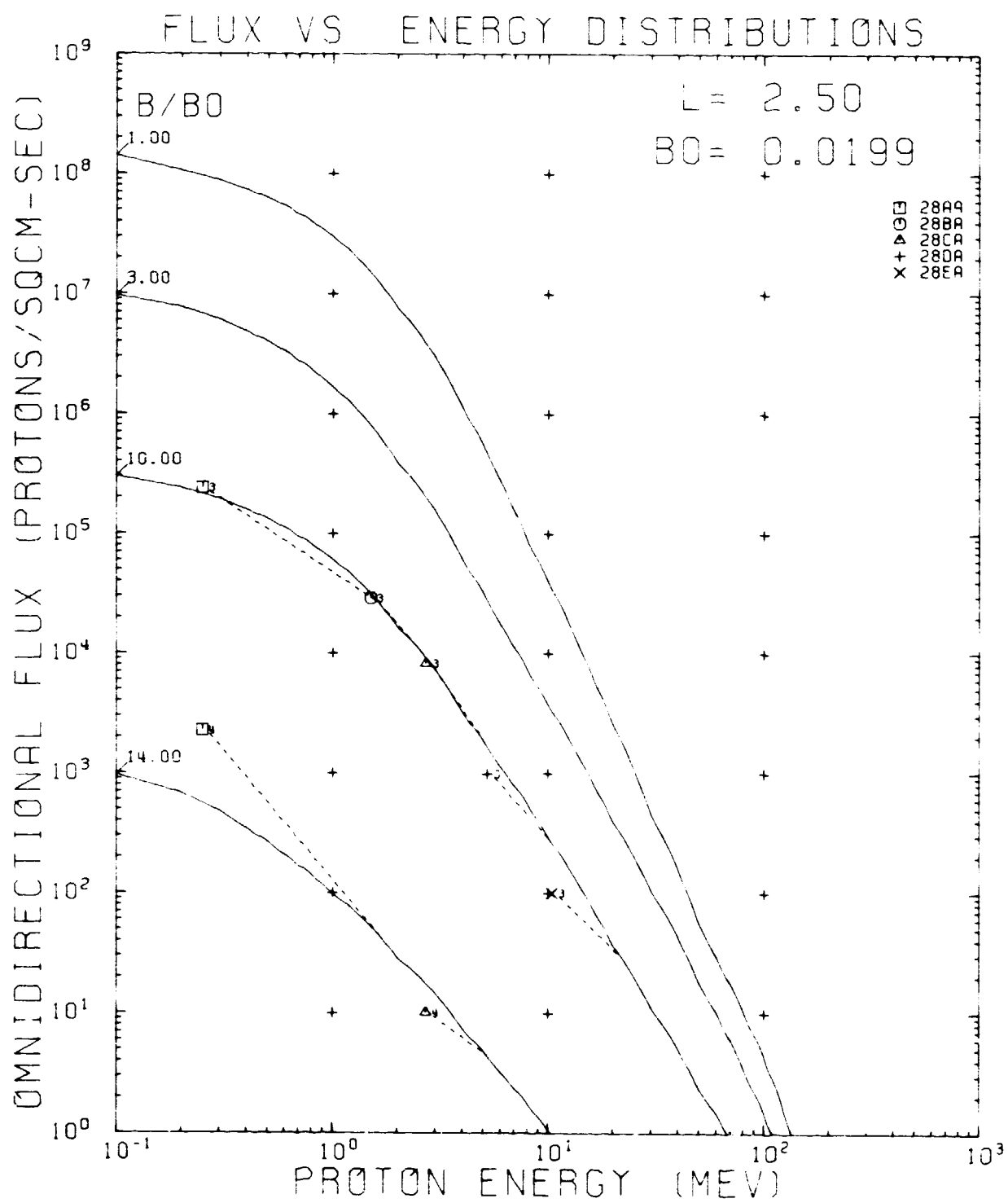


Figure 125. AP8MAX and Data Flux vs Energy Comparison Plot for $L = 2.50 R_E$

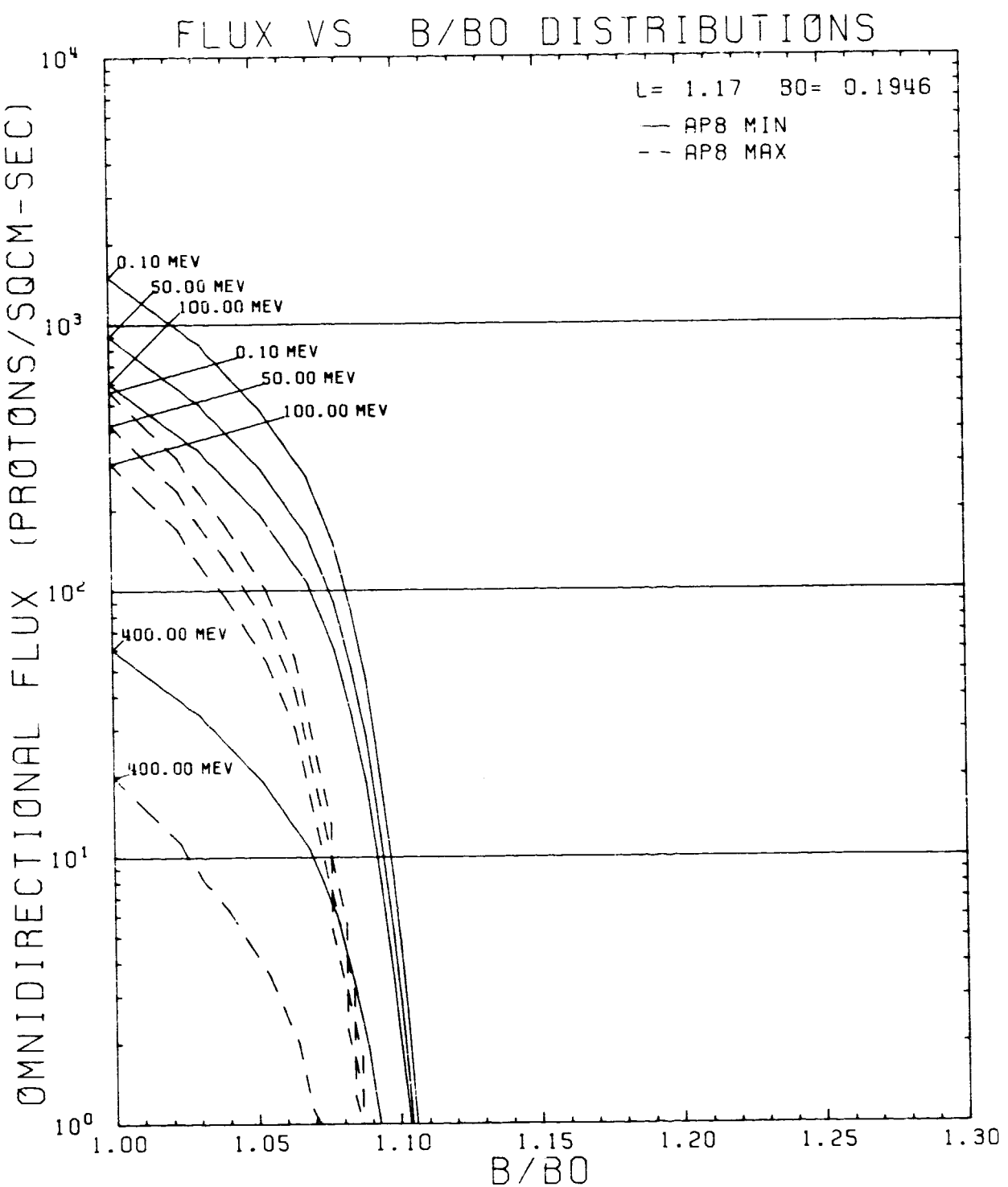


Figure 126. AP8MIN and AP8MAX Flux vs B/B_0 Comparison Plot for $L = 1.17$ RE

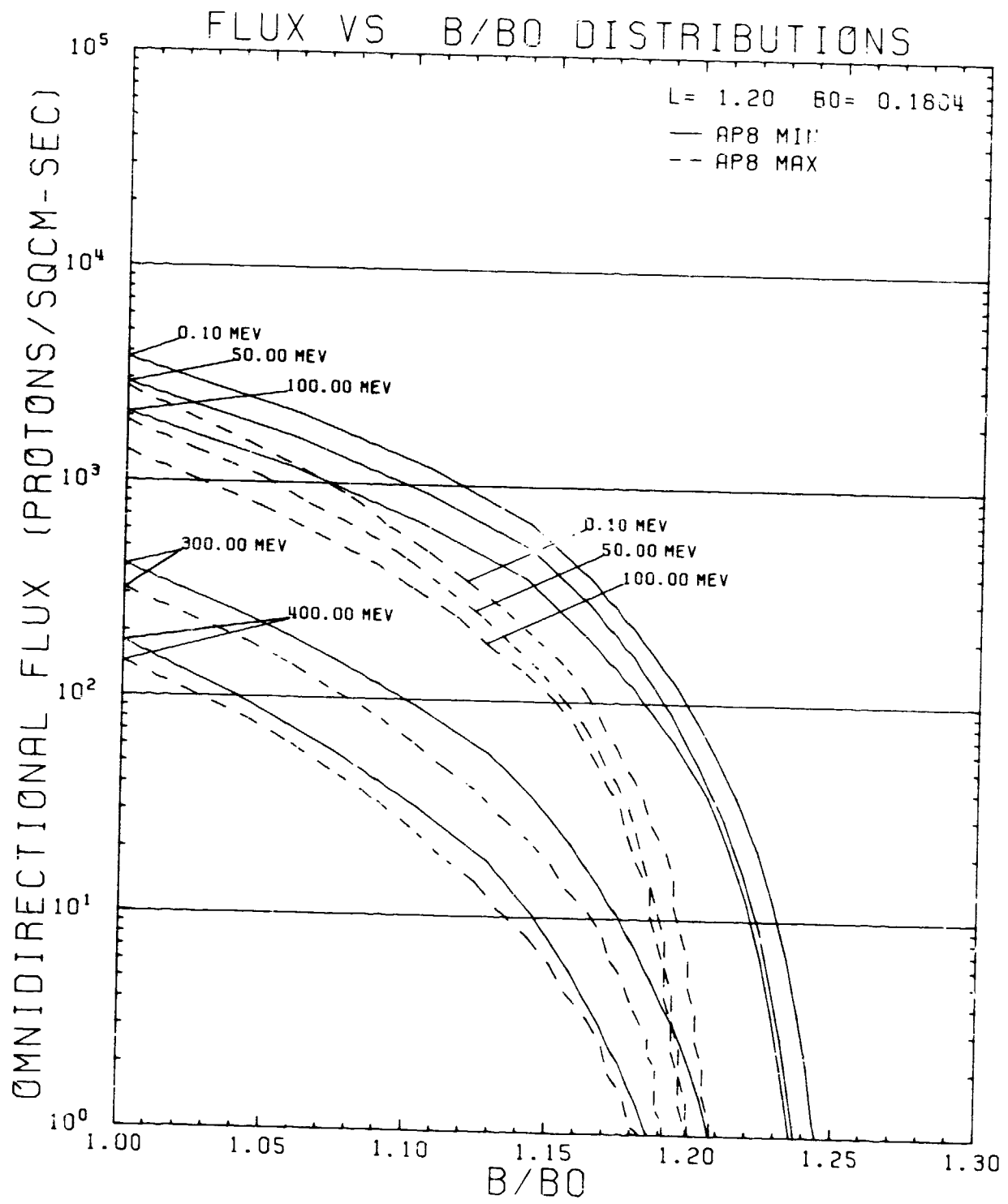


Figure 127. AP8MIN and AP8MAX Flux vs B/B_0 Comparison Plot for $L = 1.20 \text{ RE}$

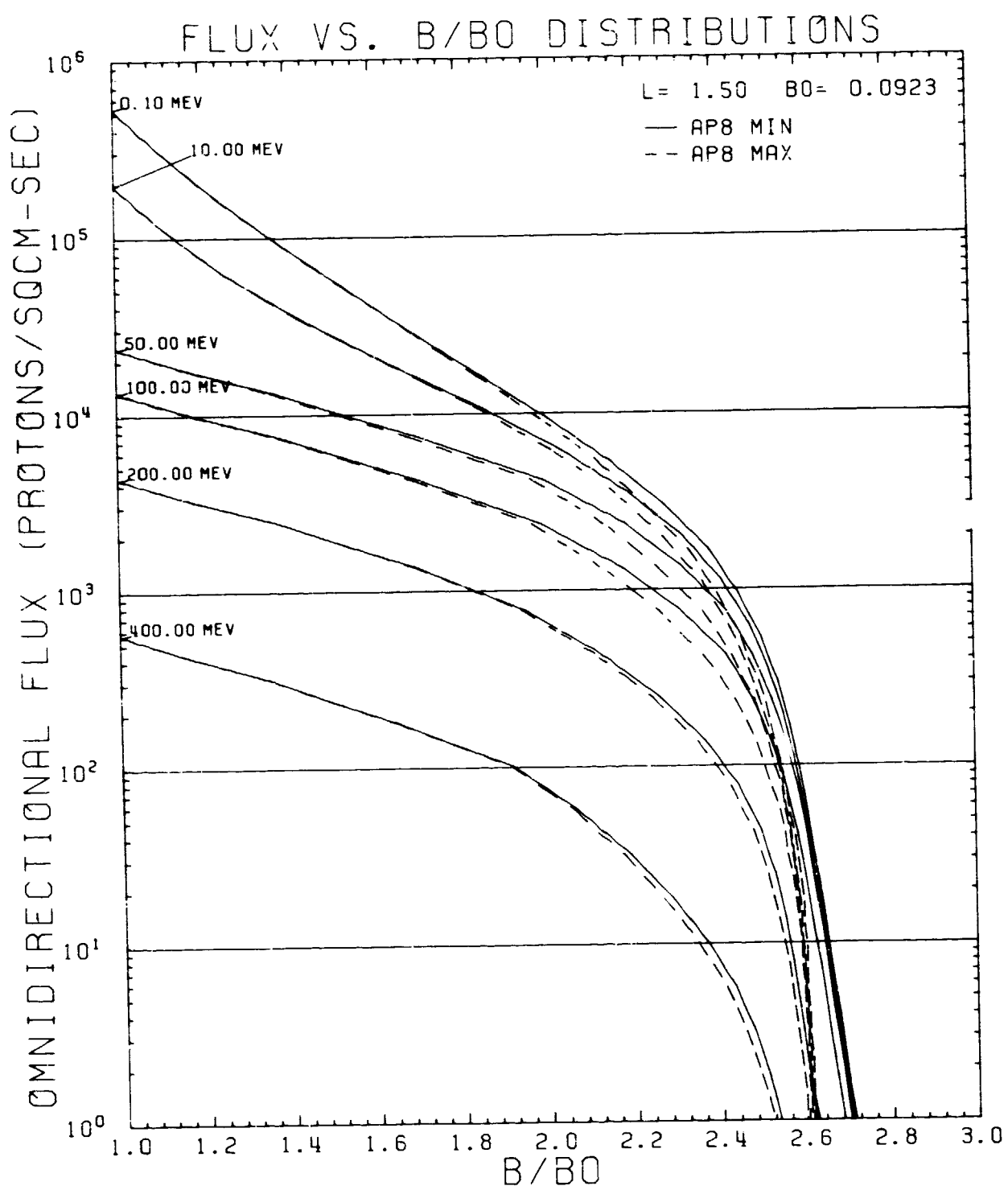


Figure 128. AP8MIN and AP8MAX Flux vs B/B_0 Comparison Plot for $L = 1.50$ RE

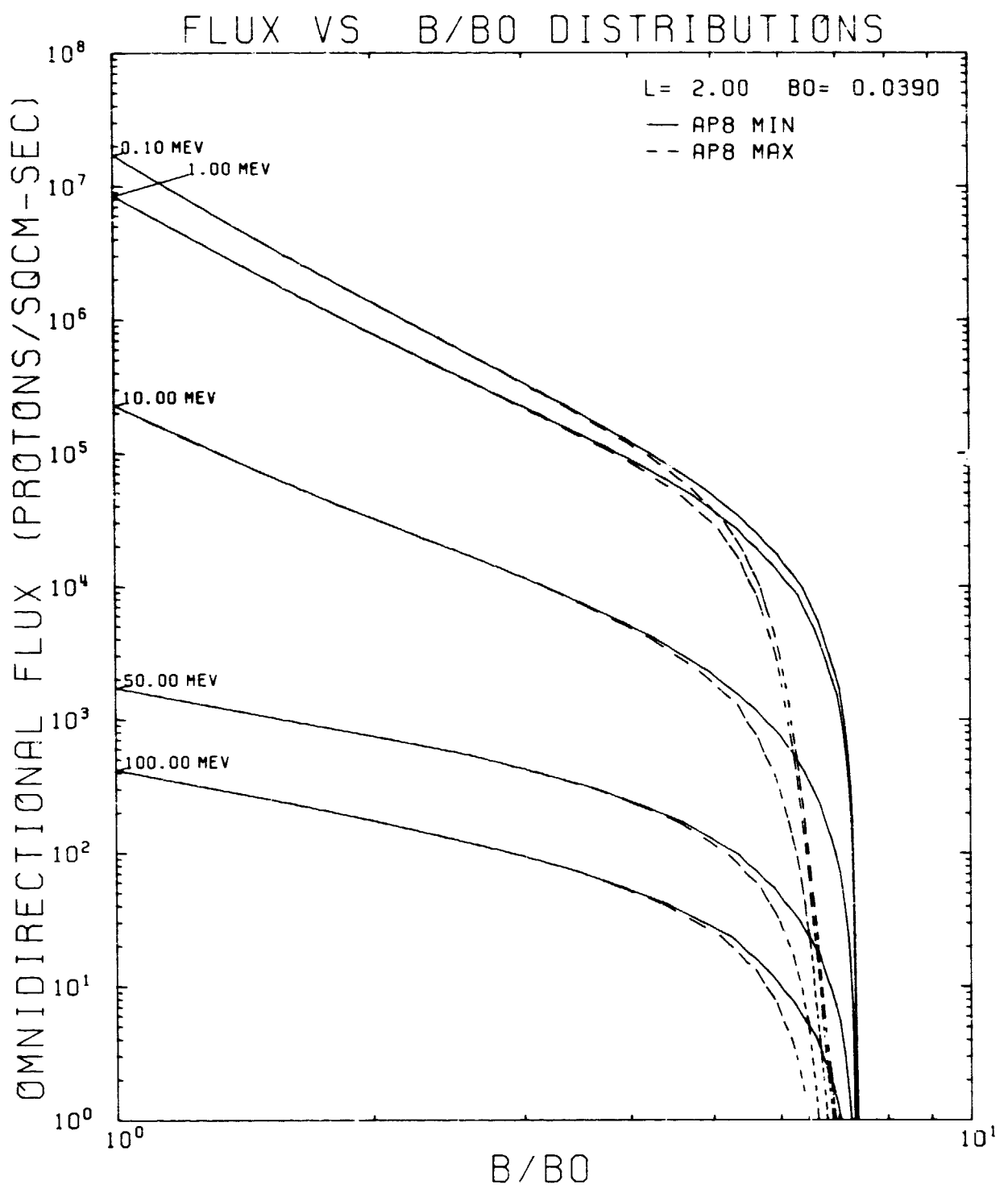


Figure 129. AP8MIN and AP8MAX Flux vs B/B_0 Comparison Plot for $L = 2.00$ RE

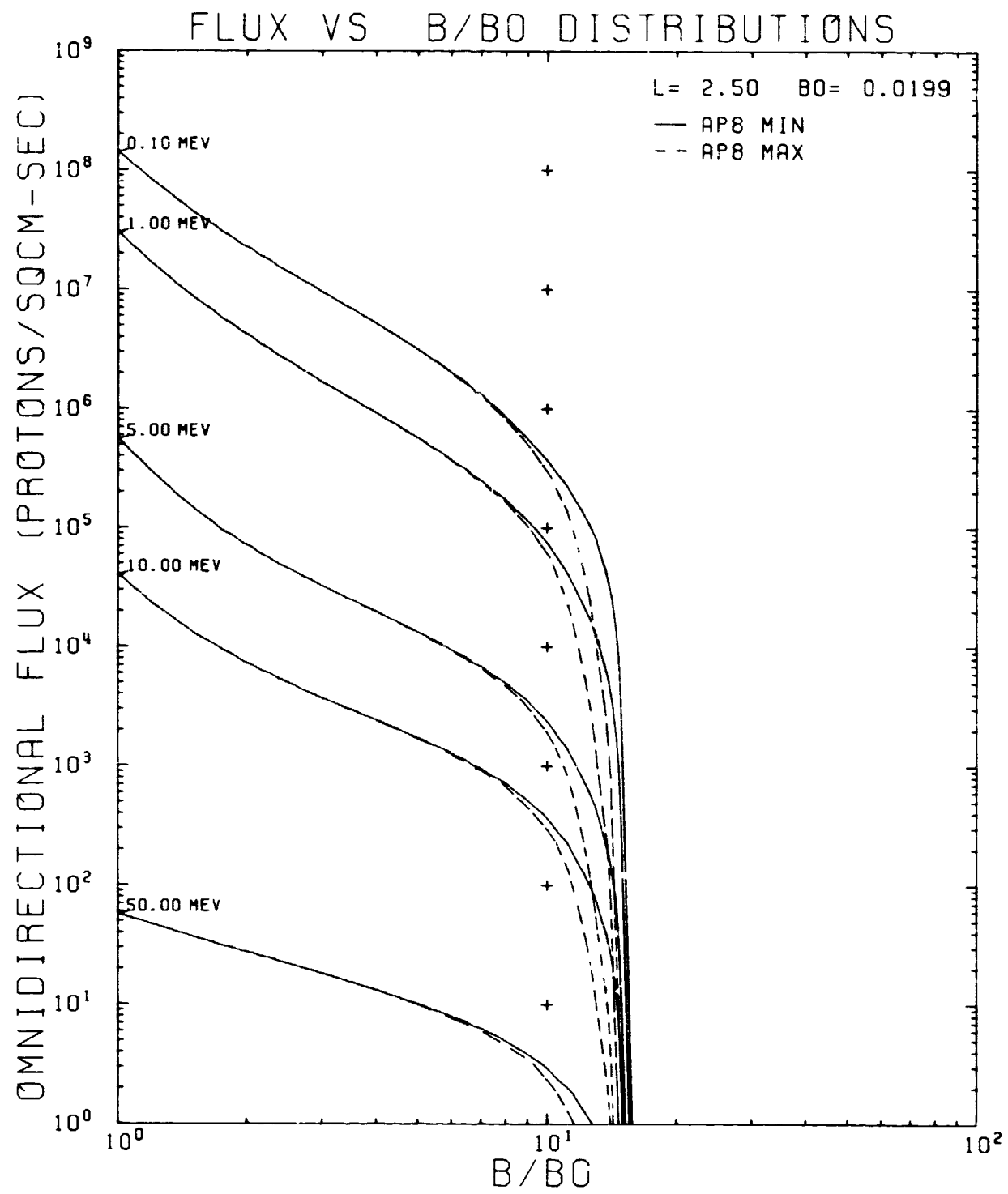


Figure 130. AP8MIN and AP8MAX Flux vs B/B_0 Comparison Plot for $L = 2.50 R_E$

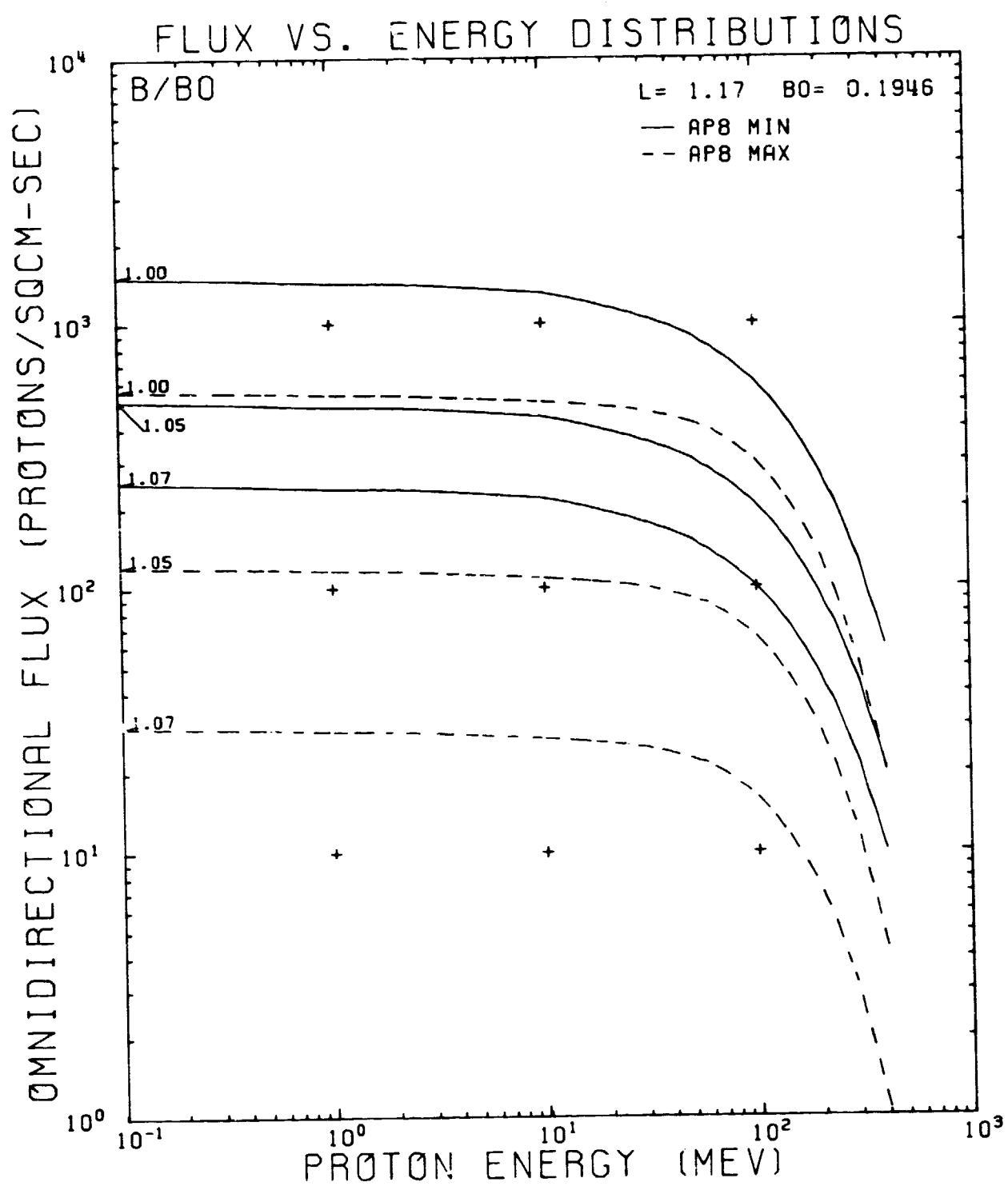


Figure 131. AP8MIN and AP8MAX Flux vs Energy Comparison Plot for $L = 1.17 R_E$

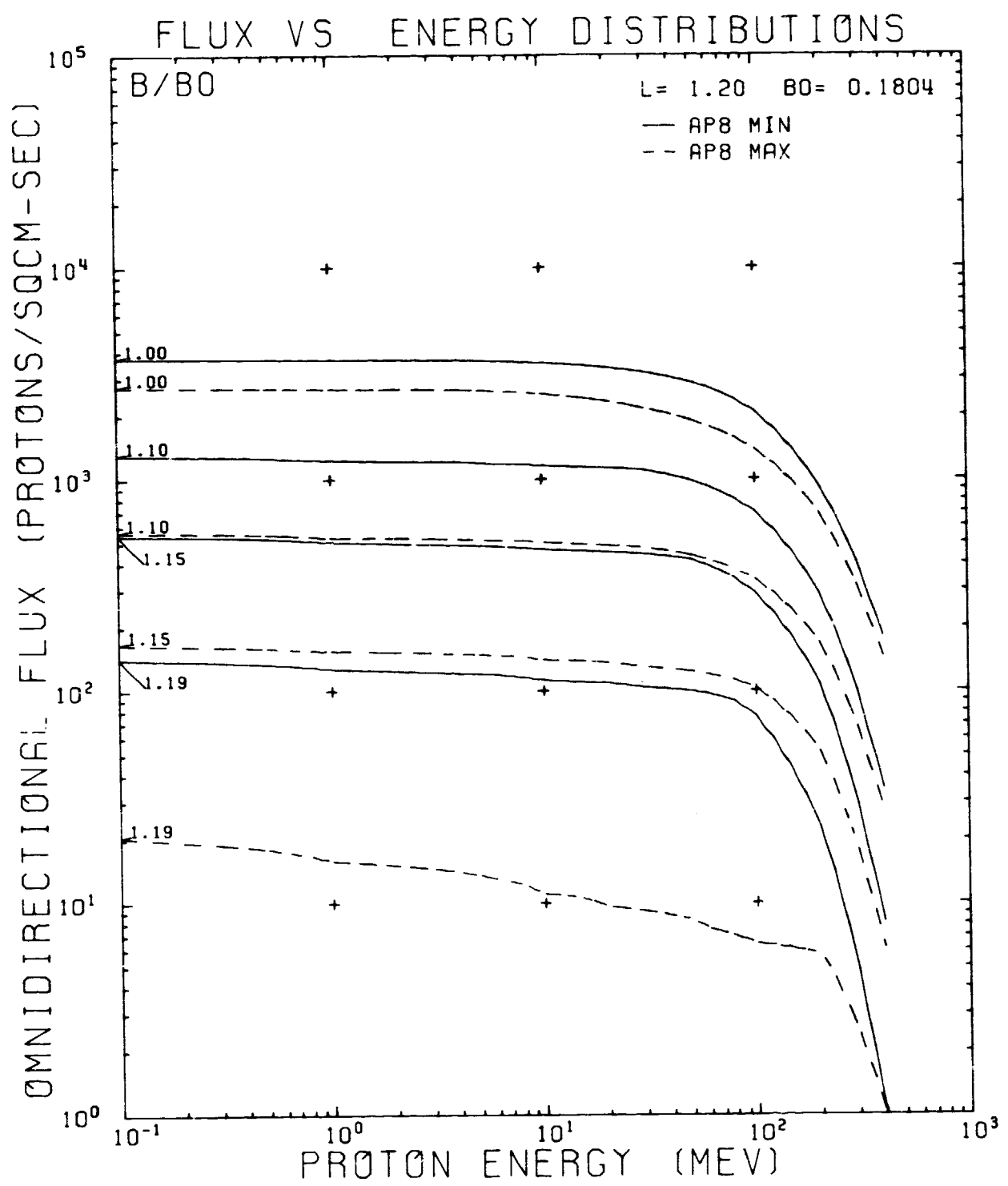


Figure 132. AP8MIN and AP8MAX Flux vs Energy Comparison Plot for L = 1.20 RE

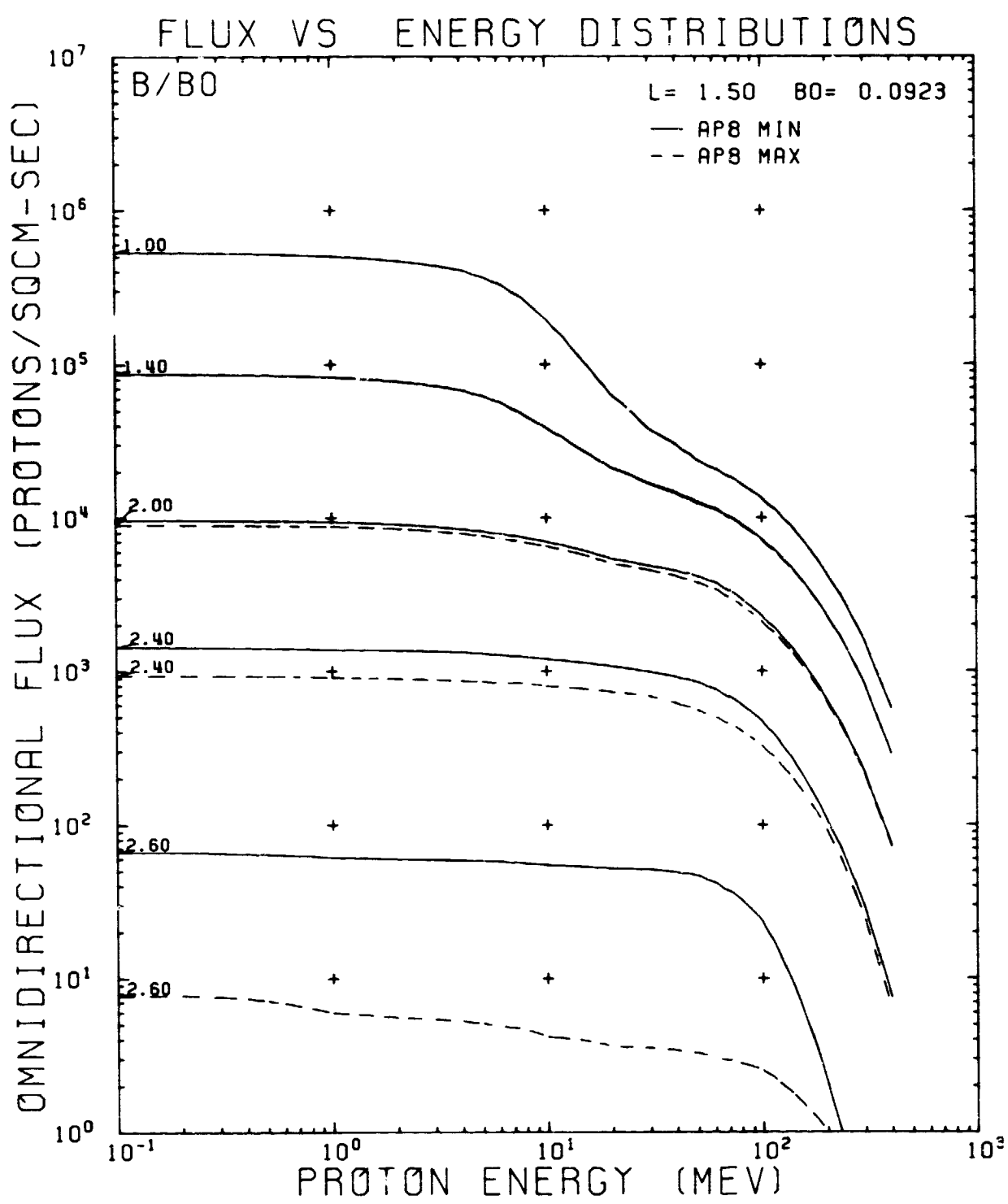


Figure 133. AP8MIN and AP8MAX Flux vs Energy Comparison Plot for $L = 1.50 \text{ RE}$

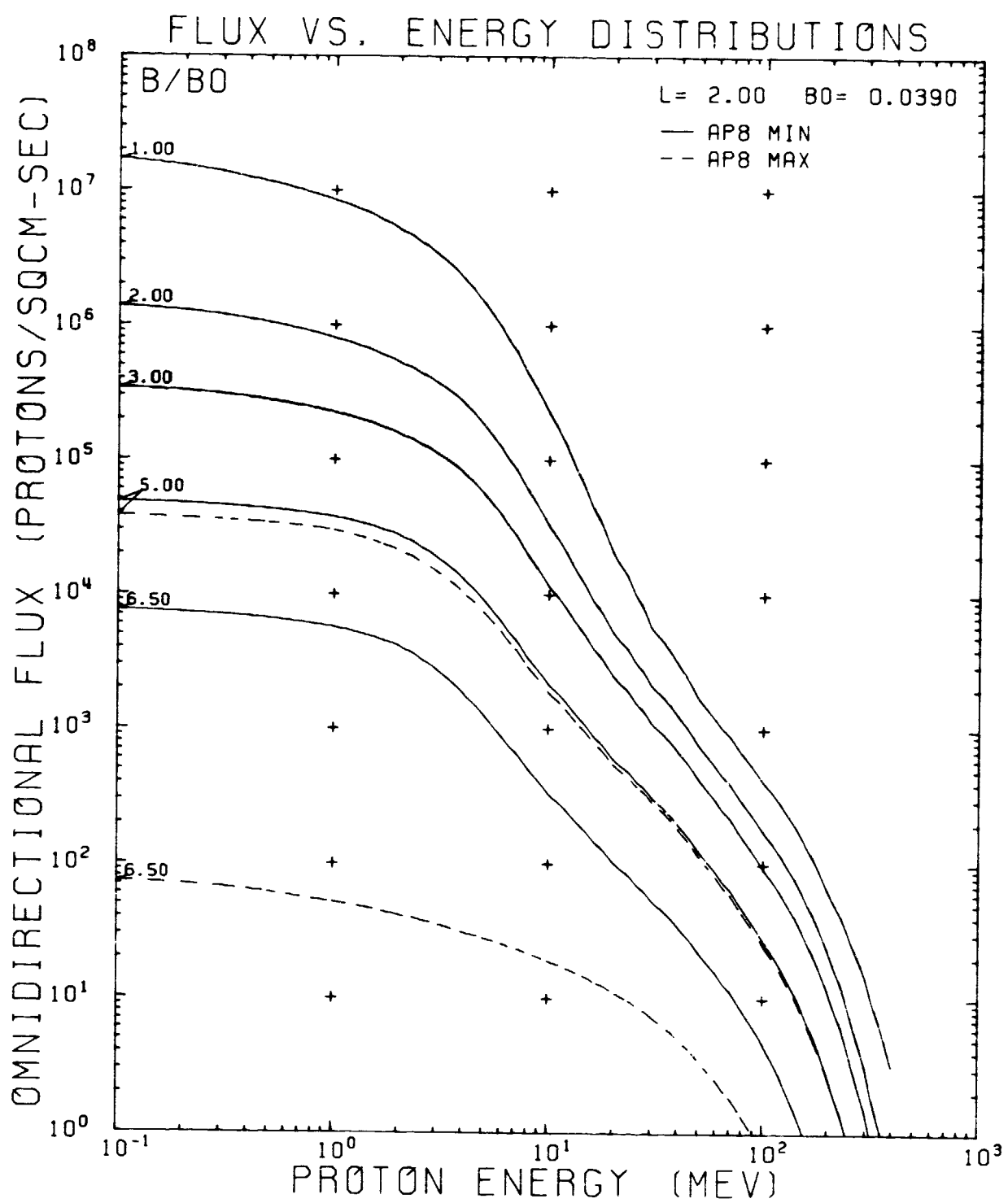


Figure 134. AP8MIN and AP8MAX Flux vs Energy Comparison Plot for $L = 2.00 \text{ RE}$

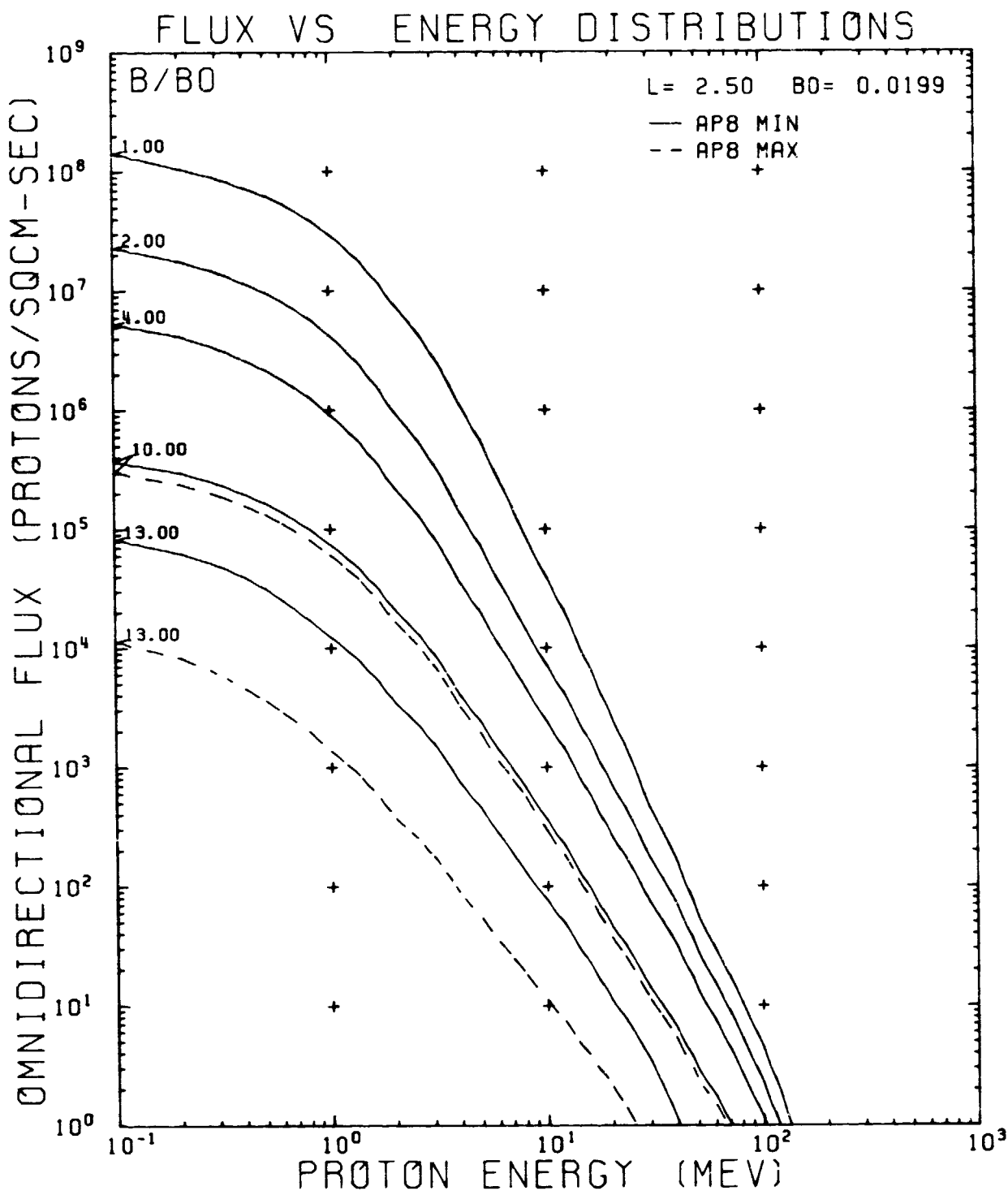


Figure 135. AP8MIN and AP8MAX Flux vs Energy Comparison Plot for L = 2.50 RE

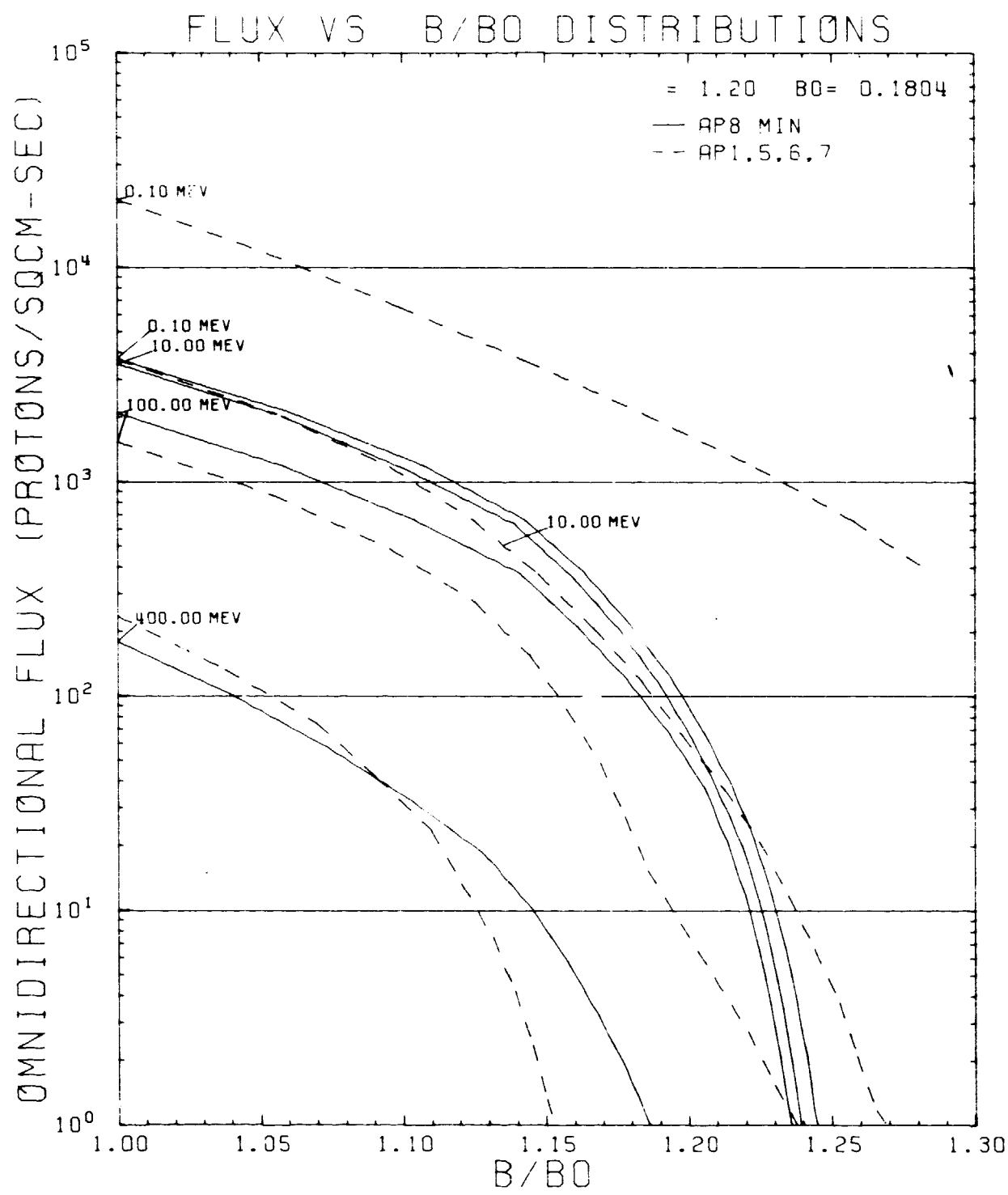


Figure 136. AP8MIN and AP-1, -5, -6, and -7 Flux vs B/B₀ Comparison Plot for L = 1.20 R_E

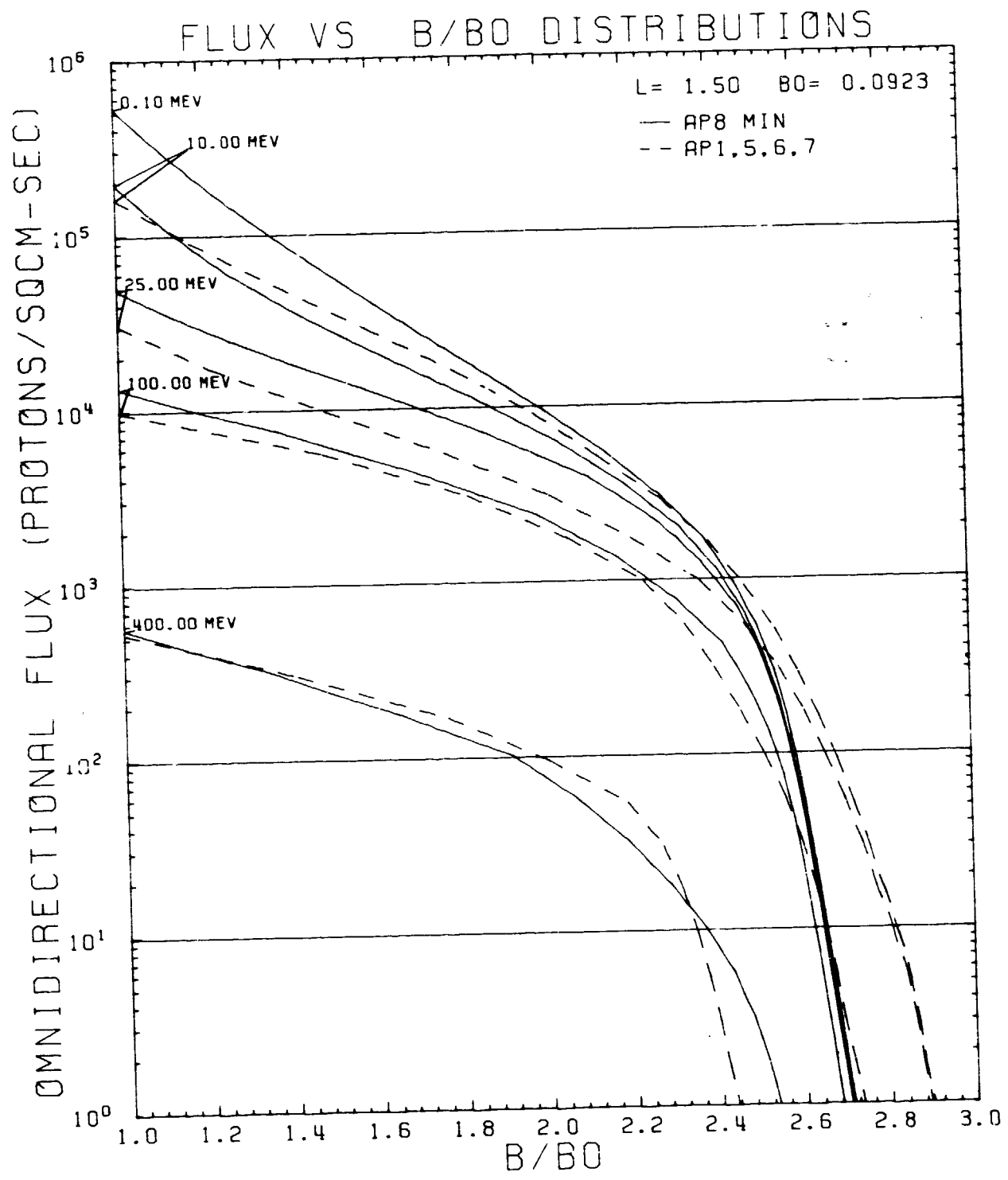


Figure 137. AP8MIN and AP-1, -5, -6, and -7 Flux vs B/B₀ Comparison Plot for L = 1.50 RE

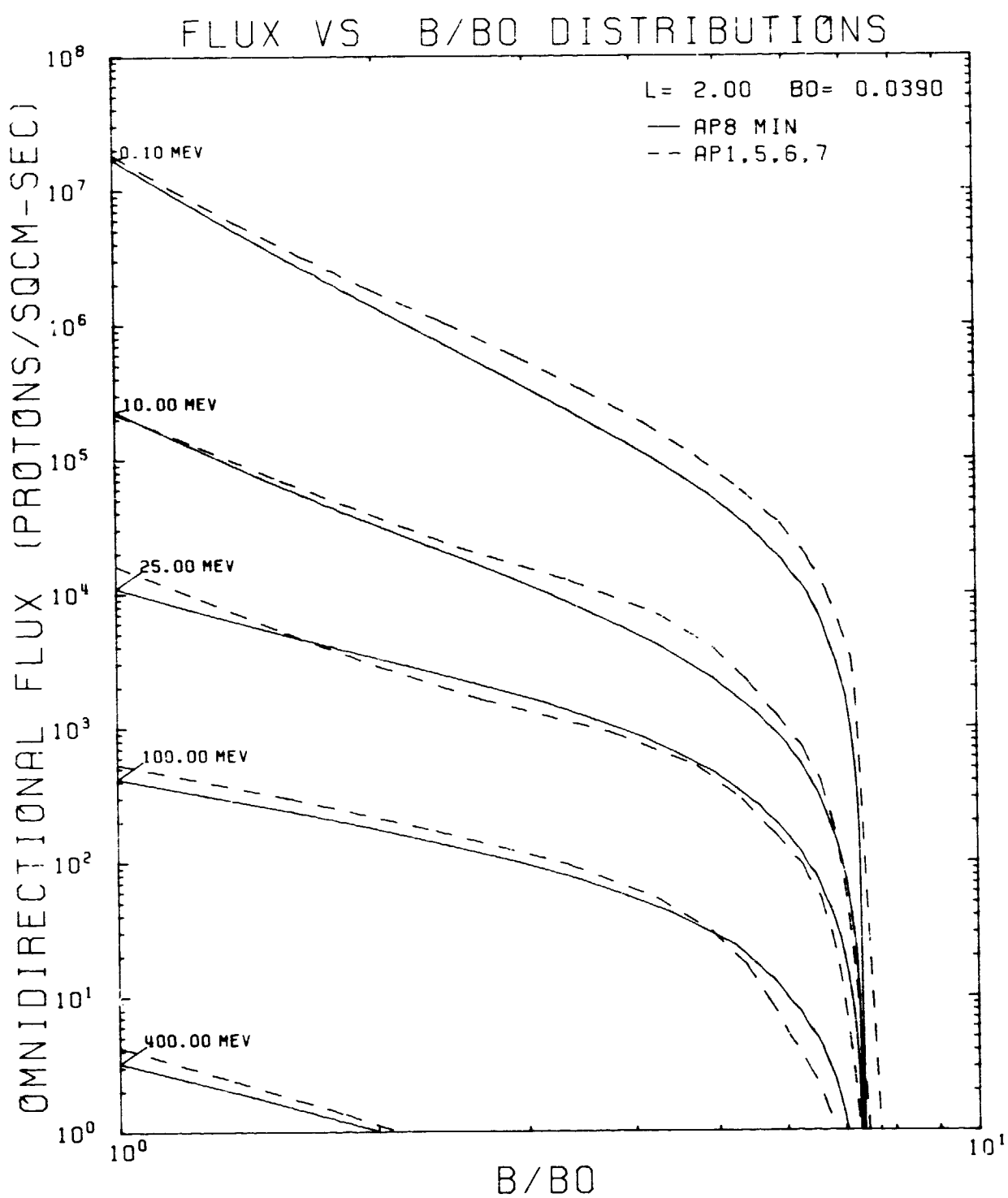


Figure 138. AP8MIN and AP-1, -5, -6, and -7 Flux vs B/B₀ Comparison Plot for L = 2.00 RE

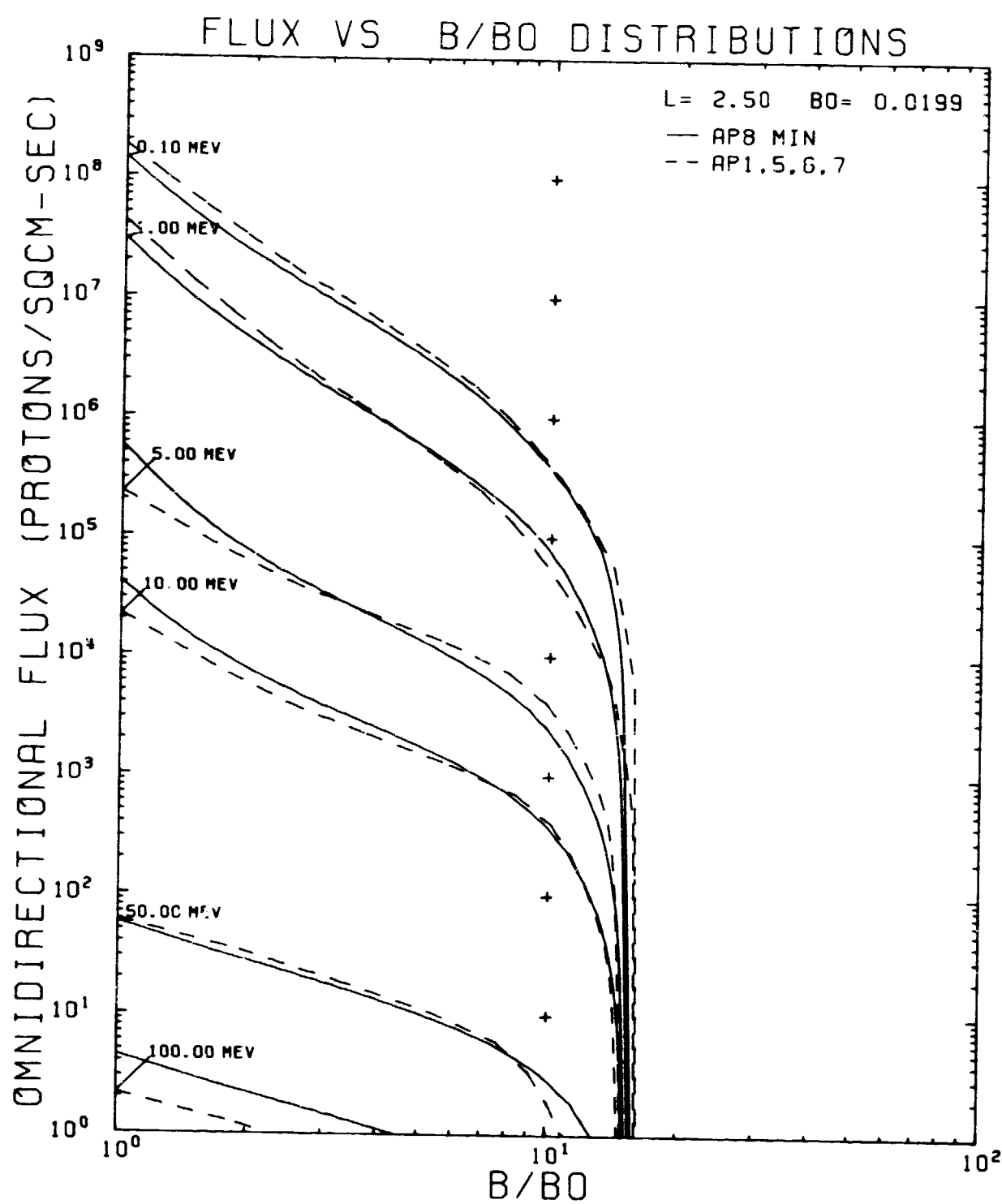


Figure 139. AP8MIN and AP-1, -5, -6, and -7 Flux vs B/B_0 Comparison Plot for $L = 2.50 R_E$

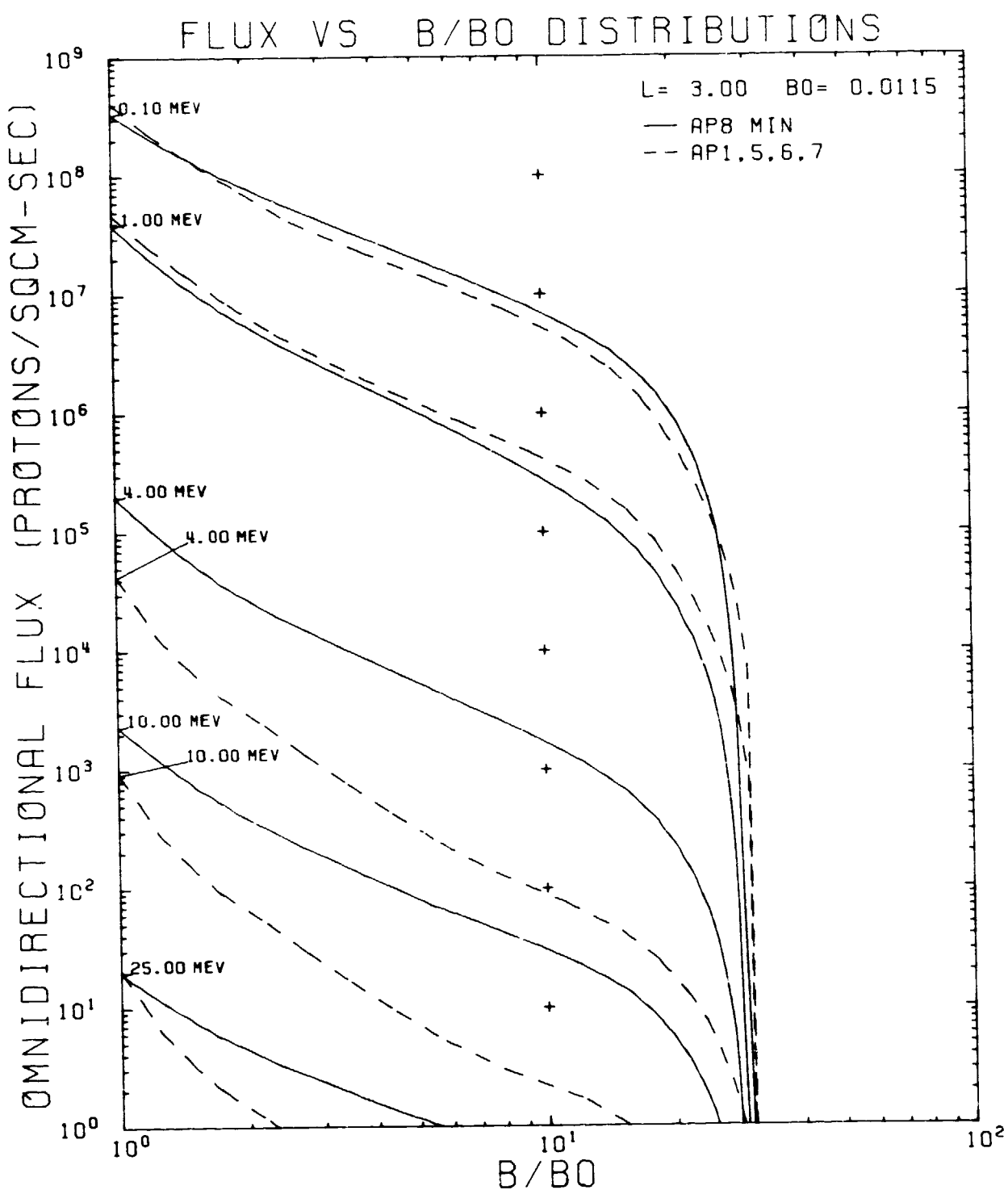


Figure 140. AP8MIN and AP-1, -5, -6, and -7 Flux vs B/B₀ Comparison Plot for L = 3.00 R_E

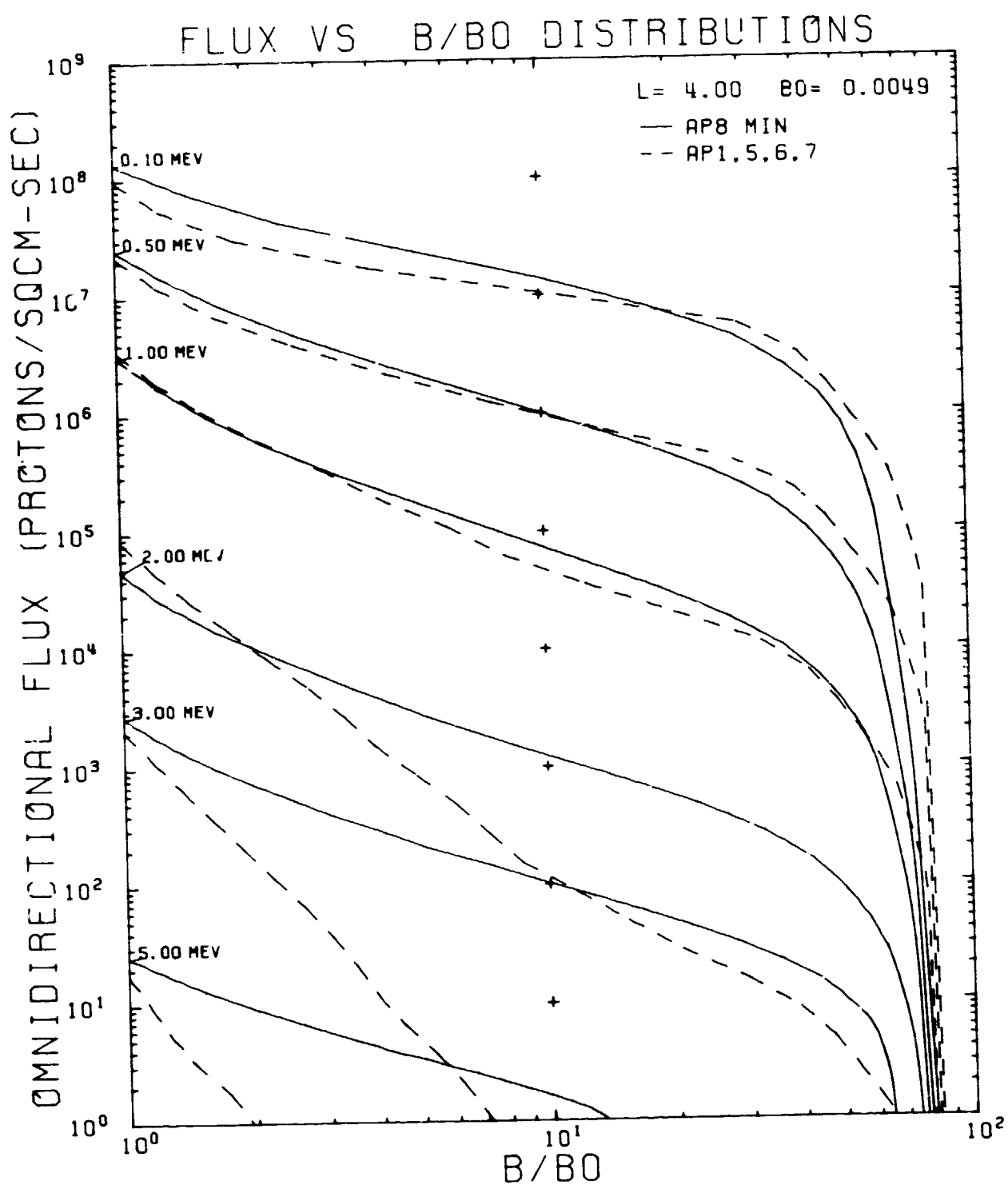


Figure 141. AP8MIN and AP-1, -5, -6, and -7 Flux vs B/B_0 Comparison Plot for $L = 4.00 R_E$

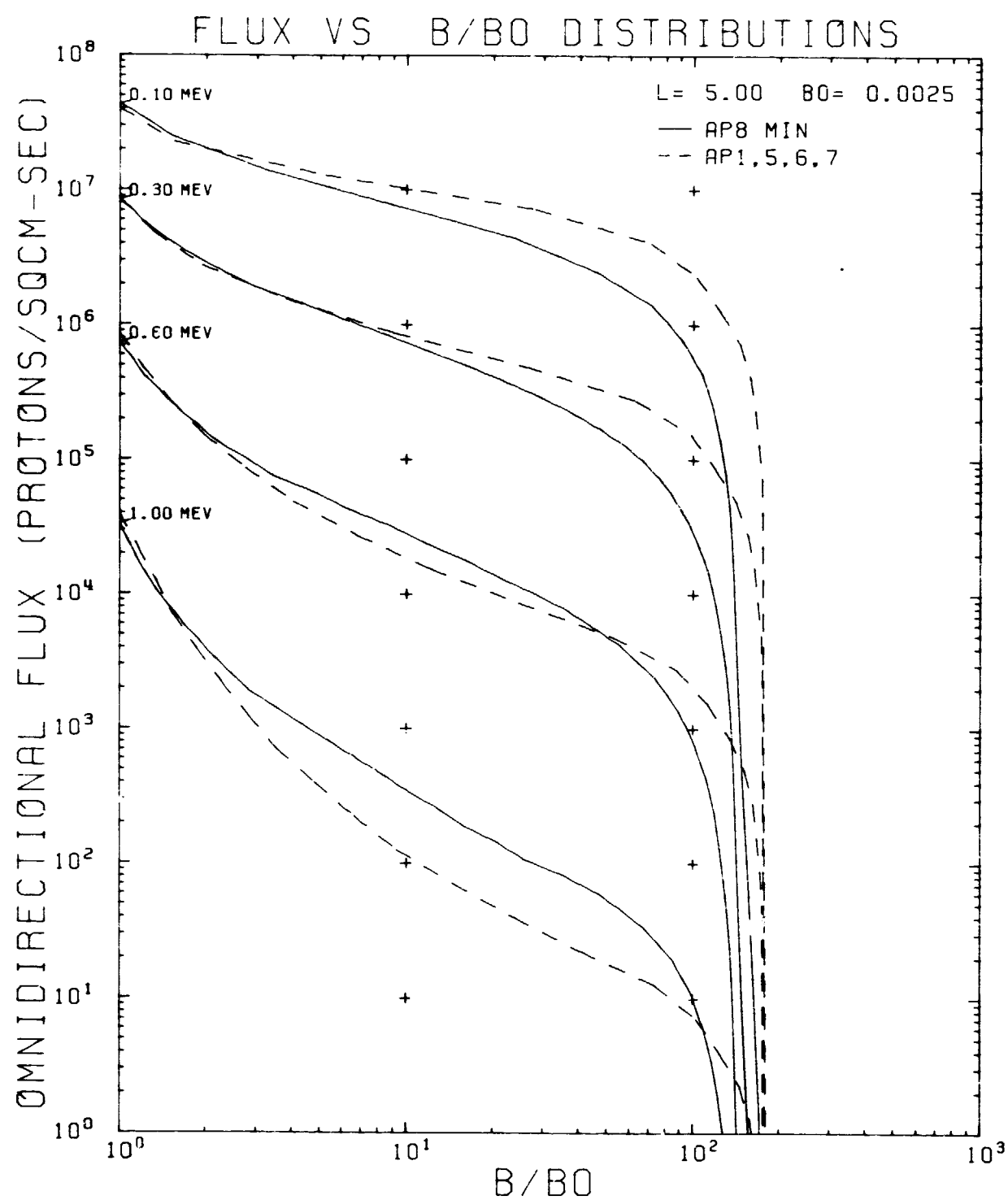


Figure 142. AP8MIN and AP-1, -5, -6, and -7 Flux vs B/B₀ Comparison Plot for $L = 5.00 R_E$

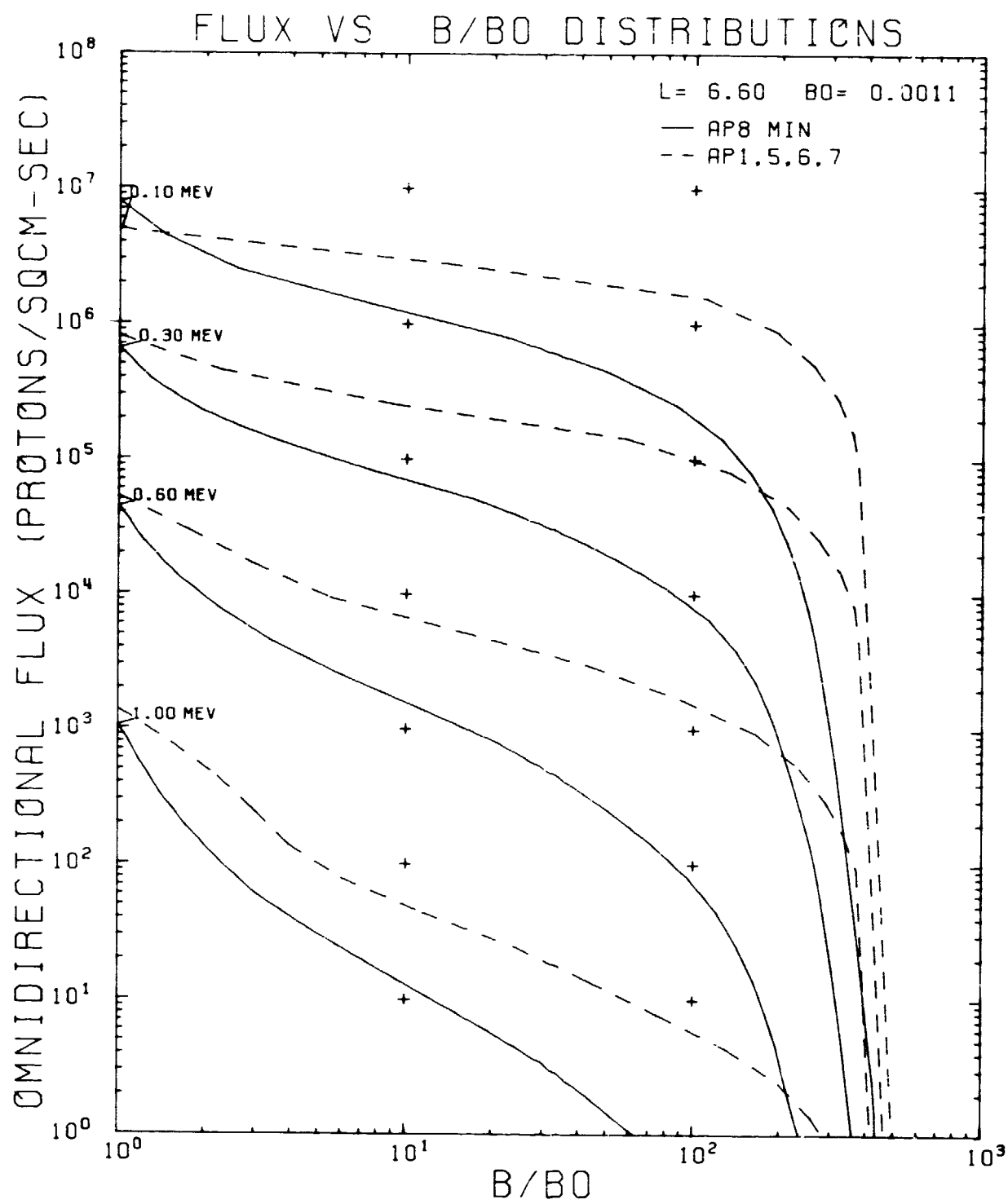


Figure 143. AP8MIN and AP-1, -5, -6, and -7 Flux vs B/B_0 Comparison Plot for $L = 6.60 R_E$

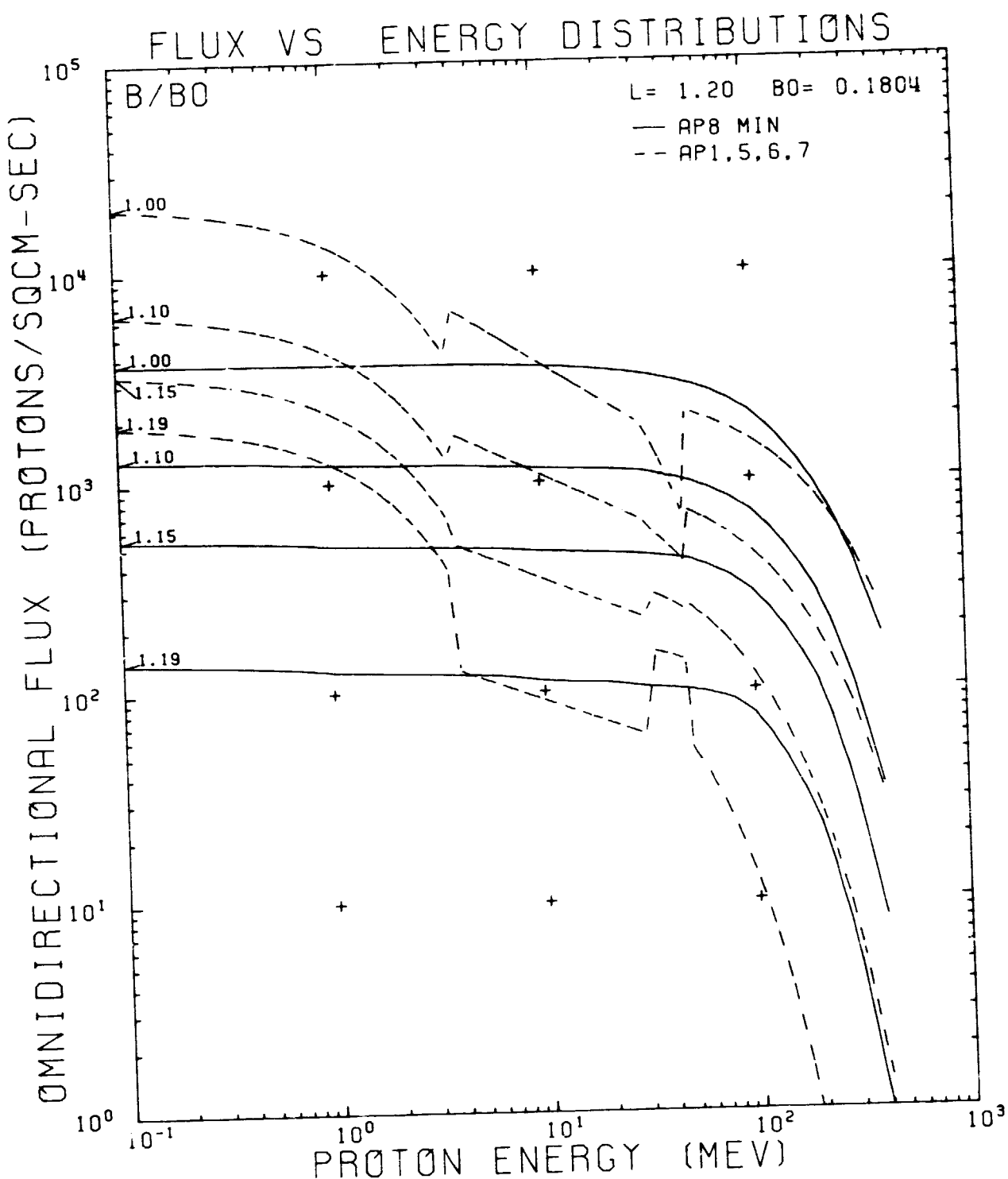


Figure 144. AP8MIN and AP-1, -5, -6, and -7 Flux vs Energy Comparison Plot for $L = 1.20 R_E$

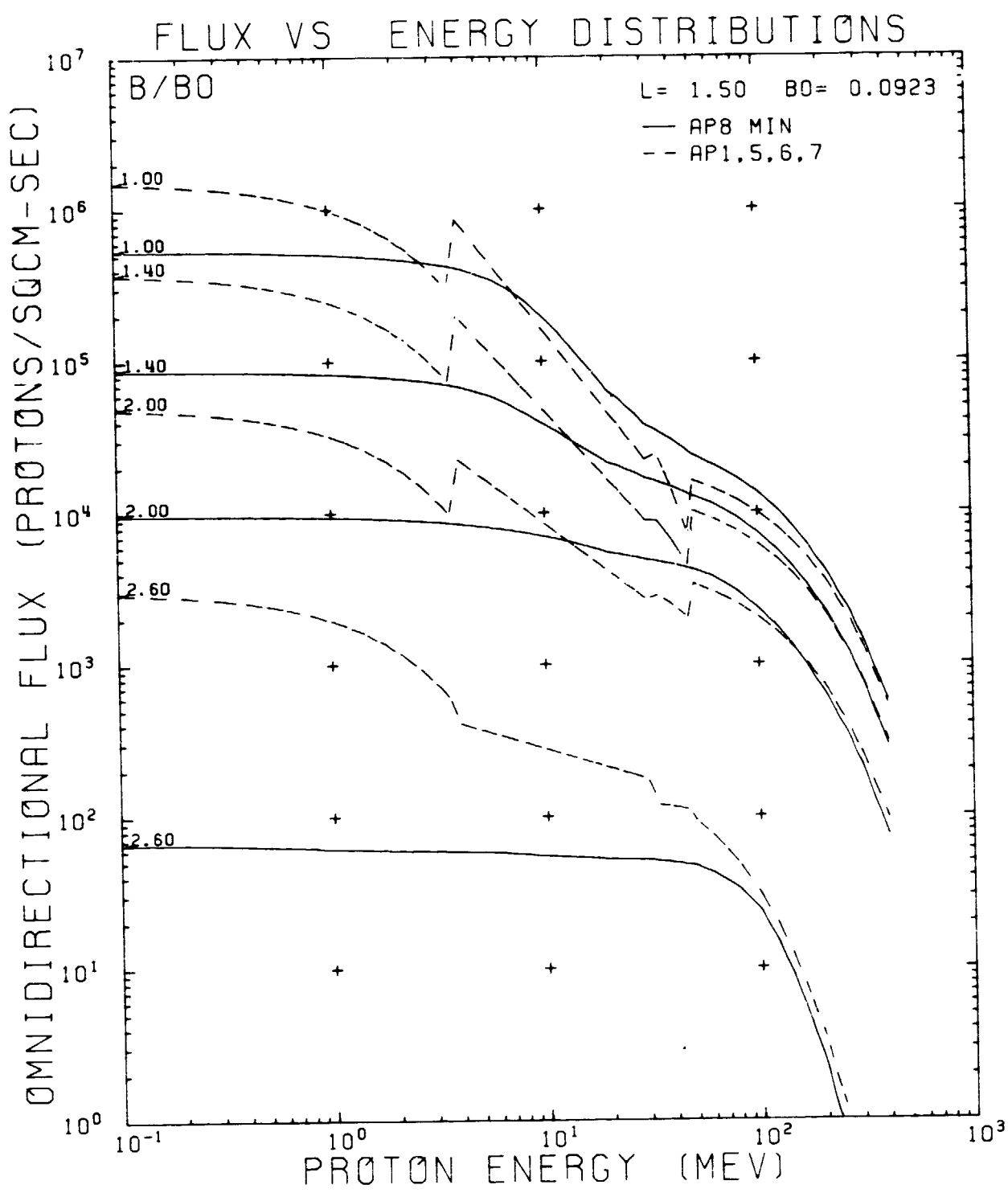


Figure 145. AP8MIN and AP-1, -5, -6, and -7 Flux vs Energy Comparison Plot for $L = 1.50 \text{ RE}$

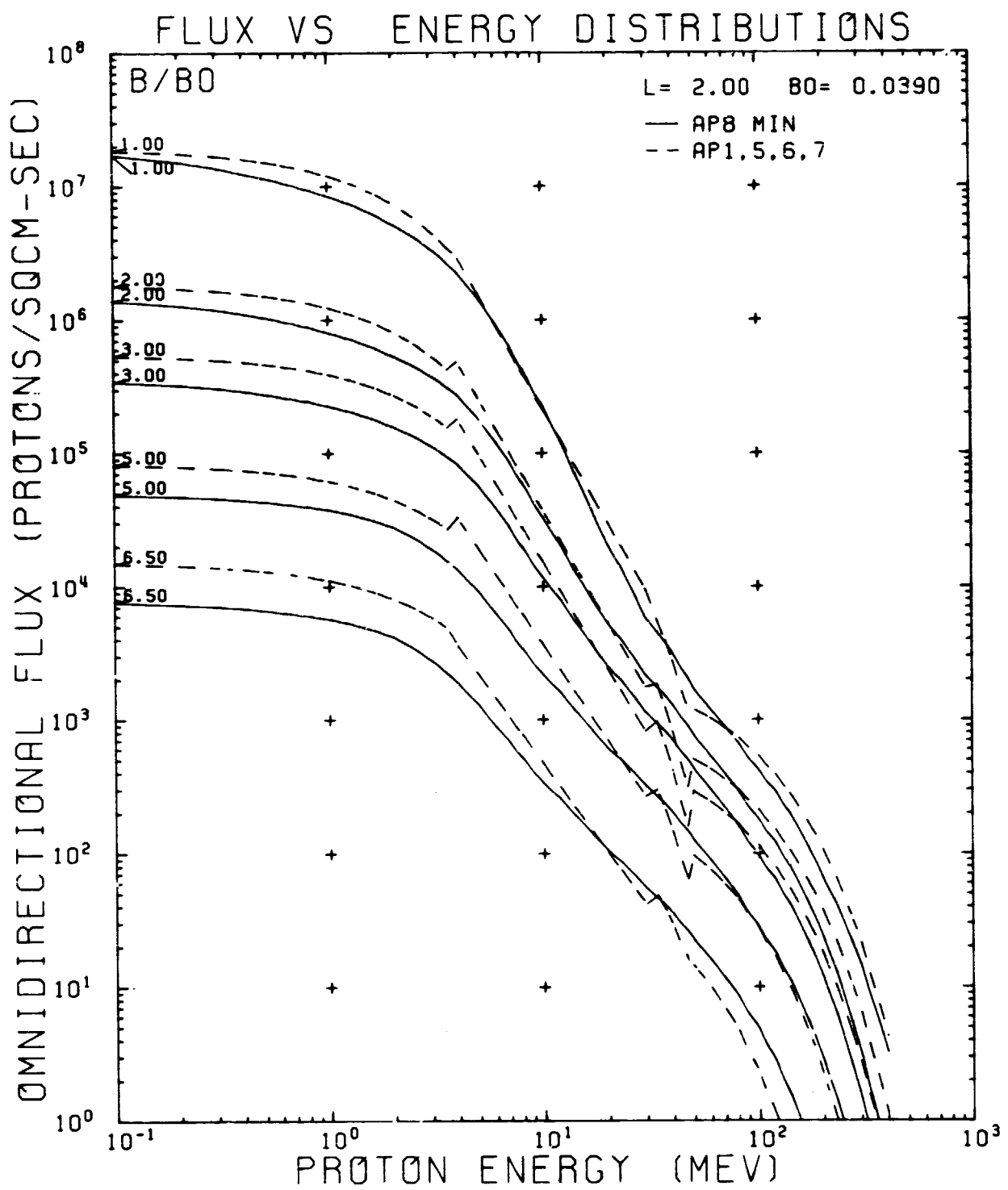


Figure 146. AP8MIN and AP-1 -5, -6, and -7 Flux vs Energy Comparison Plot for $L = 2.00 R_E$

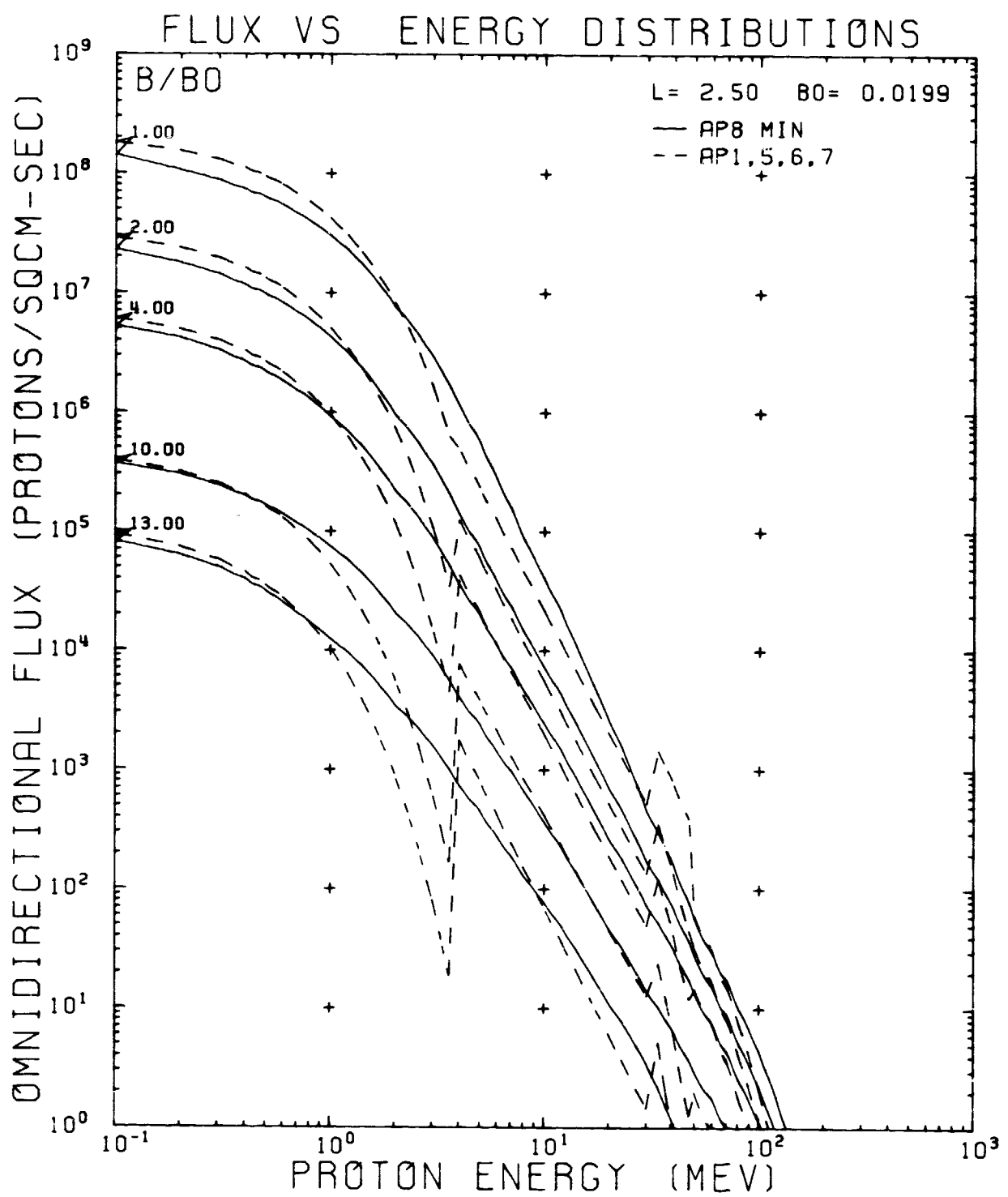


Figure 147. AP8MIN and AP-1, -5, -6, and -7 Flux vs Energy Comparison Plot for L = 2.50 RE

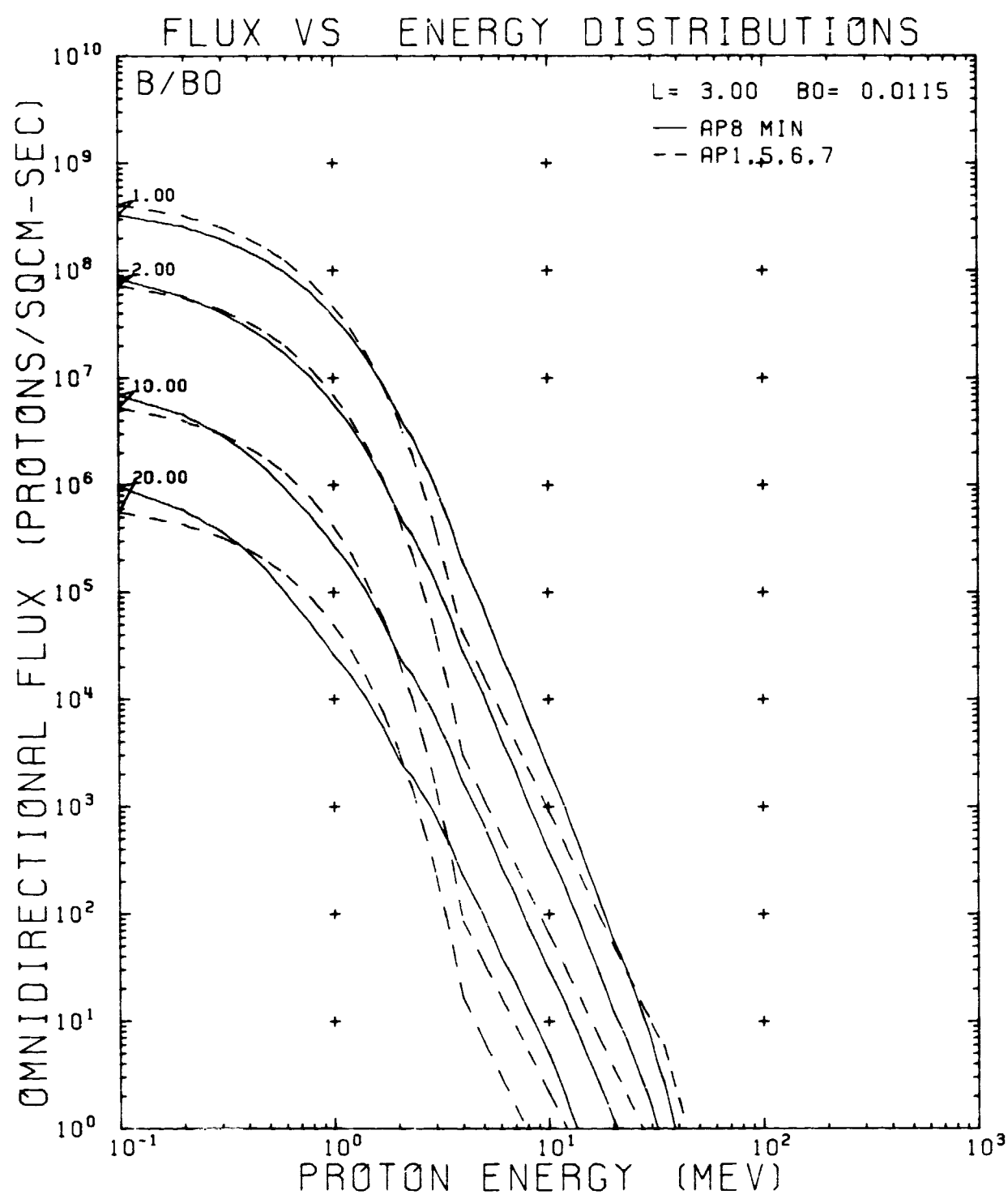


Figure 148. AP8MIN and AP-1, -5, -6, and -7 Flux vs Energy Comparison Plot for $L = 3.00 R_E$

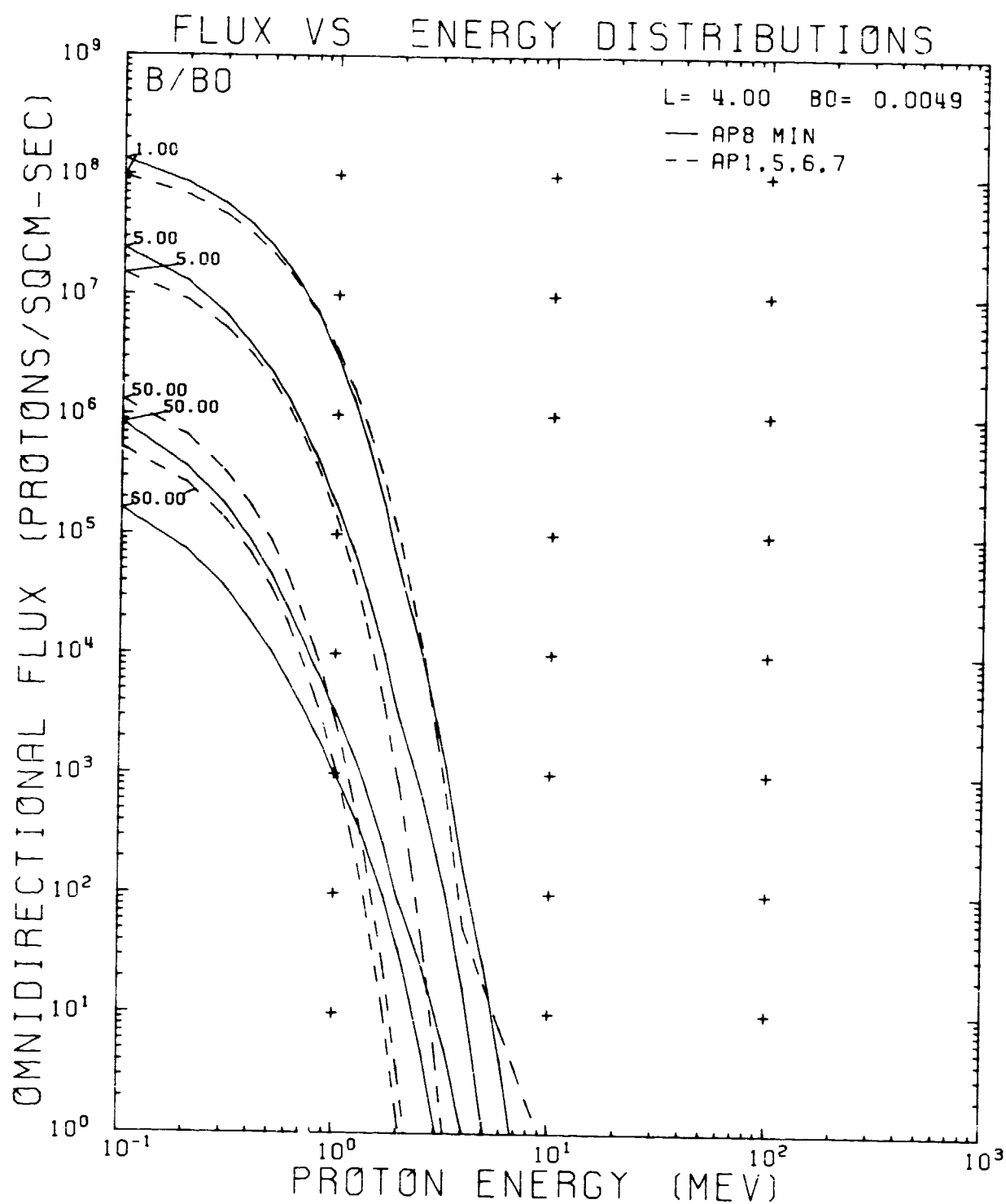


Figure 149. AP8MIN and AP-1, -5, -6, and -7 Flux vs Energy Comparison Plot for $L = 4.00 R_E$

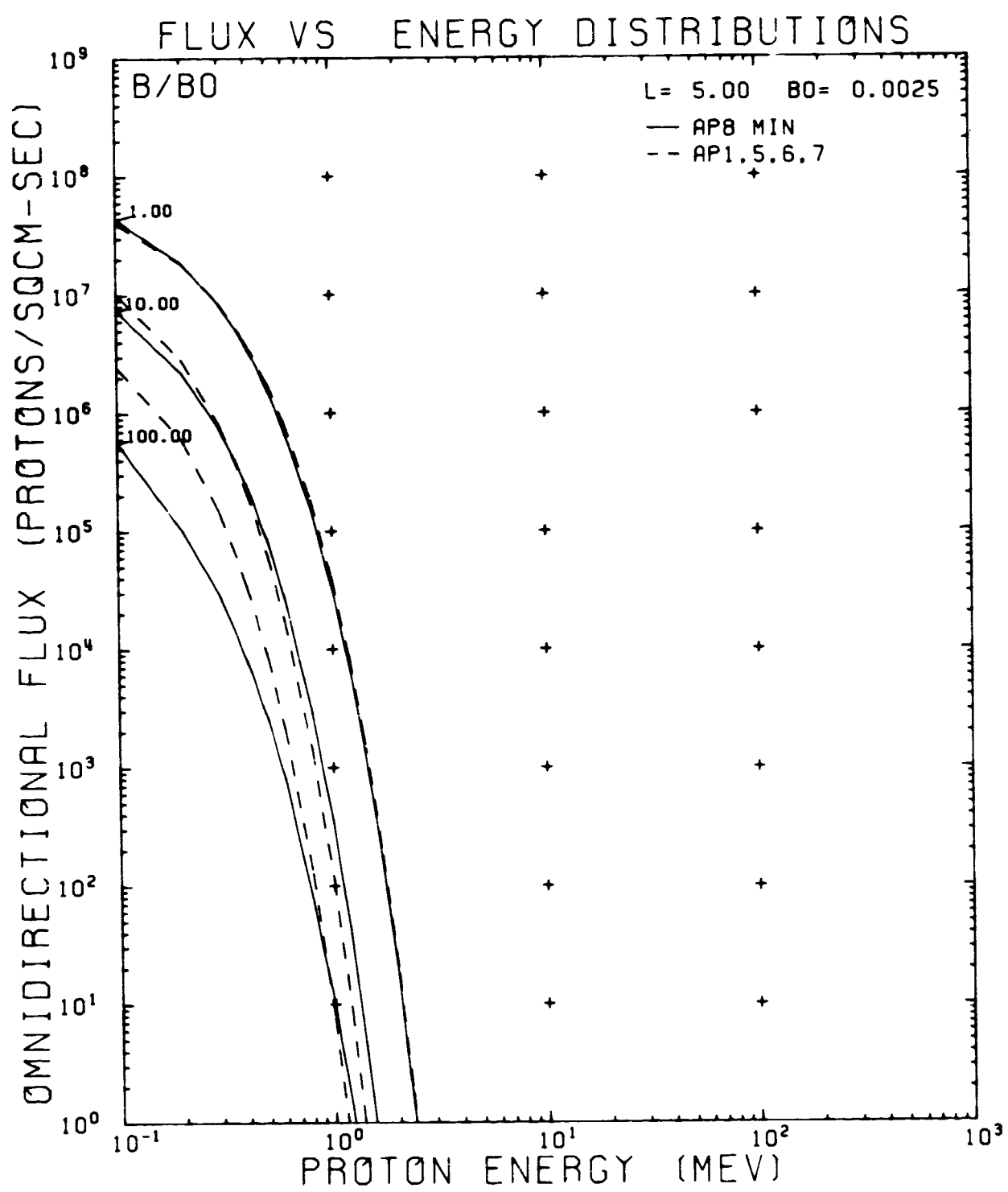


Figure 150. AP8MIN and AP-1, -5, -6, and -7 Flux vs Energy Comparison Plot for $L = 5.00 R_E$

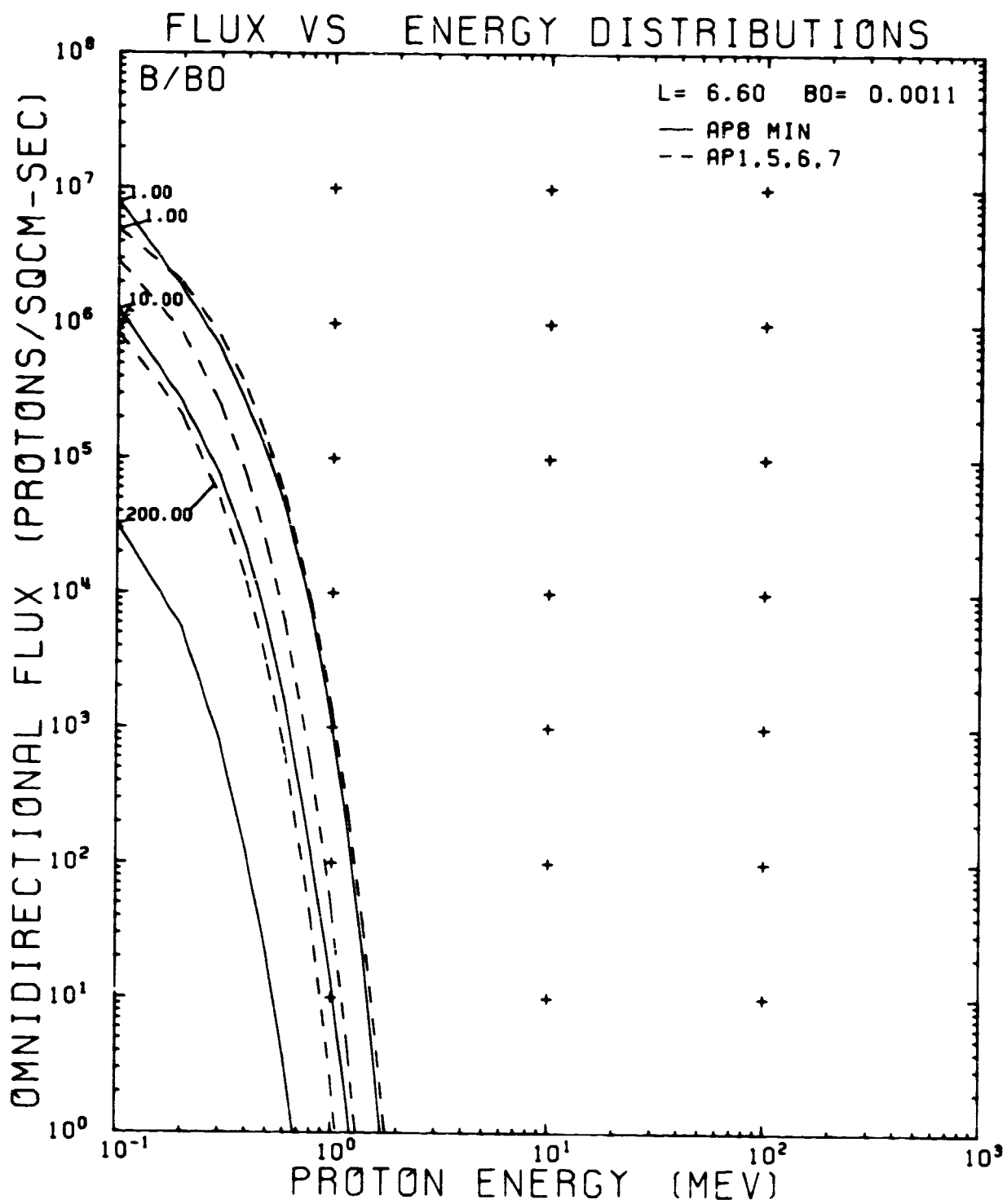


Figure 151. AP8MIN and AP-1, -5, -6, and -7 Flux vs Energy Comparison Plot for $L = 6.60 R_E$

END

DATE

FILMED

APR 15 1977